277
6

WASHINGTON UNIVERSITY

Department of Chemistry

Dissertation Committee:

Dr. Peter Gaspar, Chair
Dr. John Bleeke
Dr. Leonard Gulbransen
Dr. Edward Macias

RESIDUAL STRESSES IN NUMISMATICS

by

Mary Frances Striegel

LD 5791
.8
PhD89
S79
C.1
(AAZ 5659)

A dissertation presented to the
Graduate School of Arts and Sciences
of Washington University in
partial fulfillment of the
requirements for the degree
of Doctor of Philosophy

August 1989

Saint Louis, Missouri

DEDICATION

I dedicate this Dissertation to my longtime friend, Amy Meadows. Her devotion to me was steadfast during the difficult times associated with the completion of my Ph.D. She provided accomodations, hospitality, and comfort to me when I needed them most.

TABLE OF CONTENTS

ACKNOWLEDGEMENTS v

LIST OF TABLES vi

LIST OF FIGURES viii

I. INTRODUCTION 1
A. The Statement of the Problem. 1
1. Review of this Approach to the Problem. 2
B. Residual Stress 4
C. Review of the X-ray Measurement Technique 12
D. Plan of Investigation 16
1. Investigation of Copper Coins 17
2. Investigation of Silver and Gold Coins 19
3. Effects of Coining Pressure on Residual Stress in Struck Coins. 19
4. Residual Stress Analysis for Dating Coins. 19

II. MATERIALS AND EXPERIMENTAL PROCEDURES FOR RESIDUAL STRESS ANALYSIS 24
A. Materials - Coins and Standards. 24
B. The X-ray Diffraction System. 37
1. Diffractometer System 45
2. Sample Placement System 45
a. Sample Mounting. 47
b. Sample Alignment Technique. 47
3. Instrumental Conditions 48

III. RESULTS AND DISCUSSION 50
A. Investigation of Copper Coins 50
1. Experiments using Chromium Radiation. 50
2. Experiments using Cobalt Radiation. 53
3. Variation of Residual Stress with Sample Displacement. 53
4. Residual Stress on Annealed Coins 57
5. Variation of Residual Stress Between Similar Coins. 57
6. Variation of Residual Stress with Location. 59
7. Residual Stress Measurements on Antique Coins. 60
a. Determination of Residual Stresses in Antique Struck Coins. 63
b. Determination of Residual Stress in Cast Counterfeit Coins 66
B. Investigation of the Effects of Abrasion on Coins 70
C. Investigation of Silver and Gold Coins 73
1. Residual Stress Measurements on Silver Coins 73
2. Residual Stress Measurements on Gold Coins 76

D. Examination of the Effects of Coining Pressure on Residual Stress 77
1. Residual Stress Measurements on Coining Blanks. 77
2. Residual Stress Measurements on "Phantom" Coins. 79

IV. CONCLUSIONS 84
A. Significance of Results 84
1. Residual Stresses in Struck Coins 84
2. Effect of Coining Alloy 84
3. Residual Stresses in Cast Coins. 85
4. Differentiation of Struck and Cast Coins by Residual Stress Analysis. 85
5. Residual Stress in "Phantom" Coins 86
6. Residual Stress Analysis was a Technique for Dating Coins 86
B. Suggestions for Further Research. 87
1. Neutron Diffraction as a Technique to Study Coins 88
2. Acoustic Techniques for the Study of Coins 91
a. Basic Definitions in Physical Acoustics 91
b. Scanning Acoustic Microscopy 96
c. Acoustic Holography 104

APPENDIX A. DETERMINATION OF COIN COMPOSITION USING X-RAY FLUORESCENCE ANALYSIS. 110

APPENDIX B. STATISTICAL ANALYSIS OF DATA 117
A. Standard Deviation of Residual Stresses from Sin^2 Psi Techniques. 117
B. Weighted Average of Residual Stress Data 118
C. Comparison of Data using the Student's t-test 119

APPENDIX C. THE PRODUCTION OF "PHANTOM" COINS 120
A. An Overview of the Minting Process of the U.S. One Cent Piece. 120
B. An Investigation of the Design an Metallography of the 1968 U.S. One Cent Piece. 122
1. The Metallography of Coins and Blanks 124
a. Experimental Procedures for Metallography 124
b. Annealing of Olin blanks. 124
C. Rimming Machine and Rimming of Annealed Olin Blank. 128
D. The Design of the Die and the Die System 128
E. Experimental Procedures for Striking "Phantom" Coins 131
F. Observations on "Phantom" Coins and Coining Process. 137

APPENDIX D. D VERSUS SIN SQUARE PSI PLOTS 139

LIST OF REFERENCES 209

ACKNOWLEDGEMENTS

I would like to thank Dean J.B. Cohen of the Technological Institute at Northwestern University for providing me the opportunity to measure residual stresses on coins there. I would also like to acknowledge the members of his research group, particularly Carla Shutz and Andrew Winholtz, for providing instruction and guidance in x-ray techniques and the actual measurements. Many of the antique coins subjected to residual stress measurements were loaned by Eric P. Newman, whose interest, encouragement and financial support were vital to this project. I also acknowledge the financial support provided for the research by the Department of Chemistry and the Graduate School of Arts and Sciences at Washington University. Technical support in building the coining equipment was provided by the Chemistry Department machine shop, and particularly by Walter Nowell. Other technical support for this project was received from the following: Fred Inman, Gary Seaman, and the Olin Brass Corporation of East Alton, Illinois, donated the coining blanks and provided use of their X-ray Fluorescence Spectrometer; Paul Sinn and St. Louis Testing, provided X-radiography and electron microscopy on related work; and Julius Turk and Paulo Products provided microhardeness testing. Dr. Leonard Gulbransen of the Department of Mechanical Engineering at Washington University provided helpful discussions of this project. A special thanks goes to the members of Professor Peter Gaspar's research group for providing a warm, supportive atmosphere in which to work. Most of all, I would like to thank Professor Peter Gaspar for inspiring me and believing in me.

LIST OF TABLES

Table I. Elemental Composition of Coins and Standards Investigated in this Project. 25

Table II. Characteristics of Diffraction Profile for Each Sample 39

Table III. Instrumental Conditions for the Picker Diffractometer. 49

Table IV. The Measured Residual Stress in a 1968 U.S. One Cent (#34) using Chromium Radiation 52

Table V. Penetration Depth in Various Metals as a Function of Radiation. 54

Table VI. Effect of Sample Displacement on Residual Stress Analyses of 1968 D U.S. One Cent Piece (#34) 58

Table VII. Average Residual Stresses at Various Locations on the 1968 D US One Cent Piece (#34) 61

Table VIII. Average Residual Stresses at Various Locations on the 1968 D US One Cent Piece (#38) 62

Table IX. Residual Stresses in Struck Antique Copper Coins. 64

Table X. Residual Stresses in Cast Copper Coins 68

Table XI. Effects of Abrasion on Coins and Blanks 72

Table XII. Residual Stresses in Silver and Gold Coins. 74

Table XIII. Residual Stresses in Copper Coin Blanks. 78

Table XIV. Residual Stresses in Struck "Phantom" Coins 80

Table XV. Radioactive Processes for, and Radioactivity of Isotopes found in a Sterling Silver Coin 90

Table XVI. Acoustic Microscopy: Resolution and Penetration at Typical Operating Frequencies 102

Table XVII. Instrumental Conditions for X-ray Fluorescence Analysis of Coins. 112

Table XVIII. Peak Intensity and Composition of Coins from X-ray Fluorescence Analysis. 113

Table XIX. Peak Intensity and Composition of Calibrations Standards use in X-ray Fluorescence Analysis of Coins....114

Table XX. Dimensional Data on U.S. One Cent Pieces, "Type One" Blanks,"Type Two" Blanks, Olin Blanks, and "Phantom" Coins....123

Figure 16. Photographs of the obverse and reverse of the struck authentic Spanish 1789 Carolus IV doubloon....35

Figure 17. Photographs of the obverse and reverse of the cast counterfeit Spanish 1800 Carolus IV doubloon....36

Figure 18. A representative diffraction profile for a struck coin....38

Figure 19. A schematic showing the instrumental set-up for the measurement of $d\perp$ and $d\psi$....43

Figure 20. A schematic diagram showing the relative positions for the sample, X-ray source, and detector for various beam geometries 44

Figure 21. The instrumental system used for residual stress analysis....46

Figure 22. Longitudinal and transverse waves 93

Figure 23. Rayleigh waves....95

Figure 24. A schematic diagram of scanning acoustic microscope....98

Figure 25. A schematic diagram indicating the principal acoustic rays which contribute to the output of the acoustic lens....100

Figure 26. Optical holography 106

Figure 27. A schematic diagram of the components used in acoustic holography....107

Figure 28. The microstructure of the "type one" coin blank....121

Figure 29. The microstructure of a 1968 D U.S. one cent piece. 125

Figure 30. The microstructure of a "type two" coin blank. 126

Figure 31. A schematic diagram showing the instrumental system used to anneal Olin coin blanks before rimming....127

Figure 32. The microstructure of an annealed Olin coin blank....129

Figure 33. A schematic and actual photograph of the rimming machine. 130

Figure 34. Photographs of the obverse and reverse of the "phantom" coin....132

Figure 35. The design drawings for the construction of "phantom" coin dies. 133

Figure 36. A schematic diagram of the die system used to strike "phantom" coins. 134

Figure 37. A photograph of the actual die system used to strike "phantom" coins. 135

Figure 38. A photograph showing the protective concrete block wall which functioned as a safety shield. 136

Figure 39. The microstructure of the edges of "phantom" coins and a U.S. one cent piece 138

Figure 40. A plot of the d spacing versus $\sin^2$ psi, using chromium radiation,taken on the 1968 D mint issue U.S. one cent piece (#34), located above the date....140

Figure 41. A plot of the d spacing versus $\sin^2$ psi, using chromium radiation,taken on the 1968 D mint issue U.S. one cent piece (#34) located above the date....141

Figure 42. A plot of the d spacing versus $\sin^2$ psi, using chromium radiation, taken on the 1968 D mint issue U.S. one cent piece (#34)located above the date....142

Figure 43. A plot of the d spacing versus $\sin^2$ psi, using chromium radiation,taken on a standard cast iron sample. 143

Figure 44. A plot of the d spacing versus $\sin^2$ psi, using cobalt radiation, taken on the 1968 D mint issue U.S. one cent piece (#34), to determine the effect of sample displacement. 144

Figure 45. A plot of the d spacing versus $\sin^2$ psi, using cobalt radiation, taken on the 1968 D mint issue U.S. one cent piece (#34), with a 1mm displacement in the forward direction....145

Figure 46. A plot of the d spacing versus $\sin^2$ psi, using cobalt radiation, taken on the 1968 D mint issue U.S. one cent piece (#34) , with a 1mm displacement in the backward direction 146

Figure 47. A plot of the d spacing versus the $\sin^2$ psi, using cobalt radiation, to determine the presence of psi splitting....147

Figure 48. A plot of the d spacing versus $\sin^2$ psi, using cobalt radiation, taken on the 1968 D mint issue U.S. one cent piece (#34), aligned to within 0.00001 inch of the goniometer center. 148

Figure 49. A plot of the d spacing versus $\sin^2$ psi, using cobalt radiation, taken on the 1968 D mint issue U.S. one cent piece (#34) , aligned to within 0.00001 inch of the goniometer center. 149

Figure 50. A plot of the d spacing versus $\sin^2$ psi, using cobalt radiation, taken on the 1969 S mint issue U.S. one cent piece, which had been annealed at 525 ^{o}C for 20 minutes. 150

Figure 51. A plot of the d spacing versus $\sin^2$ psi, using cobalt radiation, taken on the 1969 S mint issue U.S. one cent piece, which had been annealed at 525 °C for 20 minutes. 151

Figure 52. A plot of the d spacing versus $\sin^2$ psi, using cobalt radiation, taken on the U.S. "Type I" one cent blank, which had been annealed at 514 °C for 20 minutes. 152

Figure 53. A plot of the d spacing versus $\sin^2$ psi, using cobalt radiation, taken on the U.S. "Type I" one cent blank, which had been annealed at 514 °C for 20 minutes. 153

Figure 54. A plot of the d spacing versus $\sin^2$ psi, using cobalt radiation, taken on the Olin. "Type I" one cent blank....154

Figure 55. A plot of the d spacing versus $\sin^2$ psi, using cobalt radiation, taken on the Olin. "Type I" one cent blank....155

Figure 56. A plot of the d spacing versus $\sin^2$ psi, using cobalt radiation, taken on the U.S. "Type I" one cent blank (#B3-1), which had been annealed at 514 °C for 20 minutes. 156

Figure 57. A plot of the d spacing versus $\sin^2$ psi, using cobalt radiation, taken on the U.S. "Type I" one cent blank, which had been annealed at 514 °C for 20 minutes. 157

Figure 58. A plot of the d spacing versus $\sin^2$ psi, using cobalt radiation, taken on the 1968 D mint issue U.S. one cent piece (#34) located above the liberty of the design. 158

Figure 59. A plot of the d spacing versus $\sin^2$ psi, using cobalt radiation, taken on the 1968 D mint issue U.S. one cent piece (#34) located above the liberty of the design. 159

Figure 60. A plot of the d spacing versus the $\sin^2$ psi, using cobalt radiation, taken on the D mint issue U.S. one cent piece (#34) to determine the presence of psi splitting. 160

Figure 61. A plot of the d spacing versus $\sin^2$ psi, using cobalt radiation, taken on the 1968 D mint issue U.S. one cent piece (#34) located on the portrait of the design. 161

Figure 62. A plot of the d spacing versus $\sin^2$ psi, using cobalt radiation, taken on the 1968 D mint issue U.S. one cent piece (#34) located on the portrait of the design. 162

Figure 63. A plot of the d spacing versus $\sin^2$ psi, using cobalt radiation, taken on the 1968 D mint issue U.S. one cent piece (#34) located on the field near the edge of the coin. 163

Figure 64. A plot of the d spacing versus $\sin^2$ psi, using cobalt radiation, taken on the 1968 D mint issue U.S. one cent piece (#34) located on the field near the edge of the coin. 164

Figure 65. A plot of the d spacing versus $\sin^2$ psi, using cobalt radiation, taken on the 1968 D mint issue U.S. one cent piece (#38) located above the date of the design. 165

Figure 66. A plot of the d spacing versus $\sin^2$ psi, using cobalt radiation, taken on the 1968 D mint issue U.S. one cent piece (#38) located above the date of the design. 166

Figure 67. A plot of the d spacing versus $\sin^2$ psi, using cobalt radiation, taken on the 1968 D mint issue U.S. one cent piece (#38) located on the field near the edge of the coin. 167

Figure 68. A plot of the d spacing versus $\sin^2$ psi, using cobalt radiation, taken on the 1968 D mint issue U.S. one cent piece (#38) located on the field near the edge of the coin. 168

Figure 69. A plot of the d spacing versus $\sin^2$ psi, using cobalt radiation, taken on the 1968 D mint issue U.S. one cent piece (#38) located on the chin of the portrait on the coin....169

Figure 70. A plot of the d spacing versus $\sin^2$ psi, using cobalt radiation, taken on the 1968 D mint issue U.S. one cent piece (#38) located on the head of the portrait on the coin. 170

Figure 71. A plot of the d spacing versus $\sin^2$ psi, using cobalt radiation, taken on the 1968 D mint issue U.S. one cent piece (#38) located on ton the field behind the portrait on the coin....171

Figure 72. A plot of the d spacing versus $\sin^2$ psi, using cobalt radiation, taken on the 1968 D mint issue U.S. one cent piece (#38) located on the head of the portrait on the coin. 172

Figure 73. A plot of the d spacing versus $\sin^2$ psi, using cobalt radiation, taken on a stress free powdered copper standard. 173

Figure 74. A plot of the d spacing versus $\sin^2$ psi, using cobalt radiation, taken on the 1699 (A) struck William III halfpenny, located near the chin. 174

Figure 75. A plot of the d spacing versus $\sin^2$ psi, using cobalt radiation, taken on the 1699 (A) struck William III halfpenny, located near the chin. 175

Figure 76. A plot of the d spacing versus $\sin^2$ psi, using cobalt radiation, taken on the 1699 (A) struck William III halfpenny, located behind the head of the portrait. 176

Figure 77. A plot of the d spacing versus the $\sin^2$ psi, using cobalt radiation, taken on the 1699 (A) struck William III halfpenny, located behind the head of the portrait, to determine the presence of psi splitting. 177

Figure 78. A plot of the d spacing versus $\sin^2$ psi, using cobalt radiation, taken on the 1699 (A) struck William III halfpenny, located on the head of the portrait. 178

Figure 79. A plot of the d spacing versus $\sin^2$ psi, using cobalt radiation, taken on the 1719 (A) struck George I halfpenny, located on the field of the coin 179

Figure 80. A plot of the d spacing versus $\sin^2$ psi, using cobalt radiation, taken on the 1719 (A) struck George I halfpenny, located on the field of the coin....180

Figure 81. A plot of the d spacing versus $\sin^2$ psi, using cobalt radiation, taken on the 1719 (A) struck George I halfpenny, located behind the head of the portrait 181

Figure 82. A plot of the d spacing versus $\sin^2$ psi, using cobalt radiation, taken on the 1719 (A) struck George I halfpenny, located on the head of the portrait....182

Figure 83. A plot of the d spacing versus $\sin^2$ psi, using cobalt radiation, taken on the 1719 (A) struck George I halfpenny, located on the head of the portrait....183

Figure 84. A plot of the d spacing versus $\sin^2$ psi, using cobalt radiation, taken on the 1719 (B) cast George I halfpenny, located on the field of the coin. 184

Figure 85. A plot of the d spacing versus $\sin^2$ psi, using cobalt radiation, taken on the 1699 (B) cast William III halfpenny, located under the chin of the portrait....185

Figure 86. A plot of the d spacing versus $\sin^2$ psi, using cobalt radiation, taken on the 1699 (B) cast William III halfpenny, located under the chin of the portrait. 186

Figure 87. A plot of the d spacing versus $\sin^2$ psi, using cobalt radiation, taken on the 1775 cast George III halfpenny, located under the chin of the portrait....187

Figure 88. A plot of the d spacing versus $\sin^2$ psi, using cobalt radiation, taken on the 1775 cast George III halfpenny, located under the chin of the portrait....188

Figure 89. A plot of the d spacing versus $\sin^2$ psi, using cobalt radiation, taken on the 1775 cast George III halfpenny, located on the neck of the portrait. 189

Figure 90. A plot of the d spacing versus $\sin^2$ psi, using cobalt radiation, taken on the 1699 (D) cast William III halfpenny, located on the field of the coin 190

Figure 91. A plot of the d spacing versus $\sin^2$ psi, using cobalt radiation, taken on the 1699 (D) cast William III halfpenny, located on the field of the coin.....191

Figure 92. A plot of the d spacing versus $\sin^2$ psi, using cobalt radiation, taken on the 1699 (D) cast William III halfpenny, located on the head of the portrait.....192

Figure 93. A plot of the d spacing versus $\sin^2$ psi, using cobalt radiation, taken on the 1968 D mint issue U.S. one cent piece (#50), abraded mechanically using a wire brush attached to a flexible shaft drill.....193

Figure 94. A plot of the d spacing versus $\sin^2$ psi, using cobalt radiation, taken on the U.S. "Type I" one cent blank (#B3-1), abraded by hand using a wire brush.....194

Figure 95. A plot of the d spacing versus $\sin^2$ psi, using cobalt radiation, taken on the U.S. "Type I" one cent blank (#B3-1), abraded by hand using a wire brush.....195

Figure 96. A plot of the d spacing versus $\sin^2$ psi, using cobalt radiation, taken on the "Phantom" coin (#B2-C), struck at 90,900 lb. coining pressure, located on the field of the coin.....196

Figure 97. A plot of the d spacing versus $\sin^2$ psi, using cobalt radiation, taken on the "Phantom" coin (#B2-C), struck at 90,900 lb. coining pressure, located on the high relief of the coin.....197

Figure 98. A plot of the d spacing versus $\sin^2$ psi, using cobalt radiation, taken on the 1968 D mint issue U.S. one cent piece (#50), abraded by hand using a wire brush.....198

Figure 99. A plot of the d spacing versus $\sin^2$ psi, using cobalt radiation, taken on the "Phantom" coin (#B1-A), struck at 40,100 lb. coining pressure, located on the field of the coin.....199

Figure 100. A plot of the d spacing versus $\sin^2$ psi, using cobalt radiation, taken on the "Phantom" coin (#B1-A), struck at 40,100 lb. coining pressure, located on the field of the coin.....200

Figure 101. A plot of the d spacing versus $\sin^2$ psi, using cobalt radiation, taken on the struck Victoria shilling, located on the field of the coin.....201

Figure 102. A plot of the d spacing versus $\sin^2$ psi, using cobalt radiation, taken on the struck Victoria shilling, located on the head of the portrait.....202

Figure 103. A plot of the d spacing versus $\sin^2$ psi, using cobalt radiation, taken on the cast Victoria shilling, located on the field of the coin.....203

Figure 104. A plot of the d spacing versus $\sin^2$ psi, using cobalt radiation, taken on the cast Victoria shilling, located on the head of the portrait 204

Figure 105. A plot of the d spacing versus $\sin^2$ psi, using cobalt radiation, taken on the "Phantom" coin (#B1-A), struck at 40,100 lb. coining pressure, located on the field of the coin. 205

Figure 106. A plot of the d spacing versus $\sin^2$ psi, using cobalt radiation, taken on the struck gold doubloon, located on the field of the coin. 206

Figure 107. A plot of the d spacing versus $\sin^2$ psi, using cobalt radiation, taken on the struck gold doubloon, located on the portrait of the coin. 207

Figure 108. A plot of the d spacing versus $\sin^2$ psi, using cobalt radiation, taken on the cast 1800 Spanish gold doubloon, located on the field of the coin. 208

I. INTRODUCTION

The scientific examination of coins can result in a wealth of new information. A coin can provide information about the artistic, technological, and economic development of a culture or society. A coin has value on many different levels. Originally its intrinsic value, or that given to it as a means of exchange, was paramount. A coin may be rare, making it valuable to a collector. The coin may be prized as a work of art, and its inscription may convey important insights. From the fabric of a coin and its metallic content questions about trade, metallurgy, and mechanical skills may be answered. Because of the manifold of information that is obtainable from coins and their possible monetary value, nondestructive methods of analysis are essential for their study.

A. The Statement of the Problem.

The focus of this research is the evaluation of residual stress analysis using X-ray diffraction techniques as a method for the investigation of coins. Specific goals for such measurements are a) the differentiation of struck authentic coins from cast counterfeit coins, b) the elucidation of manufacturing techniques, and c) the determination of the age of the coin.

The authentication of coinage is important in the field of numismatics, because the means for producing high quality forgeries of both ancient and modern pieces are widespread. Some of the most deceptive forgeries of coins are made by modern casting techniques employing extremely fine-grained molding materials with high dimensional fidelity. The problem of differentiating such a cast forgery from an authentic coin can be quite difficult.[1]

Investigation of coining methods and coining pressures is also important to numismatic studies. The earliest coins were stuck by hand. A piece of metal known as a blank or flan was first placed between a set of dies, then designs were impressed by a blow to the upper die. Machinery was first employed to strike coins about four centuries ago. These mechanical minting machines were based on simple principles

such as the screw or wedge.[2] Little is known about the forces imparted to the struck coins by these early minting machines.

The act of striking a coin may also provide a means for dating it. When a coin is struck, the metal from which the blank is made is permanently altered in order to impart a design. The nonuniform deformation of the blank introduces residual stresses within the coin, and this stress changes with time.[3,4] It may be feasible to use the time dependence of the residual stress to date the coin.

Residual stress analysis using X-ray diffraction may contribute to the solution of these numismatic problems by providing quantitative nondestructive measurements of properties related to the manufacture of the coin.

1. Review of this Approach to the Problem. X-ray diffraction techniques have been used in the past to examine works of art including medals and coins.[5], The grain size of cast, struck, and electroformed coins has been distinguished by Laue back reflection X-ray diffraction techniques.[6,7] When a collimated beam of monochromatic X-rays is impinged on a polycrystalline sample, a cone of X-rays is diffracted in specific directions.[8] The cone of X-rays can be recorded on X-ray film placed in its path. The resulting ring shaped pattern is known as a Debye ring. Grains of approximately 10 μ or larger produce discontinuous or spotty Debye rings, while smaller grains produce continuous or even Debye rings.[9,10] A schematic diagram representing typical continuous and discontinuous Debye rings is shown in Figure 1. The determination of grain size in coins and medals by this method is based on qualitative examination of the diffracted Debye rings.

Terry and De Laeter[11] demonstrated the utility of Laue techniques in differentiating between genuine seventeenth-century Spanish silver reales from the shipwrecked Dutch vessel,the *Gilt Dragon,* and reproductions of the coins. Their results showed that all genuine coins gave a continuous Debye pattern, whereas the reproductions gave spotty patterns.

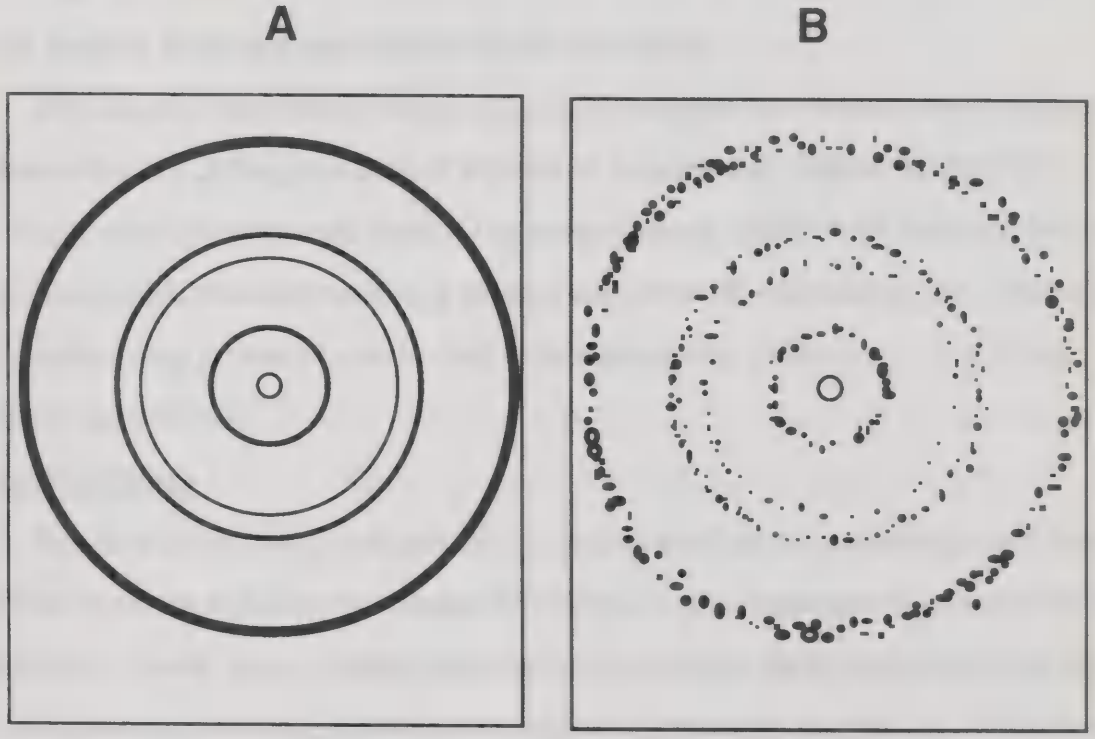

Figure 1. (a) A schematic diagram of a continuous debye pattern and (b) a schematic diagram of a discontinuous debye pattern for a Laue back reflected radiograph.

Wharton extended this technique to the differentiation of electroformed medals from cast or struck samples.[12] The cast and struck medals were composed of significantly larger grains than the fine-grained electroformed medals, making the electroformed medals easily distinguishable by the technique.

The use of X-ray diffraction techniques in this area has thus far been limited to the determination of the grain size of a piece in a qualitative manner to distinguish cast, struck and electroformed coins. The present study differs from previous work in that a quantitative measurement of a mechanical property, residual stress, related to the manufacturing process is performed nondestructively on the coin using X-ray diffraction techniques.

B. Residual Stress

Residual stress is a fundamental concept of mechanical metallurgy and must be explained in terms of basic mechanical principles.[13] It is important to understand the definitions of stress, strain, elastic deformation, and plastic deformation in order to define residual stress and explain its importance in numismatic studies. Coining processes can also be described in terms of basic mechanical principles. The coining pressure used to strike a coin can be considered to be an applied stress. The design imparted to the coin can be considered to be the resulting strain.

Stress is defined as a force acting on a unit area of a material;[14]

$$\sigma = F/A \qquad \text{eq.(1)}$$

σ = stress

F = the applied force acting in a direction

A = the area to which the force is applied.

When a stress is applied to a material, deformation takes place. A measure of the deformation of the material is called the strain and can be defined as the change in length per unit length of the material:[15]

$$\varepsilon = \frac{l - l_0}{l_0} \qquad \text{eq.(2)}$$

ε = strain

l = the length of the material after the stress is applied

l_0 = the original length of the material

Thus far, stress and strain have been defined for a uniaxial or linear system. In a volume element, nine stress components are needed to define the total stress system. The volume element can be considered a cube. When a load is placed on the cube, stresses will result on all six faces. The stresses on mutually parallel faces will be equal in magnitude but opposite in sign. Therefore, to define the stresses acting in the cube, the stresses along three orthogonal faces must be known. The stress acting on any face can be resolved into three component stresses, the normal stress acting perpendicular to the plane and two shear stresses acting in the plane. These shear stresses are the result of lateral displacement of a plane of atoms relative to another plane of atoms.[16] A schematic of the total stress in a system can be found in Figure 2. The stresses of a system can be designated by an index system, where the first number indicates the point of origin and the second number indicates the direction of action. Stresses designated with like indices are equal to each other (i.e. $\sigma_{12} = \sigma_{21}$, $\sigma_{23} = \sigma_{32}$, $\sigma_{13} = \sigma_{31}$) The complete stress system is described by the following matrix:[17]

$$\sigma = \begin{vmatrix} \sigma_{11} & \sigma_{12} & \sigma_{13} \\ \sigma_{21} & \sigma_{22} & \sigma_{23} \\ \sigma_{31} & \sigma_{32} & \sigma_{33} \end{vmatrix}$$

The diagonal elements of the matrix are known as the principal stresses and are sometimes designated σ_1, σ_2, and σ_3. The elements with mixed indices are the shear stress components of the system.

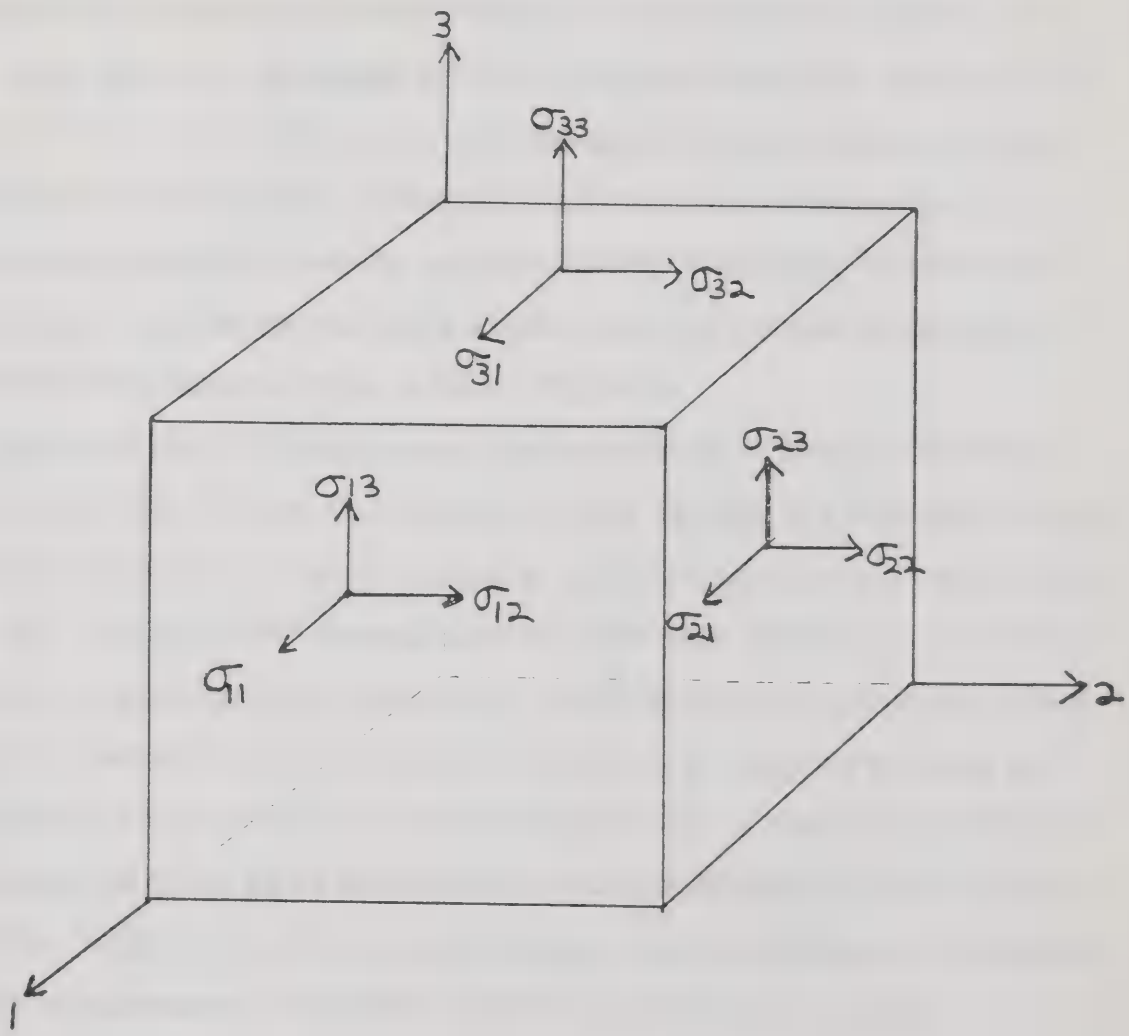

Figure 2. The complete system of stresses acting on a three dimensional body. σ_{11}, σ_{22}, and σ_{33} are the principal stresses of the system. All other stresses are shear stresses.

Two different types of deformation take place upon application of a stress to a material: elastic and plastic deformation.[18] When elastic deformation occurs, the resulting strain of the material is a linear function of the applied stress, as shown in Figure 3a. Upon removal of the applied stress, the material will return to its original size and shape. Plastic deformation occurs when the applied stress is greater than the yield stress of the material. The yield stress of the material is defined as the value of the stress beyond which the material no longer deforms linearly with respect to the applied stress. Upon the removal of the applied stress, the material will remain in some permanently deformed state, as seen in Figure 3b.

Elastic and plastic deformation can also be explained in terms of microscopic properties, as shown in Figure 4. A material, such as the metal of a coin blank, can be considered to be made up of atoms occupying equilibrium positions in a crystal lattice (Figure 4a). These positions correspond to local minima in potential energy surfaces that represent the energy of the material as a function of its atomic spacings.[19] When a stress is applied to the material, groups of extra atoms or vacancies that exist as imperfections in the crystal lattice, move within the material. In elastic deformation, the applied stress will cause atoms to move from the original equilibrium position (a) to a new position (b) possessing higher potential energy. Upon the removal of the applied stress atoms will return to their original equilibrium positions (a). In plastic deformation, defects known as dislocations will be provided with enough energy by the applied stress to surmount an energy barrier and move into a new, unoccupied equilibrium position (c) leaving behind a plastically deformed region in the crystal.

Residual stresses are internal, elastic stresses which acting in a direction within the material and arise from nonuniform plastic deformation.[20,21] Since the design of a coin is created by such nonuniform plastic deformation, coins possess residual stress.

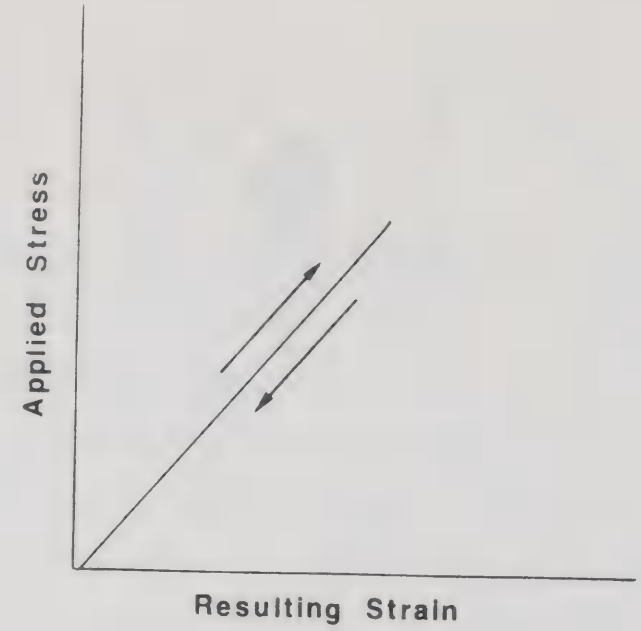

(a)

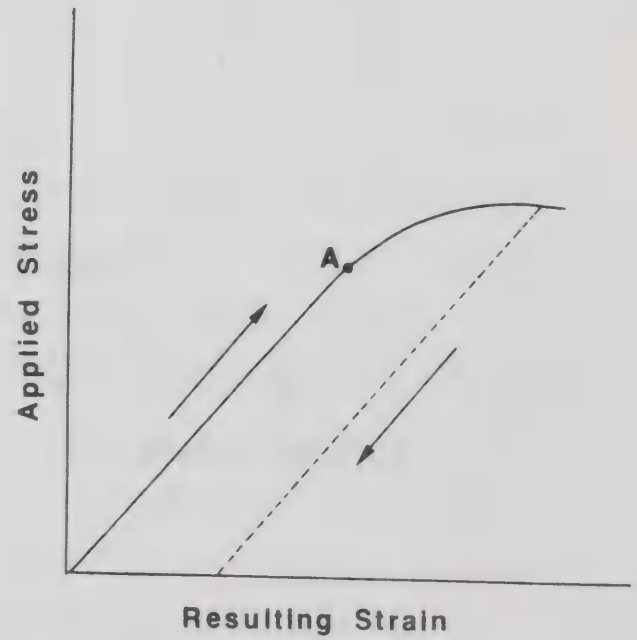

(b)

Figure 3.: (a). Elastic deformation. The resulting strain is linearly proportional to the applied stress. (b). Plastic deformation. When the applied stress is greater than the yield stress of the material, A, the resulting strain is no longer linearly proportional to the applied stress, resulting in permanent strain within the material.

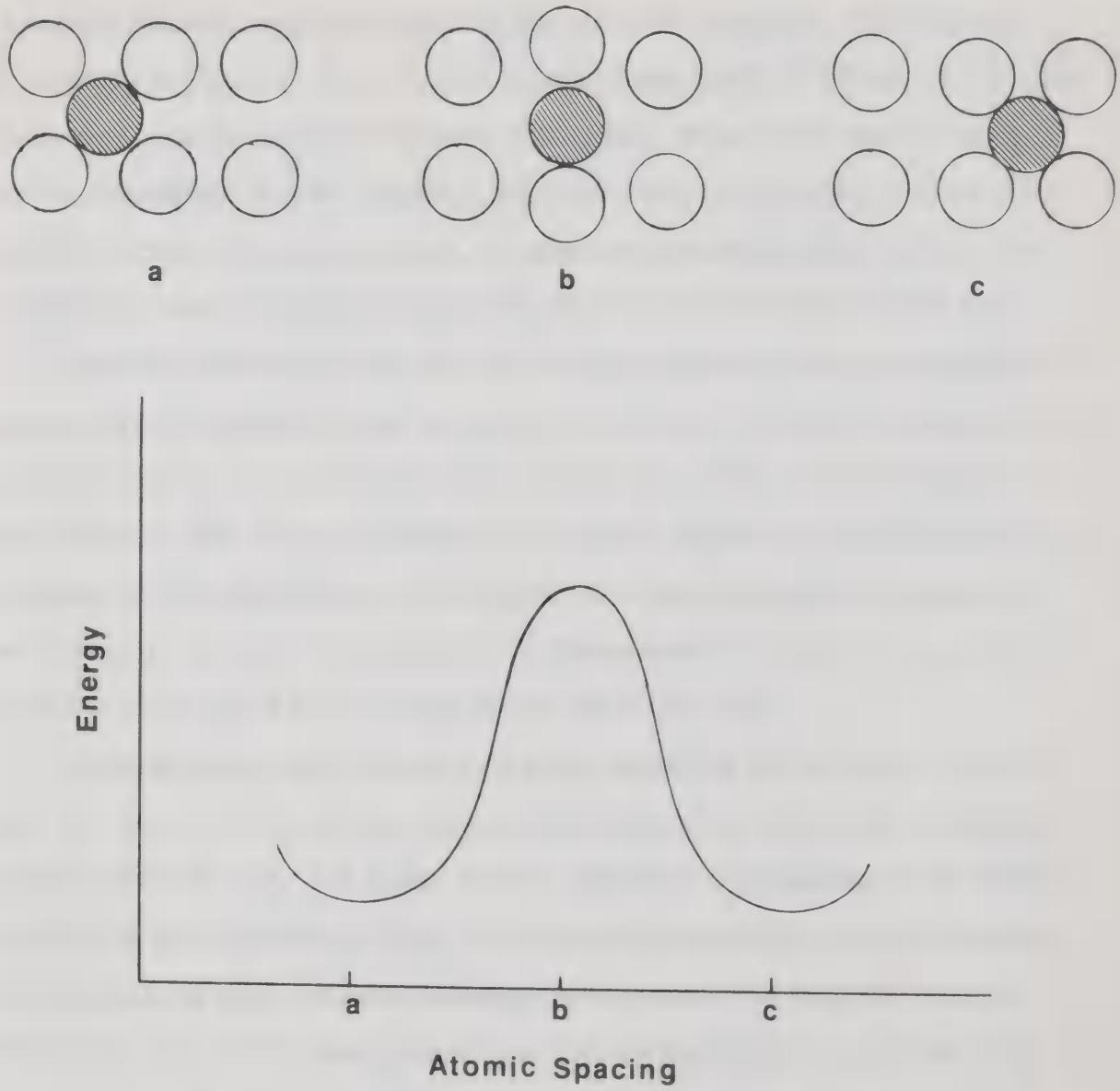

Figure 4. Potential energy diagram for movement of atoms from one equilibrium position to another. The movement of the atom from position (a) through position (b) to the new equilibrium position (c) requires that a energy barrier be surmounted.

In a coining process, neighboring regions are deformed differently. This is shown schematically in Figure 5. Some regions may undergo plastic deformation while other regions may undergo elastic deformation (Figure 5b). When these regions share common boundaries, a strain mismatch will occur along the boundary (Figure 5b).[22] After the removal of the applied stress, the plastically deformed region will not allow the elastically deformed region to relax to its original size and shape (Figure 5c).

Residual stresses can also arise from volume changes accompanying thermal changes within a material, as may be found in cast coins. The thermal changes which result from rapid quenching of the material or from the cooling and solidification of the molten metal or alloy cause contraction of the volume of grains upon cooling and create regions of non-uniform strain. The magnitude of residual stresses produced by slow cooling processes is dependent on the dimensions of the object being cast, as well as the nature of the metal or alloy and on the cooling rate.

Residual stresses may provide information about the way in which a coin is made. In a cast coin, the residual stresses are produced by the thermal changes taking place within the coin. The molten coining alloy cools and solidifies of the walls of the mold first, then solidifies inwardly. The thermal contraction of the cooler edges of the can produce a strain mismatch between the edges and the center of the coin. Coins which were cooled slowly should have low residual stress. In contrast, coins which are struck should have high residual stresses due to the non-uniformed deformation created by striking. The residual stresses arising in this manner should be much larger than residual stresses in cast coins.

Since residual stresses are elastic in nature, the residual stress of the material will be proportional to the strain in the material that arises along the boundaries of these neighboring regions:

$$\sigma_r = E \varepsilon_r.$$

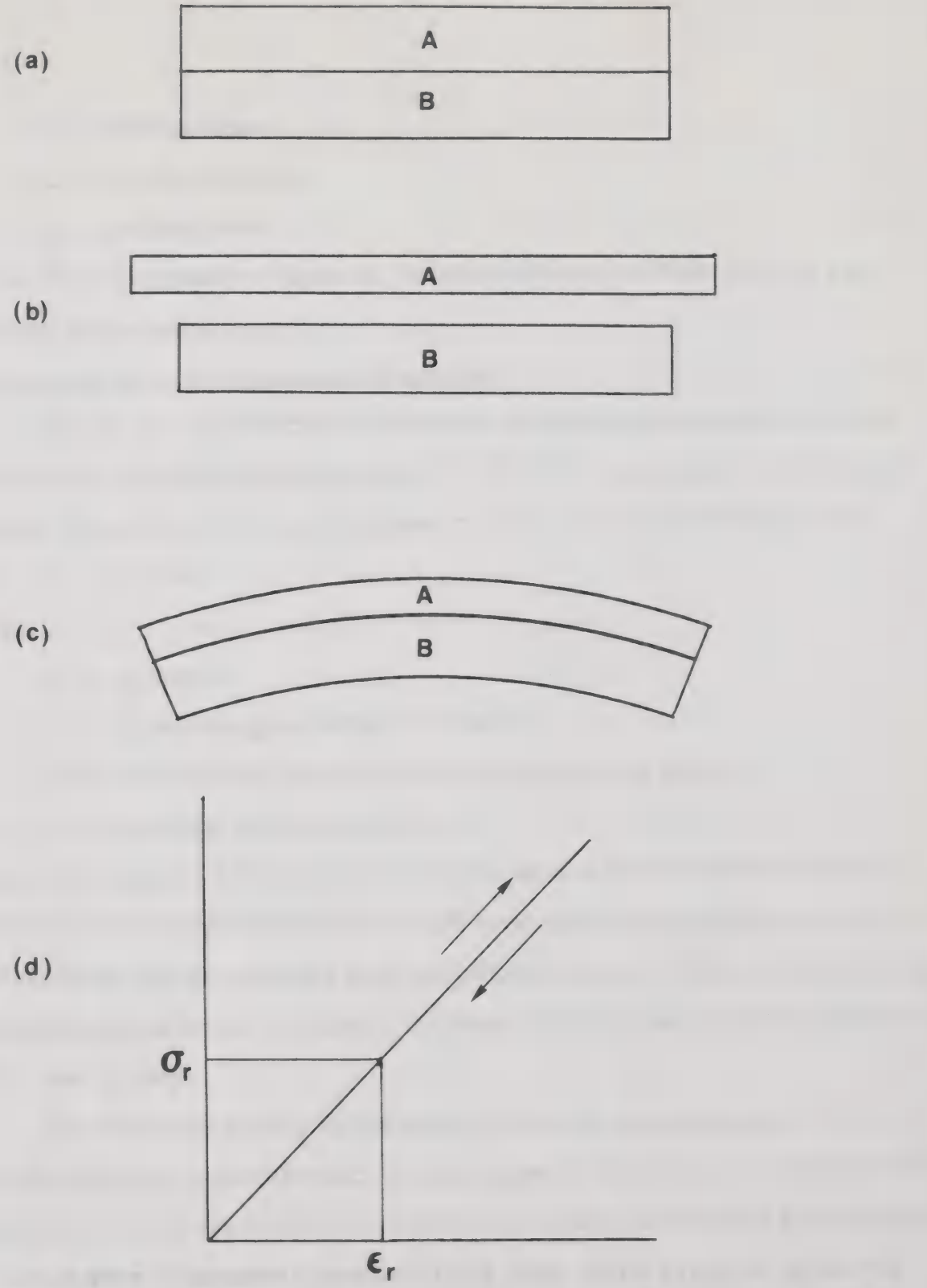

Figure 5. Residual stress in a material results from non-uniform plastic deformation. (a) shows two separate regions, A and B, of a material. (b) shows region A plastically deformed and region B elastically deformed. (c) shows the strain mismatch resulting when regions A and B are neighboring. (d) shows the relationship between the residual strain and the residual stress in the material.

σ_r = residual stress

E = Young's modulus

ε_r = residual strain

This is shown graphically in Figure 5d. Residual stresses are determined by measurement of residual strains.

C. Review of the X-ray Measurement Technique

The use of X-ray diffraction techniques to measure the near surface residual stresses of a material is well established [23, 24, 25, 26,27]. These same techniques can be used to determine the residual stresses in a coin with the aid of Bragg's Law:

$$n\lambda = 2d \sin\theta$$

where

n = an integer

λ = the wavelength of diffracted radiation

d = the interplanar spacing of the reflecting plane of atoms

θ = the Bragg angle of diffraction.

The constant spacing between planes of atoms within a polycrystalline material is known as the interplanar spacing. The interplanar spacings for a particular set of reflecting planes, can be used as a strain gauge within the coin. When an elastic stress, such as a residual stress, is present within the coin the interplanar spacing is altered to some new spacing.

The interplanar spacing can be determined in the following manner. When a collimated beam of monochromatic X-rays impinges on the surface of a polycrystalline material, the X-rays are scattered in all directions. A diffracted beam of X-ray radiation is formed when constructive interference takes place. Since X-rays are waves, the resulting X-ray beam is a vector sum of the phase and amplitude of the component waves. In certain directions the X-rays will be in phase with and reinforce each other producing a diffracted X-ray beam. This phenomenon is known as constructive

interference. The direction in which constructive interference can take place, θ, is defined by Bragg's law, and can be measured with the use of an X-ray diffractometer. The interplanar spacing is then computed from Bragg's law with the knowledge of the wavelength of the radiation used.

The total strain in the material which results from the residual stress acting in a direction within the coin can be determined from the interplanar spacings measured by X-ray diffraction. The total strain in a particular direction is given by the relationship

$$\varepsilon = \frac{\Delta d}{d_o} = \frac{d-d_o}{d_o}$$

where

ε = the strain within the coin

d = the interplanar spacing of the stressed state

d_0 = the interplanar spacing of the unstressed state.

The residual stress within the coin can then be calculated from linear stress-strain relationships derived from the theory of linear elasticity.[28] When a material is deformed in more than one direction, elastic strains can be formed in more than one direction leading to biaxial and triaxial stress fields. The elastic strain of the material can be resolved into components along the principal axes of the material as shown in Figure 6. The total strain system in any direction, ε, can then be described in terms of the component strains ε_1, ε_2, and ε_3, and the angles, ψ and ϕ, which relate the total strain to the principle axes for the object:

$$\varepsilon = a_1^2\varepsilon_1 + a_2^2\varepsilon_2 + a_3^2\varepsilon_3 \qquad \text{eq. (3)}$$

where:

$a_1 = \sin\psi \cos\phi$

$a_2 = \sin\psi \sin\phi$

$a_3 = \cos\psi$.

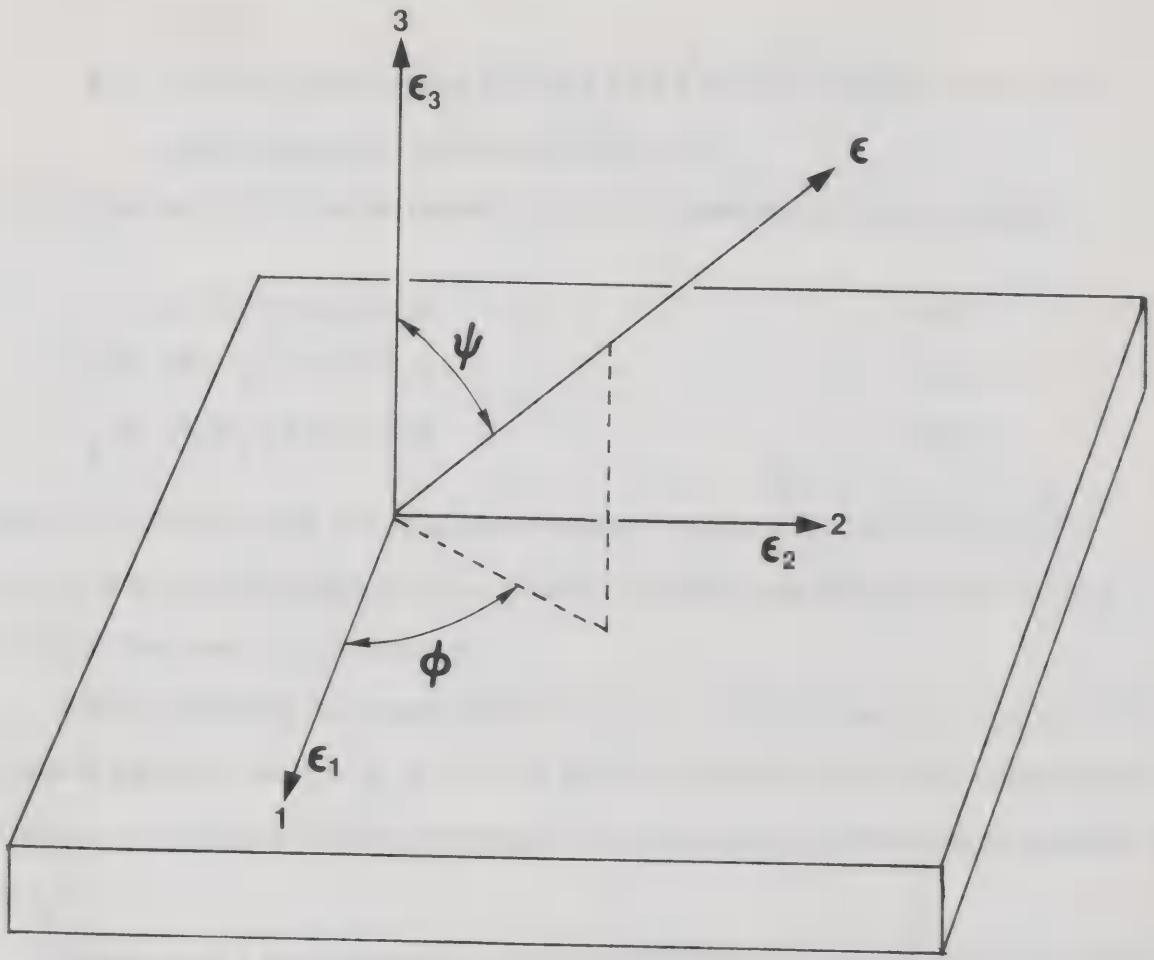

Figure 6. The geometric designation of the total strain system of a material. The total strain, ε , can be thought of as resulting from three component strains, ε_1, ε_2,and.ε_3, which lie on the principal axes of the material. ϕ is the angle between the total strain and principal axis 1. ψ is the angle between the total strain and principal axis 3.

ψ = the angle between the sample surface and the normal of the reflecting planes

ϕ = the angle between the principal axis 1 and the direction of the stress acting parallel to the surface of the coin

Each component strain can be related to stresses along the principal axes by,

$$\varepsilon_1 = 1/E\,[\sigma_1 - \nu\,(\sigma_2 + \sigma_3)] \qquad \text{eq.(4)}$$

$$\varepsilon_2 = 1/E\,[\sigma_2 - \nu\,(\sigma_1 + \sigma_3)] \qquad \text{eq.(5)}$$

$$\varepsilon_3 = 1/E\,[\sigma_3 - \nu\,(\sigma_1 + \sigma_2)] \qquad \text{eq.(6)}$$

where ν = Poisson's ratio that relates the strain in one direction to the transverse strains in the other directions and E = Young's modulus that relates the stress in a material to the strain in that material.

When measuring the stress at the surface of a material, the stress normal to the surface is equal to zero (i.e. $\sigma_3 = 0$).[29] As seen in equation 6, the strain normal to the surface, ε_3, is not equal to zero and results from the presence of transverse stresses, σ_1 and σ_2.

Equations 3-6 can be used to derive the relationship between strain and stress in a chosen direction and that lie in a plane parallel to the surface of the coin:

$$\varepsilon = \left(\frac{(1 + \nu)}{E} \sin^2 \psi \right) (\sigma_1 \cos^2 \phi + \sigma_2 \sin^2 \phi) - \varepsilon_3$$

This equation can be rewritten in terms of the stress in the plane, σ_ϕ , by defining

$$\sigma_\phi = \sigma_1 \cos^2 \phi - \sigma_2 \cos^2 \phi,$$

$$\varepsilon - \varepsilon_3 = \left[\frac{(1 + \nu)}{E} \sin^2 \psi \right] \sigma_\phi \qquad \text{eq.(7)}$$

where

$$\varepsilon - \varepsilon_3 = \frac{(d_\psi - d_o)}{d_o} - \frac{(d_\perp - d_o)}{d_o} = \frac{(d_\psi - d_\perp)}{d_o} \qquad \text{eq.(8)}$$

d_0 = the original interplanar spacing in an unstressed state

d_ψ = the interplanar spacing measured at angle ψ and

$d_\perp$ = the interplanar spacing measured perpendicular to the surface of the coin.

Since d_o, d_ψ , and $d_\perp$ are similar in value, their differences are very small. Therefore d_ψ or $d_\perp$ can be substituted for d_o in the denominator of equation (8) with negligible error.[30] This approximation allows the use of equation 7 to determine the residual stress in a plane at the surface of a material without the knowledge of the interplanar spacing in its original unstressed state. Equation 7 is the basis for multi-angle methods of residual stress measurement which we have chosen to use in our study.

The $\sin^2$ psi method of residual stress analysis utilizes equation 7 in the following way. Equation 7 can be rewritten to yield the linear equation:

$$d_\psi = \left[d_\perp \cdot \left(\frac{1 + n}{E} \right) \sigma_\phi \right] \sin^2 \psi + d_\perp \qquad \text{eq. (9).}$$

The residual stress in the plane of the coin is determined graphically from a plot of the interplanar spacing $d_\perp$ and the value of $\sin^2$ psi (See Appendix D). The slope of the plot is a function of the residual stress in the plane of the coin,

$$m = \left[d_\perp \frac{(1 + \nu)}{E} \right] \sigma_\phi$$

and the intercept of the plot is the interplanar spacing, $d_\perp$.

D. Plan of Investigation

The first phase of this research called for the measurement of residual stresses in copper, silver and gold coins. The $\sin^2$ psi X-ray diffractometer technique chosen for these measurements was a method using a semiautomated, computer controlled Picker diffractometer (See Experimental section, pp 37-48). The $\sin^2$ psi technique

uses a powder X-ray diffractometer to measure a back reflected diffraction profile from a crystallographic plane of a sample. The sample is then rotated to a new angular position, psi, while the X-ray beam and the detector remain in approximately the same position. (See Figure 19). Diffraction profiles are measured at six different psi angles. The interplanar spacing of the sample is calculated for each diffraction measurement and plotted against $\sin^2$ psi. The stress in the plane of the coin is then calculated from the slope of the plot. Once it was established that residual stresses could be determined in these coins, experiments were performed on copper "phantom" coins produced with known coining pressures to establish an empirical relationship between residual stress and coining pressure. In addition, experiments were to be performed to determine the activation energy of stress relaxation in silver dimes as a feasibility study for the use of residual stress relaxation as a means of dating a coin.

1. Investigation of Copper Coins. The feasibility of measuring residual stresses in coins was first studied by measuring stresses in modern U.S. one cent pieces. The purpose of this study was to obtain a better understanding of the nature of residual stress in struck coins and to determine the conditions which could alter residual stresses within the coin. The investigation included:

a) development of sample mounting methods for diffractometer techniques,

b) optimization of the $\sin^2$ psi X-ray diffractometer technique of measuring residual stresses for use on coins,

c) determination of variation of residual stress between similar coins, and

d) examination of variation of residual stress at various locations on coins.

The sample mounting requirements of the coin for residual stress analysis were investigated and a mounting method was established, and is reported in Chapter 2, page 47.

Optimization of the diffractometer technique is reported in Chapter 3, and includes the determination of the radiation to be used (pp. 50-53), the investigation of

beam geometry to be used (p 50), the effect of sample misalignment (p. 53), and the effect of filter thickness on peak shape and residual stress results (p. 57). Repeated measurements were performed on an uncirculated 1968 U.S. one cent piece (#34) in each of these studies.

In order to determine the variation of residual stress between similar coins, repeated measurements of residual stress were performed on a second uncirculated U.S. one cent piece (#38) and compared with the coin (#34). Results of this study is presented on pages 57-59. These residual stress measurements were taken at various locations on both coins so that the variation of residual stress with location could be investigated. A discussion of these results can be found on page 59.

Residual stress measurements were also performed on an annealed one cent in order to verify that the low residual stresses which were expected in cast counterfeit copper coins could be precisely measured. The residual stress was also determined on an annealed stress free powdered copper standard to validate the results. The results of these experiments are presented and discussed on page 57.

Results and discussion of the investigation of antique coins are presented on pages 60-70 .Two authentic copper coins and three cast counterfeit coins were examined. Authentic antique and cast counterfeit copper coins were investigated next to establish the feasibility of differentiating authentic and forged coins by residual stress analysis using diffractometer techniques. Residual stresses were measured at three locations on the obverse design of each antique and forgery coins.

To better understand the effects of surface treatment on residual stress measurements, a variety of abrasive techniques were performed on both one cent pieces and coining blanks. These pieces were abraded both by hand and by mechanical methods. The results and discussion of these effects are presented in chapter 3, pages 70-72.

2. Investigation of Silver and Gold Coins . Feasibility studies of residual stress analysis as an authentication technique were extended to other coining alloys with the measurement of stresses in two silver and two gold coins. One coin of each alloy was a struck authentic coin, while the other of the pair was a cast counterfeit. Residual stress measurements were taken at two different locations of the obverse of each coin. The results and discussion of these measurements are presented on pages 73 - 76 .

3. Effects of Coining Pressure on Residual Stress in Struck Coins. We wanted to use our ability to accurately measure residual stresses in coins to determine the coining pressure used to strike it. We sought as empirical relationship between measured residual stress and the original coining pressure by making a series of coins with known coining pressure. The "phantom" coins were to be used as calibration standards for the determination of coining pressure in antique coins. A description of the manufacture of the "phantom" coins using an hydraulic press is described in Appendix C. The use of an hydraulic press allowed accurate determination of coining pressure used to mint each "phantom" coin. The "phantom" coins were then subjected to residual stress analysis. The results and discussion of these measurements are presented on pages 79-83.

In addition, the residual stresses developed at each step of the "phantom" coin minting process were investigated by measuring residual stresses in "type one"or unrimmed and "type two" or rimmed coining blanks. This work is presented on page 77.

4. Residual Stress Analysis for Dating Coins. The proposed use of residual stress measurements for dating an object, such as a coin, is based on the fact that residual stresses in metals and alloys relax with time.[31] The act of striking the coin creates residual stress in the coin and can be thought of as setting an internal clock within the coin. The rate of relaxation can be described using absolute reaction rate theory.[32]

Elastic strains are capable of relaxing with time and temperature after the coining operation ends and the external stresses are removed. The strain relaxation, also known as creep recovery, can bring about residual stress relaxation in the material.[33] When a material is deformed by an external force and held at constant length, the stress in a body decreases exponentially with time. This process is known as stress relaxation and is a thermally activated process which is dependent on the rearrangement of groups of dislocations, from one energy state, over an energy barrier to another equilibrium position. (Cf. Figure 4). Strain relaxation is also a thermally activated process that is dependent on the movement of dislocations within the material. In the elastic range, strain relaxation is related to stress relaxation through Hooke's law. The strain relaxation rate is dependent on the effective stress acting on the material, which is the difference between the applied stress and the residual stress within the material. After the coining operation there is no applied stress. Therefore, the only stress acting on the material and providing a driving force for strain relaxation within the material is the residual stress of the material.

The strain relaxation of a material can be described phenomenologically using absolute reaction rate theory.[34] Strain relaxation can be thought of as similar to a chemical reaction starting in some initial state and crossing an activation barrier to some final state, as seen in Figure 7. The presence of the residual stress in the material drives the process in the forward direction and alters the forward activation barrier. The presence of residual stress in the material hinders the reverse process, going from the final state to the initial state.

The rate of strain relaxation within a material can be expressed in terms of a forward and a backward rate expression. Initially, the forward rate will control the rate process. As the residual stress within the material decreases with the strain relaxation, the backward rate of strain relaxation will contribute to the overall process. The rate expression for strain relaxation can be expressed in the form:[35]

$$\frac{d\varepsilon}{dt} = \alpha b \rho_m \left[A_f \exp\left(\frac{\Delta E^{\uparrow}_{f\ app}}{kT} \right) - A_b \exp\left(\frac{-\Delta E^{\uparrow}_{b\ app}}{kT} \right) \right] \qquad \text{eq.(9)}$$

where,

α = the Orowan geometrical factor relating the active slip system to the strain direction

b = the Burger's vector

ρ_m = the mobile dislocation density

A_f = the preexponential factor for the forward direction

$\Delta E_{f\ app}$ = the apparent activation energy for the forward direction

A_b = the preexponential factor for the backward direction

$\Delta E_{b\ app}$ = the apparent activation energy for the backward direction

t = time

T = temperature, ^oK

k = Boltzmann's constant, 1.38×10^{-23} joule/ ^oK.

The residual stress relaxation of the material can be determined from the strain relaxation of the material from the relationship:

$$\frac{d\sigma}{dt} = E \frac{d\varepsilon}{dt}$$

In order to use the reaction rate equations 9 and 10, activation parameters must be experimentally determined by measuring the rate of residual stress relief in a series of coins at elevated temperatures. It was proposed to measure the residual stress in a series of uncirculated 1961 U.S. D mint issue silver dimes which had been annealed at various elevated temperatures. An Arrhenius plot was to be used to determine the activation energy for stress relaxation within the silver coins. The estimate of the activation energy would have established the time scale in which residual stress

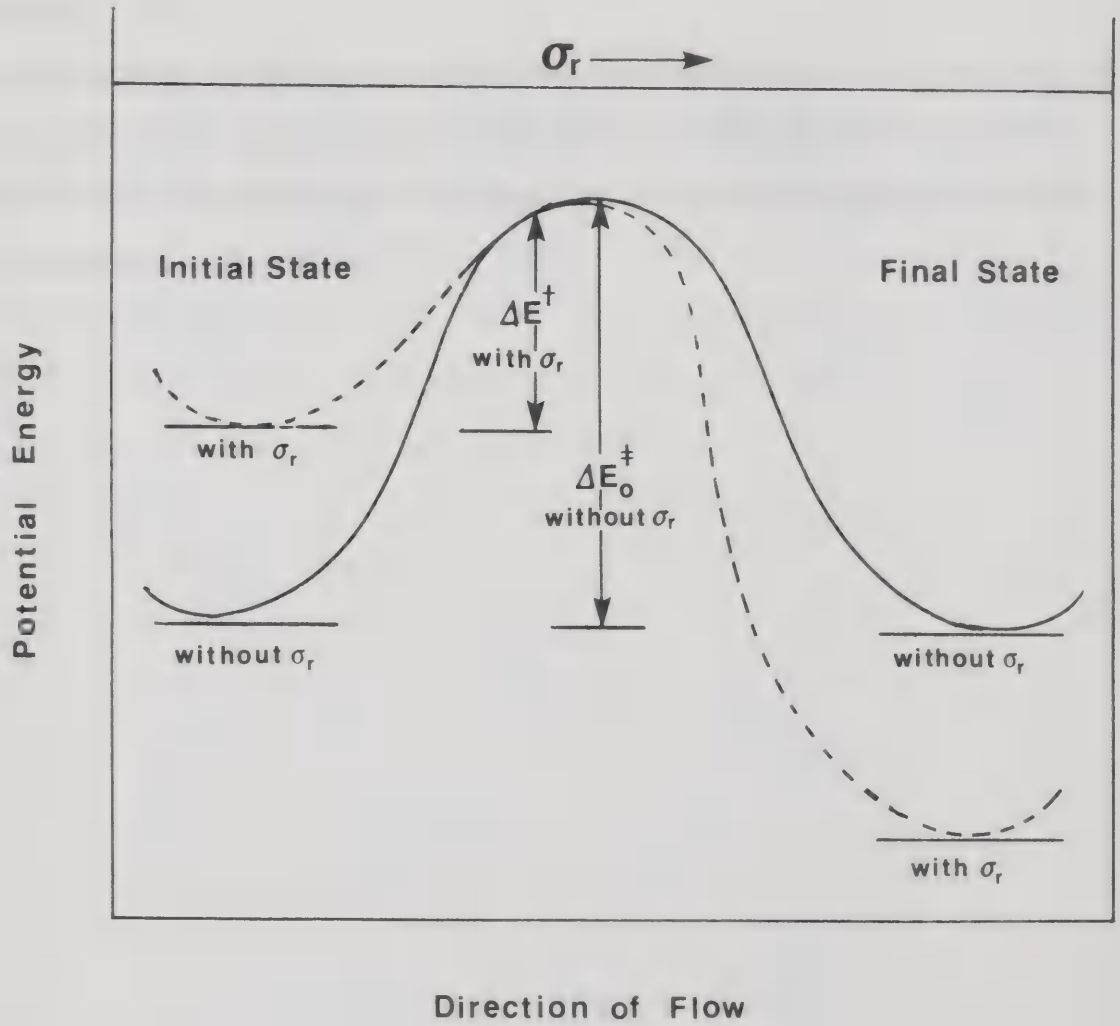

Figure 7. Potential Energy Diagram for Relaxation processes in the presence of residual stress. The energy barrier, $\Delta E_o^{\dagger}$, for relaxation processes without the presence of residual stress is indicated by the solid curve. The residual stress in the material acts in some direction. The presence and directionality of the residual stress causes the energy barrier, $\Delta E^{\dagger}$, to decrease for the forward relaxation processes. The energy barrier for the reverse direction increases.

would take place at room temperature in silver coins, assuming the same relaxation mechanisms

would occur at both elevated temperatures and room temperature. The limitations of instrumental time and funding severely restricted the number of experiments which were performed. The residual stress analyses on annealed dimes to determine activation parameters were omitted.

II. MATERIALS AND EXPERIMENTAL PROCEDURES FOR RESIDUAL STRESS ANALYSIS.

A. Materials - Coins and Standards.

The composition of each coin or standard used in this research is given in Table I. These compositions are either the known value for a given coin or the experimental value as determined by X-ray Fluorescence Analysis (see Appendix A.). (N.B. the composition of the gold doubloons was not determined experimentally due to the fact that a gold mask was used in the XRF analysis.) Residual stress analyses were performed on the following coins or types of coins:

1. Copper Coins:
    a. 1968 U.S. one cent pieces
    b. U.S. "type one" one cent blanks
    c. U.S."type two" one cent blanks
    d. struck and cast 1699 British William III halfpennies (see Figures 8 -10) [36]
    e. struck and cast 1719 British George I halfpennies (see Figures 11-12)
    f. a cast 1775 British George III halfpenny (see Figure 13)
    g. struck "phantom" coins modeled after the U.S. one cent piece;
2. Silver Coins:
    a. a struck 1849 British Victoria shilling (see Figure 14)
    b. a cast 1856 British Victoria shilling (see Figure 15);
3. Gold Coins:
    a. a 1789 struck Spanish Carolus IV doubloon (see Figure 16)
    b. a 1800 cast Spanish Carolus IIII doubloon (see Figure 17).

Residual stress analyses were also performed on a stress free pressed and annealed powdered copper standard ($\sigma_\phi \approx 0$) and a 1090D cast iron standard ($\sigma_\phi \approx 51$ ksi).

Table I.
Elemental Composition of Coins, continued.

Coin	Composition element, %						
Coin	Cu	Ag	Pb	Sn	Zn	Ni	Fe
1719 Geo I [2] A struck	96.9 ±4.5	0.11 ±0.001	1.9 ±0.12			0.06 ±0.01	
1719 Geo I [2] B cast	74.5 ± 4.7	0.11 ±0.001	11.8 ±0.36	1.8 ±0.06	0.07 ±0.02	0.59 ±0.01	0.12 ±0.03
1775 GeoIII [2] cast	97.4 ± 4.5	0.07 ±0.002	1.5 ±0.11				0.04 ±0.03
US 1c '68D [1] #50	95.0				5.0		
Olin Blank [1] B3-1 brushed	95.0				5.0		
US 1c "68D [1] #50 brushed	95.0				5.0		
Phantom [1] B2-C 90,900 lb	95.0				5.0		
Phantom [1] B1-A 40,100 lb	95.0				5.0		
Victoria Shilling struck	7.5	92.5					
Victoria [2] Shilling cast		86.6 ± 5.31		0.8 ±0.06			

Obverse

Reverse

Figure 8. Photographs of the obverse and reverse of the struck authentic British 1699 William III (A) halfpenny.

Obverse

Reverse

Figure 9a. Photographs of the obverse and reverse of the cast counterfeit British 1699 William III (B) halfpenny.

Obverse

Reverse

Figure 10. Photographs of the obverse and reverse of the cast counterfeit British 1699 William III (D) halfpenny.

Obverse

Reverse

Figure 11. Photographs of the obverse and reverse of the struck authentic British 1719 George I (A) halfpenny.

Obverse

Reverse

Figure 12. Photographs of the obverse and reverse of the cast counterfeit British 1719 George I (B) halfpenny.

Obverse

Reverse

Figure 13. Photographs of the obverse and reverse of the struck authentic British 1775 George III halfpenny.

Obverse

Reverse

Figure 14. Photographs of the obverse and reverse of the struck authentic British 1849 Victoria shilling.

Obverse

Reverse

Figure 15. Photographs of the obverse and reverse of the cast counterfeit British 1856 Victoria shilling.

Obverse

Reverse

Figure 16. Photographs of the obverse and reverse of the struck authentic Spanish 1789 Carolus IV doubloon.

Obverse

Reverse

Figure 17. Photographs of the obverse and reverse of the cast counterfeit Spanish 1800 Carolus IV doubloon.

In the $\sin^2$ psi technique for residual stress analysis by x-ray diffraction, the profile of a diffraction peak provides the information used to calculate the residual stress in a coin. The characteristics of the diffraction profile for each sample are listed in Table II. Figure 18 Shows a representative diffraction profile for a struck coin.

B. The X-ray Diffraction System.

The measurement of residual stress in coins was determined using X-ray diffraction techniques that involve the determination of the lattice spacing of a crystallographic plane at different sample inclinations and relating the change in the spacing to the stress in the coin. All experiments were performed at Northwestern University under the supervision of Dr. Jerome B. Cohen. Diffraction profiles for the crystallographic planes were acquired on a customized Picker Diffractometer, equipped with a computer controlled residual stress package designed and modified by members of Dr. Cohen's group.[37] The Picker Diffractometer was modified to allow for the rotation of the sample (the Ω axes) independent of the detection system (the 2θ axes).

The software program used allowed for the choice of the two tilt method, the $\sin^2$ psi method or the Marion-Cohen method of residual stress analysis to be used with a normal scintillation detector or a position sensitive detector. All experiments were performed using the $\sin^2$ psi method and a scintillation detector. The software allowed for complete statistical treatment of data. The diffracted peak position was located by fitting a parabola to the top 15% of the peak intensity. A series of seven points in this region was used in the fitting procedure to reduce errors in the determination of the peak position. The counting strategy was determined by the software and took into consideration an operator specified precision. The program provided an estimated time required for the specified precision and calculated the total error associated with the measurement. This error included both counting statistics and instrumental

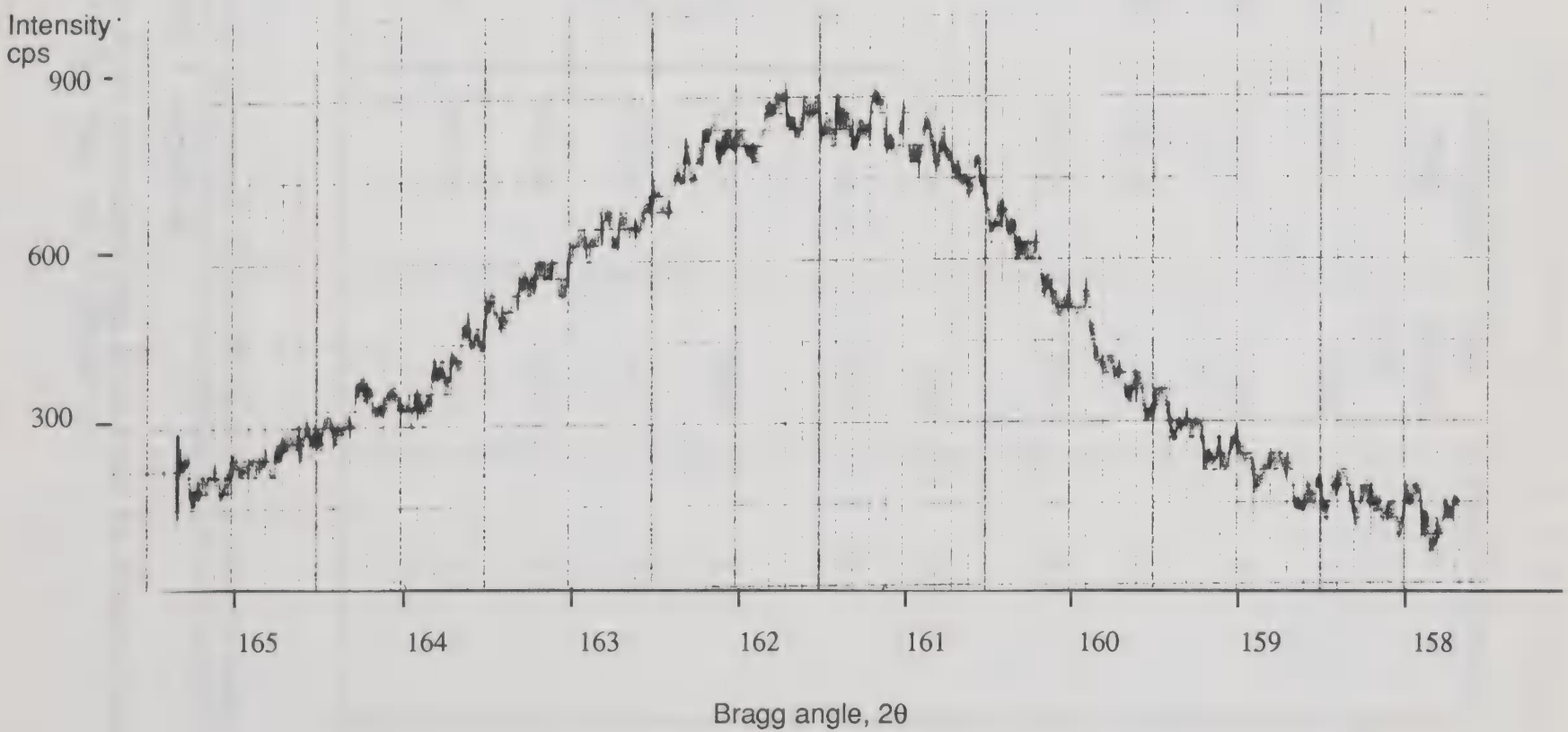

Figure 18. A representative diffraction profile for a struck coin. This diffraction profile of the [4,0,0] crystallographic plane was taken on the US 1968 D one cent (#34). The preliminary scan was performed at $\psi = 0$, $2\theta = 158$ -165 degrees.

Table II. Characteristics of Diffraction Profile for Each Sample.

Sample	Diffraction[1] Peak	Peak Intensity CPS	Peak/Background Ratio	2θ [2] psi=0^{o} $^{o}2\theta$
US 1c '68D #34	220 Cr	2368	2.2	126.31
1090D cast iron	211 Cr	1003	1.9	155.87
US 1c '69S annealed	400 Co	552	5.4	161.62
Rimmed Blank Ann. B2-G	400 Co	1901	21.3	161.66
Olin Blank #87	400 Co	248	2.1	162.17
Rimmed Blank Ann. B3-1	400 Co	2371	19.3	161.19
US 1c '68D #34	400 Co	2468	2.3	161.05
US 1c '68D #38	400 Co	601	4.5	161.09
Copper Standard	400 Co	717	5.9	163.42
1699 British Wm III (A) struck	400 Co	353	2.6	161.72

1. 220 are the miller indices for the diffraction plane; Cr or Co means that a Chromium or Cobalt X-ray tube was employed, with wavelengths of 2.2909 Å and 1.7902 Å, respectively.

2. 2θ indicates the goniometer angle about which the diffraction peak is centered, where θ is the Bragg angle of diffraction.

Table II. continued.
Characteristics of Diffraction Profile for Each Sample

Sample	Diffraction Peak	Peak Intensity CPS	Peak/Background Ratio	2θ psi=0^{o} $^{o}2\theta$
1699 British Wm III (B) cast	400 Co	541	14.1	159.55
1699 British Wm III (D) cast	400 Co	993	2.3	159.53
1775 British Geo III cast	400 Co	1088	2.8	162.86
US 1c '68D #50	400 Co	814	5.2	161.19
Olin Blank B3-1 brushed	400 Co	851	6.2	160.60
US 1c "68D #50 brushed	400 Co	711	4.1	160.66
Phantom B2-C 90,900 lb	400 Co	1177	7.7	161.32
Phantom B1-A 40,100 lb	400 Co	1770	13.2	161.40
1849 British Victoria shilling struck	420 Co	490	4.4	156.39
1856 British Victoria shilling cast	420 Co	496	4.3	156.36
1789 Spanish Carolus IV doubloon struck	420 Co	751	3.1	158.71

Table II. continued.
Characteristics of Diffraction Profile for Each Sample

Sample	Diffraction Peak	Peak Intensity CPS	Peak/Background Ratio	2θ psi=0° °2θ
1800 Spanish Carolus IV doubloon cast	420 Co	445	2.0	158.79
1719 British Geo I (A) struck	400 Co	492	3.4	161.63
1719 British Geo I (B) cast	400 Co	650	1.6	158.57

aberrations, such as errors introduced by sample misalignment and geometrical irregularities in the sample.

The $\sin^2$ psi method of residual stress analysis used in this project requires the determination of the interplanar spacing of the material at various angles psi with respect to the principal crystallographic axis of the metallic grains at the coins surface. This procedure is accomplished by first measuring the intensity of the diffracted X-ray beam with the sample normal equal to the normal of the diffracted beam, as shown in Figure 19(a). Next, the sample is rotated about the center of the goniometer, also called the omega axis, such that the sample normal and the normal of the diffracted beam differ by the angle psi, as shown in Figure 19(b), and the peak intensity is again determined.

Three types of beam focusing techniques are commonly used with diffractometer techniques of residual stress analysis: the divergent beam geometry or parafocusing, the non-focusing, and the parallel beam geometry techniques.[38] Figure 20 illustrates the relative positions of the sample, X-ray beam and detector for each of these techniques. The divergent beam geometry requires refocusing of the diffracted X-ray beam. When the $\sin^2$ psi method is used with the divergent beam geometry, the detector must be moved with each psi tilt in order to maintain the focusing of the system. The problem of accurate positioning of the detector can introduce systematic errors into the measurement of the residual stress. The parafocusing geometry uses a divergent beam, but does not attempt to refocus the beam. Certain errors are inherent in the use of this type of geometry, but these errors have been shown to be less than errors introduced by the repositioning of the detector in the divergent beam geometry. The parallel beam geometry uses a series of parallel slits, known as Soller slits, placed in the beam to create a parallel or nearly parallel incident beam. Focusing of the diffracted beam is not required in this geometry is not required, therefore it is least sensitive the surface roughness and sample misalignment.[39,40]

(a)

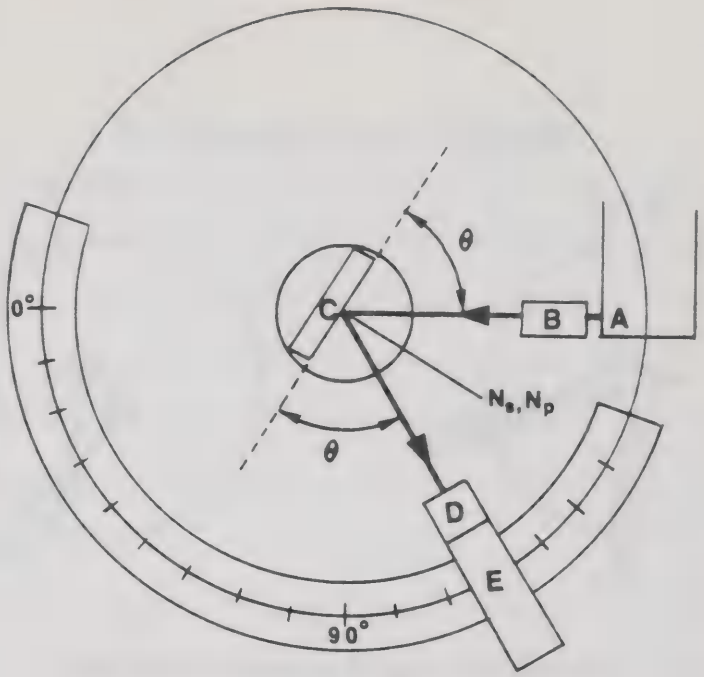

(b)

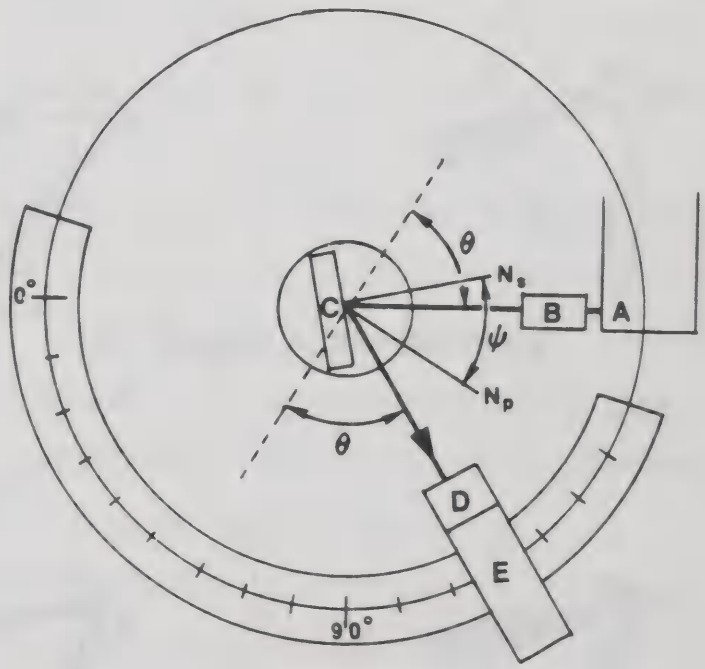

Figure 19(a). This schematic shows the instrumental set-up for the measurement of $d_{\perp}$. The components of the system are A- X-ray tube, B- divergence slits, C- sample, D- receiving slits, and E- detector. 19(b). This schematic shows the instrumental set-up for the measurement of d_{ψ}. The angle, ψ, is the angle between the normal of the sample and the normal of the reflecting planes.

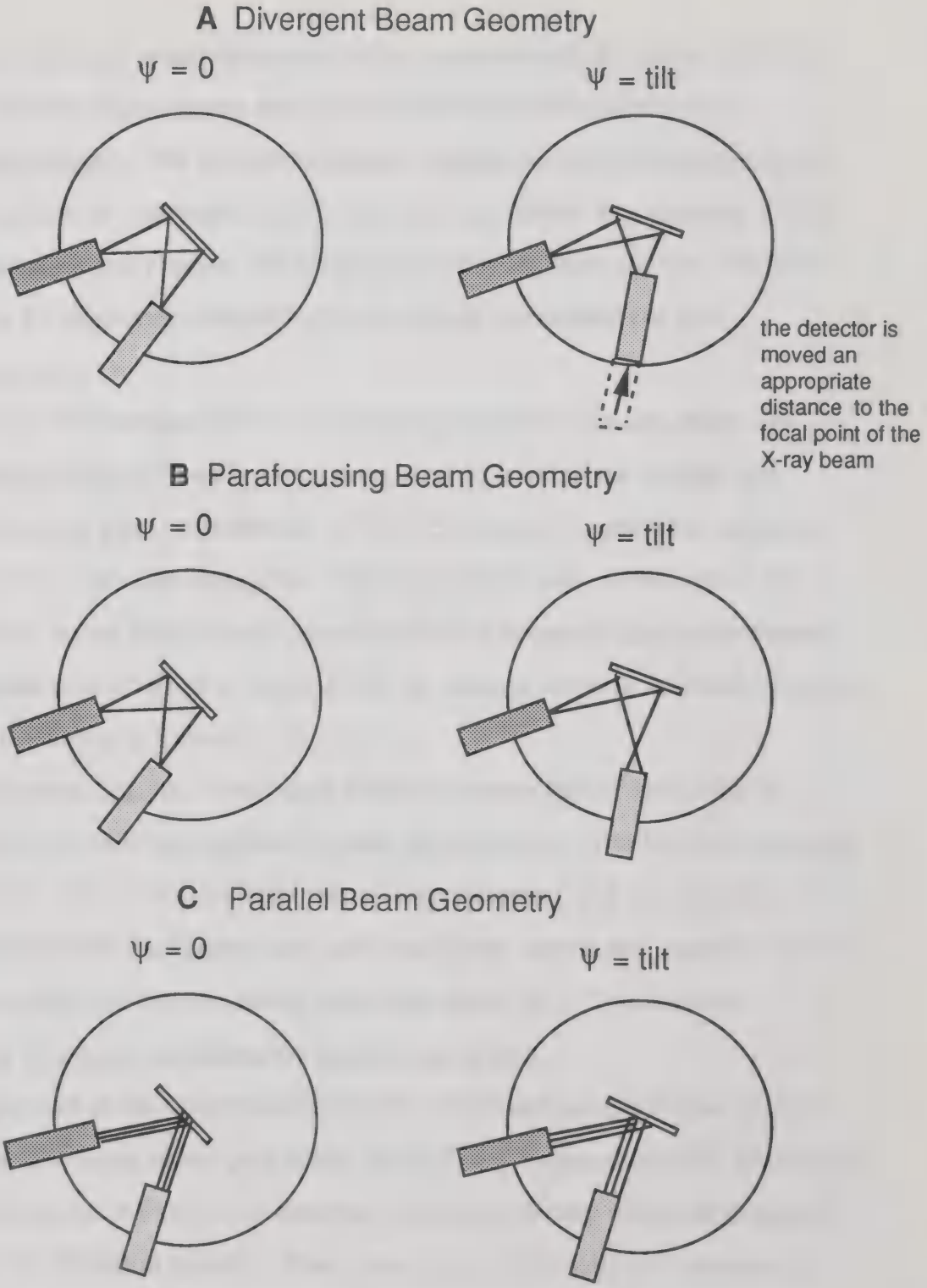
A Divergent Beam Geometry
ψ = 0
ψ = tilt
the detector is moved an appropriate distance to the focal point of the X-ray beam
B Parafocusing Beam Geometry
ψ = 0
ψ = tilt
C Parallel Beam Geometry
ψ = 0
ψ = tilt

Figure 20. This schematic diagram shows the relative positions for the sample, X-ray source and the detector for : **A**. the divergent beam geometry, **B**. the parafocusing beam geometry, and **C**. the parallel beam geometry.

A parallel beam geometry was used in the measurements to reduce errors associated with sample displacement and geometrical irregularities of the coins.

1. Diffractometer System. The total diffractometer system consisted of the goniometer, the computer system for automated control and data acquisition, the stepping motors for sample placement and rotation, the sample placement system, and the detection system. Figure 21 illustrates schematically the various components of the diffractometer system.

The Picker diffractometer served as a basic goniometer and was fitted with SLO-SYN stepping motors. These motors were used to position the sample and detector positions and were connected to a PDP8-E computer to allow for computer controlled operation. All data acquisition and manipulation was performed on the PDP-8E computer using the Residual Stress software package originally developed by Michael James and modified by members of Dr. Jerome Cohen's research Group at Northwestern University in Evanston, Illinois.[41]

2. Sample Placement System. A standard Picker specimen holder was used to position the mounted coin (see page 47) on the diffractometer. The holder is designed with fittings which slide on the dovetail track of the goniometer and are placed at the center of the goniometer. Stationary bars with positioning screws are placed in front of and behind the holder on the dovetailed track (see Figure 20). The holder is repositioned by alternately adjusting the positioning screws.

The alignment of the goniometer track was performed using a Picker "center post" located at the center of the goniometer and a 0.025 mm receiving slit. (Aluminum absorbers were placed in front of the detector as a precautionary measure to prevent an overload of the detection system). The center post was rotated until a maximum intensity was determined. The location of the maximum intensity was noted by scanning through the goniometer region located 180 ° across from the x-ray tube, commonly referred to as the $0^{o}2\theta$ region . Next, the receiving slit was moved from the

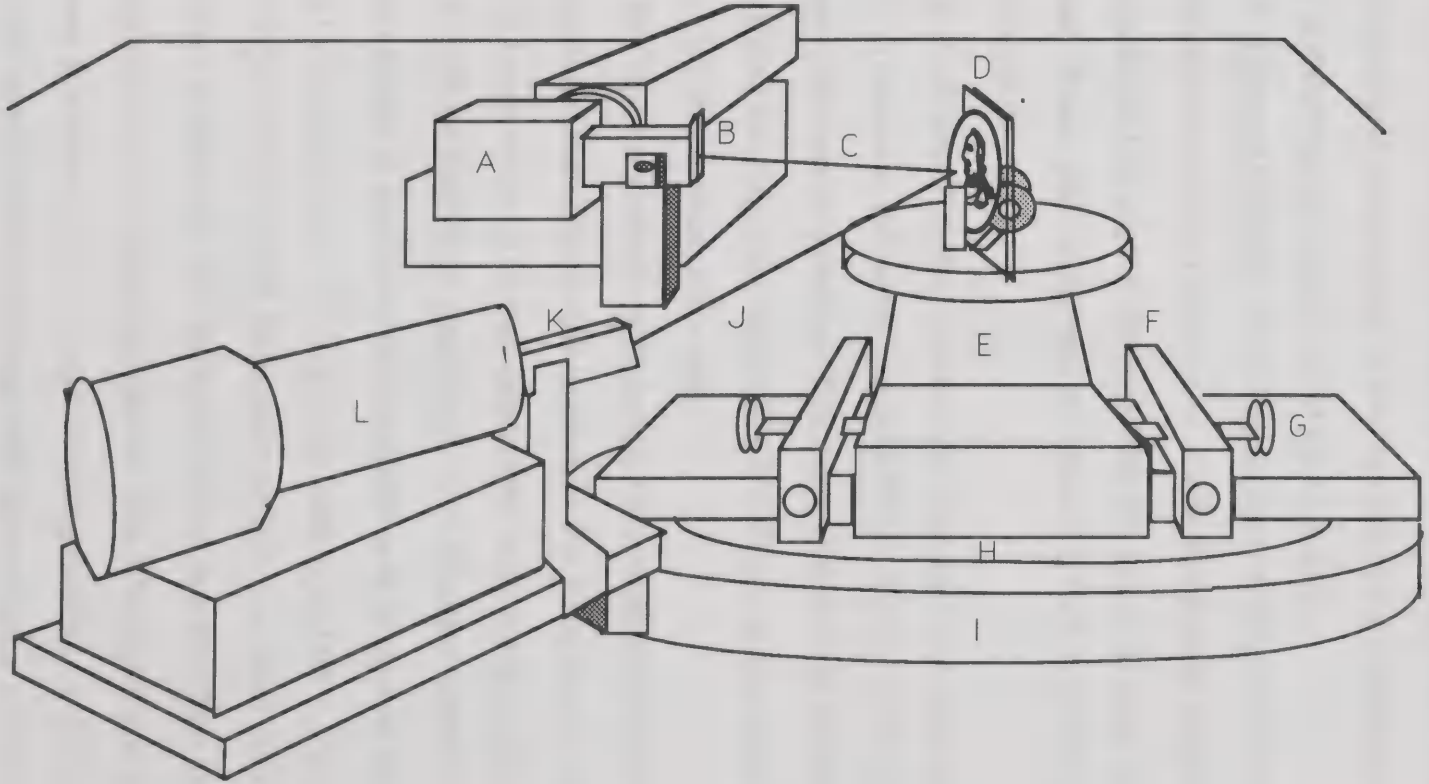

Figure 21. The instrumental system used is shown in this schematic diagram. The instrumental components are: A- X-ray tube, B-divergence slit, C- incident beam, D- coin and sample mount, F- stationary bar, G- positioning screw, H- ω axis, I- 2θ axis, J- diffracted beam, K- soller slits, and L- detector.

back of the track to the front of the track and the $0^{o}2\theta$ scan was repeated. The location of the maximum intensity was compared with the first scan. The position of the track was adjusted until no deviation in the location of the maximum intensity was observed when the receiving slit was placed in either position.

a. Sample Mounting. Requirements for residual stress measurements in coins included vertical mounting of the coin, stable positioning of the coin on the holder, and the projection of the edge of the coin from the holder in order to facilitate sample alignment. It was also critical that the mounting technique be reversible and non-destructive to the coin.

In these experiments, the coin was adhered to a clean glass microscope slide using a conservation adhesive, paraloid B72, a methyl methacrylate and ethyl acrylate copolymer dissolved in acetone. This material efficiently bonded the coin to the glass slide, allowed the coin to be removed with reagent grade acetone, and did not react in any way with the surface of the coin.

The coin was initially positioned on the microscope slide using a template which indicated the approximate location of the X-ray beam. The actual positioning of the X-ray beam on the coin was determined upon sample alignment.

b. Sample Alignment Technique. The mounted sample was first placed in the specimen holder of the Picker diffractometer and positioned approximately at the center of the goniometer. With the X-ray tube turned on at the lowest current and voltage settings, a long handled fluorescent screen was used to locate the position of the X-ray beam on the coin. The shutter of the system was then closed and the sample repositioned within the specimen holder. The procedure was repeated until the X-ray beam was positioned at the chosen sampling location on the coin.

The sample was next aligned with respect to the center of the goniometer. Aluminum absorbers were again placed over the detector as a precautionary measure. The goniometer was then rotated to the 0^{o} 2θ position, bringing the sample surface

approximately parallel to the X-ray beam. The location of the specimen holder was adjusted using the positioning screws until the edge of the coin cut the X-ray intensity in half. The sample axis, the ω axis, was then rotated slightly back and forth the insure the coin surface was parallel to the X-ray beam.

Once the sample was aligned, the actual displacement of the sample with respect to the center of the goniometer was measured using the ALIGN program of the software package. This program plots the lattice parameter versus the Nelson-Riley factor for several reflections to determine the amount of displacement from the center of the goniometer[42,43].

Once the sample was properly aligned, an initial scan of the peak in question was made to estimate the relative intensity and breadth of the peak, and to insure that the residual stress analysis of the peak would not exceed the 2θ limitations of the instrument.

3. Instrumental Conditions The operating conditions for all experiments are given in Table III. Any deviations from these conditions are noted in the results and discussion section.

Table III. Instrumental Conditions for the Picker Diffractometer.

Parallel Beam Geometry	
Target	point focus
Divergent slit	1° square
Vertical Soller slits	in diffracted beam
Goniometer Radius	5.75 in.
Radiation	Cr, (λ = 2.2909 A)
	Co, (λ = 1.7902 A)
Tube Voltage	Cr - 40 kV, Co - 40 kV
Tube Current	Cr - 20 mA, Co - 20 mA
Filter	Cr - VO, 0.00075 in. thick
	Co - FeO, 0.00035 in. thick
	Fe, 0.001 in. thick
Method	Sin^2psi with 6 tilts
psi tilts	0.00, 18.43, 26.57, 33.21
	39.23, 45.00 degrees
Rocking angle	2°
Elastic Constants[1]	Cu Coins =7.94×10^{-8} psi^{-1}
	Ag Coins =1.19×10^{-7} psi^{-1}
	Au Coins =1.24×10^{-7} psi^{-1}

1. Determined from the elastic modulus and poissons ratio from single crystal data for given element.

III.RESULTS AND DISCUSSION

A. Investigation of Copper Coins

The first phase of this research involved the investigation of copper coinage, including modern and antique coins. Residual stress determinations were performed on 1968 U.S. one cent pieces to establish the feasibility of measuring the residual stress in coins. The variations of residual stress with respect to location on the coin, as well as the variation between similar coins was examined. Annealed coins were examined to determine if accurate measurements could be made on coins possessing low residual stress values. Antique coins were examined to explore the possibility of differentiating cast counterfeit from authentic struck coins by this method.

1. Experiments using Chromium Radiation. A series of determinations, P-Cr-1 through P-Cr-4, was performed on a U.S. 1968 D mint issue uncirculated One Cent (sample #34). The results of these measurements are found in Table IV.

The goals of these experiments included the establishment of instrumental parameters for stress determinations in coins, demonstration of the reproducibility of results, and investigation of the accuracy of the determination. Establishment of instrumental parameters involved the modification of standard parallel beam methods.[9] (see p 42). The reproducibility of results was determined from duplicate determinations on one location on the coin. The accuracy of the result was investigated by a residual stress determination in a standard cast iron sample possessing known residual stress.

Chromium radiation was used in these determinations in order to compare these results to feasibility studies performed two years earlier. The results were significantly different from those of the earlier experiments owing to a systematic error in the previous experimental procedures. The earlier experiments were performed using a 2^{o} receiving slit which negated the use of the parallel beam geometry. The divergent beam geometry (see Experimental, p 42) which resulted from the presence of the receiving slit rendered the determinations extremely sensitive to displacement errors. In

this series of determinations, the receiving slit was removed producing a parallel beam geometry.

Determinations were made with and without Soller slits in the incident X-ray beam to determine the best instrumental set up for the parallel beam geometry. The purpose of Soller slits in the incident beam was to define the amount of divergence of the X-ray beam allowed for parallel beam geometry. P-Cr-1 and P-Cr-2 were performed using a 1^{o} square divergence slit without Soller slits in the incident beam. The incident divergence was limited to 1^{o} by the divergence slit which is the same amount of divergence that could be obtained using the vertical Soller slits in the incident beam. The results of these determinations, reported in Table IV, are consistent and reproducible.

P-Cr-3 was measured with Soller slits replacing the 1^{o} divergence slit in the incident beam. The result of P-Cr-3 was lower than P-Cr-1 and P-Cr-2, but is not significantly different at the 90% confidence level (See Appendix B). The poor condition of the added Soller slits may have led to the lower value by significantly reducing the intensity of the diffracted x-ray beam, thereby introducing more error into the location of the x-ray peak. The condition of the slits may also have caused a shift of the peak position by introducing systematic scatter of the diffracted x-ray beam. The comparison of these results indicated that the use of Soller slits in the incident beam did not significantly improve the accuracy of the residual stress determination. In addition, Soller slits in the incident beam lowered the X-ray intensity which lengthened experiment time. All further experiments were performed using the 1^{o} divergence slit without vertical Soller slits.

A validation of the accuracy of residual stress determinations with these instrumental conditions was performed by measuring the residual stress of a standard 1090D cast iron sample having a known residual stress value of -51 ksi. The determi

Table IV. The Measured Residual Stresses in a 1968 U.S. One Cent (#34) using Chromium Radiation.

measurement	location	stress (psi)[1]
P-Cr-1	on field above date	- 15174 ± 1137
P-Cr-2		- 15940 ± 1146
P-Cr-3		- 11413 ± 1498
P-Cr-4 cast iron sample	standard	- 51395 ± 3598

1 The error reported is one standard deviation.

nation of this sample, P-Cr-4, gave a residual stress of - 51395 ± 3599 psi which was in agreement with the known value, - 50140 ± 5362 psi.[44]

2. Experiments using Cobalt Radiation. The experiments using Chromium radiation established instrumental conditions which gave accurate, reproducible results on a U.S. 1968 D one cent piece. Careful consideration of all coins to be analyzed, i.e. copper, silver and gold coins, led to the use of Cobalt radiation for all further residual stress analyses. Cobalt radiation provided greater penetration depth than Chromium radiation in all alloys examined, and provided a higher angle back reflected X-ray beam of sufficient intensity for accurate residual stress determinations. Table V lists the infinite thickness penetration depth and Bragg angle for various radiations and coining alloys.

3. Variation of Residual Stress with Sample Displacement. Further investigation of instrumental parameters included measurements to determine the effects of sample displacement and filter thickness. Standard parallel beam methods provide accurate residual stress determinations with negligible error due to sample displacement.[45] Since the standard methods were modified, it was necessary to insure that the method of analysis used was not affected significantly by sample displacement. In addition, measurements made using two different iron filters were compared to determine affects of filter thickness on results.

A series of determinations was performed using Cobalt radiation to investigate the sensitivity of the residual stress determination to sample displacement. The instrumental arrangement included the parallel beam geometry with a 1^{o} divergence slit. Results are reported in Table VI. The six residual stress determinations for this study were performed on the U.S. 1968 D mint issue one cent piece (#34). The coin was first mounted and placed on the diffractometer with psi angle alignment but without careful alignment of sample displacement. P-Co-1 was measured above the date at the midpoint between the chin of Lincoln and the edge of the coin. The

Table V. Penetration Depth in Various Metals as a Function of Radiation.

Rad.	Metal	hkl [1] plane	2θ [2]	μ/ρ^3 cm^2/g	ρ g/cm^3	depth t $(cm)^4$
Mo 0.711 Å	Cu	[9,3,1]	139.3	49.34	8.93	5.10 (10^{-2})
	Ag	[10,4,2]	144.7	26.38	10.50	7.19 (10^{-3})
	Au	[10,4,2]	145.0	111.30	19.28	9.22 (10^{-4})
Cu 1.542 Å	Cu	[4,2,0]	145.0	51.54	8.93	4.32 (10^{-3})
	Ag	[4,2,2]	135.1	218.10	10.50	1.06 (10^{-4})
	Au	[4,2,2]	135.6	207.80	19.28	6.02 (10^{-4})
Co 1.790 Å	Cu	[4,0,0]	164.1	78.11	8.93	2.05 (10^{-3})
	Ag	[4,2,0]	156.8	323.50	10.50	4.00 (10^{-4})
	Au	[4,2,0]	157.8	303.30	19.28	2.23 (10^{-4})
Cr 2.291 Å	Cu	[2,2,0]	127.3	155.20	8.93	5.74 (10^{-4})
	Ag	[2,2,2]	152.4	617.40	10.50	2.46 (10^{-4})
	Au	[2,2,2]	153.2	568.00	19.28	1.42 (10^{-4})

1. hkl indicate the Miller indices of the reflecting plane.
2. 2θ is the expected goniometer angle for the location of the diffraction peak. This value is calculated from $n\lambda = 2d \sin\theta$; d calculated from:

   $\frac{1}{d^2} = \frac{h^2 + k^2 + l^2}{a^2}$, see reference 17, p 31.

3. μ is the X-ray absorption coefficient for the metal, and ρ is the density of the metal, see reference 46, pp 47-66.
4. Value calculated as infinite thickness, $t = \frac{3.45 \sin\theta}{\mu}$

measured residual stress was found to be - 29165 ± 3163 psi, a value higher than that measured at the same location using chromium radiation.

Since cobalt radiation has the ability to penetrate farther into the coin than chromium radiation, a larger volume of the coin was sampled. The residual stress which was determined is an value averaged over the entire sampling volume. The maximum residual stress may not always be located at the surface, but rather can be displaced beneath the surface of the coin.[47] Greater penetration depth can therefore lead to the finding of higher residual stresses with cobalt radiation versus chromium radiation, as seen in this coin.[48]

In addition the higher residual stress seen in this coin may be the sum of both planer, normal and shear stresses within the sampling volume. One way to determine whether there are high shear stresses normal to the surface of the coin is to measure d spacings at both positive and negative psi values. The observation of differences in d spacing with positive and negative values of the same psi angle, a phenomenon known as psi splitting, results from high shear stresses, $\sigma_{1,3}$ and $\sigma_{2,3}$.[49,50]

The higher residual stress observed with cobalt radiation could have been indicative of shear stresses located within the sampled volume or of a stress gradient varying with penetration depth within the coin. In order to determine if psi splitting was taking place, d spacings were measured at positive and negative psi angles on the one cent piece. No psi splitting was observed in the One Cent (#34) as measured at P-Co-4. These results suggest that there are no significant shear stresses within the sampled volume. The higher residual stress determined with Cobalt radiation could have been due to a stress gradient, with maximum residual stresses beneath the surface of the coin.[51]

To continue the investigation of the displacement affect, the coin was displaced by approximately 2 mm forward from its original position. A residual stress of - 13262 ± 5874 psi was measured at P-Co-2. Next the coin was displaced behind the original

position by approximately 1mm and P-Co-3 was measured to be - 27296 ± 1916 psi. The residual stress measured 2 mm forward from the original position has a large uncertainty associated with it, and appears to be lower in value than the residual stress at the original position or measured 1mm behind the original position. The lower value may be due to a slight shift in location when the sample placement was adjusted. The large uncertainty in the result on the sample displaced in the forward position is calculated from the error associated with the d spacing measured at each individual angle psi. In the case of the measurements on the sample which was displaced in the forward direction, a large error was associated with one particular d spacing, see figure 45, p 145. The error associated with this point may be an artifact which arises from a difficulty in the recognition of the peak location by the software due to fluctuations in the current or voltage of the x-ray tube. Alternately, some error may have been introduced from lack of parallelism of the x-ray beam. The parallelism displayed by the x-ray beam is a function of the condition and width of the Soller slits used. In these experiments a 1 degree divergence slit was used instead of incident Soller slits, as described on page 51, due to the poor condition of the available Soller slits. This results in a 1 degree divergence from the absolute parallel condition. Errors introduced by this slight divergence are minimized by careful alignment of the sample with respect to the center of the goniometer.[52] These results led to measuring the residual stresses on carefully aligned samples.

The 1968 one cent was aligned to a displacement of less than 0.00001 inch for the P-Co-5 determination. The sample displacement was calculated from the measurement of the lattice parameters at three different hkl reflections.[53] At this displacement the residual stress was found to be - 23566 ± 1329 psi. Since the coin was carefully aligned, errors for sample displacement should be negligible. While the results of P-Co-1, P-Co-3, and P-Co-5 are similar, large displacements of approximately 2 mm

do affect the residual stress analysis slightly. Sample displacement was minimized to less than 0.01 inch in all further experiments.

The study of experimental conditions included the determination of residual stresses in coin #34 using different iron filter thickness. All previous experiments were performed used a 0.00035 in. thick iron oxide filter. A 0.001 in. iron filter was used to measure P-Co-6. The residual stress was measured to be - 21428 ± 1578 psi and was located with the same sample displacement as P-Co-5 (See Table VI). The result did not differ significantly from results obtained with the thin Iron Oxide Filter, indicating that filter thickness had little effect on the residual stress results. Since the thicker Iron filter provided a better peak to background ratio which facilitated location and measurement of the diffracted X-ray peak, it was used in all further experiments.

4. Residual Stress on Annealed Coins. Once it was established that reproducible residual stresses were measurable in struck coins, it was necessary to demonstrate that residual stresses of low value could be measured in coins. The residual stress in an annealed coin was measured.

A 1968 S mint issue U.S. one cent piece was annealed for 20 minutes at 525^{o}C. The residual stress twice was measured above the date of the coin. The weighted average residual stress was - 4179 ± 469 psi. This residual stress is in agreement with the expected residual stress of an annealed material.[54]

In addition, the residual stress of a standard stress free copper sample was determined. The sample was an annealed, pressed copper powder disk. Determination of residual stress yielded 306 ± 269 psi for the sample. This result is consistent with the fact that the sample is assumed to be stress free.

5. Variation of Residual Stress Between Similar Coins. This series of determinations was performed to determine the variation of residual stress between similar coins. Residual stresses were determined at various locations on two U.S. 1968 D mint issue one cent pieces, (#34) and (#38). The coins were bank wrapped in

Table VI. Effect of Sample Displacement on Residual Stress Analyses of 1968 D U.S. One Cent[1] Piece (#34)

Meas.#	Displacement	Stress (psi)[2]
P-Co-1	not meas.	- 29165 ± 3162
P-Co-2	approx. 1 mm forward	- 13262 ± 5874
P-Co-3	approx. 1 mm backward	- 27296 ± 1916
P-Co-4	not meas.	no splitting
P-Co-5	aligned to 0.00001 in.	- 23566 ± 1328
P-Co-6	same as P-Co-5 but with 0.001 Fe filter	- 21428 ± 1578

1. All measurements were taken with approximately 2 mm of the same location, above the date on the one cent.
2. Error reported is one standard deviation of the measurement.

the same original roll of one cent pieces. Therefore the coins should have been minted on the same day and perhaps the same minting press.

Table VII lists the results of residual stress analysis on both high and low field locations on a U.S. one cent (#34). Residual stresses of -13104 ± 975 psi above the liberty and -26439 ± 1066 psi near the edge were found in the low field areas of the coin. Residual stresses of -20324 ± 1539 psi on the head and -14700 ± 1066 psi on the portrait, near the neck of the Lincoln, were found on the high field or raised areas of the coin.

Determinations on the one cent (#38) were performed on similar locations as the one cent (#34), i.e. above the liberty, near the edge and on the head of Lincoln. In addition, determinations were also performed on the chin, and above the date near the chin of Lincoln.

The residual stress was found on the chin of Lincoln and was - 28898 ± 2304 psi. The residual stress near the chin, but on the low field of the coin, was - 17687 ± 1436 psi.

The results on the U.S. one cent #38 can be compared to those of the U.S. one cent #34, located in Table VIII. An evaluation of the results using the students two sided t-test (See Appendix B) indicates that determinations near the edge on coin #38 are statistically the same as determinations on coin #34 at the 90% confidence level. The determinations of coin #38 above the liberty and on the head similar to those on coin #34. These results suggest that the residual stresses in the one cent vary with location on the coin and are reproducible from coin to coin.

6. Variation of Residual Stress with Location. The results listed in Tables VII and VIII also were used to investigate the variation of residual stress with respect to location on the coin. The variation of residual stress may be due to die design. The designs on coining dies are sunk into steel die blanks having a highly polished conical surface. The resulting coining die is given a slightly convex surface which has been shown to lower the coining pressure required to strike the coin.[55] Since the convex

"form" of the die influences the deformation of the coin blank while it is being struck into a coin, the residual stress may vary with respect to the amount of plastic flow taking place within the coin flan and to the radial distance from the center of the coin.

Delamare and Montmitonnet used upper bound methods of mechanical analysis to show possible flow patterns in a coin during striking.[56,57] Their research suggests that more plastic flow takes place near the edge of the coin and in the portrait or raised areas of the coin. Their mechanical analysis also suggests that dead spots for plastic flow can appear in some raised areas or in low field portions of the coin.

The residual stress analyses of the one cent pieces show a correlation between high residual stress and the amount of plastic flow taking place within the coin. High residual stresses were found in both coins at locations on the portrait and near the edge of the coins where more plastic flow takes place. Higher residual stresses are expected with increasing relief. Low residual stresses were found in low field areas, such as above the date and near the chin of (#38) or above the liberty on both coins, where less plastic flow occurred. The low residual stress value determined at the neck on the portrait in coin (#34) may be indicative of plastic dead spots of metal.

Two residual stress determinations were made above the liberty and above the date at the same radial distance on the (#38) coin, as shown in Table VIII. The similarity of these results suggest that the variation in residual stress may also be a function of the distance from the center of the coin.

These results demonstrate that the residual stresses in the coin display systematic variance with respect to the plastic flow taking place during striking of the coin. Areas of high plastic flow most likely create the most nonuniform deformations which lead to the high residual stresses.

7. Residual Stress Measurements on Antique Coins. Experimental results have established that reproducible residual stress determinations can be obtained on modern coins possessing both high and low residual stresses. Determination of

Table VII. Average Residual Stress at Various Locations on the 1968 US One Cent Piece (#34)

Coin	Location	Relief	Stress[1] psi
US 1c '68D #34 uncircularted	above liberty	low	-13104 ± 975
"	above date near edge	low	-26439 ± 1066
"	on head	high	-20324 ± 1539 [2]
"	on neck	high	-14700 ± 1066

1. Residual Stress reported is the weighted average of two measurements. error is reported as one standard deviation of the average value. See Appendix B.

2. Value reported is for one measurement only.

Table VIII. Average Residual Stresses at Various Locations on the 1968 D US OneCent Piece (#38).

Coin	Location	Relief	Stress[1] (psi)
US 1c '68D #38 uncirculated	above liberty	low	-16378 ± 1941 [2]
"	above date near edge	low	-24840 ± 1378
"	on head	high	-23131 ± 2238 [2]
"	on chin	high	-28898 ± 2304 [2]
"	above date near chin	low	-17687 ± 1436

1. Residual Stress reported is the weighted average of two measurements. Error is reported as one standard deviation. See Appendix B.
2. Value is reported for one measurement only.

residual stresses in antique coins pose additional problems, including surface irregularities from abrasion, and corrosion which could affect accuracy.

Residual stress determinations were made on both cast and struck antique copper coins in order to establish the reproducibility of measurements and to evaluate residual stress analysis as a method for differentiating struck from cast coins.

a. Determination of Residual Stresses in Antique Struck Coins. Table IX reports results of residual stress analyses on the following two authentic antique struck coins (n.b. When there are multiple coins of the same type, the struck authentic coin is designated A. The cast counterfeits are designated B,C, etc.):

1. a 1699 British William III halfpenny, designated (A), and
2. a 1719 British George I halfpenny, designated (A).

Residual stresses were determined on three locations on the obverse of each coin, on the field near the chin, on the field behind the portrait, and on the portrait. Analysis of the William III halfpenny yielded residual stresses of -21775 ± 1715 psi on the field near the chin, -41160 ± 2075 psi on the field behind the portrait, and -35855 ± 2542 psi on the portrait. Similarly, residual stresses of -32990 ± 1577 psi on the field near the chin, -28338 ± 1777 psi on the field behind the portrait, and -46009 ± 1368 psi on the portrait were found on the George I halfpenny. Duplicate determinations at one location on each coin gave consistent, reproducible results.

Results on both coins display variation in residual stress at different locations. Statistical evaluation of results determined on the field near the chin, and on the portrait of the George I halfpenny indicate that the differences are significant at 90% confidence level (See Appendix B). Low field residual stress determinations tend to be lower in value than residual stress determinations made on the raised portrait areas.

The residual stresses determined in these antique coins are higher in value than residual stresses determined in the modern U.S. one cents, and may arise from wear of the coin. As with the one cents, higher residual stresses are found on the

Table IX. Residual Stresses in Struck Antique Copper Coins.

Coin	Location	Stress[1] (psi)
1699 William III 1/2 d	on field near chin	-21775 ± 1715
	on field	-41160 ± 2075 [2]
	on portrait	-35855 ± 2542 [2]

Table IX. continued on next page.

1. Residual stress reported as weighted average value of two measurements. Error reported as one standard deviation. See Appendix B.
2. Value is reported for one measurement only.

Table IX. continued.

Coin	Location	Stress [1]
1719 George I 1/2 d	 on field	-32990 ± 1577
	 on field	-28338 ± 1777 [2]
	 on portrait	-46009 ± 1368

raised areas of the coin, where more nonuniform deformation was likely to have taken place. On the William III halfpenny, the residual stress determined on the field behind the portrait does deviate from the trend established in the modern coins and the George I halfpenny. The residual stress of -41160 ± 2075 is higher in value than that found on the portrait of the coin. This anomaly may be due to surface manipulation, such as abrasion (vide infra).

These experiments establish that residual stresses can be measured on struck antique coins. Results are consistent with those of the modern coins which display higher residual stress in areas of more plastic flow.

b. Determination of Residual Stress in Cast Counterfeit Coins. Table X shows the results of residual stress analyses on the following cast counterfeit coins:

1.,2. two 1699 British William III cast counterfeit halfpennies, designated (B) and (D)

3. a 1719 George I cast counterfeit halfpenny, designated (B)

4. a 1775 George III cast counterfeit halfpenny.

Quantitative residual stress results were not obtainable on the 1699 William III (B) and the 1719 George I (B) halfpennies due to severe oscillations in the d versus $\sin^2$ psi plots (see Figures 84 and 85, pp 184-185). The $\sin^2$ psi method is based on a linear relationship between d and $\sin^2$ psi, and the residual stress is calculated from the slope of the plot. Therefore deviation from linearity results in large errors in the determined residual stress. Residual stresses were measured at two locations, on the portrait and on the field, of the 1775 George III and the 1699 William III (D) halfpennies. Analysis of the 1775 George III halfpenny yielded residual stresses of -30094 ± 839 psi on the field and -33789 ± 1147 psi on the portrait. Residual stresses of -41669 ± 1921 psi on the field and -23449 ± 2994 psi on the portrait were determined on the 1699 William III halfpenny.

The oscillatory behavior of the $\sin^2$ psi plots for the 1719 George I (B) and the 1699 William III (B) halfpennies may result from dendritic growth and, or large grain size within the cast coins.[18] Dendritic growth within as cast coin can result in non random orientation of grains within the coin. Large grain size can affect the peak intensity of the diffracted beam.[58]

Oscillations in d versus $\sin^2$ psi plots commonly result from non random orientation of grains within a polycrystalline material known as texture.[59] The $\sin^2$ psi method of residual stress analysis measures the interplanar spacing of many grains at various psi tilts. Since different grains are sampled at different psi tilts, non random orientation of the grains can significantly alter the intensity of the diffracted X-ray beam at different psi tilts and thus effect the method. The peak may literally disappear at some psi tilts. In addition, x-ray elastic constants vary with psi tilts in strongly textured materials because grains of different orientations are sampled at each tilt. This elastic anisotropy results in the observed oscillatory behavior.[60]

Thus, it is not surprizing to observe oscillations of the d versus $\sin^2$ psi plots in the cast counterfeit coins. The presence of oscillatory behavior could be used to differentiate cast from struck coins, but absence of oscillations is not significant.

The high residual stresses measured on the 1775 George III and the 1699 William III (D) halfpennies are not expected results and complicate the use of residual stress analysis as a method to differentiate between cast and struck coins. High residual stresses in these coins could be due to abrasion and wear of the surface of the coin. The surface of the 1775 George III halfpenny shows considerable wear, as does the surface of the 1699 William III (D) halfpenny. Once a coin is cast, it may undergo surface modifications such as brushing or burnishing which could lead to higher residual stresses.

These experiments demonstrate that some cast coins show severe oscillations in the d versus $\sin^2$ psi plots which could provide a means of identification while other

Table X Residual Stress in Cast Copper Coins

Coin	Location	Stress[1] (psi)
1719 George I (B) cast countefeit 1/2 d	 on field	severe oscillations
1699 William III (B) cast counterfeit 1/2 d	 on field	severe oscillations
1775 George III cast counterfeit 1/2 d	 on field	-30094 ± 839
	 on portrait	-33789 ± 1147 [1]

Table X. continued on next page.

[1] Result reported as weighted average value of two determinations. Error reported as one standard deviation. See Appendix B.

Table X. Continued.

Coin	Location	Stress[1] (psi)
1699 William III (D) cast counterfeit 1/2 d	on field	-41668 ± 1921
	on portrait	-23449 ± 2994 [2]

2. Value is reported for one measurement only.

cast coins show high measurable residual stresses. The results of this series of experiments led to an investigation of the effects of abrasion on residual stress.

B. Investigation of the Effects of Abrasion on Coins

Abrasion may affect the residual stress of both struck and cast coins. Residual stresses in both struck and cast coins could have been altered by wear and abrasion during circulation. In addition, finishing methods used in the manufacture of cast objects could have altered the residual stresses in cast coins.

A series of measurements was performed to determine the effects of abrasion on both moderately stressed and low stressed coins or blanks. The coins and blanks were abraded using common methods of finishing for jewelry or cast materials; these are similar to methods which may have been used on the cast counterfeit coins.

The U.S. D mint issue one cent piece was first abraded above the date using a flexible shaft jewelry drill to which a small wire brush was affixed. After brushing, the area was buffed with polish, and a residual stress measurement was made. The coin was then abraded by hand using a wire brush and a second residual stress determination was performed. The residual stress in an annealed type I blank (Olin, B3-1) was determined both before and after abrasion by hand using the wire brush.

The results of residual stress measurements on an abraded one cent piece and a type I blank are listed in Table XI. Analysis of the U.S. one cent piece after brushing and buffing with a flexible shaft yielded a residual stress of -18759 ± 1557 psi. After wire brushing the same location of the one cent piece, the residual stress was -36271 ± 1988 psi. The residual stress of the annealed type I blank was - 1782 ± 366 psi. A residual stress of -41999 ± 1631 psi was determined on the type I blank after it was abraded by hand.

The residual stress located above the date of the one cent (#50), after brushing and buffing, was similar to the residual stress of -17697 ± 1436 psi found on the unabraded one cent (#38) (see table VIII). The similarity of these results indicates that

mechanical manipulation using the flexible shaft jewelry drill did not significantly alter the residual stress at this location. This result is in agreement with that found by Wharton[61] on the effects of surface treatment on Laue photographs of medals.

Brushing the same surface of the coin by hand produced a significantly higher stress in this region. It is probable that brushing in this manner caused groove formation and the removal of material as microchips. The material plastically deformed at the ridges and side of the grooves, creating large compressive stresses.[62] As the material is cold worked it may become strain hardened, which alters the yield stress of the surface grains. Continued working will cause more severe deformation to take place on the grains beneath the surface grains which have a lower yield stress. This results in lower residual stresses near the surface and higher residual stresses beneath the surface of the material. A stress gradient thus can be introduced by mechanical methods which cause strain hardening within a material.[63,64]

The differences seen between the mechanical and hand brushing may be due the amount of plastic deformation below the surface of the coin. The mechanical brushing could have created a more uniform deformation over the surface of the coin than brushing by hand, leading to less residual stress in the coin. Also, the mechanical manipulation may have produced frictional heating of the surface and resulted in some amount of stress relaxation.

The results of these experiments indicate that residual stresses in moderately stressed coins are significantly affected by hand brushing, while mechanical brushing produces little change. In all cases abrasion produced compressive stresses in the coin. The abrasive wear of coinage from handling, etc. should produce similar changes in the residual stress system of the struck coin, dependent on the amount of abrasion and strain hardening taking place on the surface of the coin.

High compressive residual stresses were determined in the annealed blank after abrasion. The residual stress of -41999 ± 1631 psi is near the -45000 psi yield

Table XI. Effects of Abrasion on Coins and Blanks

Coin	Method of Abrasion	Location[1]	Stress[2] (psi)
US 1c '68 D #50	brush/buff'	above date near chin	-18759 ± 1557
"	wire brushed by hand	above date near chin	-36271 ± 1988
Type I Blank Olin B3-1	annealed	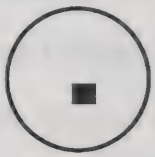 near center	- 1782 ± 336
"	wire brushed by hand	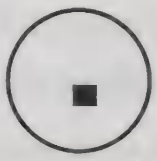 near center	-41999 ± 1631

1. Measurements were performed within approximately 2 mm of each other for means of comparison.
2. Error reported is one standard deviation.
3. Result reported is weighted average of two measurements. See Appendix B.

stress of the copper alloy from which the blank is made. The causes of these compressive stresses are the same as those discussed above. From these results it seems that the low stressed coins are more significantly affected by abrasion than the moderately stressed coins.

This series of experiments demonstrates that abrasion can produce severe changes in the residual stress system within the coin. High compressive stresses can be introduced into low stressed coins, such as the cast counterfeit coins, by surface manipulation from finishing techniques or from handling and wear.

C. Investigation of Silver and Gold Coins

As an extension of the copper studies on antique coins, residual stresses were also determined on struck authentic and cast counterfeit silver and gold coins. Residual stress measurements were performed on the following coins:

1. a 1849 struck authentic British Victoria shilling (silver),
2. a 1856 cast counterfeit British Victoria shilling (silver),
3. a 1789 struck authentic Spanish Carolus IV gold doubloon, and
4. a 1800 cast counterfeit Spanish Carolus IIII gold doubloon.

The results of these measurements are given in Table XII.

1. Residual Stress Measurements on Silver Coins. Residual stress measurements were performed at two locations on both the cast counterfeit and the struck authentic British Victoria shillings. Measurements on the authentic 1849 British Victoria shilling yielded residual stresses of - 8814 ± 989 psi on the low field area behind the head, and - 8984 ± 875 psi on the portrait of the coin. In comparison, residual stresses of - 8673 ± 983 psi and - 10057 ± 886 psi were found respectively on the field behind the head, and on the portrait of the cast counterfeit 1856 British Victoria shilling.

The residual stresses determined in both coins are near the 10 ksi yield stress of the 92.5% Silver - 7.5% Copper coining alloy. No significant differences can be

Table XII. Residual Stresses in Silver and Gold Coins.

Coin	Alloy	Location	Stress[1] (psi)
1849 Struck Victoria shilling	Silver	on field behind head	8814 ± 989
1849 Struck Victoria shilling	Silver	on head	- 8984 ± 875
1856 Cast Victoria shilling	Silver	on field behind head	-10057 ± 886
1856 Cast Victoria shilling	Silver	on head	- 8984 ± 875

Table XII. Continued on next page.

1 Result reported is one individual determination.

Table XII. Continued.

Coin	Alloy	Location	Stress[1] (psi)
1789 Spanish doubloon struck	Gold	on field	-16370 ± 906
1789 Spanish doubloon struck	Gold	on portrait	-17136 ± 1058
1800 Spanish doubloon cast	Gold	on field	-32653 ± 980

1. Result reported is one individual determination.

noted in the residual stress resulting from difference in location on the coin or mode of manufacture of the coin. Since the yield stress of the coining alloy is low, higher residual stresses would not be expected. Affects of abrasion or temperature on silver coins may be much more significant due to the ease of plastic deformation indicated by the lower yield stress. It is also possible that the counterfeit piece was struck rather than having been cast.

2. Residual Stress Measurements on Gold Coins. Residual stress measurements were performed on the portrait of the authentic 1789 Struck Spanish gold doubloon and on the low field area of both the authentic and the cast counterfeit 1800 Spanish gold doubloon. Residual stresses determined on the authentic coin were - 16370 ± 906 psi on the low field and - 17136 ± 1058 psi on the portrait of the coin. These results indicate that the residual stress does not vary significantly with location on the gold coin. The residual stress analysis of the cast counterfeit Spanish 8 gold doubloon yielded a much higher residual stress of - 32653 ± 980 psi. The high residual stress may be the result of the surface manipulations which led to the polished finish seen on the surface on this counterfeit coin. Also, the actual composition of the gold coins was not determined prior to these residual stress analyses. The counterfeit coin may consist of a more alloyed gold which possesses a significantly higher yield stress than that of pure gold.

The expected residual stress in a plastically deformed material which has undergone little relaxation is the yield stress of the material. The residual stress found in the authentic struck coin is near to the 18 ksi yield stress of gold.[65] The significantly higher residual stress in the cast counterfeit is indicative of strain hardening which can alter the yield stress of a material and result in stresses higher than the expected yield stress value.

D. Examination of the Effects of Coining Pressure on Residual Stress

The second phase of this project involves the investigation of residual stresses throughout the striking process. Residual stresses were determined in various coin blanks and "phantom" coins struck at known pressures using a hydraulic press.

1. Residual Stress Measurements on Coining Blanks. The coin blank undergoes many manipulations in the process of producing a coin. The blank is first punched out of a rolled sheet of coining metal, then is annealed to a specified grain size and hardness. After annealing, the blank is mechanically rimmed to achieve a strain hardened protective edge and to decrease the amount of coining pressure needed to strike the coin. The blank is then ready for striking.[66,67]

Residual stresses were measured in coin blanks at various stages in the coining process in order to better understand the stress system established by each manipulation of the blank. Investigation of residual stress in coining included the measurement of stresses in the following blanks:

1. a "type one" blank, as rolled and punched (Olin #87)
2. a "type one" blank, after annealing at 514^{o}C for 20 minutes (Olin B3-1)
3. a "type two" blank, after rimming (Olin B2-G).

Results of these measurements are listed in Table XIII.

The residual stress of the rolled and punched "type one" blank (Olin #87) was -4084 ± 1395 psi. After annealing a "type one" blank (B3-1) the residual stress was found to be -1782 ± 336 psi. The lower residual stress value in an annealed blank is expected. Rimming an annealed "type one" blank to produce the "type two" blank led to the tensile residual stress of 4504 ± 298 psi. The rimming process shears the blank at its edge and pushes the material of the inward and up to create a lip or rim. The flow of the metal in these directions may slightly compress the polycrystalline material perpendicular to the surface and elongate the grains parallel to the surface of the blank. This elongation could lead to the tensile stress seen in the "type two" blank.

Table XIII. Residual Stress in Copper Coining Blanks.

Blank	Condition	Stress[1] (psi)
Type I Olin #87	 as rolled and punched	-4084 ± 1395
Type I Olin B3-1	 annealed[2]	- 1782 ± 336
Type II Olin B2-G	 annealed[3] then rimmed	4504 ± 298

1. Result reported is weighted average of two determinations. Error is reported as one standard deviation. See Appendix B.
2. Annealed at 514°C for 20 minutes.
3. Annealed at 515°C for 20 minutes.

The residual stresses in all coining blanks were low in value and indicate only mild forms of deformation. The "type one" blanks show compressive tensile stresses both before and after annealing. The "type two" blank displays tensile stresses on the surface of the blank. Some caution should be taken in the interpretation of these low residual stresses due to the fact that the "d spacing" undergoes such small changes at low stress and measurement of these changes is near the detection limit of the technique.

2. Residual Stress Measurements on "Phantom" Coins. Residual Stress measurements were taken on "Phantom" coins to investigate the change of residual stress with respect to coining pressure. A goal of the research was to establish an empirical relationship between coining pressure and residual stress in order to estimate coining pressures produced by early mechanical minting methods. A series of "phantom" coins was struck using a hydraulic press as described in Appendix C. The results of residual stress determinations on "phantom" coins struck at 90,000 lbs and 40,000 lbs is given in Table XIV.

The design of the coins consisted of a high field circular area and cylindrical area, and a low field area, as seen in Figure34, p 132. The residual stress measurements of the 90,000 lb phantom coin yielded a tensile residual stress of 17407 ± 1871 psi on the low field portion and a compressive residual stress of -11864 ± 1763 psi on the high field portion of the coin. Residual stresses of -2252 ± 1365 psi and 2774 ± 840 psi were found on the low field and high field portions respectively of the 40,000 lb "phantom" coin.

The residual stresses appear to differ somewhat randomly in the two "phantom" coins. Tensile residual stresses were found in the low field and compressive stresses were found in the high field of the 90,000 lb. "phantom" coin. The results of the 40,000 lb "phantom" coin were opposite, with the high field in tension and the low field in

Table XIV. Residual Stresses in Struck Phantom Coins

Coin	Coining Pressure	Location	Stress[1] (psi)
B2-C	90,900 lbs	on reverse on field	17407 ± 1871
"	"	on reverse on high relief	- 11864 ± 1763
B1-A	40,100 lbs	on reverse on field	- 2252 ± 1365
"	"	on reverse on high relief	2774 ± 840
B1-A[2]	40,100 lbs	on reverse on field	- 525 ± 1997

1. Result reported is one individual determination. Error reported is one standard deviation.
2. Result determined with the following instumental conditions: 1^{o} x $1/2^{o}$ divergence slit; 4^{o} sample rocking angle.

compression. Results on both coins differ from those determined on the U.S. one cent pieces.

The "phantom" coins differ in design and mode of striking from a U.S. one cent piece, and this may have led to the notable differences in the residual stresses found. The design of the one cent piece has more varied areas of relief and a more gradual slope into the highest relief areas than the design of the "phantom" coins. Also the U.S. one cent is struck on a knuckle-action press with a striking blow imparted to the coin rather than the squeeze or forming deformation imparted the "phantom" coins by the hydraulic press. Strain rates effect metalworking by increasing the flow stress of the metal and increasing the temperature of the work piece through adiabatic heating. The hydraulic press has a much slower deformation velocity than the knuckle action press which affects the strain rate of the material.[68] Since residual stress analysis of the one cent pieces has shown that results are altered by the flow processes taking place during the striking of the coin, it is possible that changes in flow stress would result in different residual stresses. Therefore, it is not unreasonable to see differences in the residual stresses of coins minted by an hydraulic press versus those minted by a knuckle action press.

The residual stress analyses of "phantom" coins did not lead to an empirical relationship by which to determine coining pressures imparted by early mechanical minting methods. Limitations of the technique resulted from differences in die design and mode of deformation.

Some explanation of the resulting residual stresses in the "phantom" coins may be deduced. While the compressive residual stress determined on the high field area of the 90,000 lb "phantom" coin would be expected in a struck coin, the high tensile residual stress is not. When the 90,000 lbs "phantom" coin was sectioned for metallographic studies it was observed that the coin had warped. The obverse design of the "phantom" coin was convex. This observation leads to two important inferences: a) the

tensile residual stress seen on the low field area of the coin may arise from the warping of the coin, and b) the warping indicates an unbalanced stress system within the coin which could have resulted from peculiarities in the striking of the coin or dimensional instability of the coin.

When a material warps, the convex surface is slightly elongated while the concave surface is compressed. Since the obverse face for the "phantom" coin was convex, the grains of the polycrystalline material were probably elongated resulting in the observed tensile stress. Since the 90,000 lb "phantom" coins were the last coins to be struck in the series of "phantom" coins, it is possible that the die system or dies were beginning to fail and led to unbalanced deformation in the coin.

Visual examination of the die system found that the lower die holder was hubbing or sinking into the base plate of the system. In addition, the face of the upper die was cracked. Both observations may be symptomatic of an unbalanced deformation system.

Low residual stresses were observed in the 40,000 lb "phantom" coin. The amount of plastic deformation was much less at this coining pressure than at the higher pressure, and would result in the lower residual stresses seen. The high field or raised area of the coin was not completely formed at this coining pressure. The tensile residual stress of 2774 ± 840 psi seen on the high field portion of this coin may have resulted from incomplete formation of the design and may have been remnant from the tensile residual stress seen in the "type two" coining blank.

In addition to the -2252 ± 1365 psi determined in the low field area of the coin, a second determination was performed using a 4 degree rocking angle. The latter experiment was performed to determine if large grain size contributed significantly to the slight oscillations seen in the "d" versus $\sin^2$ psi plot. The larger rocking angle samples more grains in a large grained polycrystalline material and leads less oscillation in "d" versus $\sin^2$ psi plots. A residual stress of -525 ± 1997 was determined on the

low field portion of the coin using the 4 degree rocking angle. The residual stress at this rocking angle is in agreement with the earlier measurement. The 4^{o} rocking angle did slightly effect the oscillations seen in the d vs. $\sin^2$ psi plots. This indicated that the grain size may be affecting the residual stress determination. It may be possible to more accurately determine the residual stress in coins which display severe oscillations in the d vs. $\sin^2$ psi plots by increasing the rocking angle.

IV. CONCLUSIONS

This final chapter deals with the significance of the results in light of the problems posed. In addition, alternate techniques for investigating these problems are suggested.

A. Significance of Results

The results in this study lead to conclusions about each of the problems set forth in the investigation. The results were evaluated with regard to the differentiation of struck and cast coins, the determination of an estimate of the force used to strike a coin, and the estimation of the age of a coin.

1. Residual Stresses in Struck Coins. The experiments performed show that accurate residual stresses can be measured in non-ideal samples such as struck coins. The residual stresses found in copper coins varied systematically with location on the struck coin, and resulted from the plastic flow taking place during the striking of the coin.

2. Effect of Coining Alloy. Few differences were seen in the residual stresses of struck and cast silver and gold coins. It may be possible that statistically significant differences would be seen upon measurement of more silver or gold coins. The results in this study indicated the significance of differences in the yield stress of various coining alloys. Coins made from alloys of lower yield stress can be more easily deformed and more severely affected by wear and abrasion. The lack of variation in residual stress with location on silver and gold coins is most likely due to the ease of deformation of these alloys. Since these coins are made of a more plastic material than copper coins, the variation in deformation from region to region within the coin may be more uniform and therefore result in less residual stress.

Also, if the material can be more easily deformed, it will be more severely affected by particle abrasion and handling associated with the circulation of a coin, or mechanical manipulation associated with the manufacture of a cast counterfeit. Strain hardening may even occur at the surface of coins made of a low yield stress material due to abrasion or surface manipulation and result in residual stresses which are higher than the yield stress of the material, as was seen with the cast gold doubloon.

3. Residual Stresses in Cast Coins. Low residual stresses were not found in the cast counterfeit coins studied, as originally expected. Some cast copper coins displayed oscillations in the d versus $\sin^2$ psi plots resulting from the large grains found in their microstructure. It is the presence of large grains which lead to a nonrandom sample within the X-ray beam and results in the appearance of texture or preferred orientation. The fact that cast coins display oscillations while struck coins did not is a possible means of distinguishing between struck and cast coins.

It is crucial to note, however , that not all cast coins exhibited these severe oscillations. Some of the cast copper coins displayed high residual stresses which were near to the yield stress of the material. The high stresses found in these cast coins may be attributed to manipulations of the surface of the coin after casting. Results in this investigation demonstrated that manual abrasion of the surface significantly altered the residual stress of the coin.

4. Differentiation of Struck and Cast Coins by Residual Stress Analysis. The results demonstrate that residual stress analysis by X-ray diffraction as a means of authenticating coins is severely limited by the depth which the X-ray beam can penetrate into the surface of the coin. While manipulations of cast coins, and wear and abrasion of struck or cast coins alter residual stresses near the surface of the coin, structural and mechanical differences between struck and cast coins should still be seen at depths farther into the coin. Thus far, this technique provides limited information in differentiating struck and cast coins. Coins which display d versus $\sin^2$ psi

oscillations are likely to be cast. A measurable residual stress in a coin can not provide conclusive evidence that it is struck.

5. Residual Stress in "Phantom" Coins. The purpose of striking a series of "phantom" coins at known pressures was to establish an empirical relationship between the coining pressure used to strike a coin and the residual stress induced in the coin. Once this empirical relationship was determined, it was to be used to estimate the coining pressure used to strike an actual coin. The "phantom" coins struck in this investigation were modeled after the U.S. one cent piece.

The residual stresses measured on the "phantom" coins were not the compressive residual stresses expected of a struck, compressed material, nor were they similar to the residual stresses found in U.S. one cent pieces. The use of a hydraulic press to "strike" the "phantom" coin may result in a different residual stress pattern than that found in the U.S. one cent piece struck by the knuckle-action press, due to differences in strain rates and deformation velocities which result in different flow stresses.[3]

Also, since the design of the "phantom" coin was not the actual design of the U.S. one cent piece, the "phantom" coin may have resulted in a unsuitable model. The topography of the portrait of the one cent piece was not represented in the "phantom" coin. Thus the plastic flow of the coining alloy during the striking process may have been significantly different than that of the one cent piece.

The "phantom" coins which were struck during this project did not provide information which could be used to correlate the residual stress in an authentic coin to the coining pressure used to strike that coin.

6. Residual Stress Analysis was a Technique for of Dating Coins. Experiments needed to determine the activation energy of stress relaxation in Silver coins were not performed. In light of the results found in this study, residual stress analysis using X-ray diffraction techniques may not be able to provide information on the age of the coin. Residual stresses vary with location and are altered by wear and abrasion.

While the differences due to location between coins can be minimized, changes in residual stress brought about by stress relaxation may not be distinguished from changes brought about by mechanical means.

This study has illuminated the following significant facts about residual stress analysis as a technique to investigate coins: a) X-ray techniques are limited by their depth of penetration for the differentiation of struck authentic and cast counterfeit coins; b) differences in residual stress between struck and cast coins is dependent on the yield stress of the coining alloy; c) in certain incidences, cast coins can be distinguished from struck coins by severe oscillation in the d versus $\sin^2$ psi plots; d) the residual stress in a struck coin is dependent of the location where it is measured; and e) the residual stresses located at the surface of a coin can be altered by wear and abrasion. In addition, the use of residual stress as a technique for investigating the force used to strike a coin is dependent on the accurate modeling of the system, from the design of the "phantom" coin to the actual deformation mechanism employed. While the possibility of using residual stresses to date coins was not investigated in this study, the feasibility of the technique is limited due to time independent changes, such as wear and abrasion, in residual stress which may occur during the lifetime of the coin.

B. Suggestions for Further Research.

Some alternative methods of studying coins may be suggested for future research. While the measurement of residual stresses near the surface of coins could not provide sufficient evidence to distinguish between cast and struck coins, it is still possible that the measurement of residual stresses at greater depths may show significant differences between cast and struck examples. It may be possible to distinguish struck and cast coins by residual stress analysis using neutron diffraction

experiments require exposure for approximately 10 hours, in thermal neutron fluxes of 10^{14}-10^{16} neutrons per cm^2 per sec.

The radioactivity of a typical coin after irradiation in a thermal neutron flux can be calculated. For example, the isotopic composition of a 2.5 gram sterling silver (92.5% Ag, 7.5% Cu) coin can be calculated, from natural abundances, to be: 1.19g of $^{107}_{47}Ag$, 1.1g of $^{109}_{47}Ag$, 0.14g of $^{63}_{29}Cu$, and 0.06g of $^{65}_{29}Cu$.[75] Upon irradiation in a thermal neutron flux, a some of the individual isotopes will capture neutrons and produce new radioactive isotopes of the same element in excited nuclear states. The excited species will emit gamma radiation to reach the ground state then decay via emission of beta particles or electron capture to stable isotopes of a different element. The radioactive processes for the coin are summarized in Table XV.

The decay rate of the radioactive species at the end of irradiation can be calculated from:

$$R = \frac{m}{M} N \phi \sigma \left(1 - e^{-\lambda t} \right)$$

where,

R = the decay rate, in Curies (1 Ci = 3.7×10^{10} disintegrations per sec)

m = grams of isotope

M = atomic weight of isotope

N = Avogadro's number, 6.022×10^{23}

ϕ = the neutron flux, 10^{12} $cm^{-2}s^{-1}$

σ = cross section, in cm^2 (the total probability of the neutron interacting with the nucleus of the isotope)

t = the duration of irradiation

λ = the decay constant of the radioactive species being formed.

Table XV. Radioactive Processes for, and Radioactivity of Isotopes found in a Sterling Silver Coin.[1]

neutron reaction	cross section, σ, barnes[2]	decay reactions	half life $t_{0.5}$
$^{107}_{47}Ag + n \rightarrow {}^{108}_{47}Ag + \gamma$	37	$^{108}_{47}Ag \rightarrow {}^{108}_{48}Cd + \beta^-$	2.4 m
$^{109}_{47}Ag + n \rightarrow {}^{110}_{47}Ag + \gamma$	88	$^{110}_{47}Ag \rightarrow {}^{110}_{48}Cd + \beta^-$	24.4 s
$^{65}_{29}Cu + n \rightarrow {}^{66}_{29}Cu. + \gamma$	2.17	$^{66}_{29}Cu \rightarrow {}^{66}_{30}Zn + \beta^-$	5.10 m
$^{63}_{29}Cu + n \rightarrow {}^{64}_{29}Cu + \gamma$	4.4	$^{64}_{29}Cu \rightarrow {}^{64}_{30}Zn + \beta^-$	
		$^{64}_{29}Cu \rightarrow {}^{64}_{28}Ni + \beta+$	12.7 h
		$^{64}_{29}Cu \rightarrow {}^{64}_{28}Ni$ (electron capture)	

Isotope	Amount of Radioactivity at time t after irradiation, in Ci[3]				
	t = 0	t = 1 m	t = 5 m	t = 24 h	t = 72 h
$^{108}_{47}Ag$	6.7	5.02	1.58	0	0
$^{110}_{47}Ag$	14.6	2.65	2.91×10^{-3}	0	0
$^{66}_{29}Cu$	1.21	1.06	0.62	0	0
$^{64}_{29}Cu$	6.71×10^{-2}	6.70×10^{-2}	6.29×10^{-2}	1.81×10^{-2}	3.56×10^{-4}

1. See Reference 75, pp 614, 622-623.
2. A barn is a unit used to express a geometrical cross-sectional area, $1\ b = 1 \times 10^{-24} cm^2$.
3. Curie is a unit of measurement for radioactivity, $1\ Ci = 3.7 \times 10^{10}$ disintegrations per second.

After irradiation the radioactive species will continue to decay with no further radioactive species being formed. The amount of radioactivity remaining can then be calculated from:

$$R = R_o e^{-\lambda t}$$

where:

R = the amount of radioactivity present at time t after irradiation, in Ci

R_o = the amount of radioactivity at end of irradiation

$\lambda = \ln \frac{1}{t_{0.5}}$, the decay constant

t = time elapsed after irradiation

$t_{0.5}$ = the characteristic half life of decay

Table XV lists the amount of radioactive species formed, in Curies, and the amount radioactivity remaining at different time intervals after irradiation. After 96 hours the coin is no longer radioactive.

Finally, the limited access of reactors and the cost of neutron beam time may make this technique prohibitive.

2. Acoustic Techniques for the Study of Coins. It is possible that valuable information on the microstructure and porosity of coins may be obtained using acoustic methods of investigation. Techniques such as scanning acoustic microscopy and acoustic holography are non-destructive methods of analysis based on the propagation of sound through a medium. Sound waves are mechanical disturbances which propagate through a material, such as a solid, and therefore interact with properties of the material, such as changes in density, viscosity, elasticity, and other physical properties.[76,77,78] Acoustic techniques are based on the changes in phase and/or amplitude of the sound wave as it is transmitted through or diffracted from a material.

a. Basic Definitions in Physical Acoustics. A review of some fundamental principles of sound is presented here to provide a background for the acoustic

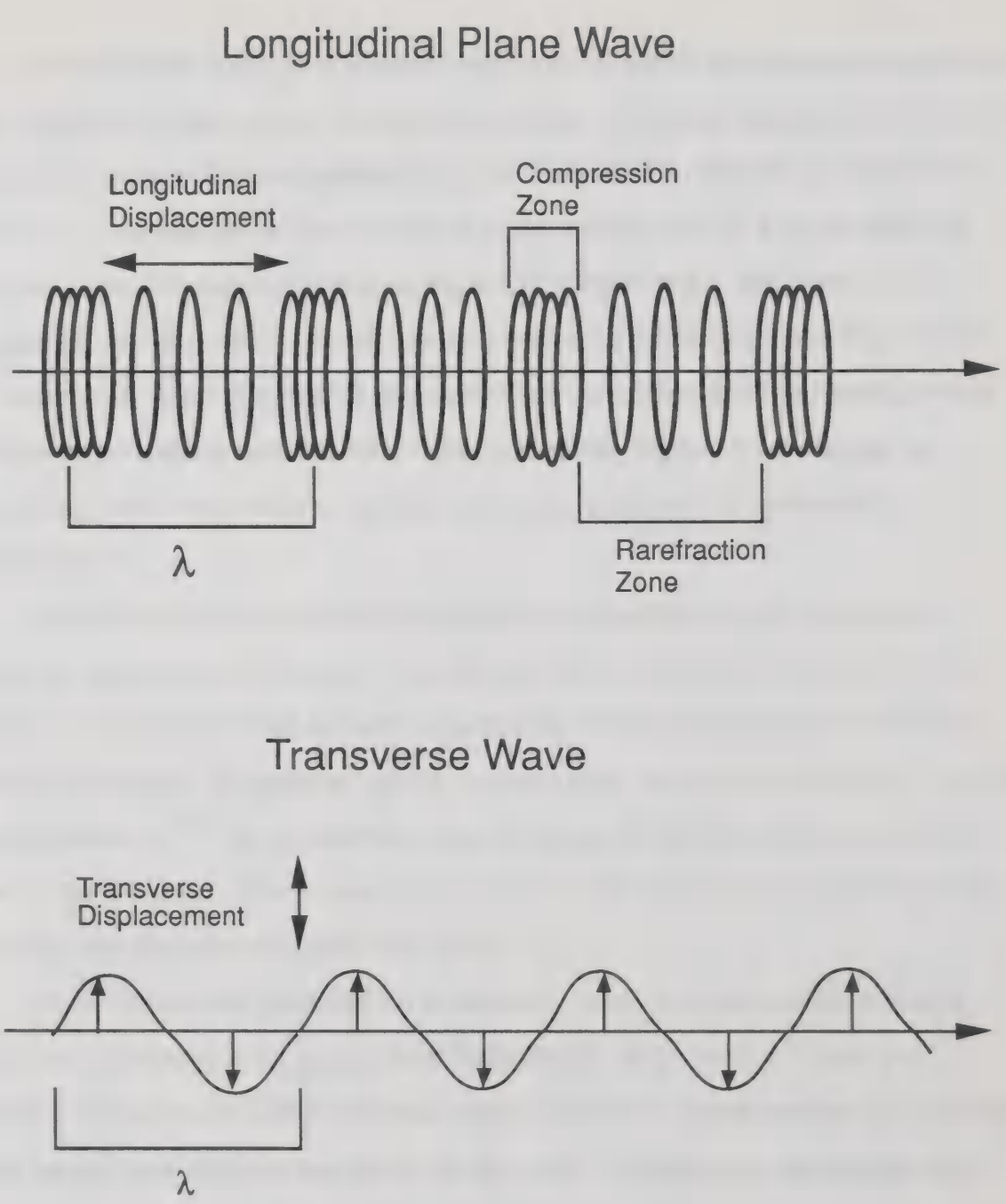

Figure 22. Longitudinal and transverse waves. In longitudinal waves the particle displacement is in the same direction as the propagation of the wave. In transverse waves, the particle motion is perpendicular to the propagation of the wave.

It is the ability of solids to support two modes of sound propagation which gives rise to Rayleigh surface waves in a bounded media. A Rayleigh surface wave is a two dimensional wave which propagates along the surface of a material at a boundary interface.[83] The particle motion is elliptical at the surface, due to a combination of longitudinal waves traveling parallel to the to the surface and in the direction of propagation, and transverse waves traveling normal to the surface, see Figure 23.[84] The amplitudes of the longitudinal and transverse components of the Rayleigh wave decrease exponentially with distance from the surface. Rayleigh waves play a fundamental role in the mode of contrast of images produced by an acoustic microscope.[85]

Sound waves can be refracted, reflected, and scattered from, transmitted through, or absorbed in a material. The behavior of an acoustic wave when it hits a boundary is a function of the acoustic impedances of the materials at the boundary. Acoustic impedance, Z, is defined as the product of the propagation velocity, v, and the material density, ρ.[86] At the boundary, part of the wave will be transmitted and the other will be reflected. The amount of transmission and reflection are determined by the ratio of the impedances of the two media.

Sound waves are classified on a frequency scale relative to audible sound. Audible sound ranges in frequency from 20 to 20,000 Hz (1 hertz = 1 cycle per second). Sound waves with frequencies below 20 Hz are called infrasonic. Ultrasonic sound waves have frequencies above 20,000 Hz.[87] The acoustic techniques to be discussed in this paper utilize high frequency ultrasonic waves.

High frequency ultrasonic waves, above 100 MHz, are generated using piezoelectric transducers, which are based on the fact that certain materials undergo dimensional changes when placed in an electrically charged field. Conversely, if this material is deformed by an external force, an electrical charge is formed on its surface.

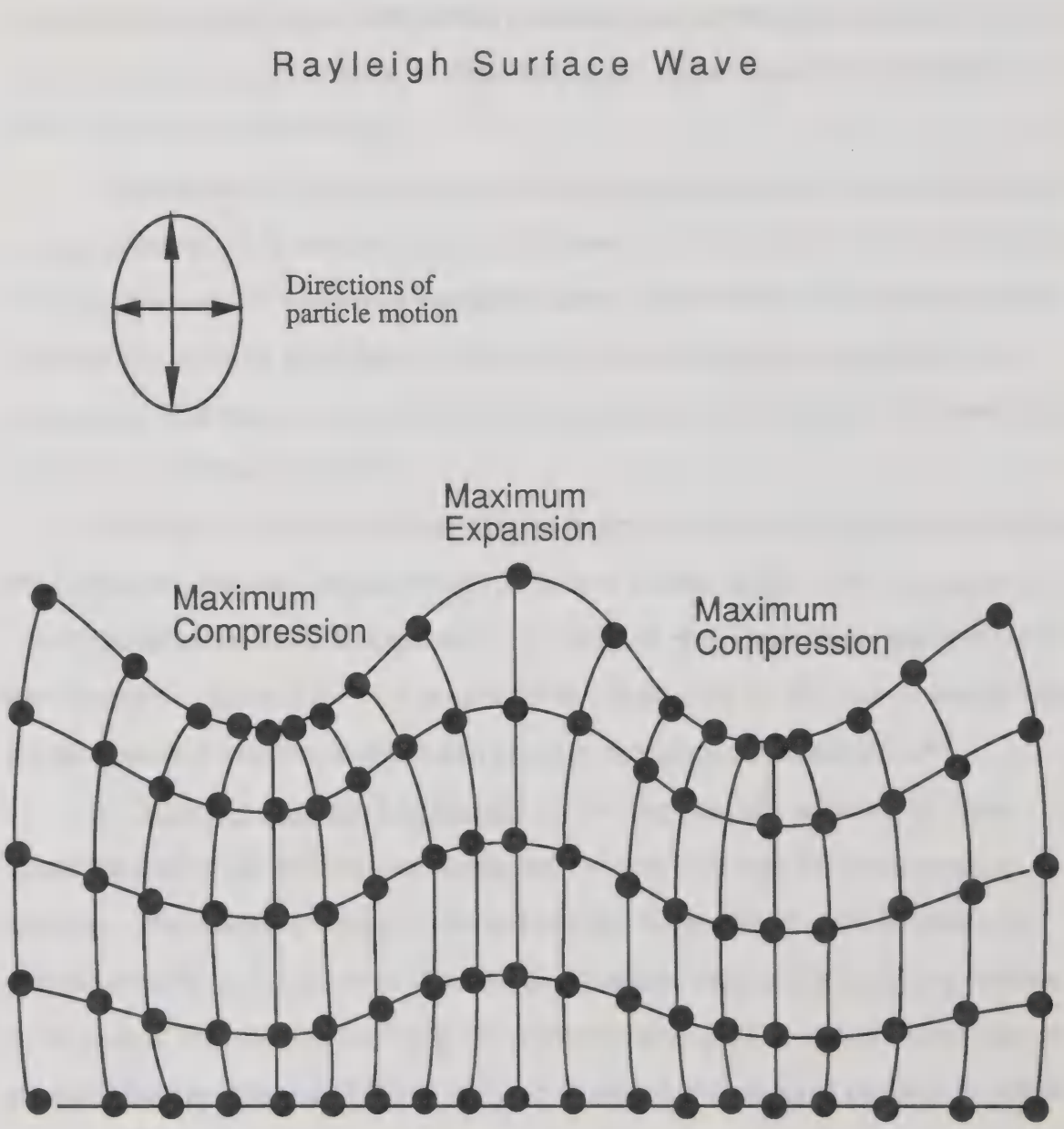

Figure 23. Rayleigh waves. The Rayleigh wave is a two dimensional wave composed of longitudinal and transverse waves. The particle motion is elliptical in nature, and decreases exponentially with depth from the surface.

This phenomenon is known as the piezoelectric effect. The electrical charge arises from the polarization of the material's crystal axes due to the displacement of atoms or molecules by the external force.[88] Materials which show these characteristics are called piezoelectric materials.

A Piezoelectric transducer is an electro-mechanical device used to generate ultrasonic waves. It is constructed of a thin layer of a piezoelectric material placed between two vacuum deposited electrode layers. Oscillations in the dimensions of the piezoelectric material result when a current is switched on and off between the electrodes. The frequency produced by the piezoelectric transducer is dependent on the thickness of the material.[89]

Piezoelectric transducers are utilized in scanning acoustic microscopy for the generation of ultrasonic waves in the 100 Mhz to 3 GHz range. The transducer is usually constructed of PZT (a ceramic consisting of ~55% lead zirconate and ~45% lead titanate) or $LiNbO_3$ for frequencies up to 150 MHz.[90,91] For higher frequencies, the piezoelectric material is a thin film of radio frequency sputtered ZnO.[92]

b. Scanning Acoustic Microscopy. Scanning acoustic microscopy uses ultrasonic waves rather than electromagnetic waves to image the features of a material. The scanning acoustic microscope can be operated in transmission or reflection mode and measures the intensity of sound waves in a scanning manner analogous to that used in scanning electron microscopy. The use of sound waves as a probe provides the possibility of imaging based on the physical properties of the material.

A variety of instrumental designs and methods exists for acoustic microscopy.[93,94] The methods generally differ in the mode of visualization of the sound wave.

The most commonly used acoustic microscope is based on a scanning design by Ross Lemmons and Calvin Quate.[95] The basic elements of this type of reflection acoustic microscope are shown in Figure 24.

An ultrasonic beam is generated by a transducer and focused by a spherical sapphire lens on to the sample. A coupling medium, usually, water, is used between the sample and the lens. The change in impedance from the sapphire lens to the coupling medium provides a high refractive index, and eliminates problems of spherical aberration. But high acoustic impedance in the coupling medium creates a problem by attenuating the sound wave and causes a reflected pulse off the surface of the lens. A coating, commonly referred to as a quarter wave layer, made of a lower acoustic impedance than the coupling medium, is applied to the surface of the lens to the lessen the effects of the acoustic impedance mismatch.

The system is operated in a pulse-echo mode.[96] Since piezoelectric material is sensitive to pressure changes which cause an electrical charge on the surface of the material, the transducer can function both as a transmitter and a receiver. In order to perform both functions, the transducer is rapidly switched between transmitting and receiving mode by a complicated electronic system. The pulsed sound wave is transmitted in 20 ns intervals.[97] The received pulses consist of the reflected pulse produced by the surface of the lens, and the reflected pulse from the sample. The pulses are then separated electronically by time of flight. The highly focused sound source is scanned in a raster fashion over the area to be imaged, and the received intensities are viewed on a video monitor.

When the acoustic microscope is operated in focus, all sound waves impinge at a single spot on the sample, and are diffracted. This mode of operation only provides information from the surface of the sample. If, however, the instrument is operated with the focus not on the surface but beneath the surface of the material, several events occur as can be seen in Figure 25. The acoustic rays which are normal, A, or near

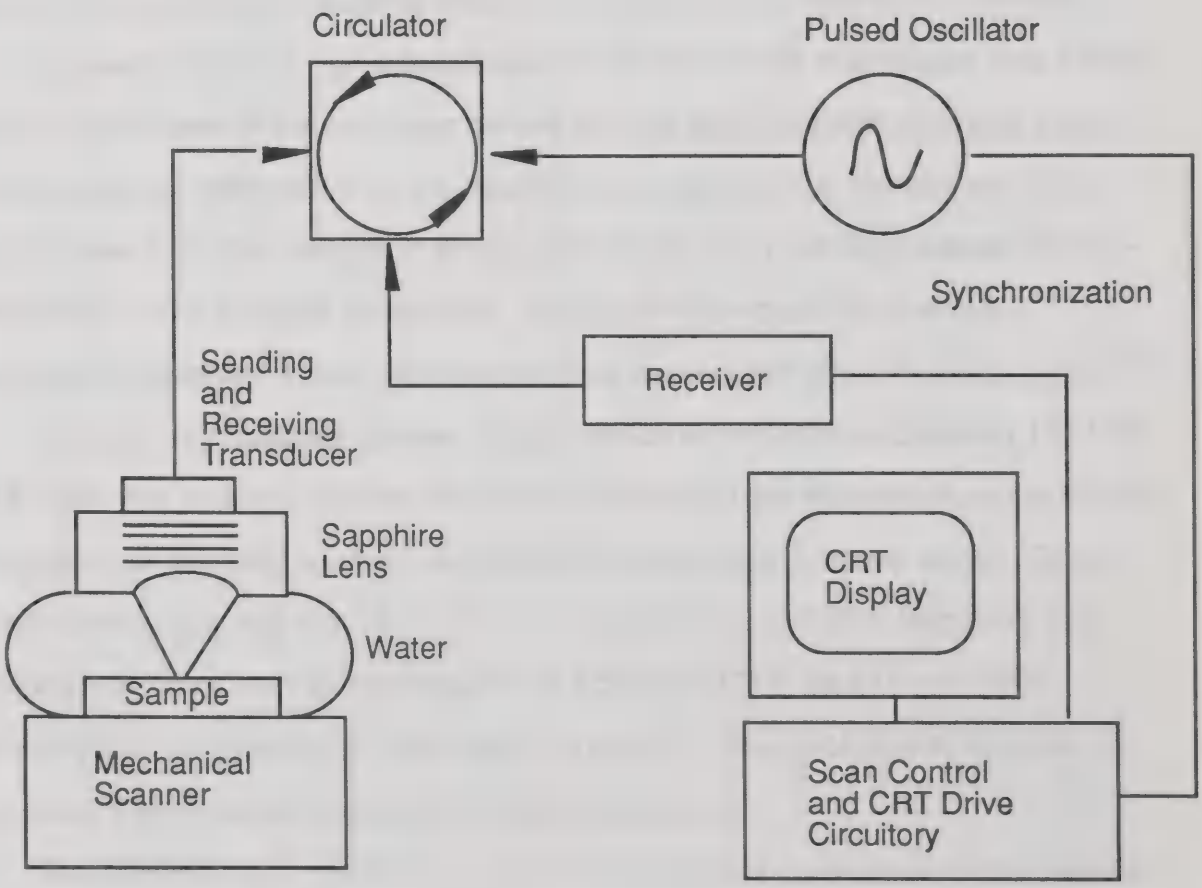

Figure 24. A schematic diagram of a scanning acoustic microscope, showing the components of a reflection mode.

normal, C, to the sample surface will be diffracted into the lens and received at the transducer to produce and output voltage. Acoustic rays which impinge on the sample at the Rayleigh angle, θ_R, will excite a Rayleigh surface wave, B.[98]

The leaky Rayleigh wave is one of the most important phenomena in acoustic microscopy. The leaky Rayleigh wave propagates along the surface of the material and leaks energy into the coupling medium at the solid-liquid interface. This wave travels a specific distance then diffracts back to the lens of the microscope (see Figure 25). The vector sum of the rays near normal and the leaky Rayleigh rays give rise to the output signal. Information on the mechanical properties near the surface of the material come from the changes in propagation of the leaky Rayleigh waves and provide contrast in the acoustic micrograph. The penetration depth from which information is obtained is also dependent on the wavelength of the Rayleigh wave.[99]

Acoustic microscopes operate at high ultrasonic frequencies between 100 MHz and 3 GHz. The resolution of the instrument is limited by the wavelength of the sound produced in the coupling medium surrounding the specimen, usually water. Since sound travels at a speed of 1.55×10^3 m/s in water (60°C), at 3 GHz frequency the wavelength of sound can be calculated from equation (10) to be 516 nm which approaches the wavelength of green light, 550 nm.[100] The resolution of acoustic microscopy therefore approaches that of light microscopy.

The resolution of a scanning acoustic microscope at the surface of the material is given by,

$$d_{min} = \left[\frac{D}{F}\right] \lambda$$

where:

d_{min} = the resolution of the system,

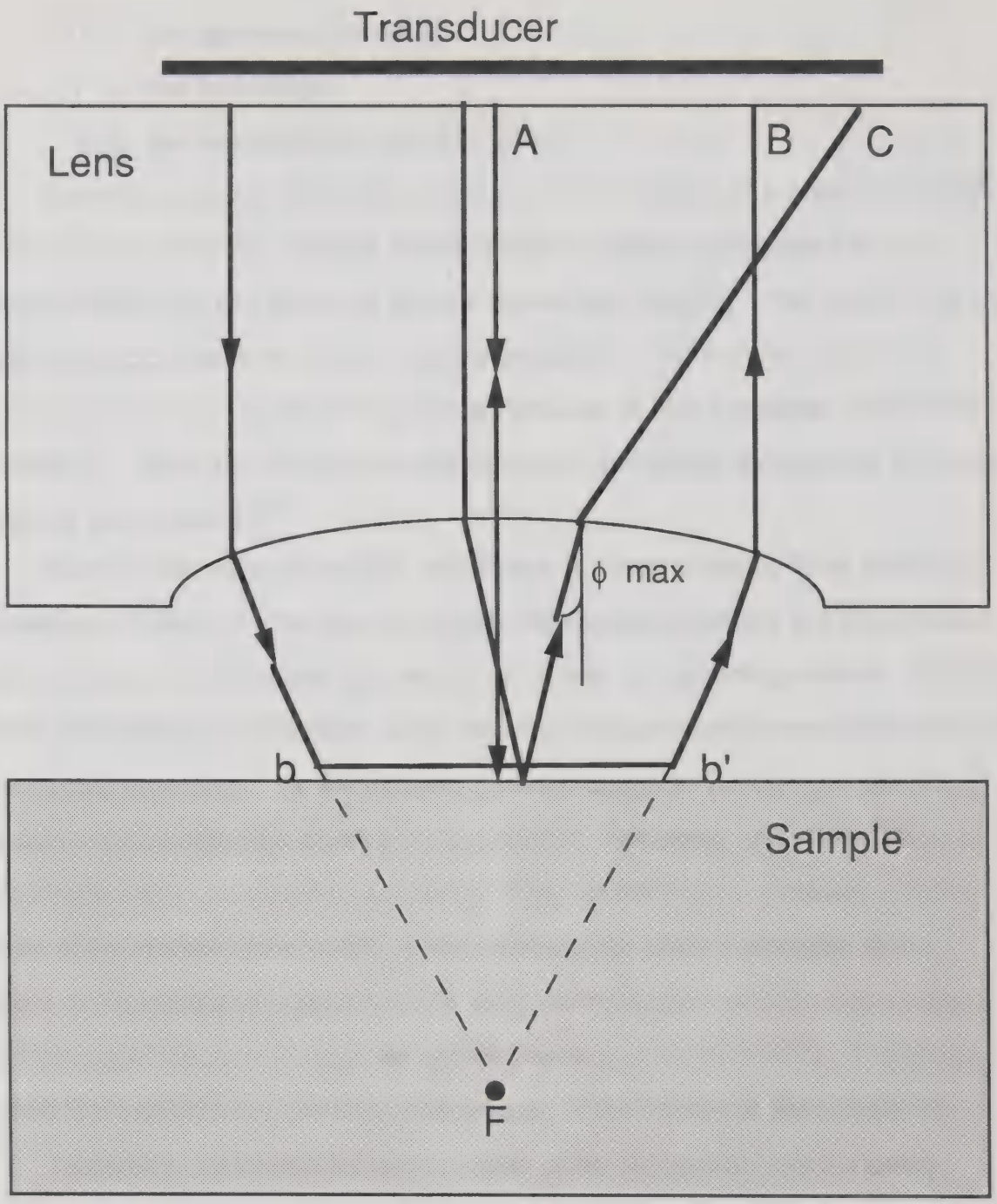

Figure 25. A schematic diagram indicating the principal acoustic rays which contribute to the output of the acoustic lens. Path A is the ray normal to the surface. Path B is the path of the leaky Rayleigh ray. Path C is the limiting ray - any ray with incident grater than ϕ will miss the transducer.

Table XVI. Acoustic Microscopy: Resolution and Penetration at Typical Operating Frequencies.

Frequency MHz	Wavelength in water µm	Resolution, µm surface	interior	depth penetration µm (typical figures)
30	50	35	70 - 175	0 to 7000
50	30	20	40 - 100	0 to 5000
100	15	10	20 - 50	0 to 2000
500	3	2	4 - 10	0 to 20
1000	1.5	1	2 - 5	0 to 10
2000	0.75	0.5	1 - 3	0 to 5

image may consist of flaws, grains, and surface topography,and may be difficult to interpret.[105]

Scanning acoustic microscopes, operating in the reflection mode, have been used to produced images of the microstructure of various alloys including among others steels, titanium, nickel, and gold. Therefore, it may be possible to non-destructively image the metallic grain structure of coins using acoustic microscopy. A high quality acoustic micrograph of Inconel steel having grain size of approximately 10 μm has been imaged using 2.7 GHz frequency at Standford University by L. Lam.[106] This is approximately the same size grains found in the U.S. one cent, Figure 29. However, it should be noted that the technique is sensitive to changes in surface topography, because the main mode of contrast results from the propagation of Rayleigh waves along the surface of the material. The imaging of a coin may only be possible on a smoothly finished surface of a coin.

Alternately, while imaging the microstructure of the coin may or may not be possible, qualitative interpretation of the acoustic image may still provide a means to distinguish struck from cast coins. Most metals show a particularly pronounced attenuation of sound if their cast structure is destroyed by either hot or cold working.[107] The image produced by the struck coin may lack intensity when compared under similar conditions to a cast coin of similar shape and alloy.

Scanning laser acoustic microscopy may offer the advantage that it interacts with the bulk of the coin. While abrasion and wear of the surface of cast coins may result in a "deformation skin", the interior of the coin should still be significantly different from that of a struck coin. Since scanning laser acoustic microscopy derives its information from the bulk of the coin, these differences should be seen.

Evaluation of scanning acoustic microscopic techniques for investigating the microstructure of coins requires the optimization of instrumental parameters to provide sufficient resolution with maximum penetration depth. The interpretation of the

acoustic image of a coin requires the differentiation of the effects of surface topography and microstructure on the contrast of the image. The analysis of an authentic struck coin and an exact replica cast from a high quality mold of the original may provide information which would allow this differentiation. Studies on coins of varying condition and alloy composition are necessary to evaluate the possibilities of the analytical technique.

c. Acoustic Holography. Acoustic holography is an imaging technique using sound waves and is based on recording, then reconstructing the phase and amplitude information of an object wavefront . (An object may be considered to consist of a multiplicity of point scatterers, capable of reflecting waves in all directions.The sum of these reflected waves is considered the object wavefront.)[108] Principles of acoustic holography derive from techniques of optical holography. A hologram is a record of the interference pattern created between a reference wave and an object wavefront, usually recorded on photographic film and using light as the wave source. A three dimensional image of the object is then produced upon reconstruction of the wavefront by shining a reference light source through the photographic record of the hologram.[109] Acoustic holography uses sound as the wave source instead of light. Optical procedures are presented to clarify the holographic technique before describing acoustic methods.

The conventional technique used to produce an optical holograph requires the use of a monochromatic, coherent light source, such as a laser.[110] A coherent light source produces waves which travel in time with a constant phase difference, ϕ.[111] The light wave is then split into two portions, one which illuminates the object and is reflected onto a photographic film, and the second, a reference wave, which directly illuminates the film. See Figure 26. The interference pattern of the two wavefronts is recorded on the film as a function of the light intensity. Upon development of the film the image seems to be an unrecognizable jumble of light and dark areas. However,

any portion of the hologram, as recorded on film, contains complete information pertaining to the entire irradiated object, including its three dimensionality.[112]

The visual image of the object is formed by illuminating the photographic film containing the hologram with the same coherent light source. The light source is diffracted by the dark areas and transmitted through the light areas of the hologram. The hologram acts like a simple lens, focusing the light source to recreate a real and a virtual image of the object.[113] When the light source is skewed with respect to the hologram, the virtual image is viewed without interference from the real image.[114]

The focus of acoustic holography is to produce a hologram by means of sound waves and to image the interior of an object which is opaque to light.[115] Acoustic waves which serve as both reference and irradiation sources can be made coherent by using the same generator to continuously energize two transducers of the same material. Figure 27 shows a schematic diagram of the acoustic holography process. An object is placed in a water bath containing the transducers fixed at angles which provide the intersection of the sound waves. The object is then placed in the direct path of one sound wave. The sound wave interacts with defects, such as voids, interfaces, etc. as it propagates through the object. When the reference wave and the object wave intersect at the surface of the water, a interference pattern is created in the form of ripples in the water. A laser is then scanned along the surface and is diffracted by the ripples. The intensity of the laser source is monitored, displayed on a video screen,or photographed to record the holographic image.[116] It should be noted that the acoustic image produced in this manner suffers distortion of the scale of depth because the wavelength of the light used to record the image is different from the wavelength of sound used to produce the hologram. As a result, the idea of obtaining a three dimensional image is abandoned, and two dimensional images at a specific zone in depth are produced by limiting the depth of focus of the optical recording system.[117] The dimension in depth is dependent of the ratio of the acoustic

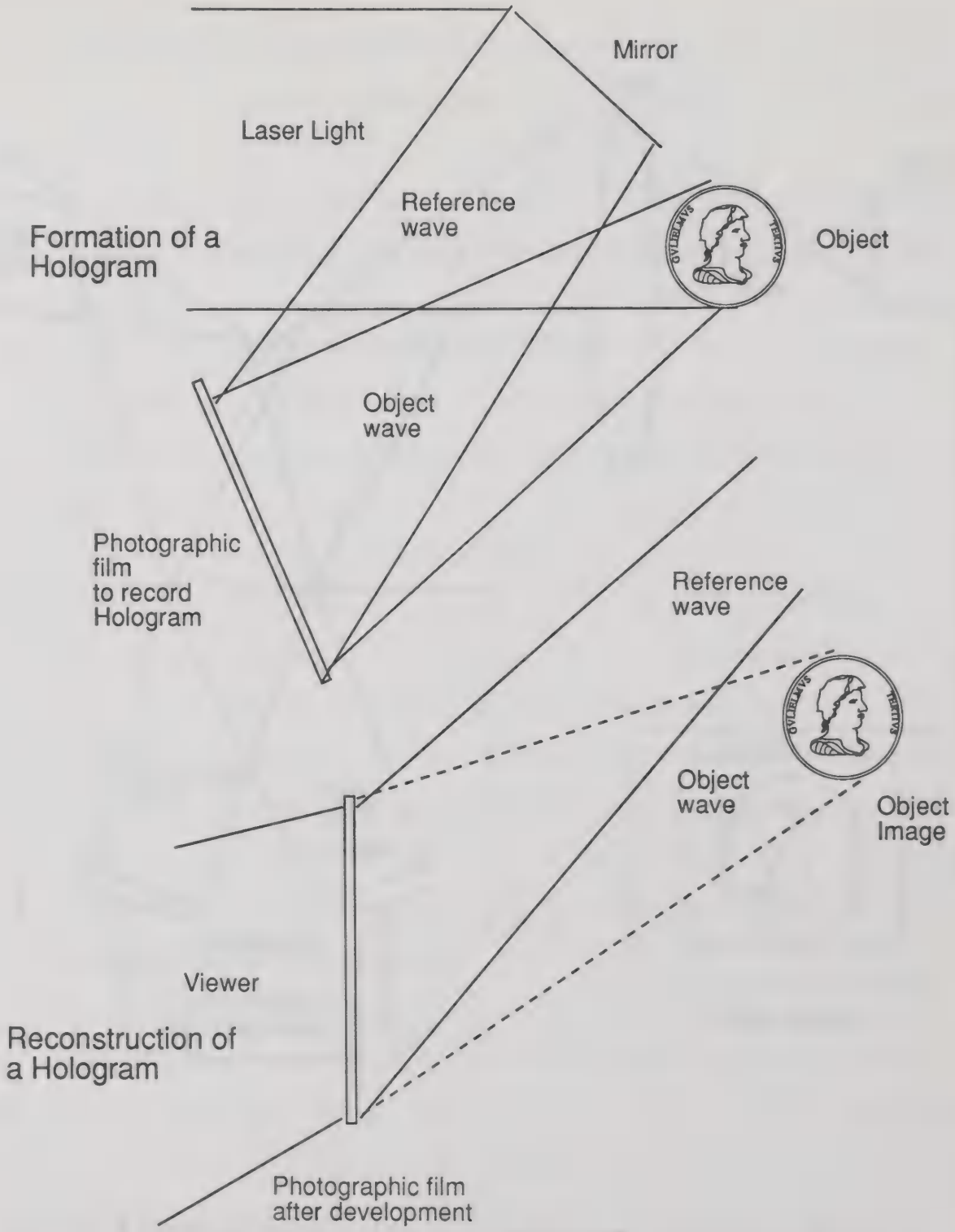

Figure 26. The optical hologram is constructed by splitting a laser light source into a reference and an object wavefront. The reference beam is reflected directly onto a photographic film. The object wavefront is formed from reflection off the object. The interference ppattern of the two waves is recorded on film. The holographic image is reconstructed by shining the reference laser light source through the developed photographic film.

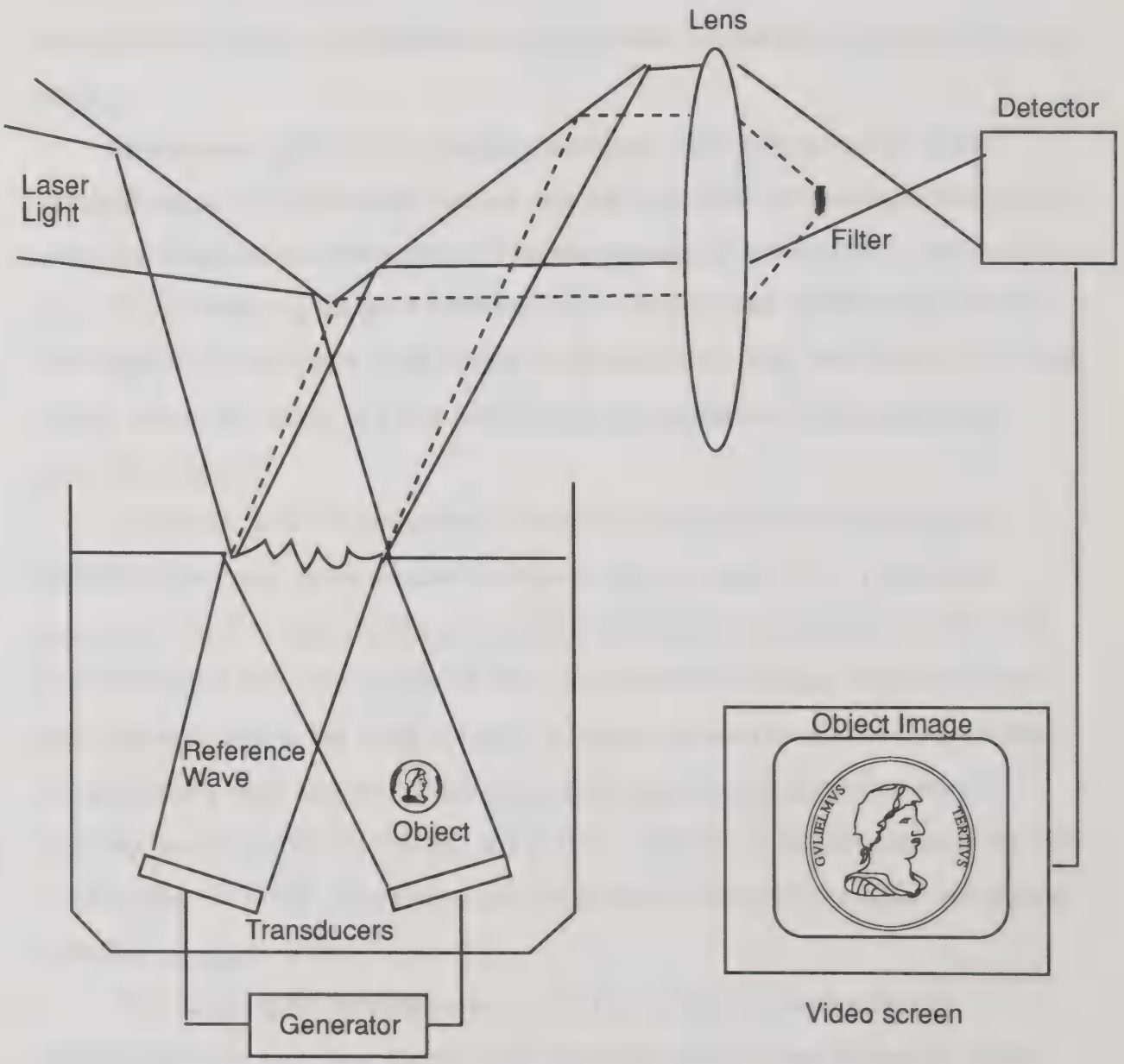

Figure 27. A schematic diagram of the components used in acoustic holography. A reference and a object wavefront are generated wusing two ultrasonic transducers which are oriented to overlap at the surface of the water bath. A ripple pattern representing the interference pattern of the two waves is formed on the water surface and scanned using a laser source. the real image is filtered from the virtual image and displayed on a video screen.

wavelength used to produce and the optical wavelength used to record the hologram, thus the zone of depth to be perceived can be altered to view different areas within the object.

An alternate system uses a single transducer to irradiate the object in the reflection mode. The transducer acts as both the transmitter and receiver, analogous to the scanning acoustic microscope. The received signal is mixed with a reference wave signal, which is generated electronically, to produce the interference pattern. The image is reconstructed using optical computing of the data, and viewed on a video screen. Again, the image is a two dimensional reconstruction at a focused depth within the object.[118]

In general, acoustic holography operated at much lower frequencies than acoustic microscopy, in the frequency range of 3 to 10 MHz.[119,120] The lateral resolution is approximately 0.33 mm in a steel sample at a frequency of 10 MHz.[121] The technique is used to find defects which are millimeters in size. This resolution would not lend itself to the study of coins. However, recent developments by Kessler and co-workers have shown that principles of holography can be combined with scanning laser acoustic microscopy, (c.f. p 101), operating at frequencies ranging from 10 -200 MHz.[122,123,124] This technique can provide holographic images with lateral resolution of approximately 10 μm.[125]

This holographic technique uses a standard scanning laser acoustic microscope which has been electronically modified using inverse filtering to record both complex amplitude and phase information from the object wavefront. Digitalized data from the microscope is then recorded using a microcomputer and manipulated to reconstruct the object wave front. This reconstruction requires consideration of the diffraction of the object wavefront by propagation through the object and is computed by back propagation calculations.[126] The resulting holographic image can accurately reproduce the actual size, shape, and depth of subsurface defects in an optically

opaque material. The holographic scanning acoustic microscopic technique provides advantages over the standard scanning acoustic microscopic technique in that overlapping defects within the material can be resolved.

Holographic scanning acoustic microscopy is this in developmental stages, but the technique may be able to provide information about the defects ,voids, and possibly grains within a coin. The potential to image at different depths within the coin may overcome the problem of effects of wear and abrasion on the surface of the coin masking the "characteristic" microstructure of a cast coin.

APPENDIX A. DETERMINATION OF COIN COMPOSITION USING X-RAY FLUORESCENCE ANALYSIS.

The composition of each coin was analyzed using X-Ray Fluorescence Spectrometry. The compositional analyses were required for two reasons: 1) to insure that the coins being compared were relatively similar in composition and 2) to determine the appropriate elastic constants to be used in calculating the residual stress in each coin.

The experiments were performed at Olin Brass Corporation, located in East Alton, Illinois. The instrument used in the analyses was a Siemens model 200 wavelength dispersive X-Ray Fluorescence Spectrometer. A 23 mm gold mask was used to hold each coin in place.

A scan of wavelengths was performed on each coin and used to qualitatively identify the major and minor elements in each coin. Quantitative estimates of each coin's composition were then made by comparing the intensities of characteristic peaks to acalibration curve derived from standards or coins of known composition. Table XVII lists the instrumental conditions used in the quantitative analyses for each element within a coin. Table XVIII displays the intensities and concentrations of the element found in each coin and standard. The intensities and elemental concentrations of the standards use for quantitative analysis are give in Table XIX.

X-ray fluorescence anaylsis is a surface analysis technique. Therefore, any process which results in surface alteration, such as corrosion, may result in the selective change of the elemental composition of the coin as determined by XRF.[127,128] In order to maintain the non-destructive nature of the testing, the surface of the coins were not prepared or cleaned prior to XRF analysis. The results of these analyses may be as less reiable than those taken on a freshly cleaned surface a coin.[129] Therefore, the elemental composition of the coins stated in Table XVII

represent only an estimate of the actual value. The error reported with each value is one standard error of the individual measurement. The standard error of each value was determined from the standard error of the linear correlation coefficients for each calibration curve as determined by linear regression analysis using Microsoft ® Chart software on a IBM ® personal computer. The actual composition of the gold coins could not be investigated using the instrument available at Olin Corporation, due to the fact that a gold mask was used throughout the XRF experiments.

In all residual stress analyses, single crystal values of the elastic modulus and poissons ratio for copper, silver, and gold, were used to calculate the elastic constant used in the residual stress analysis.

Table.XVII. Instrumental Conditions for X-ray Fluorescence Analysis of Coins.[1]

El.	Crystal (hkl)[2],	2θ Bragg Angle	Detector	Collimator (degree)	Count (sec)
Ag	LiF (200)	16.09	Scintillation Counter	0.40	20
Cu	LiF (110)	58.55	"	0.40	20
Pb	LiF (200)	33.93	"	0.40	40
Ni	LiF (200)	48.66	"	0.15	40
Sn	LiF (110)	19.80	"	0.40	40
Fe	LiF (200)	57.46	"	0.40	40
Zn	LiF (200)	41.79	"	0.15	40

1. Chromium radiation was used in all experiments. The X-ray tube was operated at 45 Kv and 40 mA. A gold mask was used to hold the sample coin in place. The sample was placed under vacuum and rotated throughout the measurement. Average intensities from tripicate measurements were used for the analysis of each coin.
2. (hkl) indicates the crystallographic plane of the crystal used.

Table XVIII. Peak Intensity and Composition (%) of Coins from X-ray Fluorescence Analysis.

Coin	Ag		Cu		Pb		Sn		Zn		Ni		Fe	
	Int.	Comp.	Int.	Comp.	Int.	Comp.	Int.	Comp.	Int.	Comp.	Int.	Comp.	Int.	Comp.
1699 Wm III A Struck	29650	0.15 ± 0.001	678992	96.9 ± 4.5	60102	2.7 ± 0.11	44272	0.4 ± 0.06			37315	0.16 ± 0.01		
1699 Wm III B Cast	21496	0.09 ± 0.002	555907	78.0 ± 4.6	206309	5.8 ± 0.19	106742	2.6 ± 0.07	28361	0.43 ± 0.02	41746	0.32 ± 0.01	52937	0.25 ± 0.03
1699 Wm III D Cast	20229	0.09 ± 0.002	589208	83.1 ± 4.6	99980	2.7 ± 0.11	104556	2.5 ± 0.07	28811	0.44 ± 0.02	39953	0.25 ± 0.01	49408	0.23 ± 0.03
1719 Geo I A Struck	24229	0.11 ± 0.001	678378	96.8 ± 4.5	73173	1.9 ± 0.12					34699	0.06 ± 0.01		
1719 Geo I B Cast	23476	0.11 ± 0.001	534022	74.5 ± 4.7	408254	11.8 ± 0.36	85060	1.8 ± 0.06	10832	0.07 ±0.02	49589	0.59 ± 0.01	27231	0.12 ± 0.03
1775 Geo III Cast	18208	0.07 ± 0.002	681992	97.4 ±4.5	60102	1.5 ± 0.11					32829	0.01 ±0.01	11914	0.04 ±0.03
1856 Vic. Shilling Cast	4661959	91.6 ± 5.34					55715	0.8 ± 0.06						

Table XIX. Peak Intensity and Composition (%) of Calibrations Standards use in X-ray Fluorescence Analysis of Coins.

Standard	Ag		Cu		Pb		Sn		Zn		Ni		Fe	
	Int.	Comp.	Int.	Comp.	Int.	Comp.	Int.	Comp.	Int.	Comp.	Int.	Comp.	Int.	Comp.
Olin Std.	4888386	99.999												
U.S. Quarter	4442837	90.0												
Olin Std.	4281409	79.85												
	3739991	64.0												
British 6p	2805233	50.0												
Mex. Peso	2196158	30.0												
Olin Std.	1531445	21.3												
	1434553	10.0												
Olin Std.	21775	0.098												
Olin Std.	20813	0.094												
Olin Std			707634	99.9										
Olin Std. C1113			659246	95.03										
Olin Std. C1116			632107	90.37										

Table XIXContinued.

Standard	Ag		Cu		Pb		Sn		Zn		Ni		Fe	
	Int.	Comp.	Int.	Comp.	Int.	Comp.	Int.	Comp.	Int.	Comp.	Int.	Comp.	Int.	Comp.
Olin Std. C1110			596197	84.5										
Olin Std. C1101			506235	69.5										
Olin Std.					180866	5.2								
Olin Std.					141627	3.75								
Olin Std.					18068	0.31								
Olin Std.					7874	0.01								
Olin Std.							315022	9.95						
Olin Std.							179277	5.08						
Olin Std.							74259	1.52						
Olin Std.							55512	0.78						
Olin Std.									465960	9.44				
Olin Std.									240981	4.80				
Olin Std.									153730	3.02				
Olin Std.									45322	0.76				
Olin Std.									21998	0.31				

Table XIX. Continued.

Standard	Ag		Cu		Pb		Sn		Zn		Ni		Fe	
	Int.	Comp.	Int.	Comp.	Int.	Comp.	Int.	Comp.	Int.	Comp.	Int.	Comp.	Int.	Comp.
Olin Std.									7393	0.01				
Olin Std.											242638	6.18		
Olin Std.											124931	3.19		
Olin Std.											68608	1.5		
Olin Std.											32517	0.48		
Olin Std.											15540	0.01		
Olin Std.													167225	0.82
Olin Std.													64045	0.32
Olin Std.													38286	0.20
Olin Std.													11347	0.01

APPENDIX B. STATISTICAL ANALYSIS OF DATA.

This appendix contains the statistical techniques used in the evaluation of the data generated in this research. The statistical error for a residual stress measurement by the $\sin^2$ psi method is defined. The error reported with each residual stress measurement represents one standard deviation as calculated from the error associated with the X-ray counting statistics. Statistical methods of weighted averages and the Students t-test for comparison of data were used throughout the evaluation of the residual stress results reported in Chapter 3, Results and Discussion, and are presented here.

A. Standard Deviation of Residual Stresses from $\sin^2$ Psi Techniques.

The residual stress of a coin was determined form the slope of the interplanar spacing, d_ψ versus the $\sin^2\psi$. The slope of the plotted data is determined by linear regression analysis. The regression coefficient is of a least squares fit to a line is given by:[130]

$$m' = \frac{\sum_i (x_i - x)(y_i - y)}{\sum_i (x_i - x)^2} \qquad \text{eq. (10),}$$

where x_i is the independent variable and y_i is the dependent variable. The regression coefficient can be expressed in terms of the variables used in the $\sin^2\psi$ method in the following equation:[131]

$$m' = \frac{\sum (\sin^2\psi - \sin^2\psi)(d_\psi - d_\psi)}{\sum (\sin^2\psi - \sin^2\psi)^2} \qquad \text{eq. (11),}$$

where:

$$\sin^2\psi = \frac{\sum \sin^2\psi}{N}$$

$$d_\psi = \frac{\sum d_\psi}{N}$$

and N is the total number of observations.

The variance of the slope in the $\sin^2$ psi technique can then be written as:

$$\sigma^2 m' = \frac{\sum (\sin^2\psi - \sin^2\psi)^2 \cdot \sigma^2(d_\psi)}{[\sum (\sin^2\psi - \sin^2\psi)^2]^2} \qquad \text{eq. (12)}$$

where the variance of the interplanar spacing,$\sigma^2(d_\psi)$, arises from the variance in the Bragg angle due to fluctuation on the intensity of the X-ray beam.

The variance in the interplanar spacing, $\sigma^2(d_\psi)$, with respect the the variance in the Bragg angle can be determined through Bragg's law:

$$n\lambda = 2d_\psi \sin\theta.$$

The variance in the interplanar spacing, $\sigma^2(d_\psi)$, is given by:[132]

$$\sigma^2(d_\psi) = \left[\frac{d\,(\,\lambda/2 \sin\theta_p\,)}{d\theta}\right]^2 \cdot \sigma^2(\theta_p) = \left[\frac{\lambda \cos\theta_p}{2\sin^2\theta_p}\right]^2 \cdot \frac{\sigma^2(2\theta_p)}{2} \cdot \left[\frac{\pi}{180}\right]$$

eq.(13) .

The residual stress is determined from the slope of the plot using the following relationship:

$$\sigma_\phi = \frac{1}{\left(d_o \cdot \frac{1+\nu}{E}\right)} \cdot m'$$

The variance in the surface stress,$\sigma^2(\sigma_\phi)$ is given by:

$$\sigma^2(\sigma_\phi) = \sigma^2(m') \cdot \frac{1}{\left(d_o \cdot \frac{1+\nu}{E}\right)^2} \qquad \text{eq. (14).}$$

B. Weighted Average of Residual Stress Data.

A weighted average method was use to calculate the average of multiple residual stress measurements on one location on a coin. The purpose for using the

weighted average was to take into consideration the error associated with each individual measurement. The weighted average is given by:[133]

$$X_w = \frac{\left(\frac{\Sigma x_i}{\sigma_{xi}^2}\right)}{\left(\frac{1}{\Sigma\sigma_{xi}^2}\right)} \qquad \text{eq. (17)},$$

where x_i is the measured quantity and σ_{xi} is the variance associated with the individual measurement.

The weighted variance for this average is the calculated from:

$$\frac{1}{\sigma_w^2} = \frac{1}{\Sigma\sigma_{xi}^2} \qquad \text{eq. (18)}.$$

C. Comparison of Data using the Student's t-test.

The t-test is a significance test used to determine if two sample sets with mean values could have been drawn from the same population.[134] One set of data is defined as having a mean value, X_1, a variance of σ_{X1}, and n_1 number of data points. The second set of data is defined as having a mean value,X_2, a variance of σ_{X2}, and n_2 number of data points. The calculated t value is then derived from:

$$t = (X_1 - X_2)\left[\left(\frac{n_1 n_2}{n_1 + n_2}\right)\left(\frac{n_1 + n_2 - 2}{n_1(\sigma_{X1})^2 + n_2(\sigma_{X2})^2}\right)\right]^{\frac{1}{2}} \qquad \text{eq. (19)},$$

and compared to the two sided t-distribution tables for the specified degrees of freedom to determine the probability of the two data sets originating from the same population.

APPENDIX C. THE PRODUCTION OF "PHANTOM" COINS.

A series of "phantom" coins were struck, each at a known coining pressure, for use as calibration standards in the investigation of residual stress analysis for determining the force used to strike a coin. The geometric design and its relief were modeled after the 1968 U.S. one cent piece. The production of these "phantoms" required an investigation of the design and metallography of the U.S. one cent piece, as well as designing a rimming machine, and the dies and die system for striking the coins.

A. An overview of the Minting process of the U.S. one cent piece.

An understanding of the process of striking one cent pieces can be found in the Report on Visit to U.S.A. and Canadian Mints[135], written for the Royal Mint in 1949. An overview of the minting process is presented here.

A bar of base metal, i.e. a copper zinc alloy, is first cold rolled, in seclusive passes through a motorized 10" roller, to a thickness of 0.0485 inches. The "type one" or unrimmed blanks are then cut from the finished strip to a 0.754 inch diameter. The microstructure of the "type one" blank is shown in Figure 28, and displays severe deformation and elongation of the grains of the alloy. The preferred orientation of the grains in the rolling direction is evident.

Next, the cut blanks are annealed in gas fired rotary furnaces. The annealed blanks display scale which is removed in a blanching process using a mixture of argol, soap and 0.75% sulfuric acid. The "type one" blanks are the rimmed or edged with a rotating tapered marking machine. The blank is fed between a central grooved ring and two small grooved marking segments. The marking process produces a raised lip on the blank which serves several purposes. The rimming creates a more uniform blank which can be automatically fed more easily into a coining press. The striking

_____ = 0.1 mm

Figure 28. The microstructure of the "type one" coin blank. The grains are severely deformed and oriented in the direction of rolling. (200X).

force required to strike the coin is lowered by the formation of a thickened edge on the coin. The rim of the coin also protects the design of the coin from wear and abrasion during circulation. The diameter of the rimmed blank is 0.741 inch,with a rim thickness of 0.060 inch.

The rimmed blank, known as a "type two" blank, is then struck into the one cent piece using a knuckle action, Bliss-pattern coining press. The press is so called because the upper die is placed in a jointed column which moves up and down similar to the bending and straightening of a finger. The type two" blank in mechanically fed onto a lower die centered in a collar. The upper column then straightens imparting a blow to the blank and deforming it into the design of the dies.

B. An Investigation of the Design an Metallography of the 1968 U.S. One Cent Piece.

In order to more accurately design a "phantom" coin, a series of measurements of the design of U.S. one cent pieces were implemented using a ball micrometer. In addition, authentic "type one" and "type two" blanks were purchased for investigation of size and microstructure. The dimensional data acquired from these coins and blanks is summarized in Table XX.

Originally, the manufacture of "type one" blanks was planned. Later it was learned that the Olin Corporation in East Alton, IL once supplied the U.S. Mint with "type one" blanks. With the permission of Dr,. George Hunter, assistant director of technologies at the U.S. Mint, the Olin Corporation donated 133 "type one" blanks to the research. The average diameter of the Olin blanks is listed in Table XVIII. From the data obtained on the measurement of one cent pieces a dies and die system were designed for striking "phantom" coins using a hydraulic press. The production of "type two" blanks from the acquired Olin blanks required an investigation of the microstructure of the U.S. one cent pieces, the "type one' blanks, and the "type two" blanks for

Table XX. Dimensional Data on U.S. One Cent Pieces, Type One Blanks,Type Two Blanks, Olin Blanks, and Phantom Coins.

Coin type	# of samples	diameter inch	thickness inch max.	thickness inch min.	edge thickness inch
U.S. one cent piece	32	0.7481 ± 0.0001			
	20		0.0536 ± 0.0010	0.0416 ± 0.0010	
	30				0.0613 ± 0.0048
type one blank	10	0.7420 ± 0.0010	0.0496 ± 0.0005		
type two blank	10	0.7378 ± 0.0020			
	18		0.0493 ±0.0003		
Olin blank	113	0.7421 ± 0.0004			
	90		0.0497 ± 0.0002		
"Phantom" Coins	# of meas.				
B2-C 90,900 lb	3	0.7467 ± 0.0003	0.0560 ± 0.0010		0.0625 ± 0.0013
B1-A 40,100 lb	3	0.7468 ± 0.0001	0.0550 ± 0.0002		0.0566 ± 0.0025

determination of annealing conditions, as well as the design of a rudimentary rimming machine for marking the blanks.

1. The Metallography of Coins and Blanks The purpose for determining the microstructure of the one cent piece was to establish the size and the approximate amount of deformation of the metallic grains. A micrograph at 200x magnification of the microstructure of the one cent piece is shown in Figure 29.

The investigation of the "type one" blanks provided the initial or starting microstructure, and is shown in Figure 28 at 200x magnification. To determine the desired microstructure for the Olin blanks after annealing, a"type two" blank was sectioned, mounted, etched and micrographed. Figure 30 shows this microstructure.

a. Experimental Procedures for Metallography. Each coin or blank was sectioned using a band saw. The sections were then mounted in a methylmethacrylate quick setting material, Quickmount™, which set in approximately 30 minutes at room temperature. The mounted sections were rough polished with 320 grit, and 600 grit carbide paper on a lapping wheel. This procedure was followed by polishing with a 1 micron alumina and billiard cloth on a lapping wheel. Final polishing was performed on the lapping wheel using 0.3 micron alumina with a polishing cloth. A 1:1:1 ratio of ammonia, hydrogen peroxide, and water was prepared fresh and used as the etchant.

b. Annealing of Olin blanks. The Olin blanks were annealed in a quartz glass tube fitted with cork stoppers and ports for entry and exit of argon gas, and a digital thermocouple. The blanks were placed in the quartz tube at ambient temperature under a continuous, slow stream of argon for approximately two hours. Meanwhile, a tube furnace was preheated with a ceramic tube and thermocouple to the temperature of 540 ^{o}C Figure 31 is a schematic of the instrumental system. Once the desired temperature was reached in the tube furnace, the ceramic tube was replaced by the quartz tube containing the blanks. The temperature of the blanks was

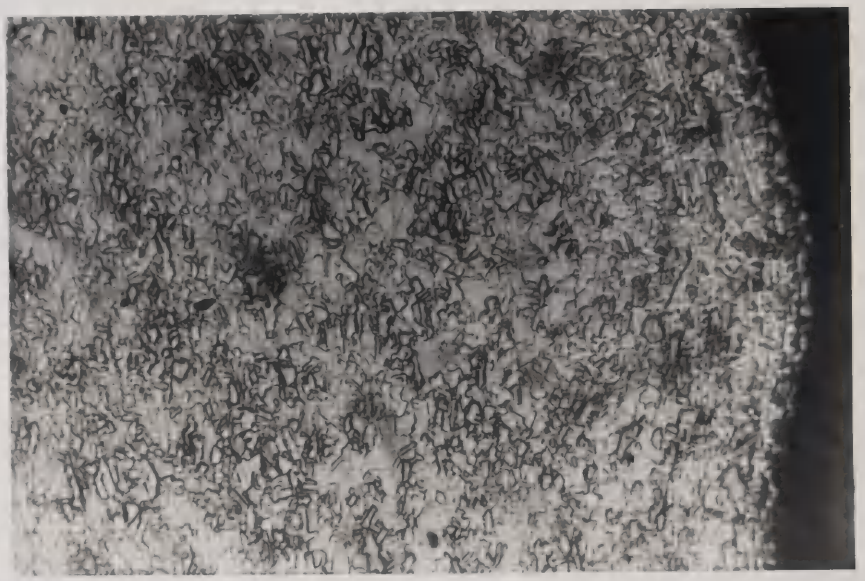

_____ = 0.1 mm

Figure 29. The microstructure of a 1968 D U.S. one cent piece. The grains are deformed and strain lines can be seen near the surface (200X).

_____ = 0.1 mm

Figure 30. The microstructure of a "type two" coin blank. The grains are more nearly equiaxed and showing twinning indicative of annealing. (200X).

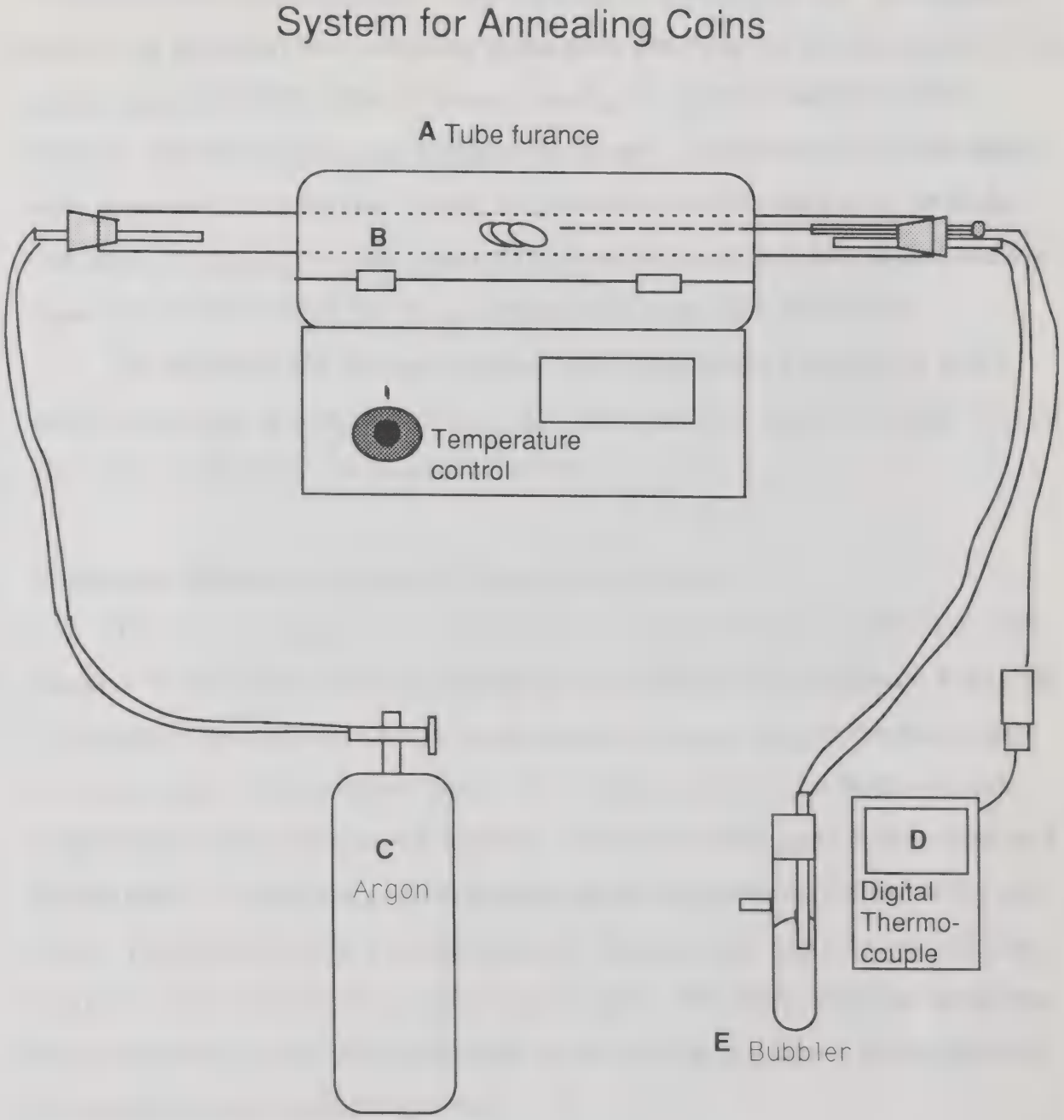

Figure 31. This schematic diagram show the instrumental system used to anneal Olin coin blanks before rimming. The components of the system are A- the tube furnace, B- the quartz glass tube containing Olin coin blanks, C- Argon (for inert atmosphere), D- the digital readout thermocouple, and E- the bubbler (to monitor gas flow in system).

monitored with a thermocouple in 1 min intervals for a total of 39 min. The starting time on the annealing time was taken as the point when the internal temperature of the system reached 495°C (within 19 min of inserting the quartz tube into the tube furnace). The blanks were then annealed for 20 min. Two batches of 10 Olin blanks were annealed in this manner. Figure 32 shows the microstructure of an annealed Olin blank. A comparison of this microstructure with that of the U.S. one cent and the "type two" blank indicated that the annealing procedures were satisfactory.

The annealed Olin blanks were then lightly blanched in a solution of 0.75% sulfuric acid, soap, and potassium bitartrate. The amount of material removed from the blank during blanching was less than 0.00022 g.

C. Rimming Machine and Rimming of Annealed Olin Blank.

The design of the rimming machine used in this research is based on an early design.[2] A schematic and an photograph of the machine are presented in Figure 33. The design of the system took into consideration the type of groove required to give the proper edge on the one cent piece. The machine consists of a fixed, grooved segment and a movable grooved segment. The motion of the plate is generated by a geared crank. A blank was placed between the two segments at one end of the machine. The compression of the blank between the segments was adjusted with the wing nuts and screws pushing against a guide plate. The blank was then forced into the grooves and rotated along the length of the machine by frictional forces between the stationary and movable segments.

D. The Design of the Die and The Die System.

The dies for striking the "phantom" coins were designed with consideration of the design of the U.S. one cent piece. The obverse and reverse design of the "phantom" coins consist of a central circular raised portion whose height and area

_____ = 0.1 mm

Figure 32. The microstructure of an annealed Olin coin blank. The grains are similar to the "type two" coin blank seen in Figure 30. The grains show twinning and are equiaxed.
(200X).

Design for Rimming Machine

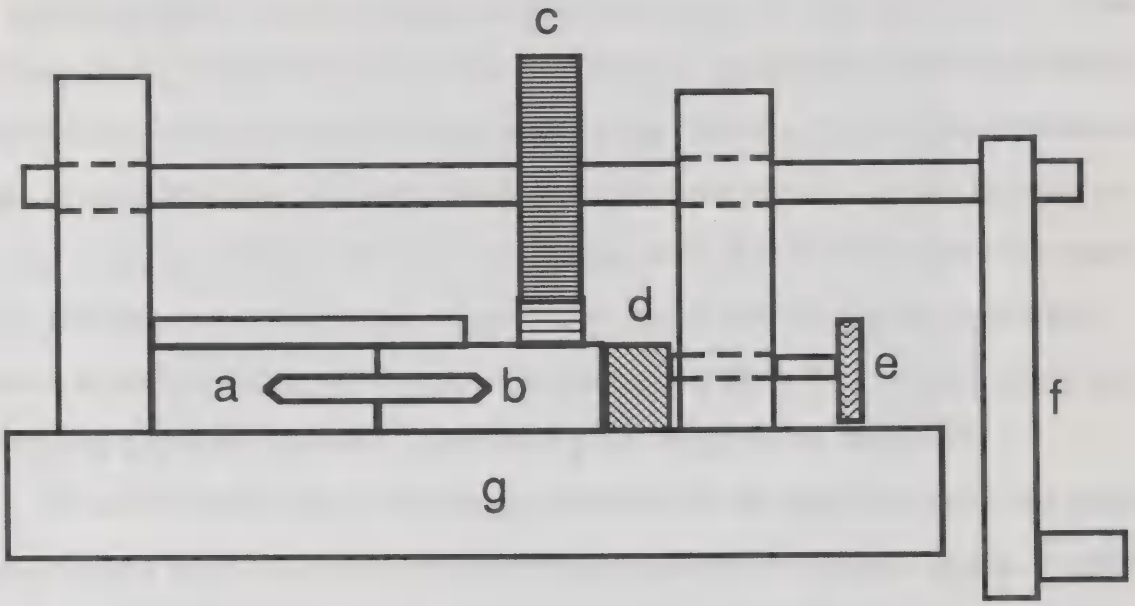

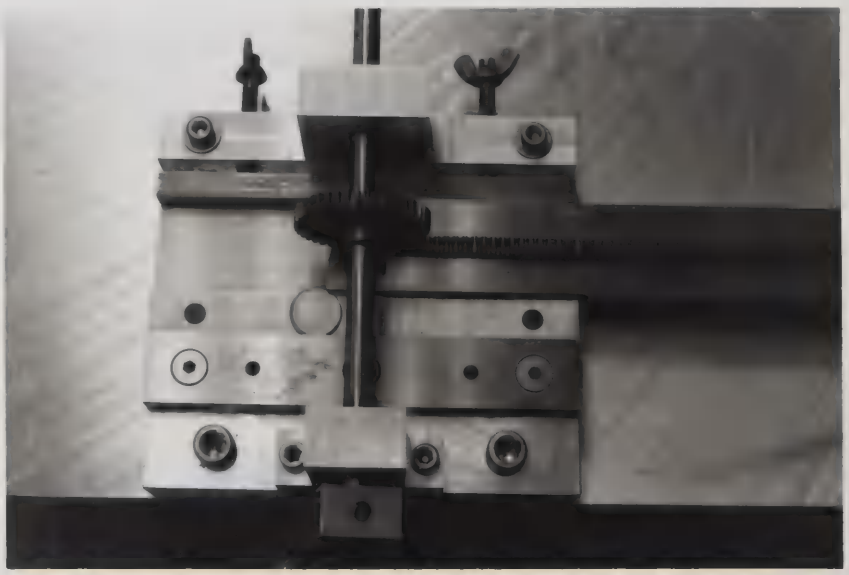

Figure 33. A schematic and actual photograph of the rimming machine. The components of the instrument are a-the stationary grooved segment, b- the moveable grooved segment, c- the gear, d- the compression plate, e- positioning screws, f- the crank. As the crank is turned counterclockwise, the movable plate slides to the left, forcing the coin blank into the grooves.

approximate the average height and area of the obverse portrait or reverse design of the one cent piece. Figure 34 shows photographs of the obverse and reverse of the phantom coin. The lettering on the one cent piece is modeled by a raised cylindrical portion surrounding the central circular area on the "phantom" coin. The dimensions of the cylindrical portion is based on the average height and area of the lettering on the one cent piece. Figure 35 shows the design of the dies for striking the "phantom" coin. The face of the die and the edges of the circular and cylindrical areas were beveled at a slight angle, as is found in actual coining dies. The beveled edges lower the coining pressure required to produce a good image of the design.[136]

In addition to the die, a die system consisting of an upper and lower die holder, a collar, and a system support, was designed for use with a hydraulic press. Pettiford has performed pressure studies on a hydraulic press using actual coining dies to determine the coining pressure needed to produce a good image of the design on a coin.[20] The design system used in this research is based on Pettiford's design, and is schematically represented in Figure 35.

E. Experimental Procedures for Striking "Phantom" Coins.

The actual system used in striking "phantom" coins is shown in Figure 36 . A Universal Testing machine, capable of loads up to 120,000 lb was used for striking the coins. The die system was placed in the center on the testing machine and a concrete block wall was assembled on the front side of the system, as shown in Figure 37. The purpose of the concrete wall was to act as a safety shield in the event that the dies or the die system failed.

The rimmed blank was placed on the lower die in the center of the collar. The base of the testing machine was then raised until the top plate of the machine was just touching the die system. The specified load was then applied to the system, causing the deformation of the blank. The actual load was recorded and removed from the

Obverse

Reverse

Figure 34. Photographs of the obverse and reverse of the phantom coin.

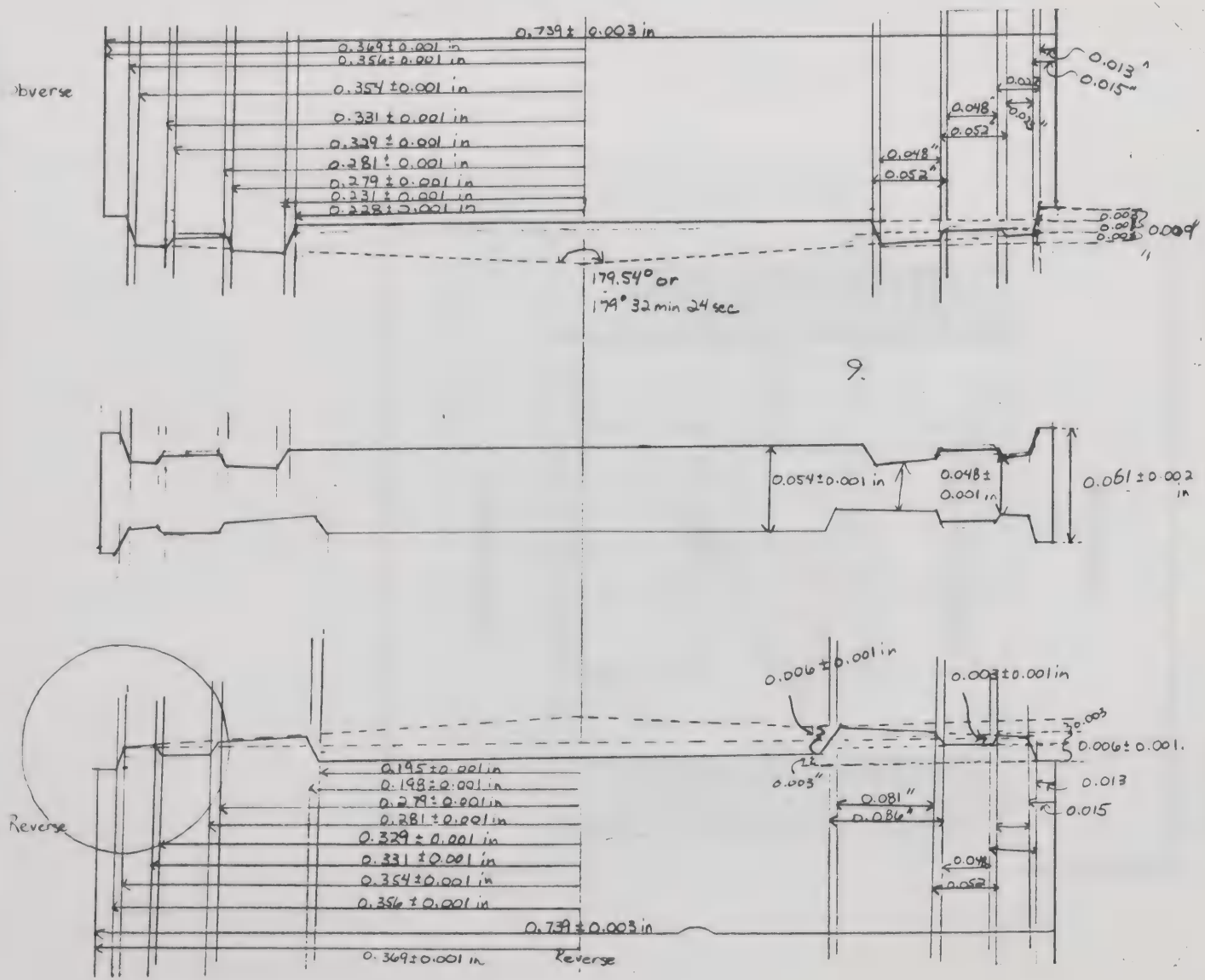

Figure 36. The design drawings for the construction of "phantom" coin dies.

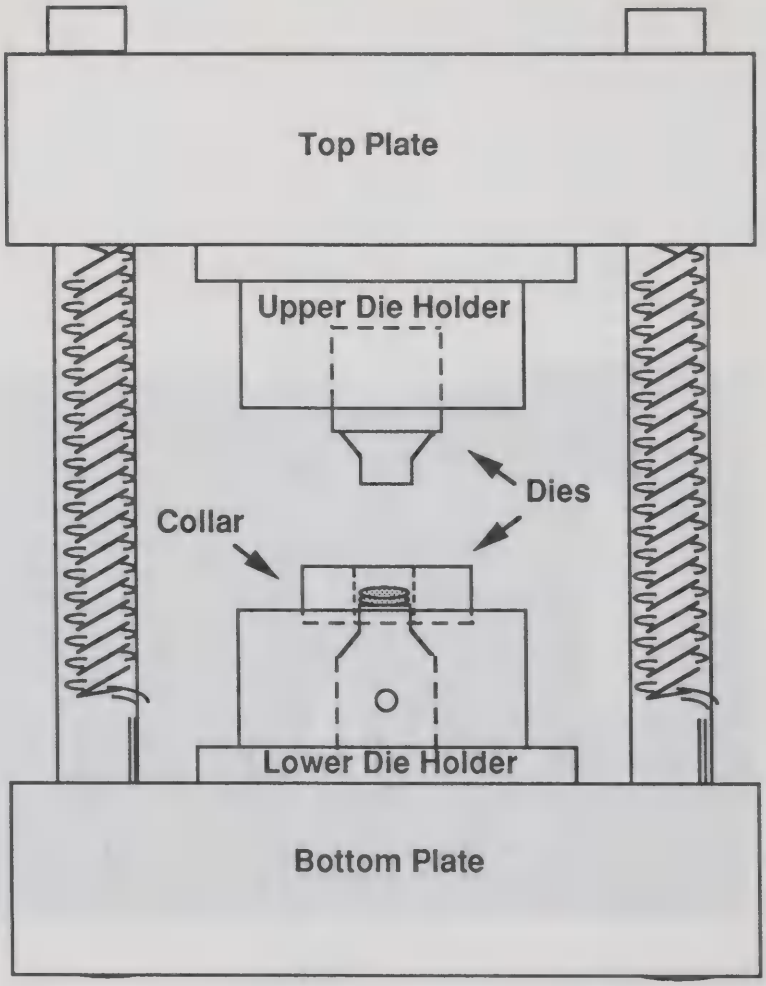

Figure 36. A schematic diagram of the die system used to strike "phantom" coins.

Figure 37 A photograph of the actual die system used to strike "phantom" coins.

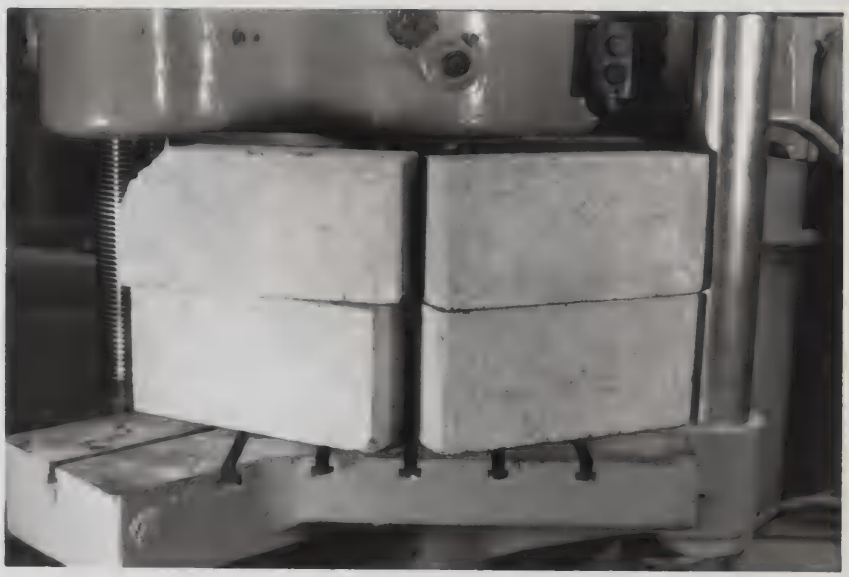

Figure 38. A photograph showing the protective concrete block wall which functioned as a safety shield.

system. The newly formed "phantom" coin was then lightly tapped out of the collar of the system using a wooden dow rod. Photographs of the obverse and reverse "phantom" coin are shown in Figure 34, page 132.

F.Observations on "Phantom" Coins and Coining Process.

The dimensions of the "phantom" coins used in this study are given in Table XX and can be compared to those of the U.S. one cent piece. The microstructural features of the edges of the "phantom" coins and the U.S. one cent piece can be compared in Figure 39 . The dimensions of the "phantom"coin B1-A, struck at 40,100 lb, are smaller in edge thickness and slightly thicker in maximum thickness than the U.S. one cent. "Phantom" coin B2-C, struck at 90,900 lb, is more similar to the U.S. one cent with the exception that the maximum thickness is slightly larger in the "phantom" coin. The micrographs of the edges of the "phantom" and one cent pieces show the following: a) the edge of the B1-A "phantom" coin is not as well formed as the other pieces; b) the grains on the edge of the B2-C "phantom" coin is much more severely deformed than in the one cent piece; and c.) the corners of the U.S. one cent piece are more gently rounded than those of the "phantom" coins.

Three other important observations should be noted. The B2-C phantom coin was warped or curved slightly, indicating an unbalanced stress system during striking. In addition, a crack was formed in the upper die and was noticeable in the design of the "phantom" coins. A visual investigation of the die system after striking the "phantom" coins found that the holder of the lower die had sunk slightly into the base support system.

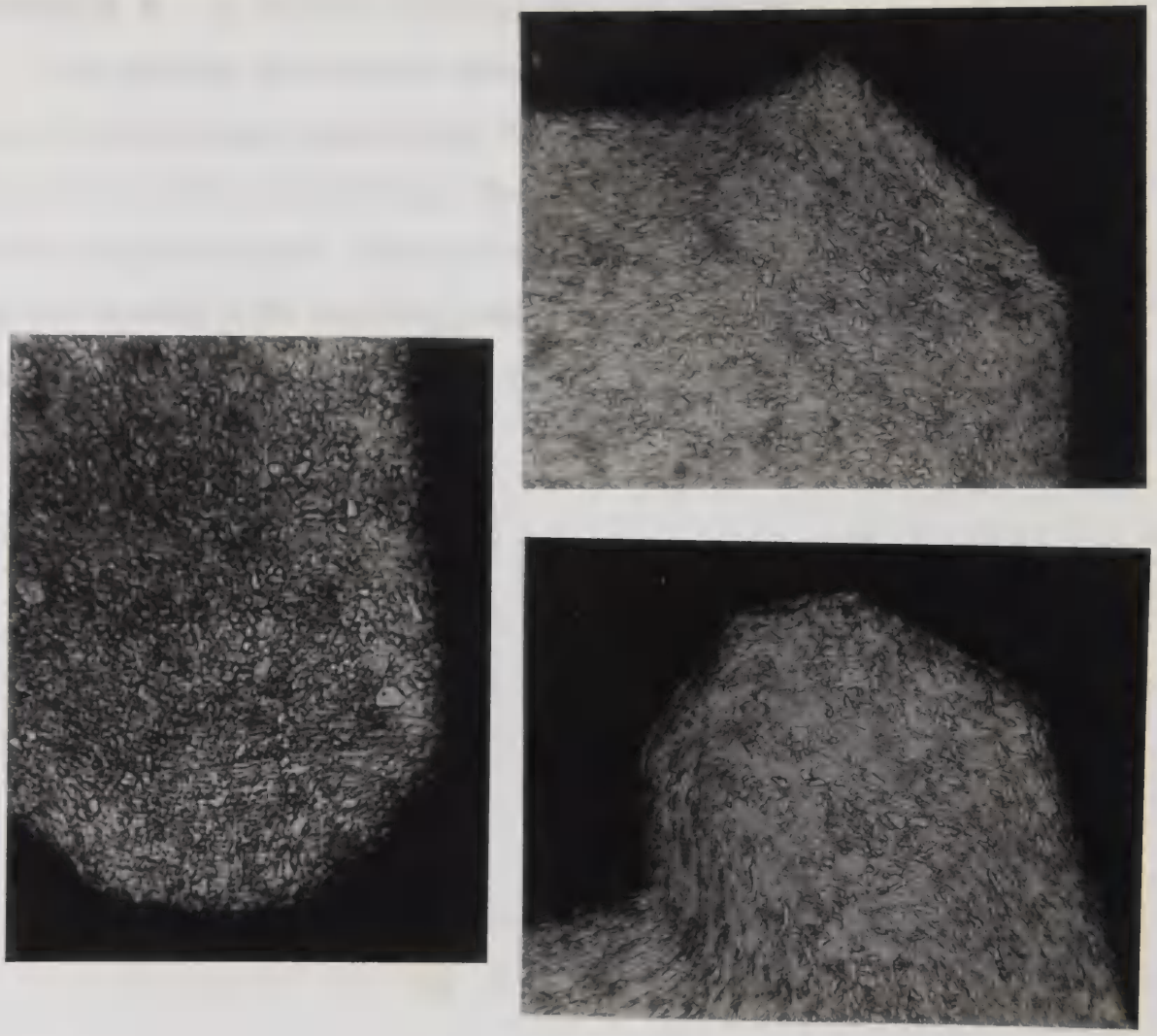

_____ = 0.2 mm

Figure 39. The microstructure of the edge of: A- "phantom" coin B1-A, struck at 40,100 lb, B- "phantom" coin B2-C, struck at 90,900 lb, and C- a 1968 D U.S one cent piece. (100X).

APPENDIX D. D VERSUS SIN SQUARE PSI PLOTS

This appendix contains the d versus $\sin^2$ psi plots from which the residual stress in a coin was calculated. Each point of the plot represent s the interplanar spacing of the plane of the alloy at a specific psi tilt and is calculated from the diffraction profile taken on the diffractometer. The error bars associated with each point represent one standard deviation of the calculated d spacing and is determined from counting statistics. In cases where severe oscillations occur, it is noted on the plot.

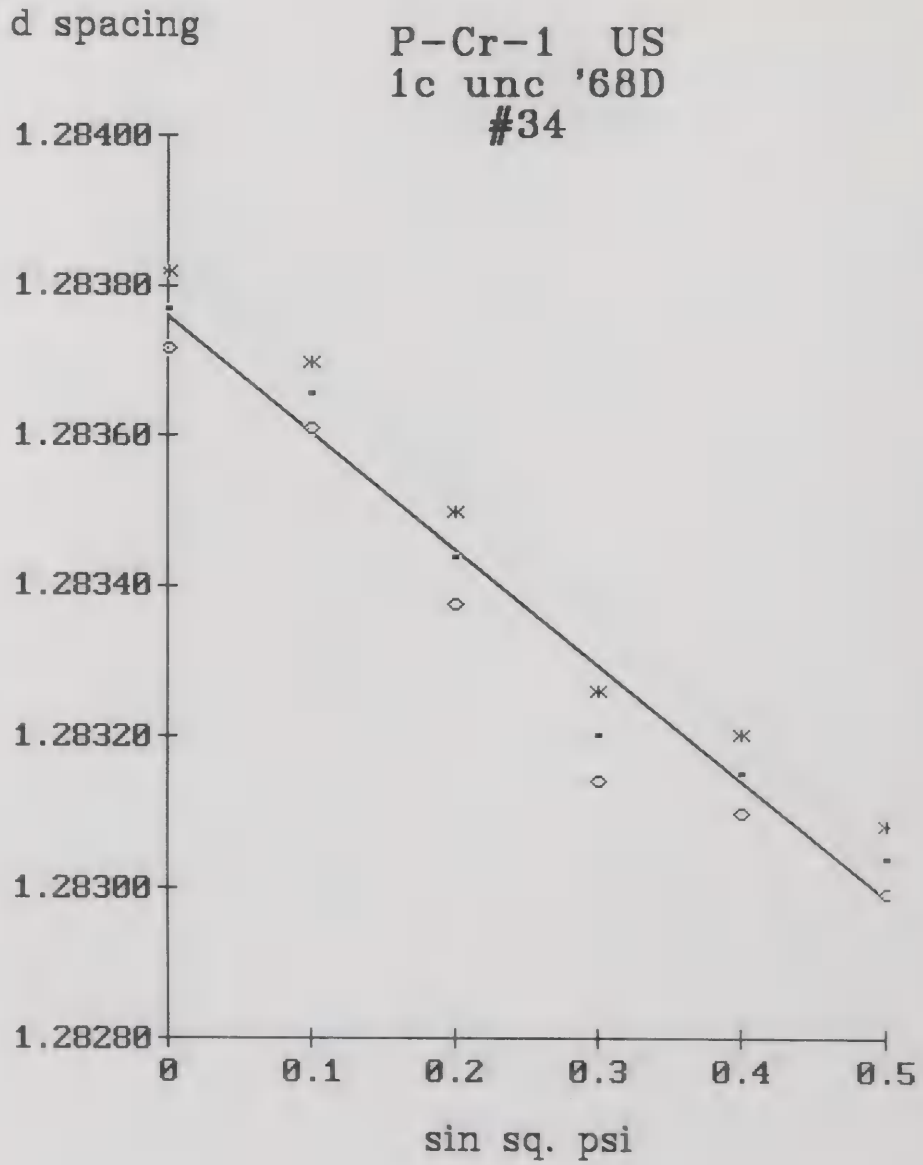

Figure 40. A plot of the d spacing versus $\sin^2$ psi, using chromium radiation, taken on the 1968 D mint issue U.S. one cent piece (#34), located above the date. (#P-Cr-1).

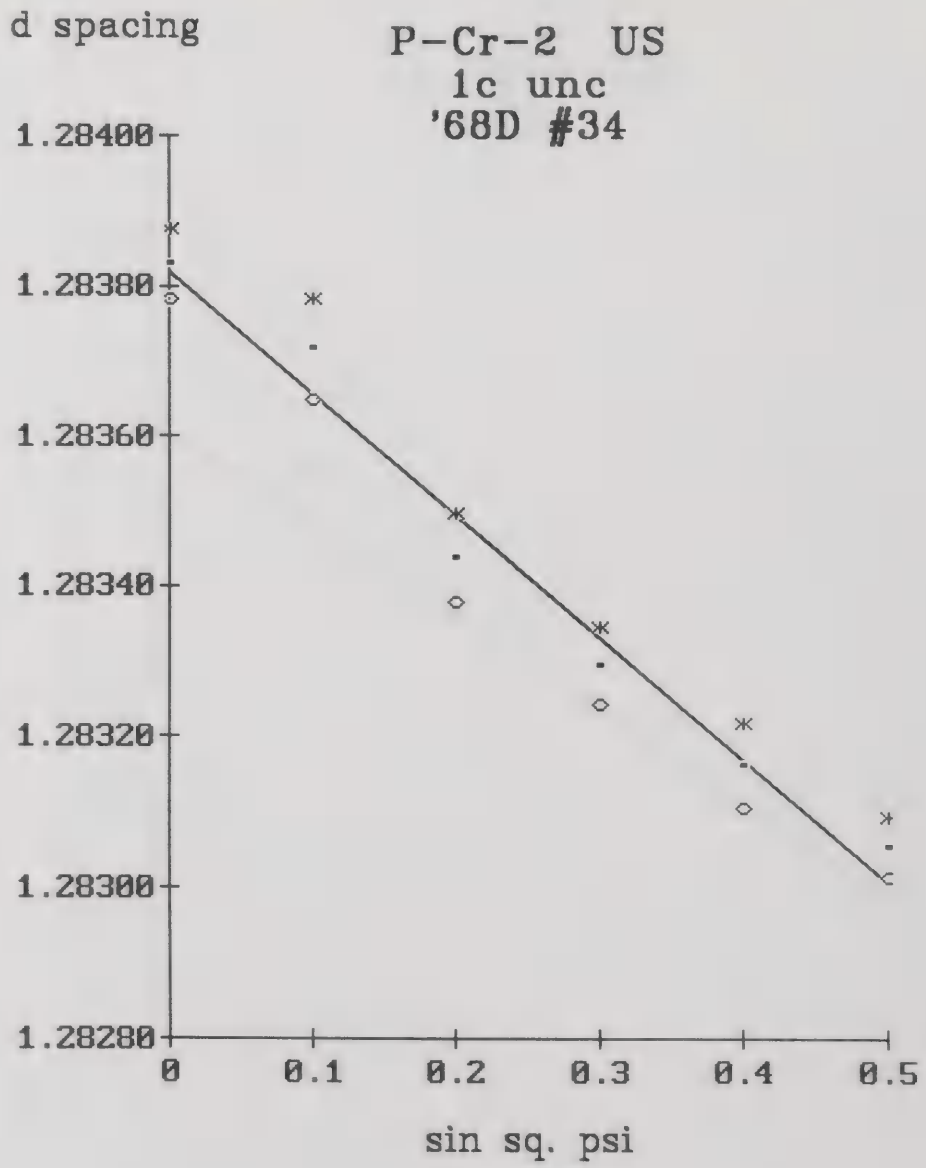

Figure 41. A plot of the d spacing versus $\sin^2$ psi, using chromium radiation, taken on the 1968 D mint issue U.S. one cent piece (#34) located above the date. (#P-Cr-2).

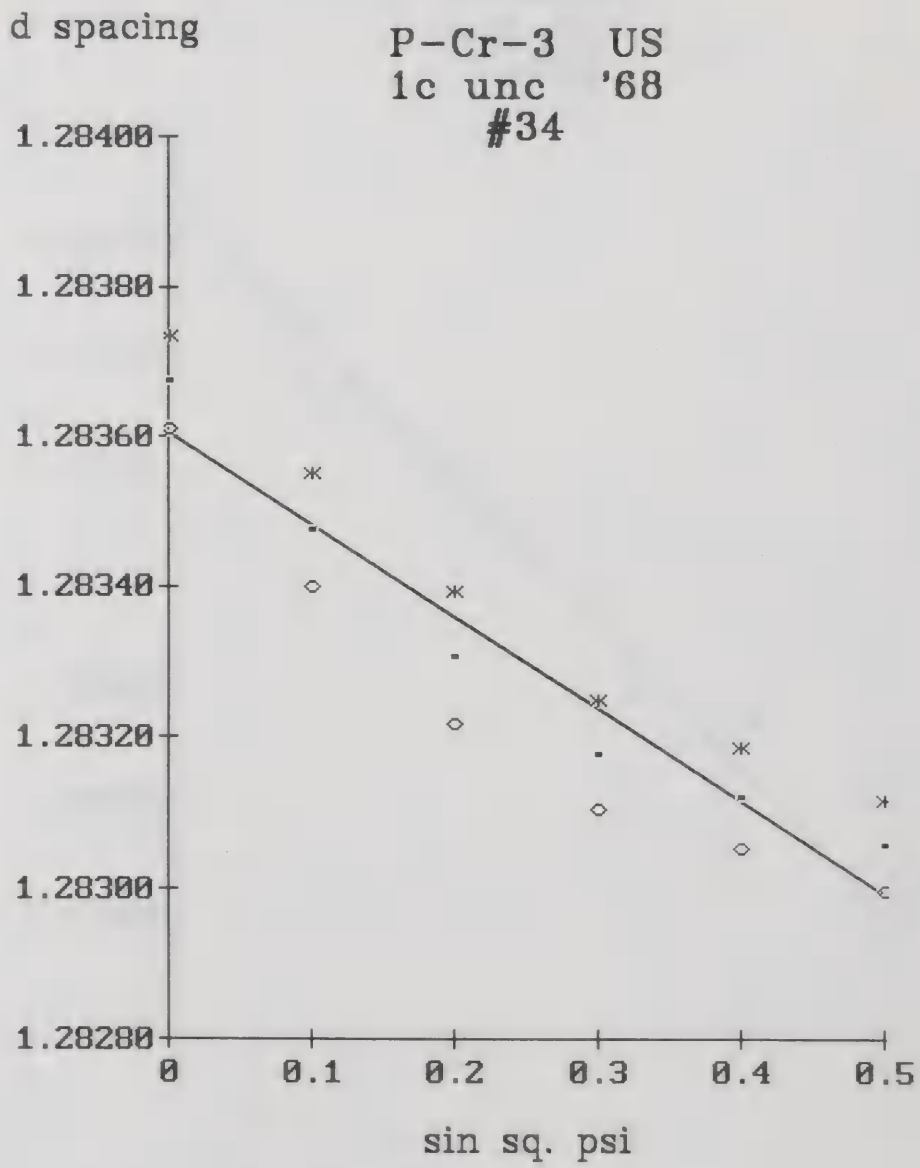

Figure 42. A plot of the d spacing versus $\sin^2$ psi, using chromium radiation, taken on the 1968 D mint issue U.S. one cent piece (#34)located above the date. (#P-Cr-3).

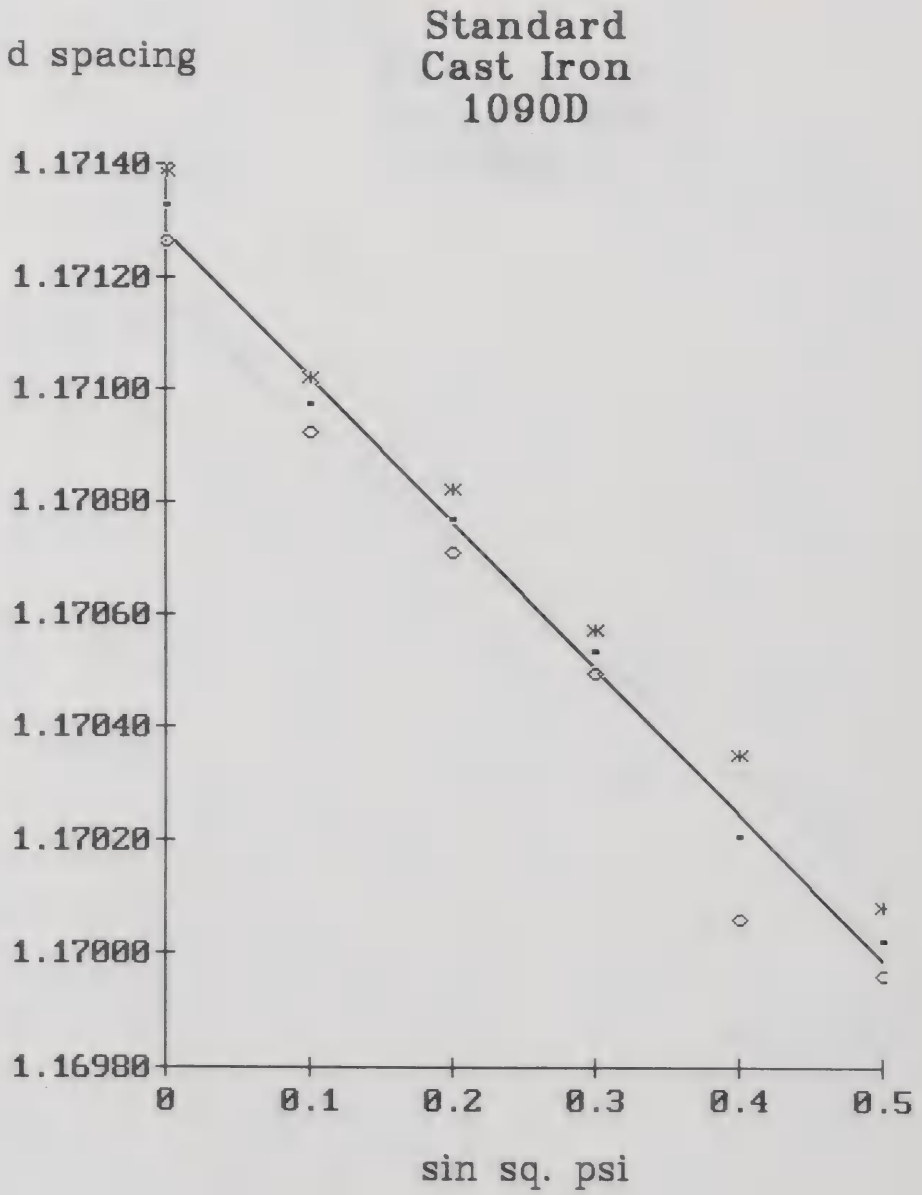

Figure 43. A plot of the d spacing versus $\sin^2$ psi, using chromium radiation, taken on a standard cast iron sample.
(#P-Cr-4).

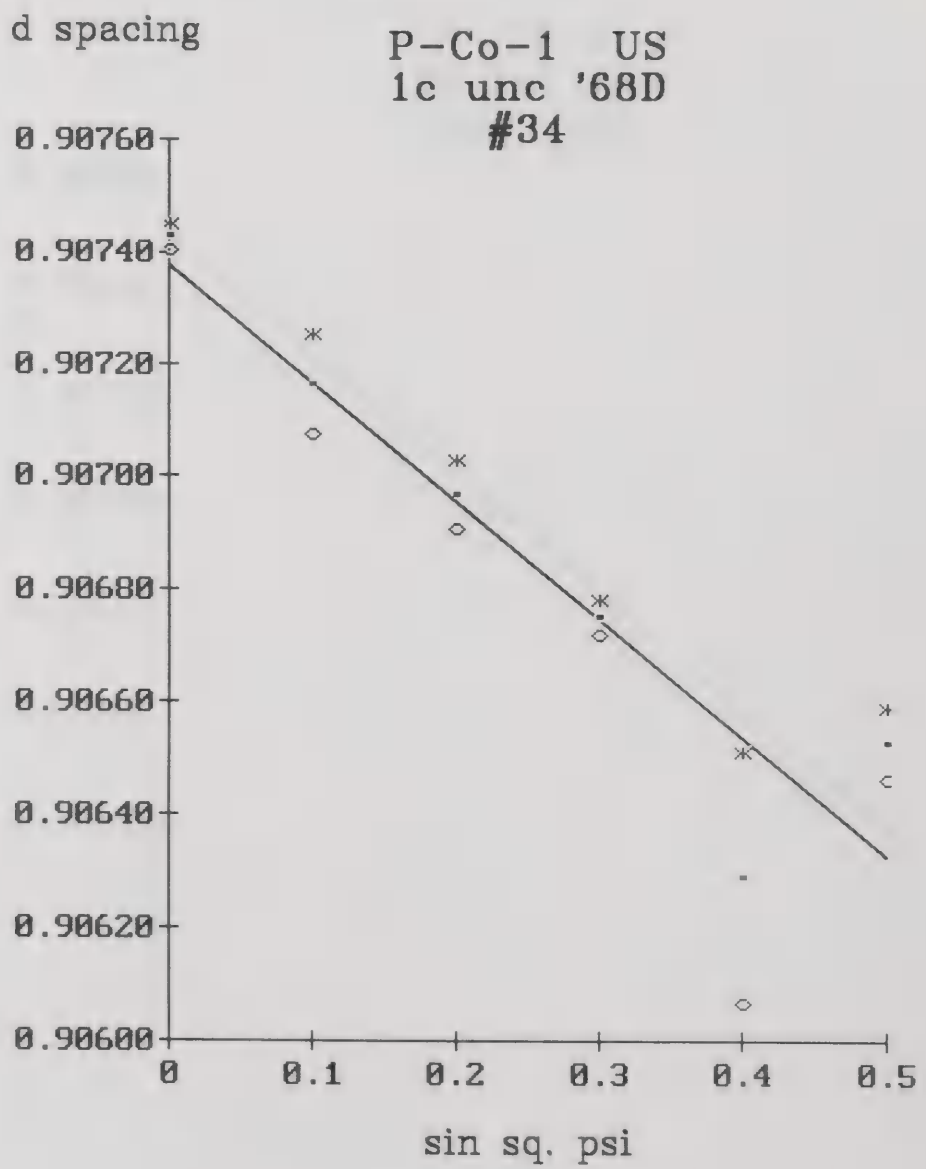

Figure 44. A plot of the d spacing versus $\sin^2$ psi, using cobalt radiation, taken on the 1968 D mint issue U.S. one cent piece (#34), to determine the effect of sample displacement.
(#P-Co-1).

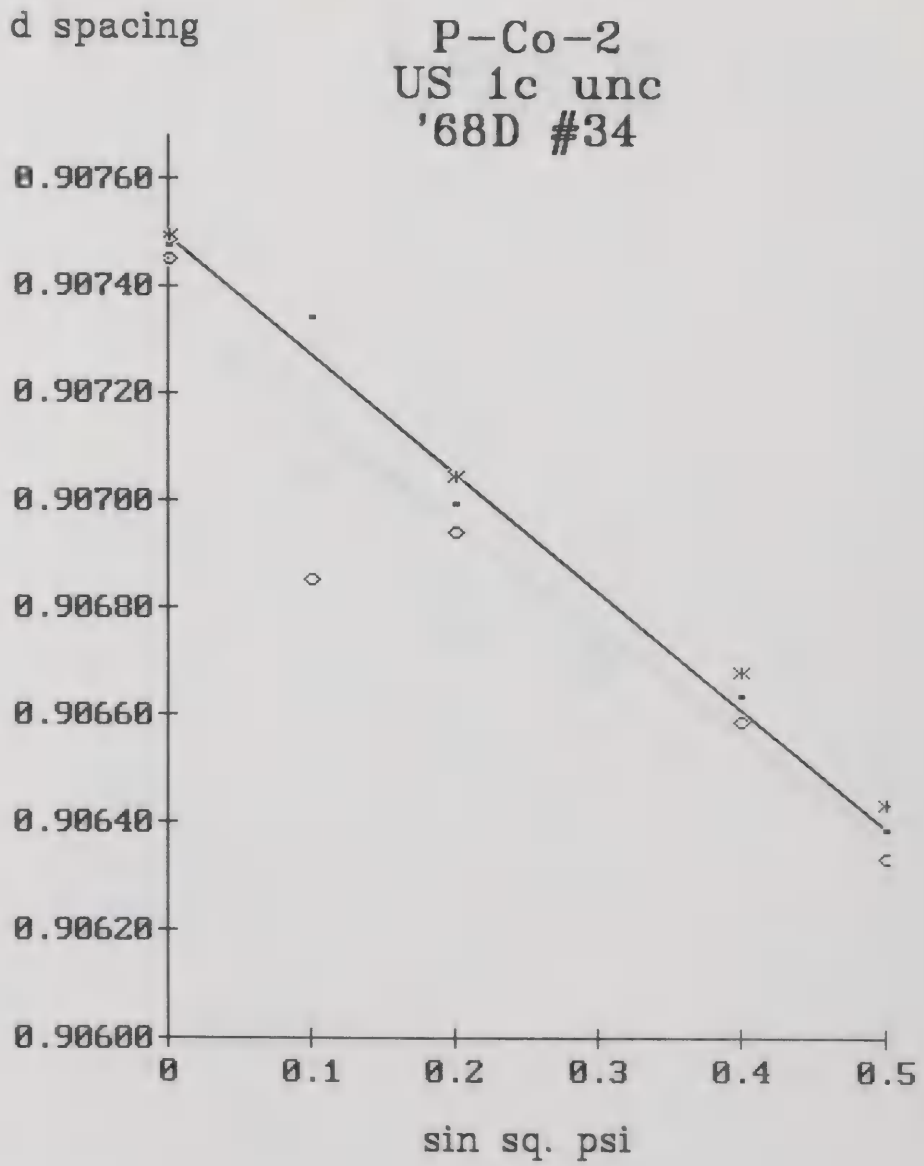

Figure 45. A plot of the d spacing versus $\sin^2$ psi, using cobalt radiation, taken on the 1968 D mint issue U.S. one cent piece (#34), with a 1mm displacement in the forward direction.
(#P-Co-2).

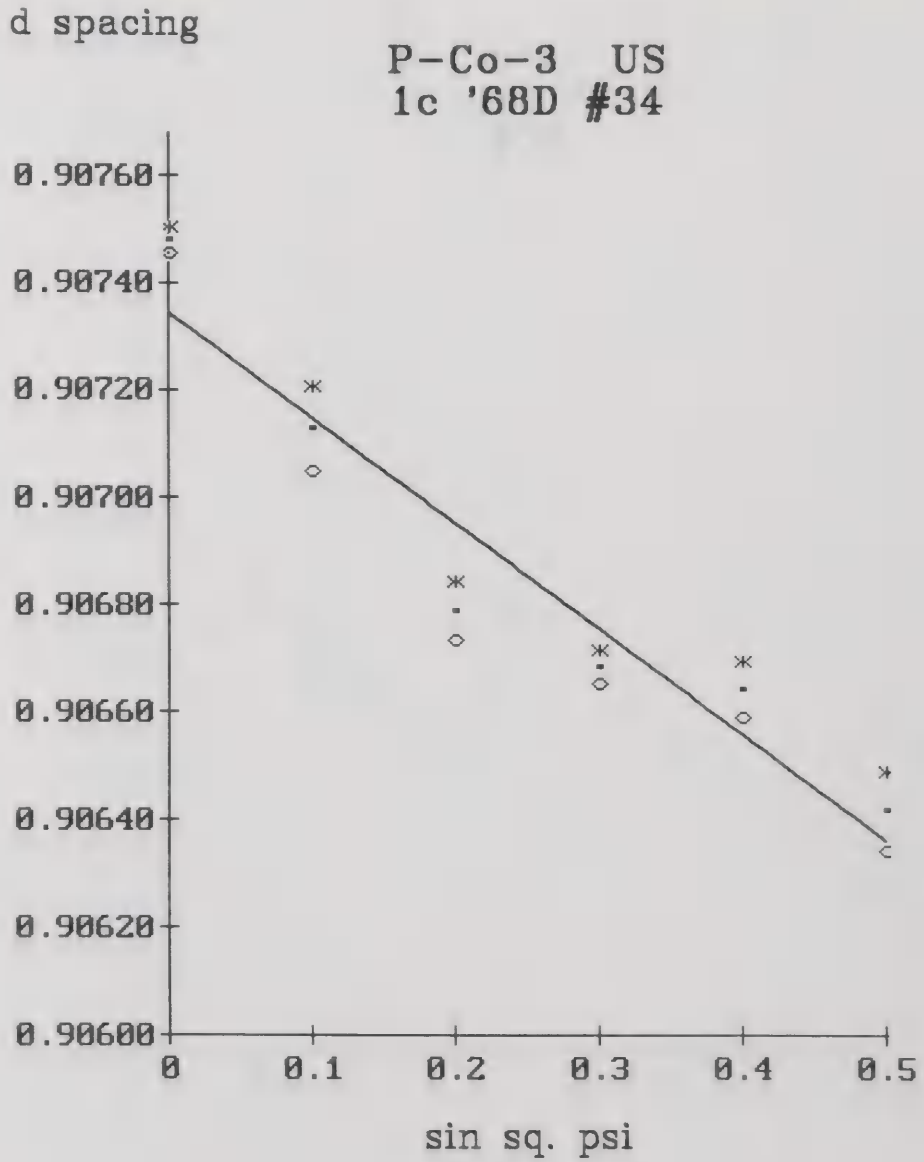

Figure 46. A plot of the d spacing versus $\sin^2$ psi, using cobalt radiation, taken on the 1968 D mint issue U.S. one cent piece (#34) , with a 1mm displacement in the backward direction
(#P-Co-3).

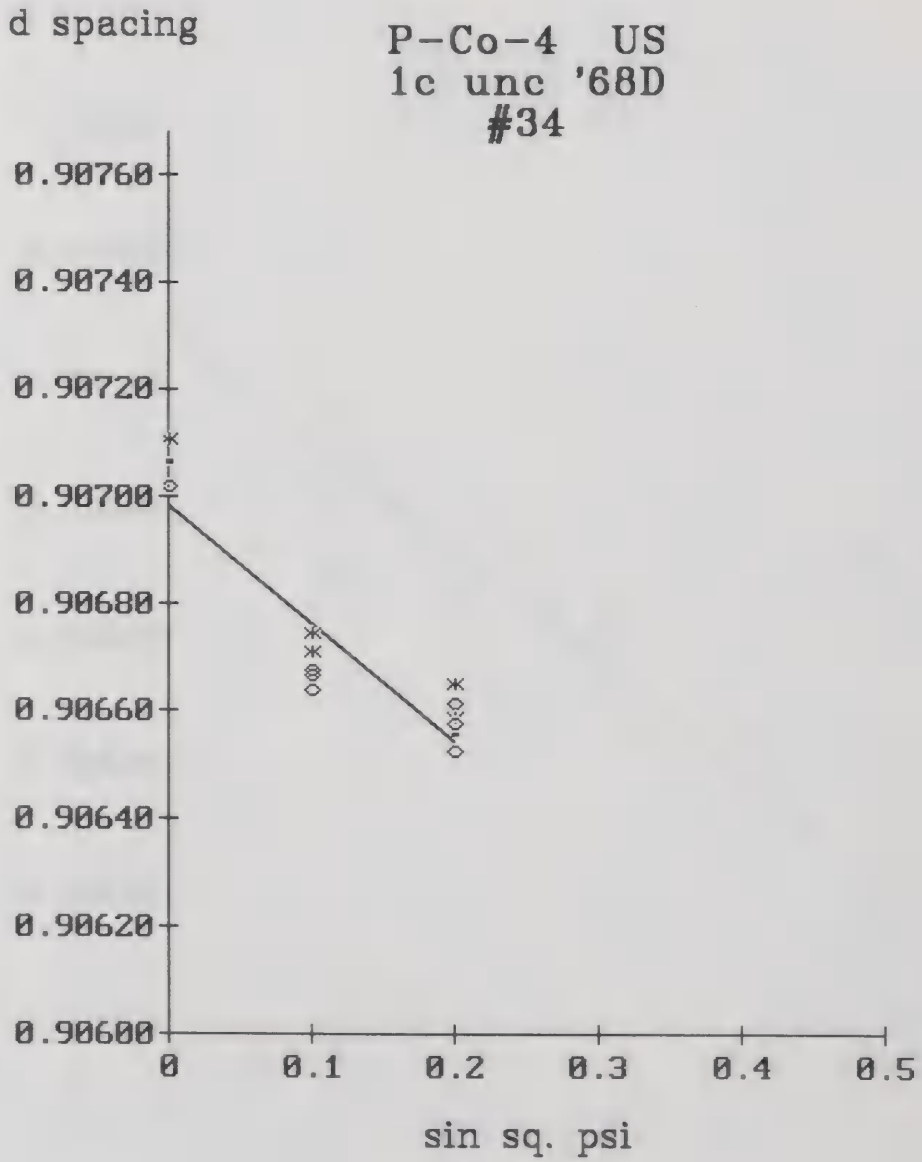

Figure 47. A plot of the d spacing versus the $\sin^2$ psi, using cobalt radiation, to determine the presence of psi splitting.
(#P-Co-4).

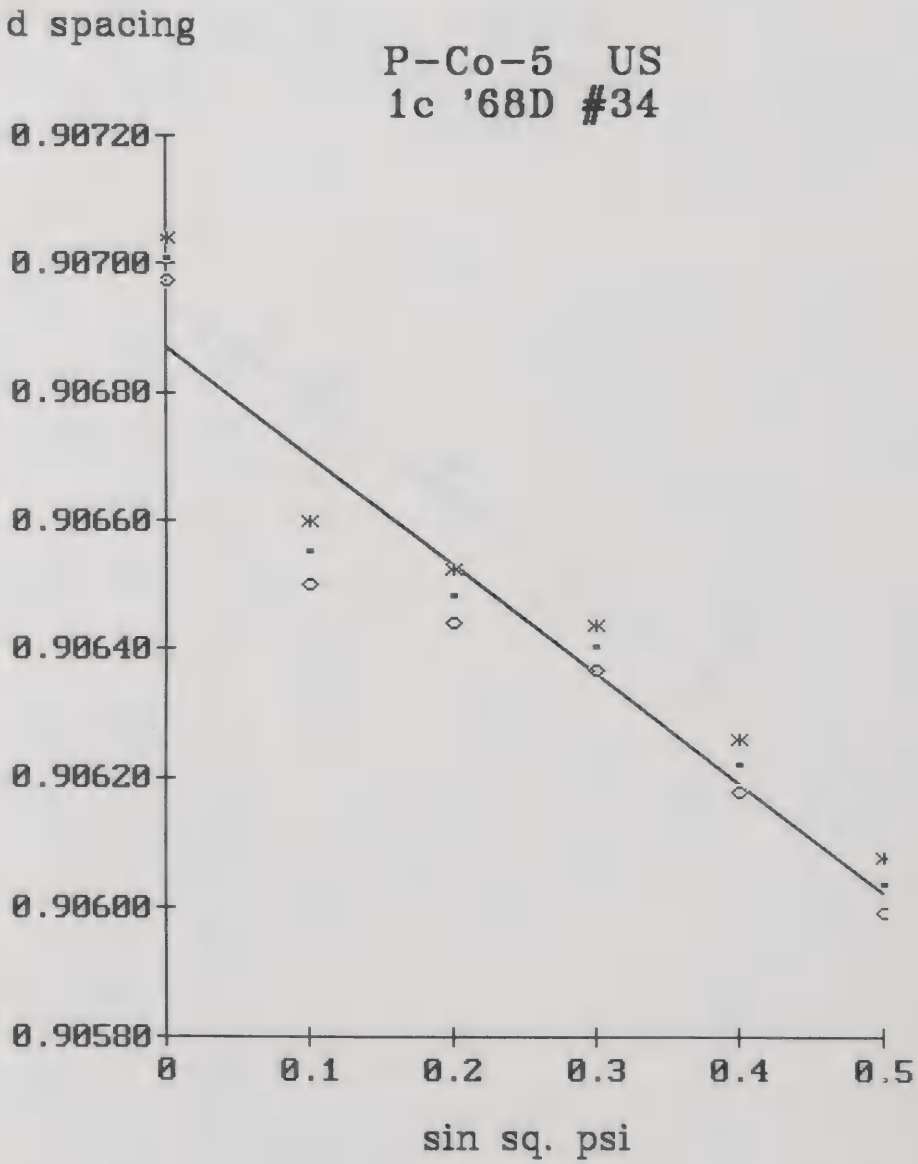

Figure 48. A plot of the d spacing versus $\sin^2$ psi, using cobalt radiation, taken on the 1968 D mint issue U.S. one cent piece (#34), aligned to within 0.00001 inch of the goniometer center.
(#P-Co-5).

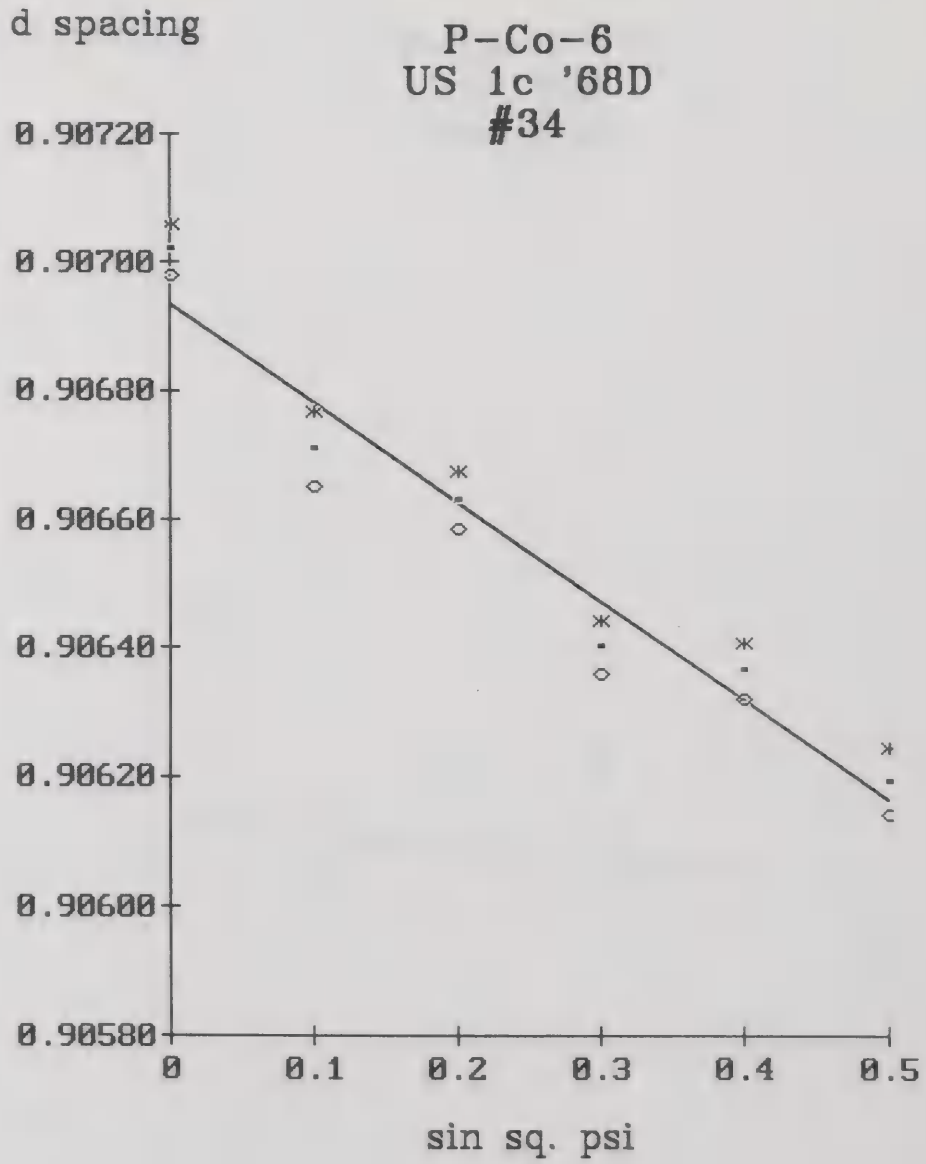

Figure 49. A plot of the d spacing versus $\sin^2$ psi, using cobalt radiation, taken on the 1968 D mint issue U.S. one cent piece (#34) , aligned to within 0.00001 inch of the goniometer center.
(#P-Co-6).

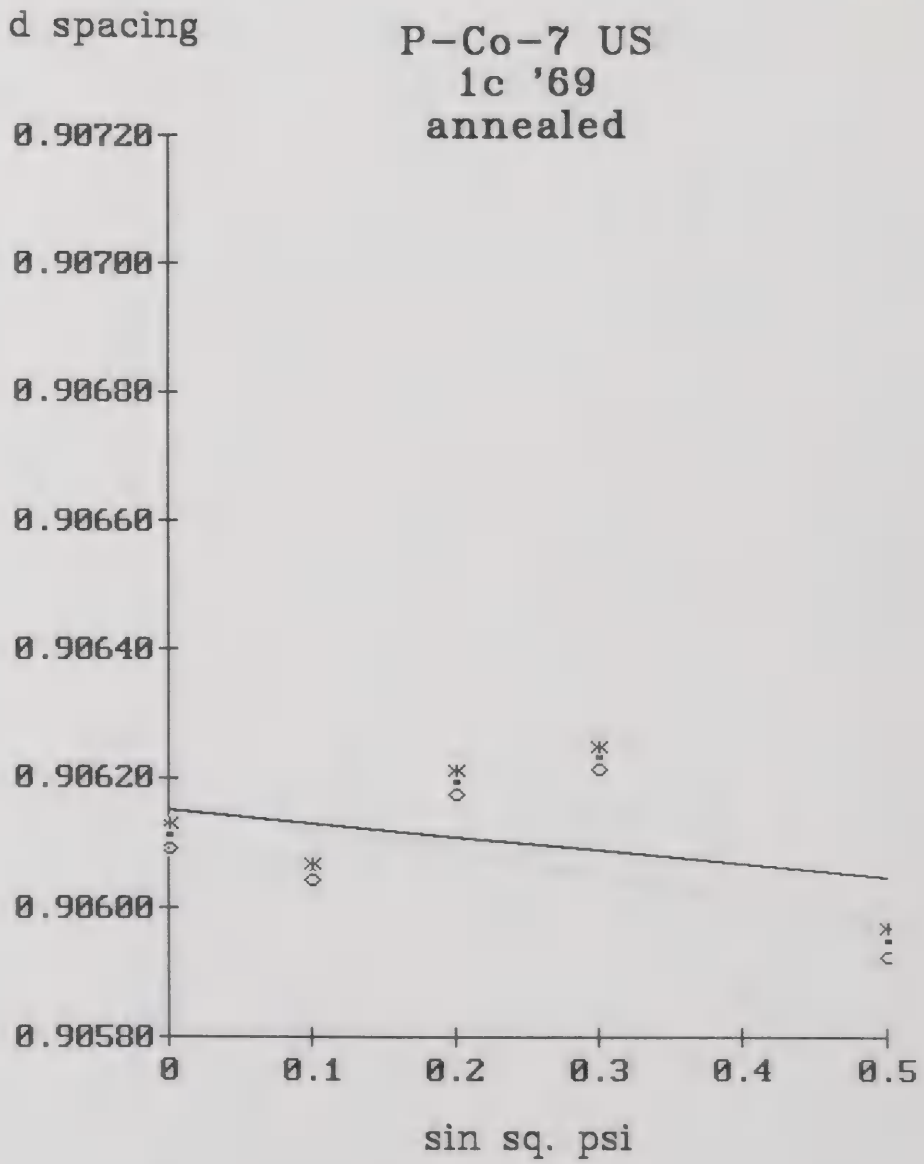

Figure 50. A plot of the d spacing versus $\sin^2$ psi, using cobalt radiation, taken on the 1969 S mint issue U.S. one cent piece, which had been annealed at 525 ^{o}C for 20 minutes.
(#P-Co-7).

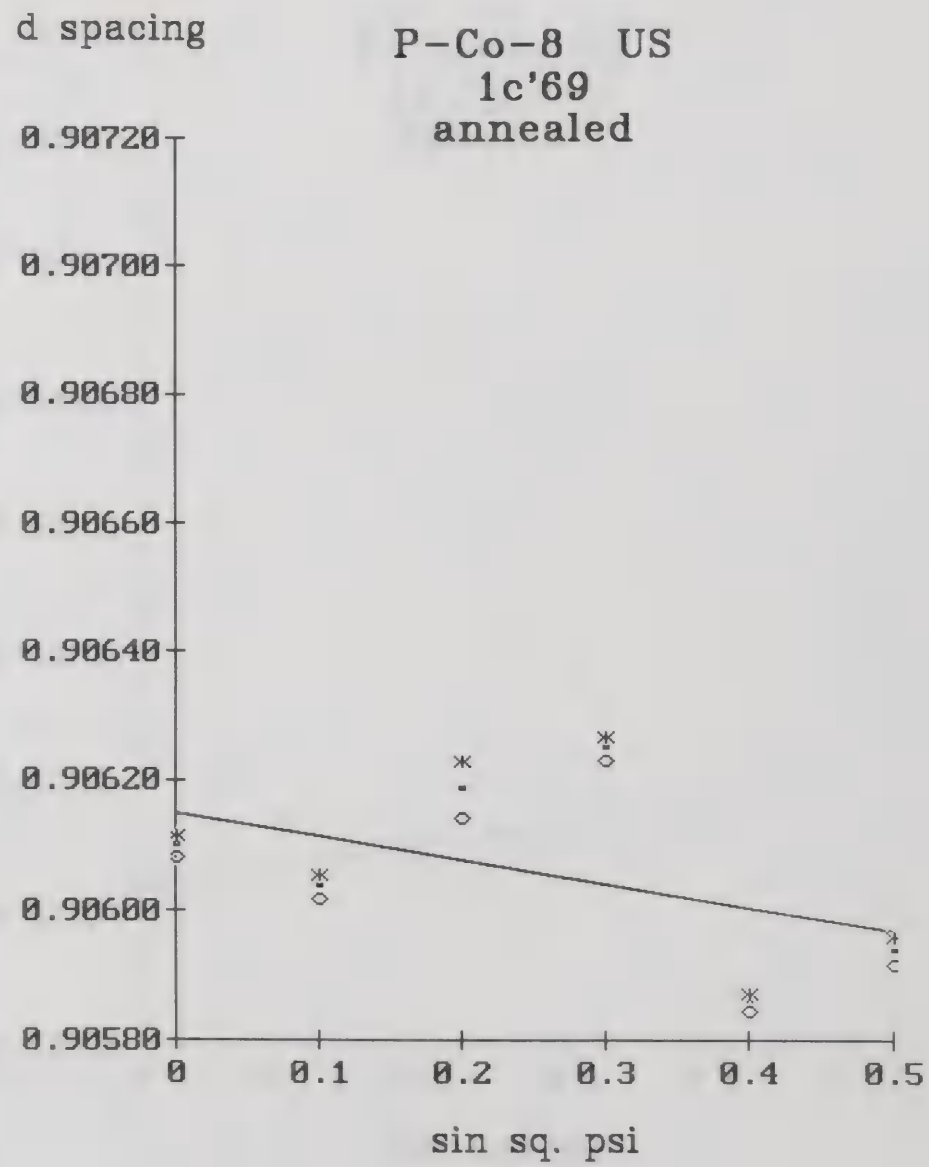

Figure 51. A plot of the d spacing versus $\sin^2$ psi, using cobalt radiation, taken on the 1969 S mint issue U.S. one cent piece, which had been annealed at 525 ^{o}C for 20 minutes.
(#P-Co-8).

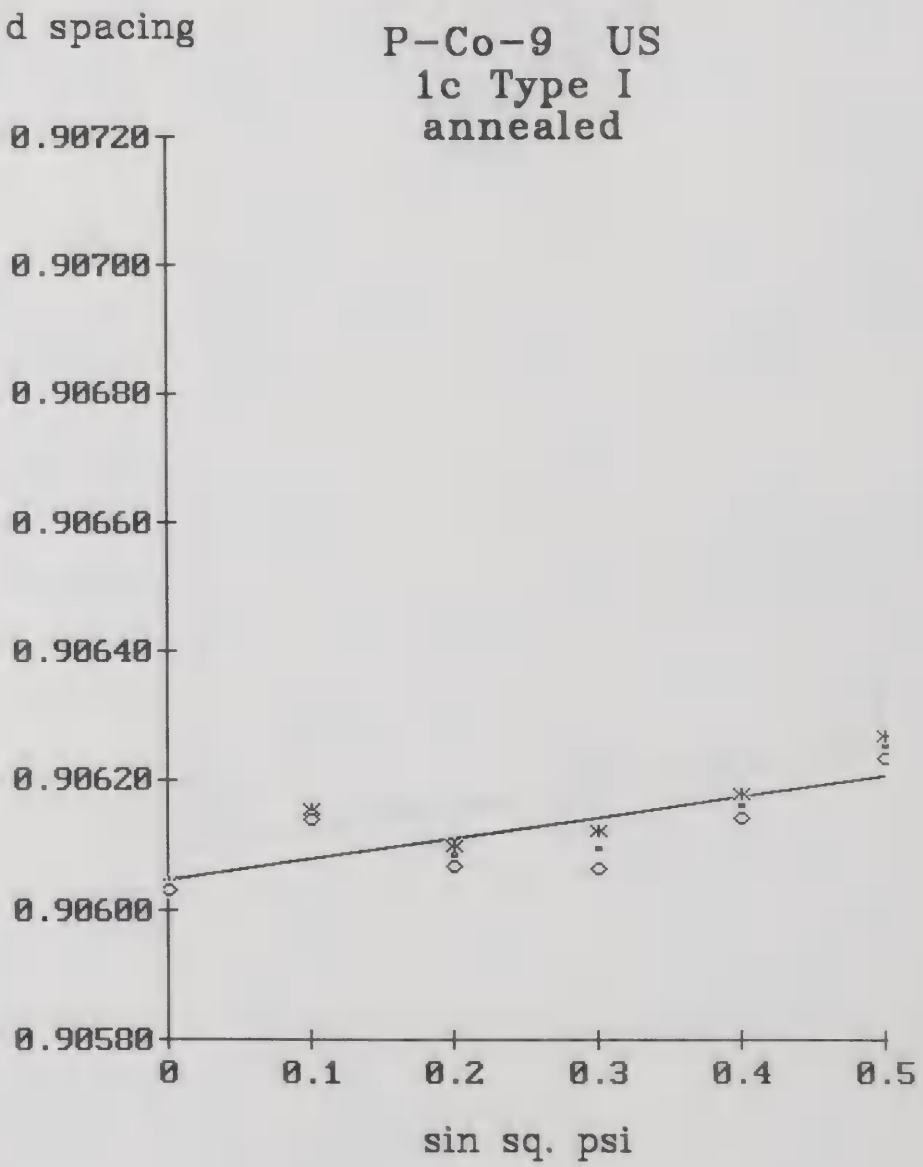

Figure 52. A plot of the d spacing versus $\sin^2$ psi, using cobalt radiation, taken on the U.S. "Type I" one cent blank, which had been annealed at 514 ^{o}C for 20 minutes. (#P-Co-9).

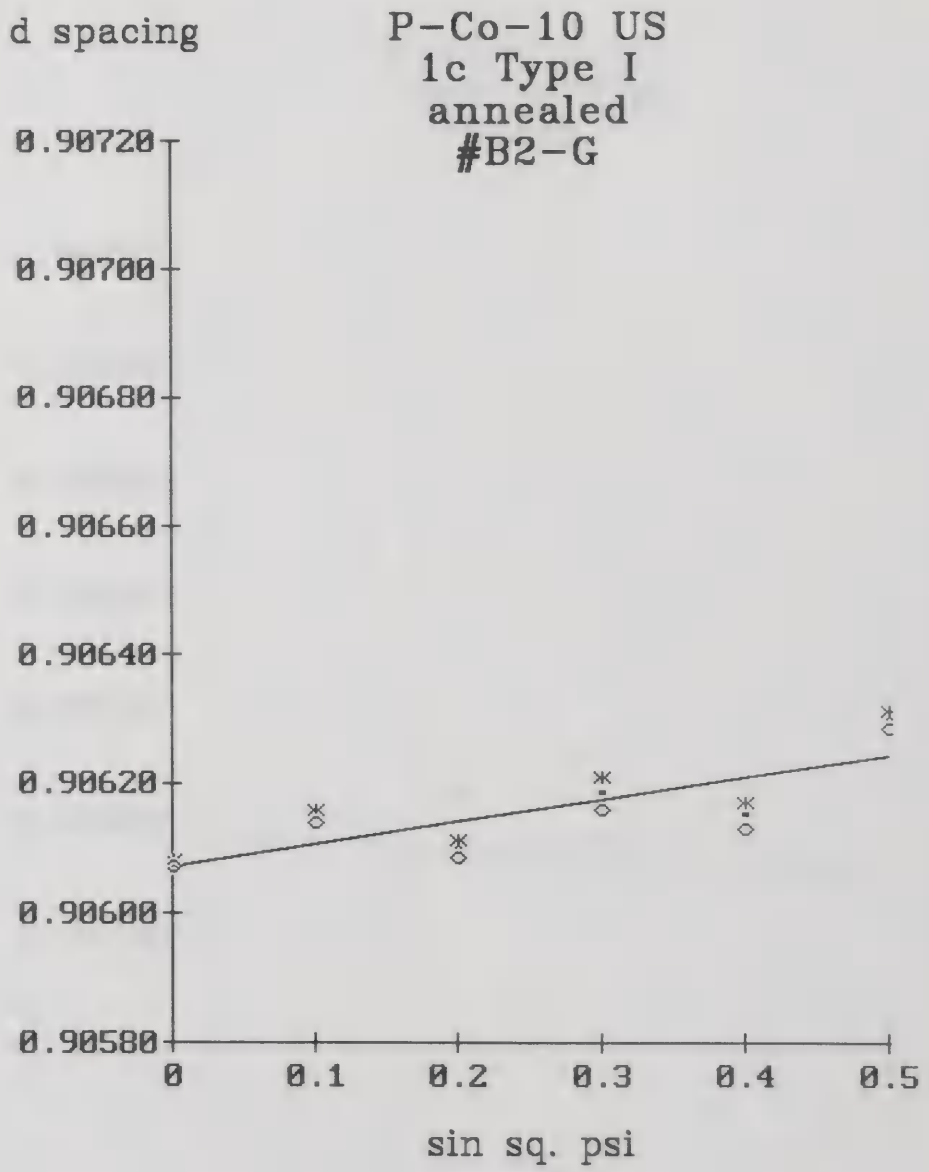

Figure 53. A plot of the d spacing versus $\sin^2$ psi, using cobalt radiation, taken on the U.S. "Type I" one cent blank (#B2-G), which had been annealed at 514 ^{o}C for 20 minutes.
(#P-Co-10).

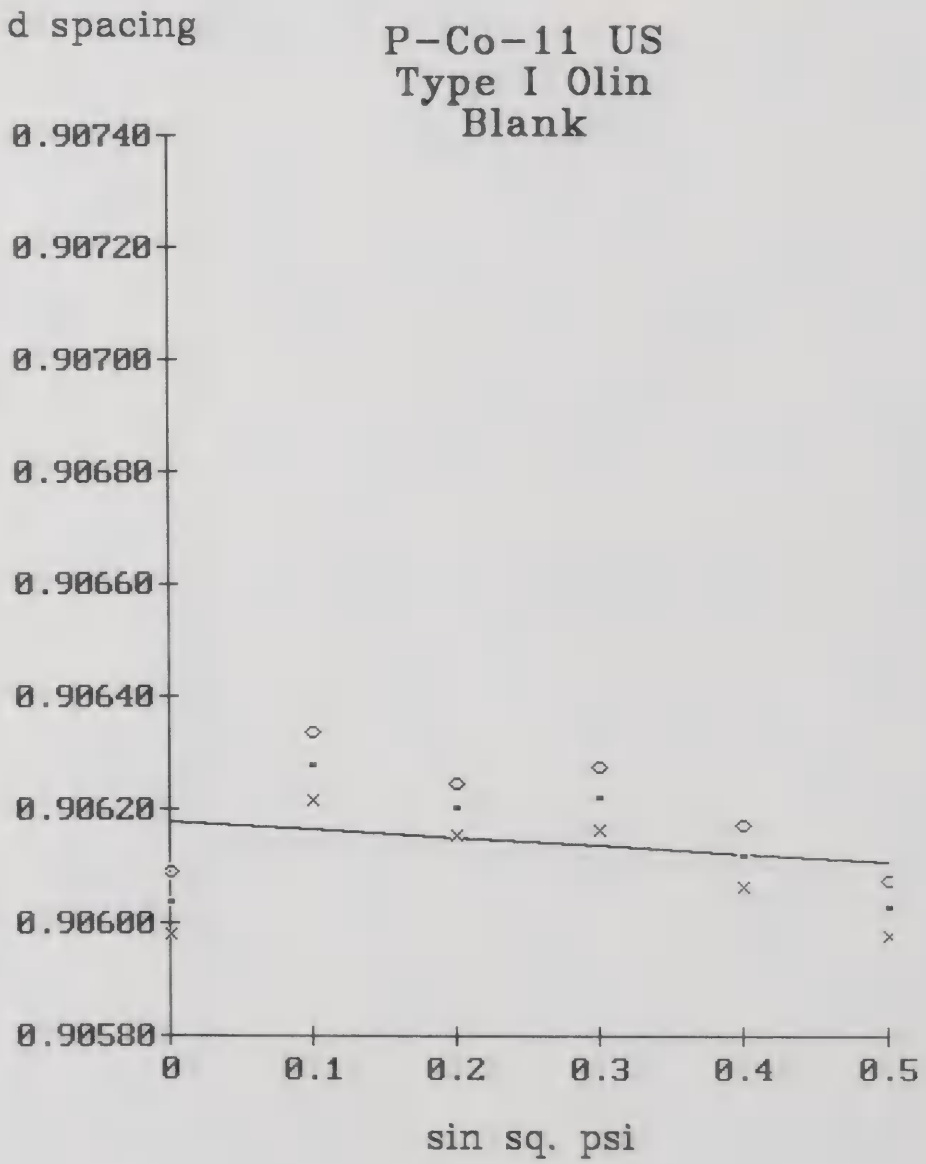

Figure 54. A plot of the d spacing versus $\sin^2$ psi, using cobalt radiation, taken on the Olin. "Type I" one cent blank.
(#P-Co-11).

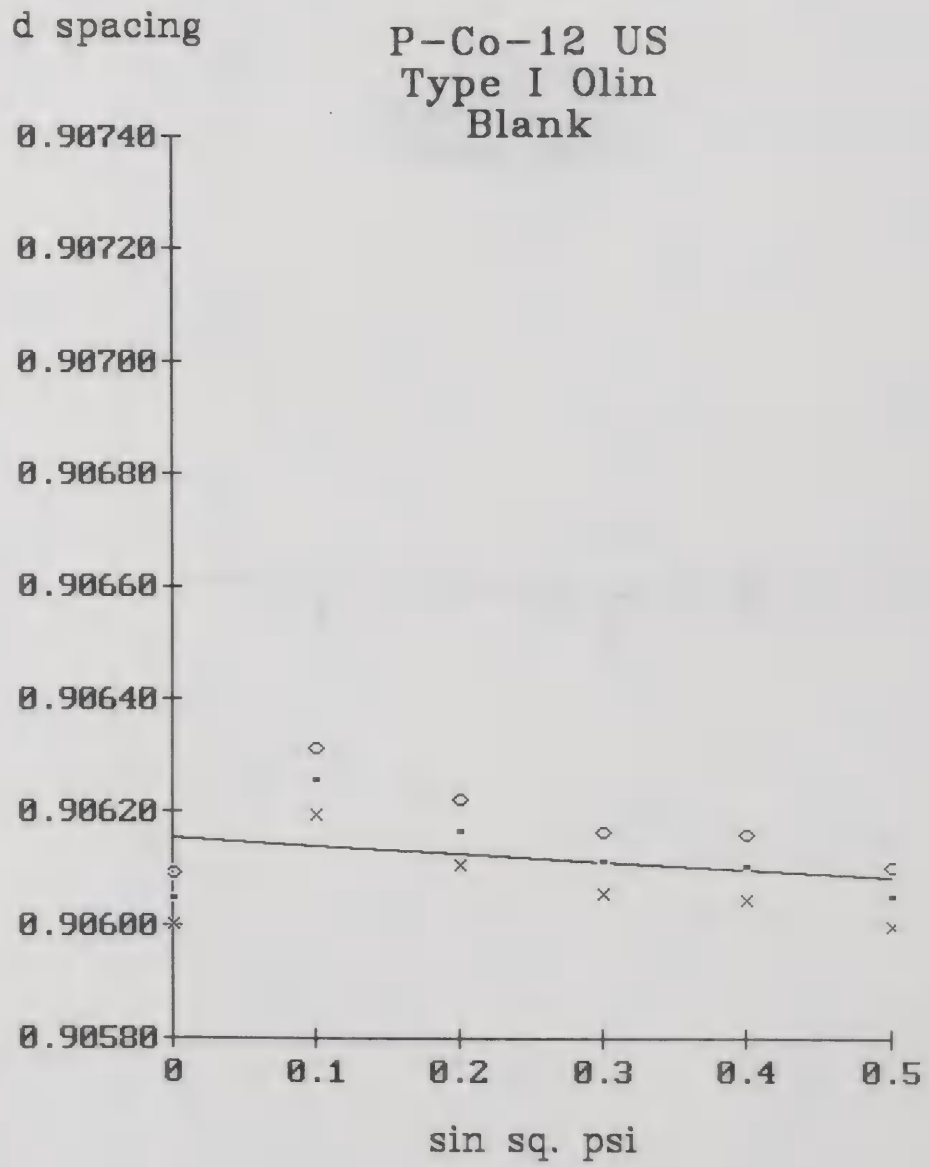

Figure 55. A plot of the d spacing versus $\sin^2$ psi, using cobalt radiation, taken on the Olin. "Type I" one cent blank.
(#P-Co-12).

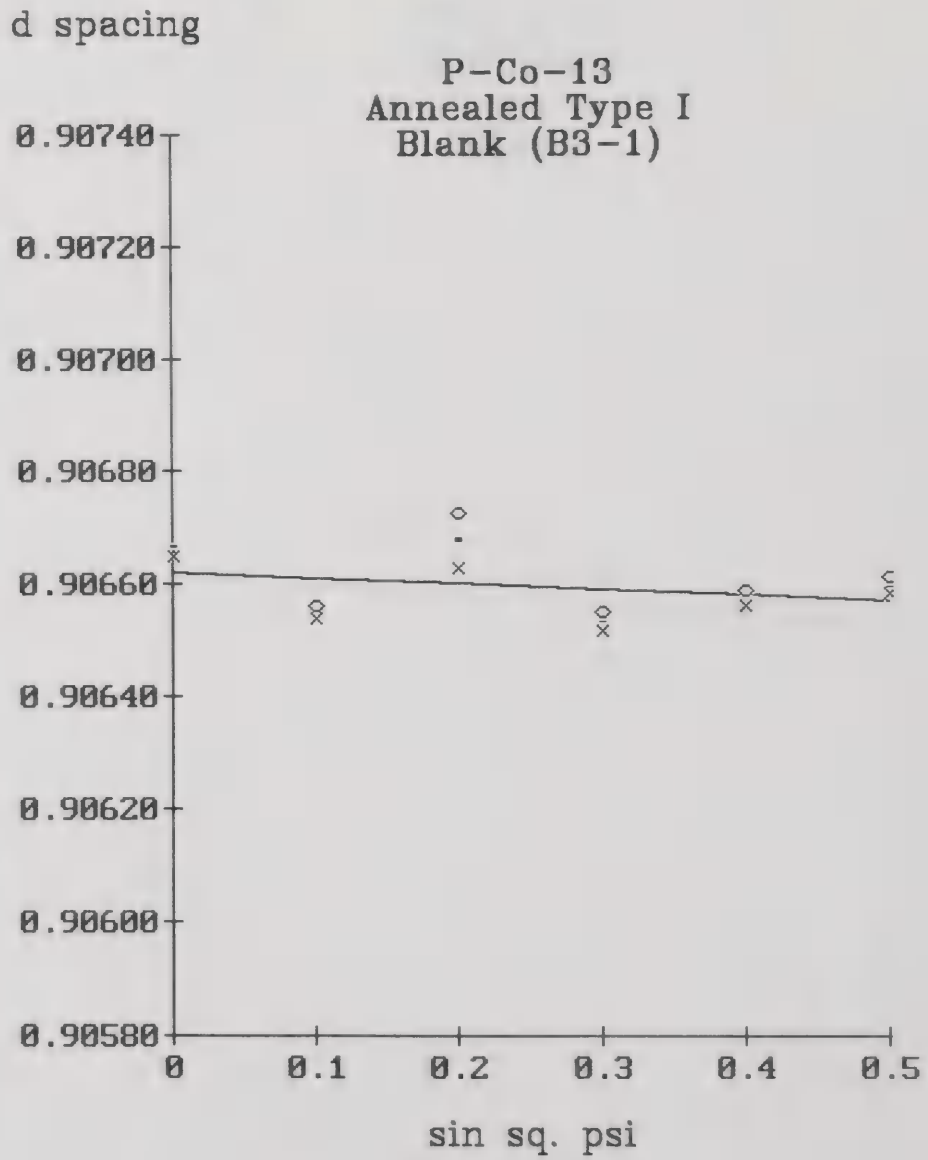

Figure 56. A plot of the d spacing versus $\sin^2$ psi, using cobalt radiation, taken on the U.S. "Type I" one cent blank (#B3-1), which had been annealed at 514 ^{o}C for 20 minutes.
(#P-Co-13).

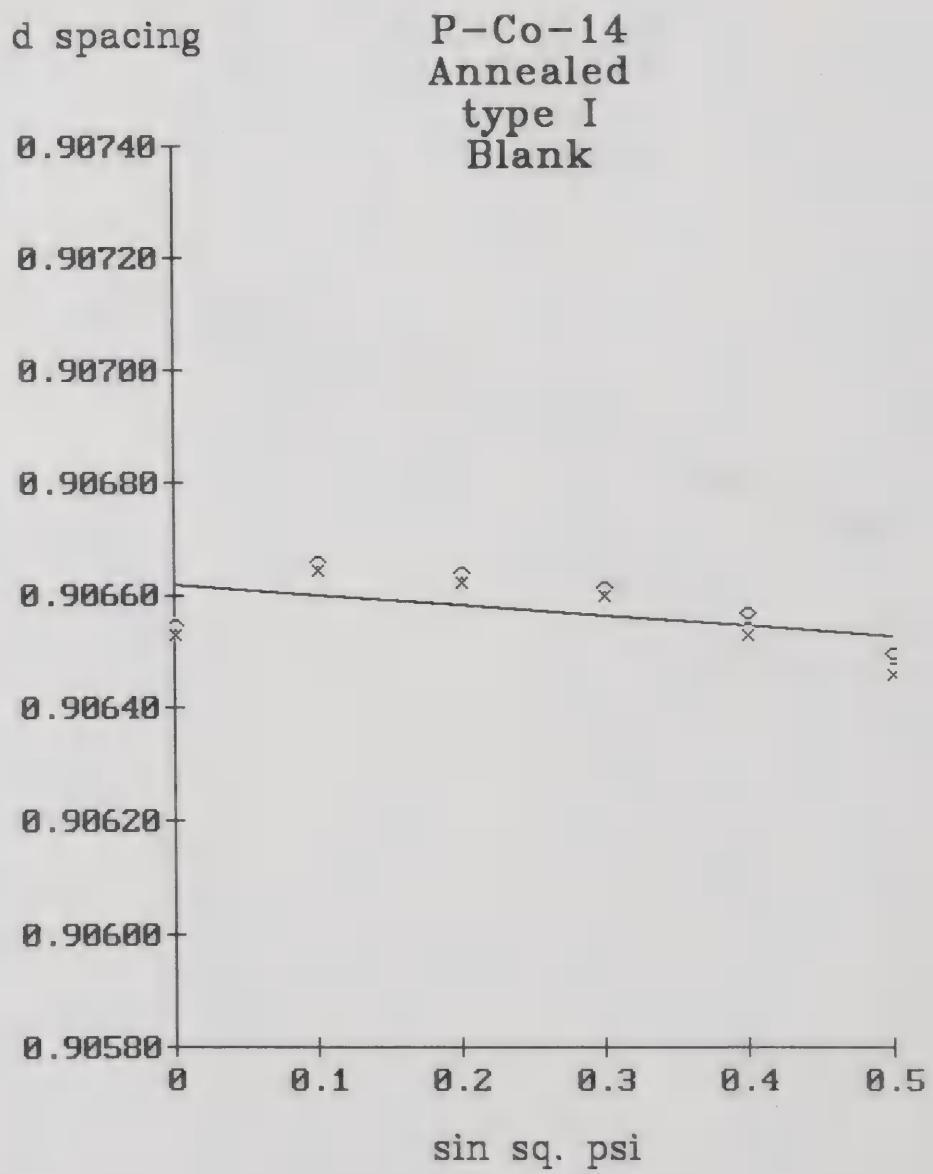

Figure 57. A plot of the d spacing versus $\sin^2$ psi, using cobalt radiation, taken on the U.S. "Type I" one cent blank, which had been annealed at 514 ^{o}C for 20 minutes. (#P-Co-14).

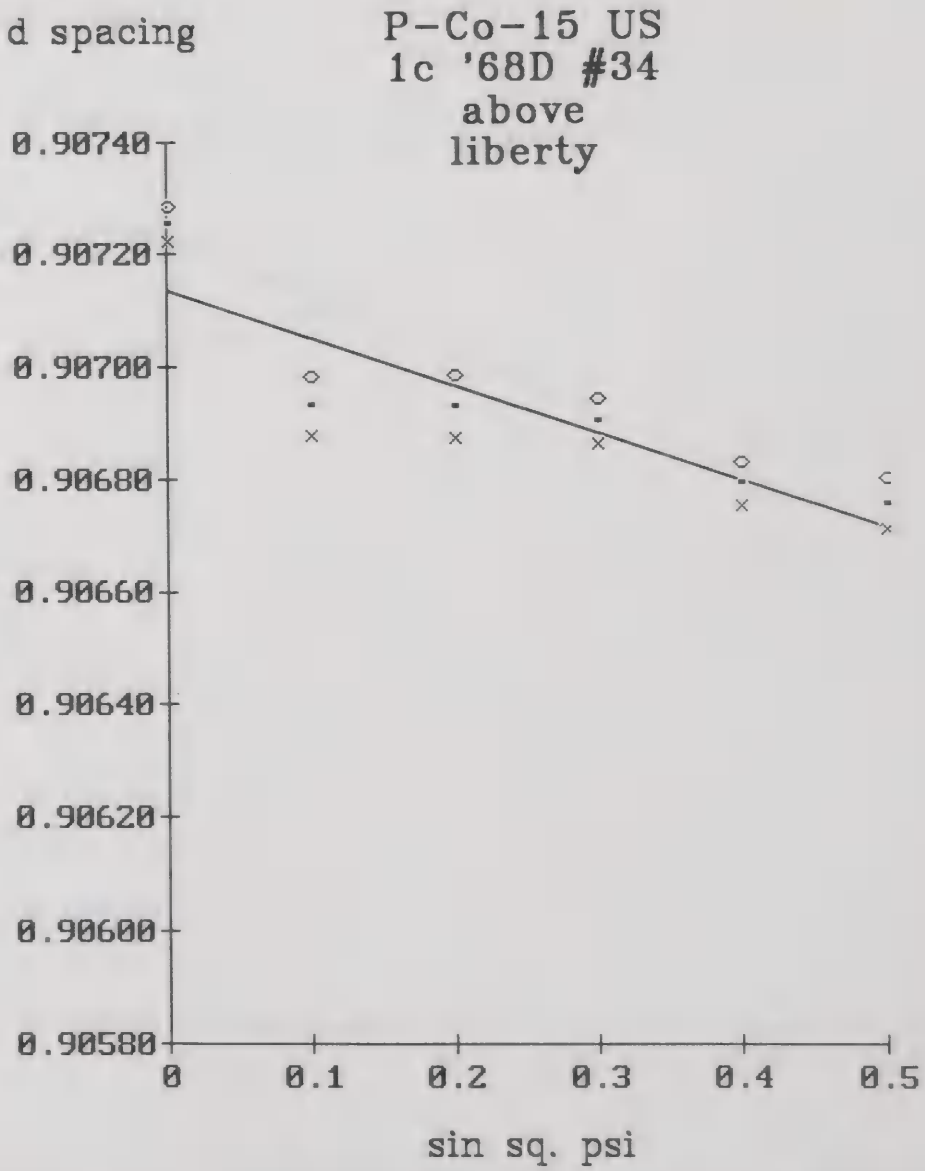

Figure 58. A plot of the d spacing versus $\sin^2$ psi, using cobalt radiation, taken on the 1968 D mint issue U.S. one cent piece (#34) located above the liberty of the design. (#P-Co-15).

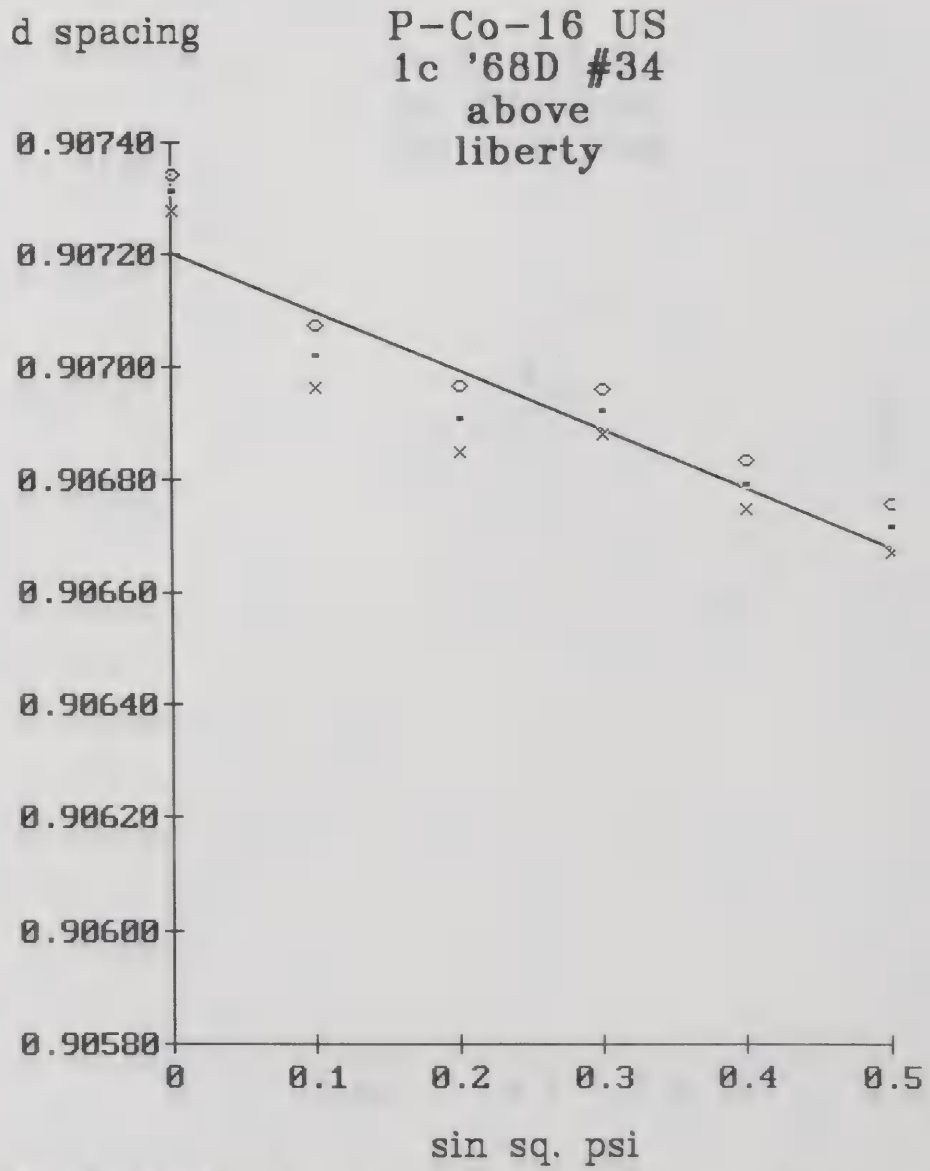

Figure 59 A plot of the d spacing versus $\sin^2$ psi, using cobalt radiation, taken on the 1968 D mint issue U.S. one cent piece (#34) located above the liberty of the design. (#P-Co-16)

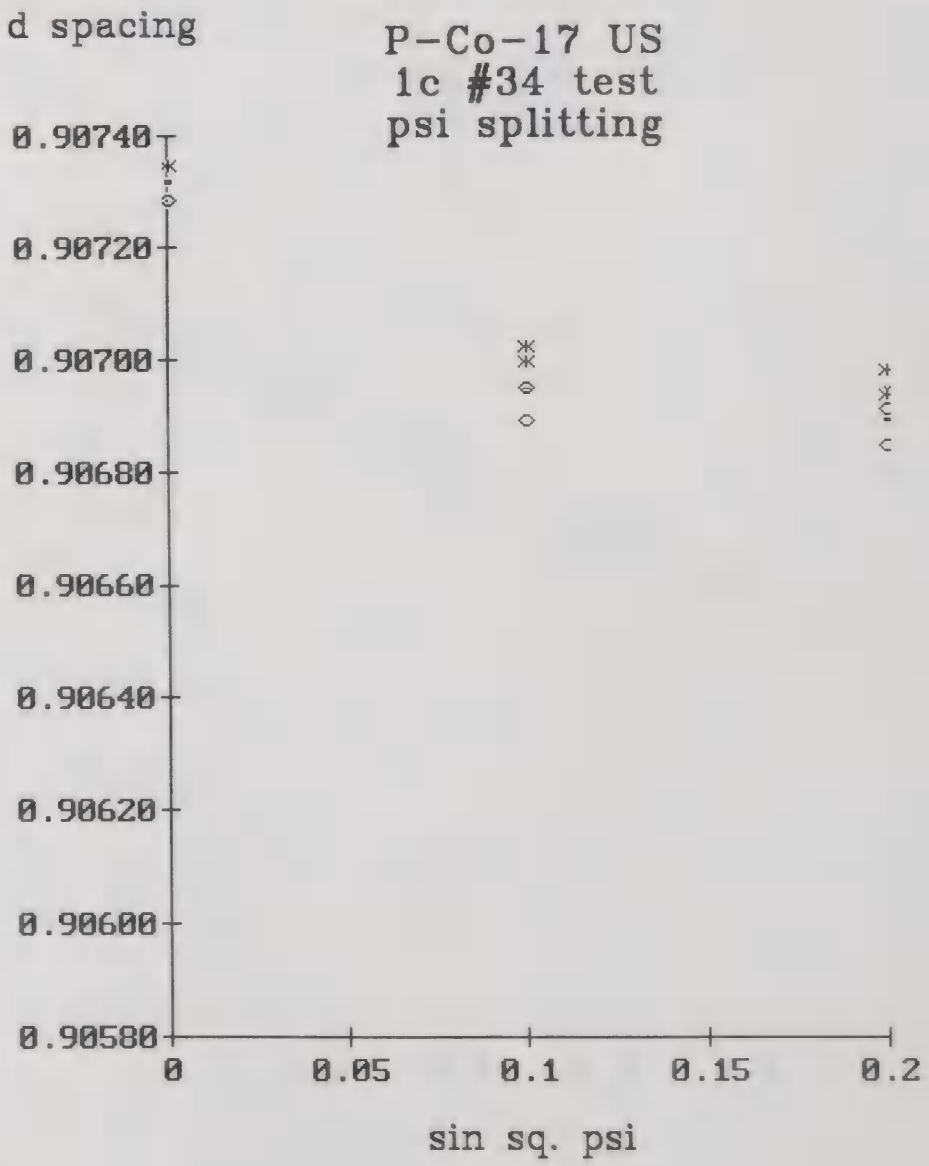

Figure 60. A plot of the d spacing versus the $\sin^2$ psi, using cobalt radiation, taken on the D mint issue U.S. one cent piece (#34) to determine the presence of psi splitting. (#P-Co-17).

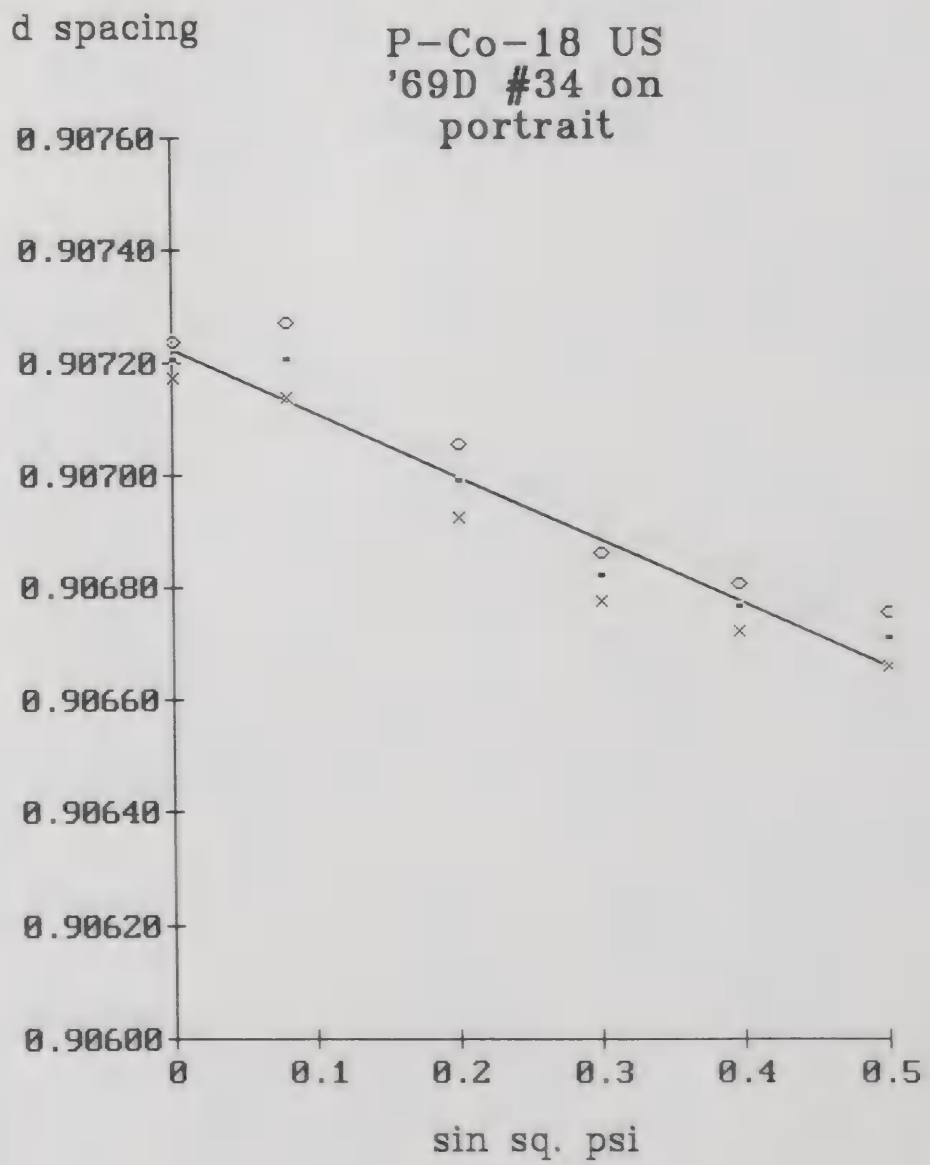

Figure 61. A plot of the d spacing versus $\sin^2$ psi, using cobalt radiation, taken on the 1968 D mint issue U.S. one cent piece (#34) located on the portrait of the design. (#P-Co-18).

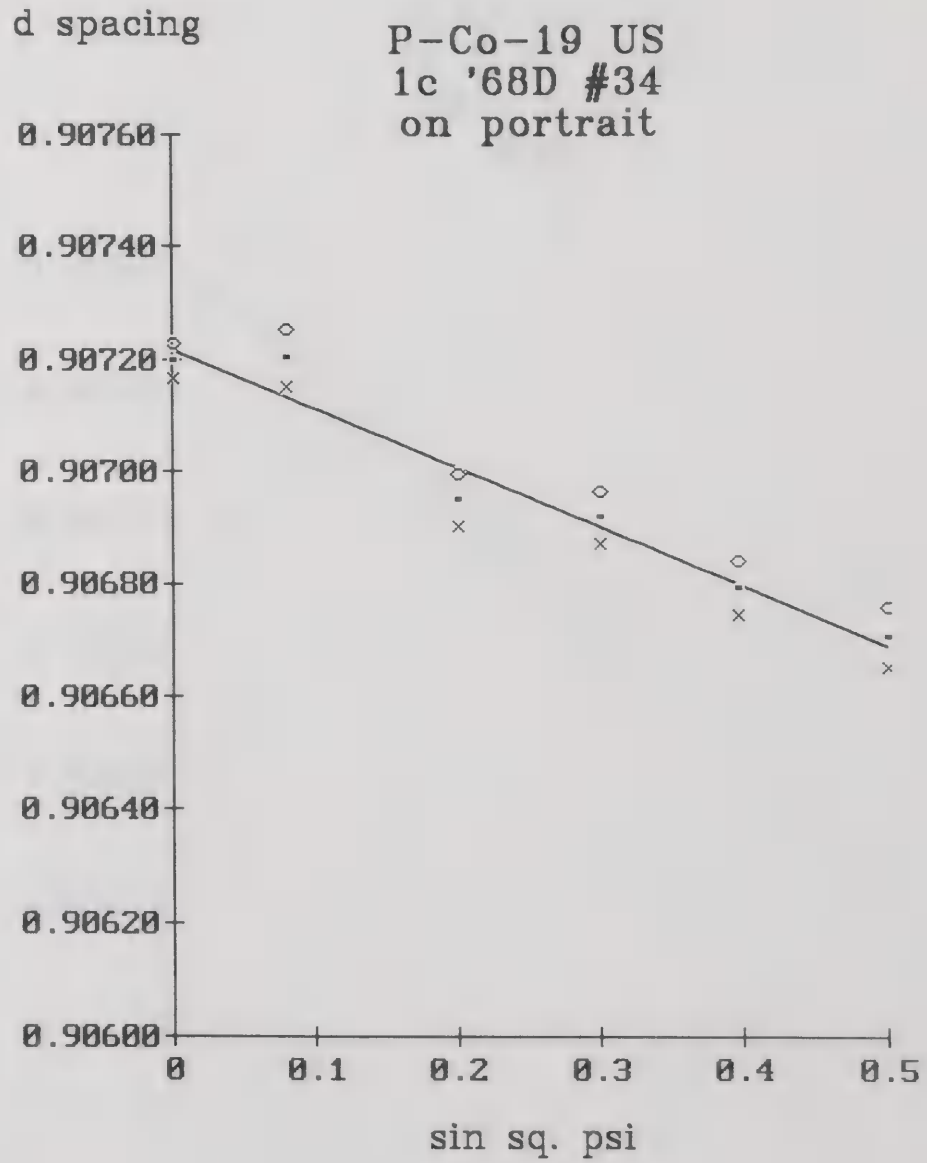

Figure 62. A plot of the d spacing versus $\sin^2$ psi, using cobalt radiation, taken on the 1968 D mint issue U.S. one cent piece (#34) located on the portrait of the design. (#P-Co-19).

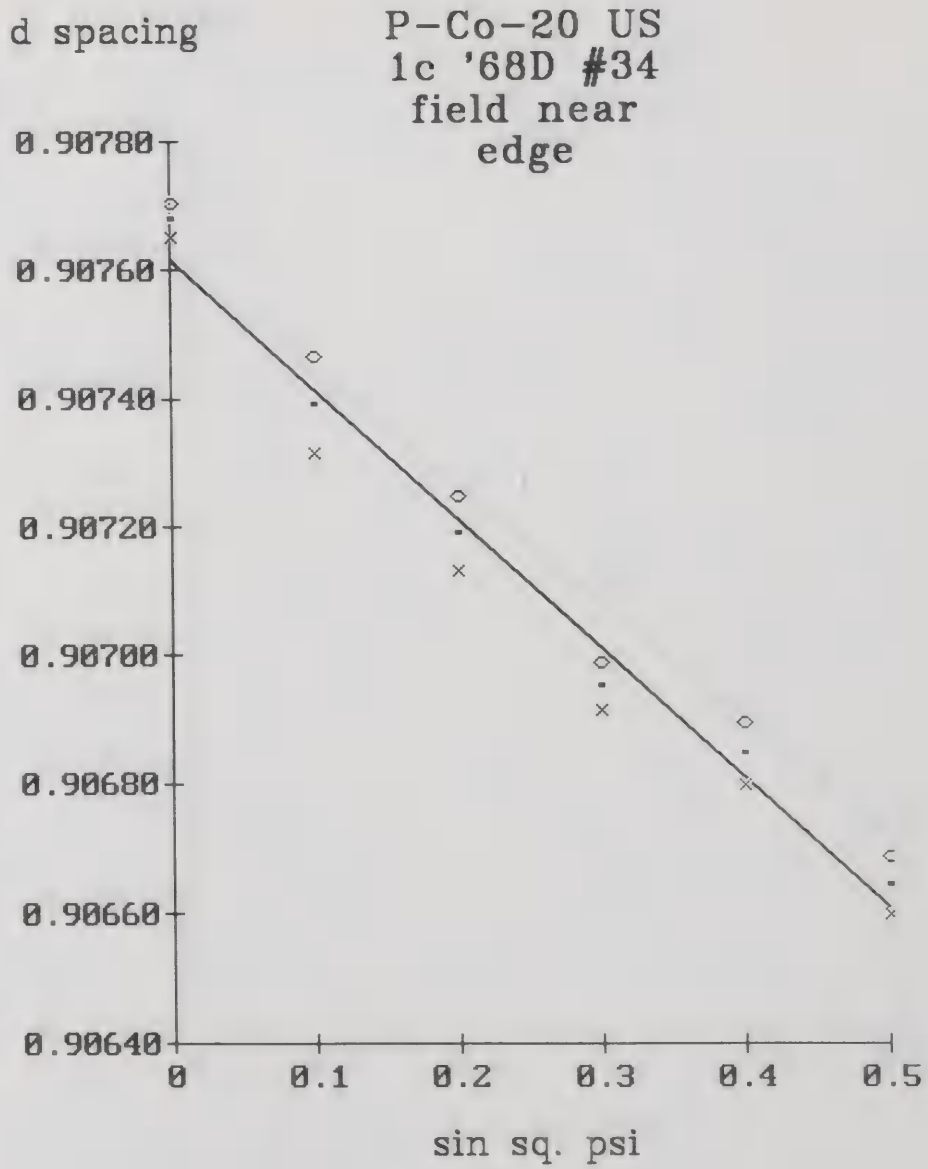

Figure 63. A plot of the d spacing versus $\sin^2$ psi, using cobalt radiation, taken on the 1968 D mint issue U.S. one cent piece (#34) located on the field near the edge of the coin.
(#P-Co-20).

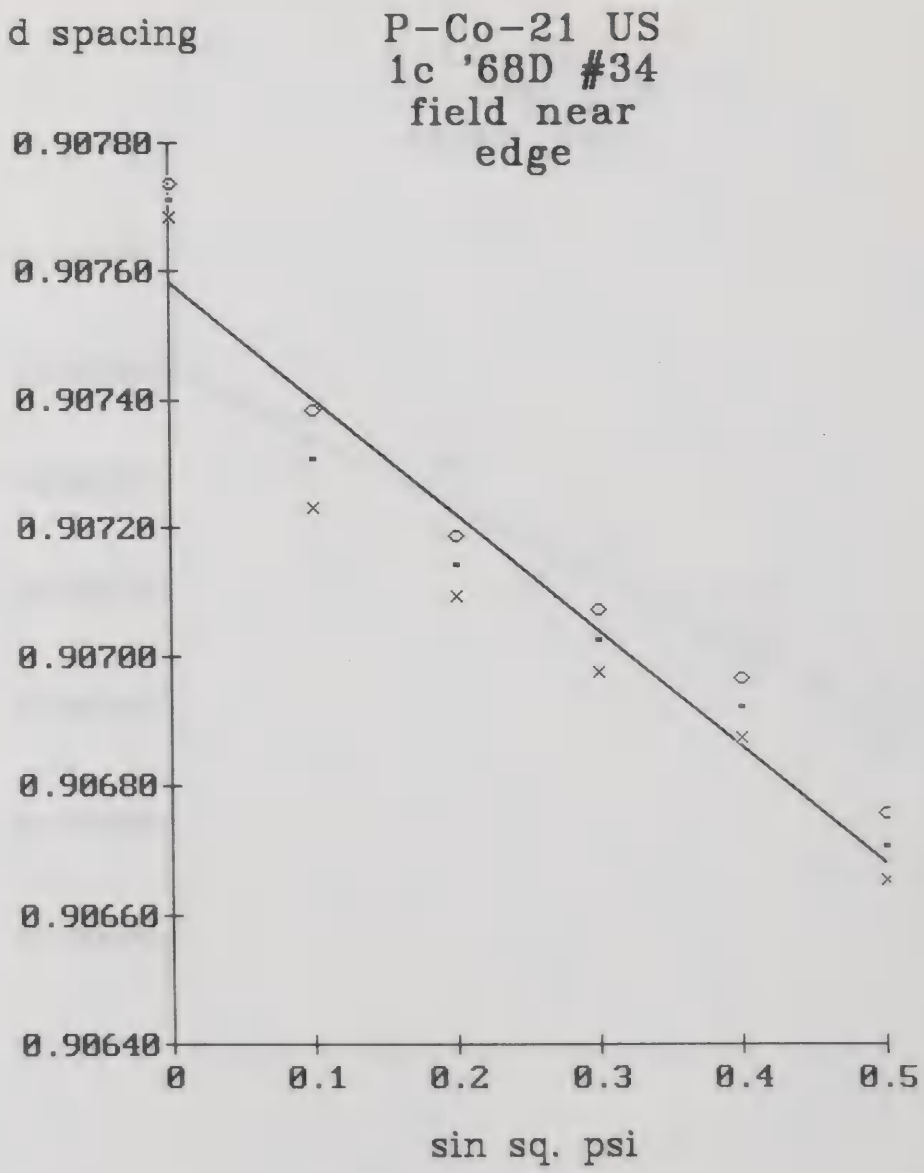

Figure 64. A plot of the d spacing versus $\sin^2$ psi, using cobalt radiation, taken on the 1968 D mint issue U.S. one cent piece (#34) located on the field near the edge of the coin.
(#P-Co-21).

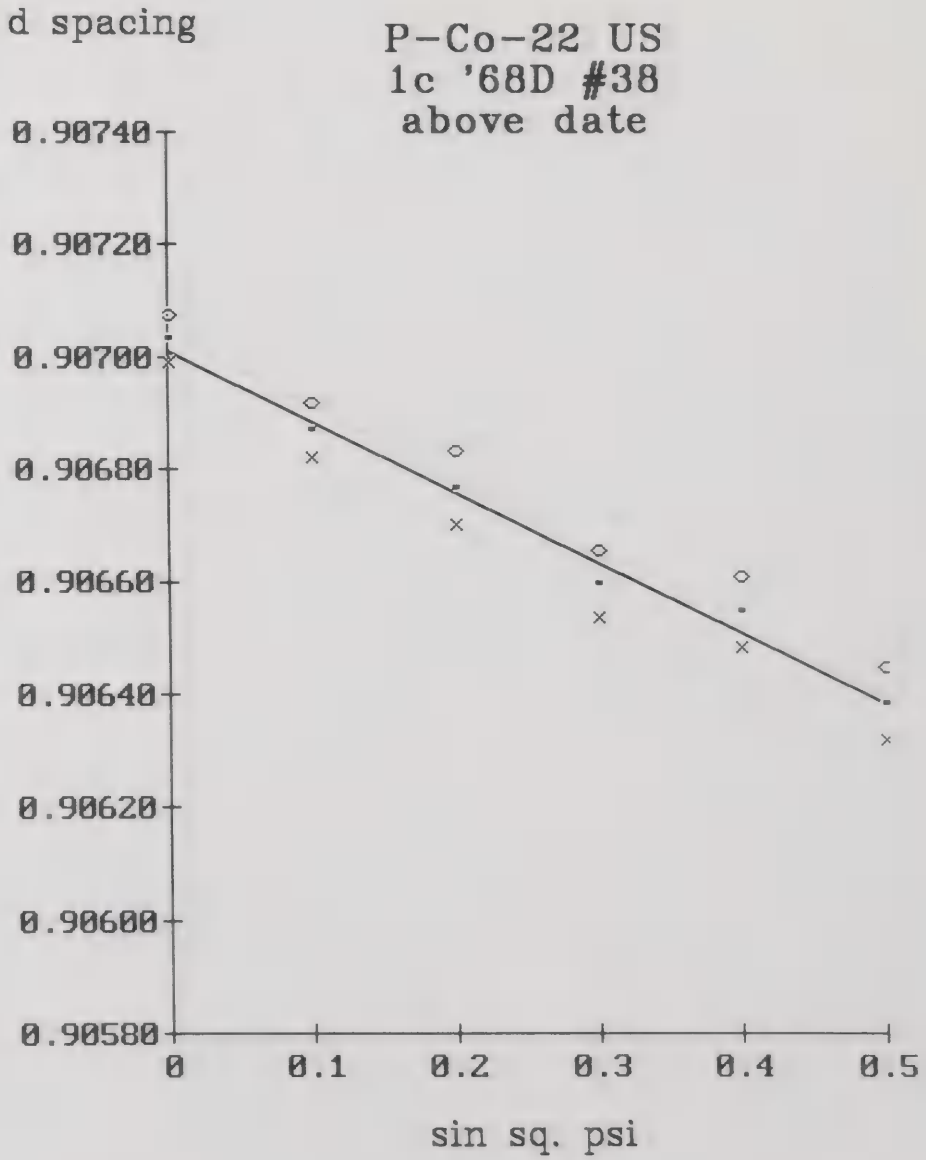

Figure 65. A plot of the d spacing versus $\sin^2$ psi, using cobalt radiation, taken on the 1968 D mint issue U.S. one cent piece (#38) located above the date of the design. (#P-Co-22).

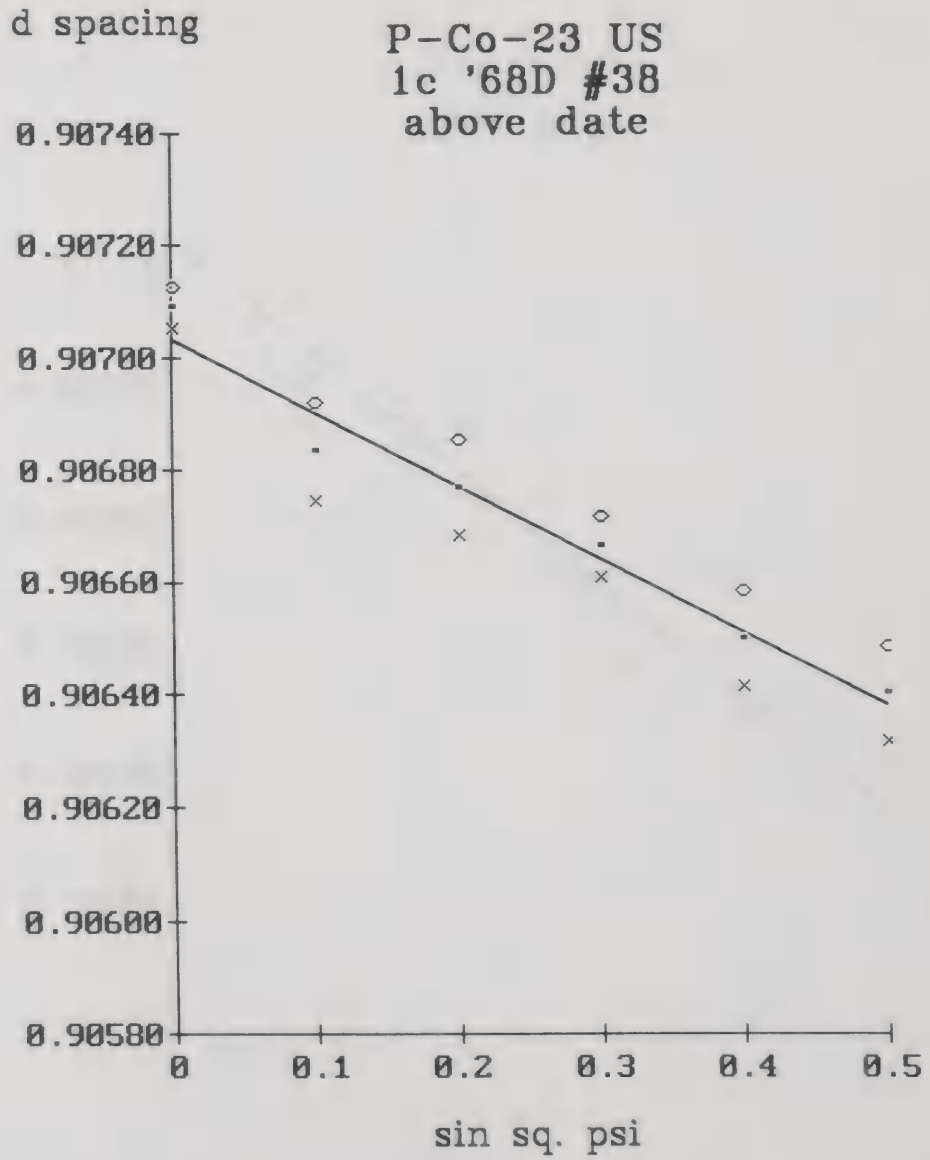

Figure 66 A plot of the d spacing versus $\sin^2$ psi, using cobalt radiation, taken on the 1968 D mint issue U.S. one cent piece (#38) located above the date of the design. (#P-Co-23).

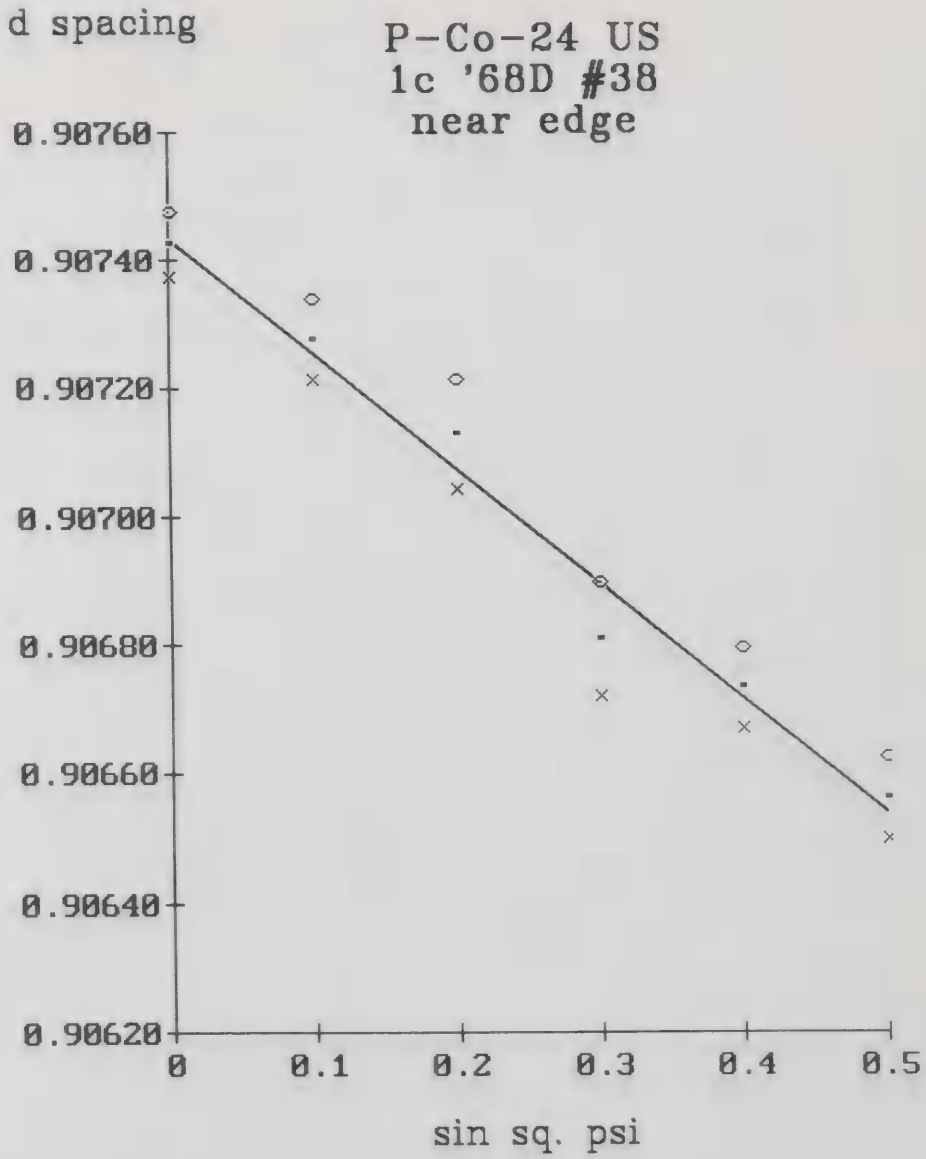

Figure 67. A plot of the d spacing versus $\sin^2$ psi, using cobalt radiation, taken on the 1968 D mint issue U.S. one cent piece (#38) located on the field near the edge of the coin.
(#P-Co-24).

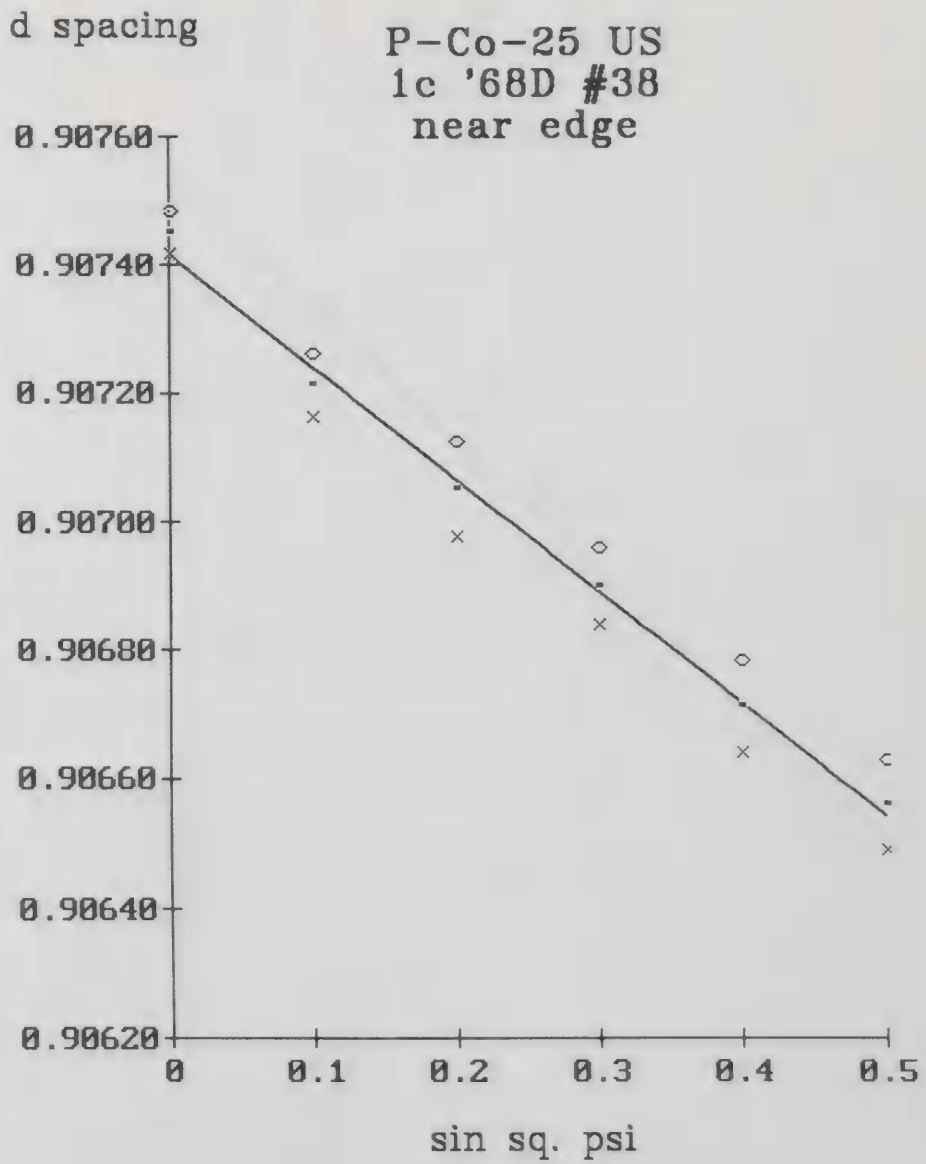

Figure 68. A plot of the d spacing versus $\sin^2$ psi, using cobalt radiation, taken on the 1968 D mint issue U.S. one cent piece (#38) located on the field near the edge of the coin.
(#P-Co-25).

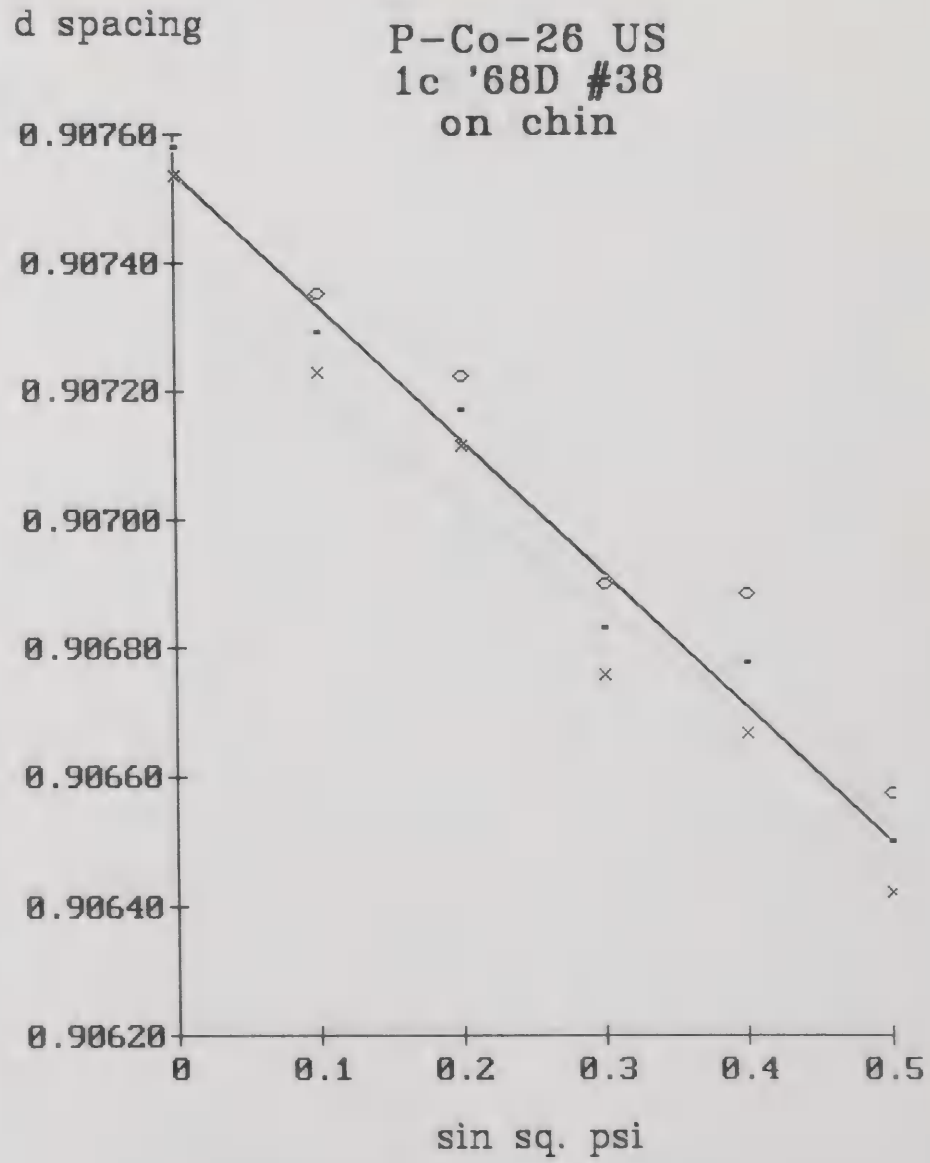

Figure 69 A plot of the d spacing versus $\sin^2$ psi, using cobalt radiation, taken on the 1968 D mint issue U.S. one cent piece (#38) located on the chin of the portrait on the coin.
(#P-Co-26).

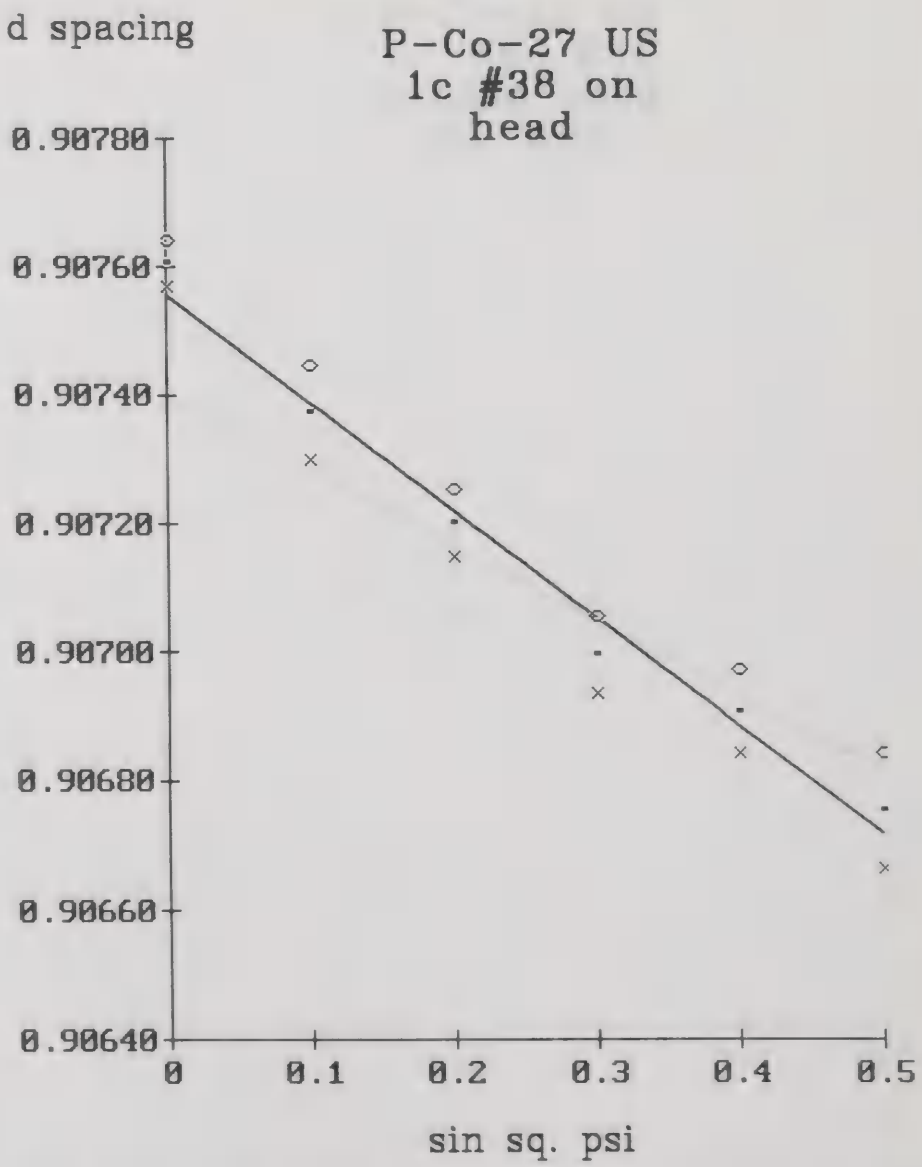

Figure 70 A plot of the d spacing versus $\sin^2$ psi, using cobalt radiation, taken on the 1968 D mint issue U.S. one cent piece (#38) located on the head of the portrait on the coin.
(#P-Co-27).

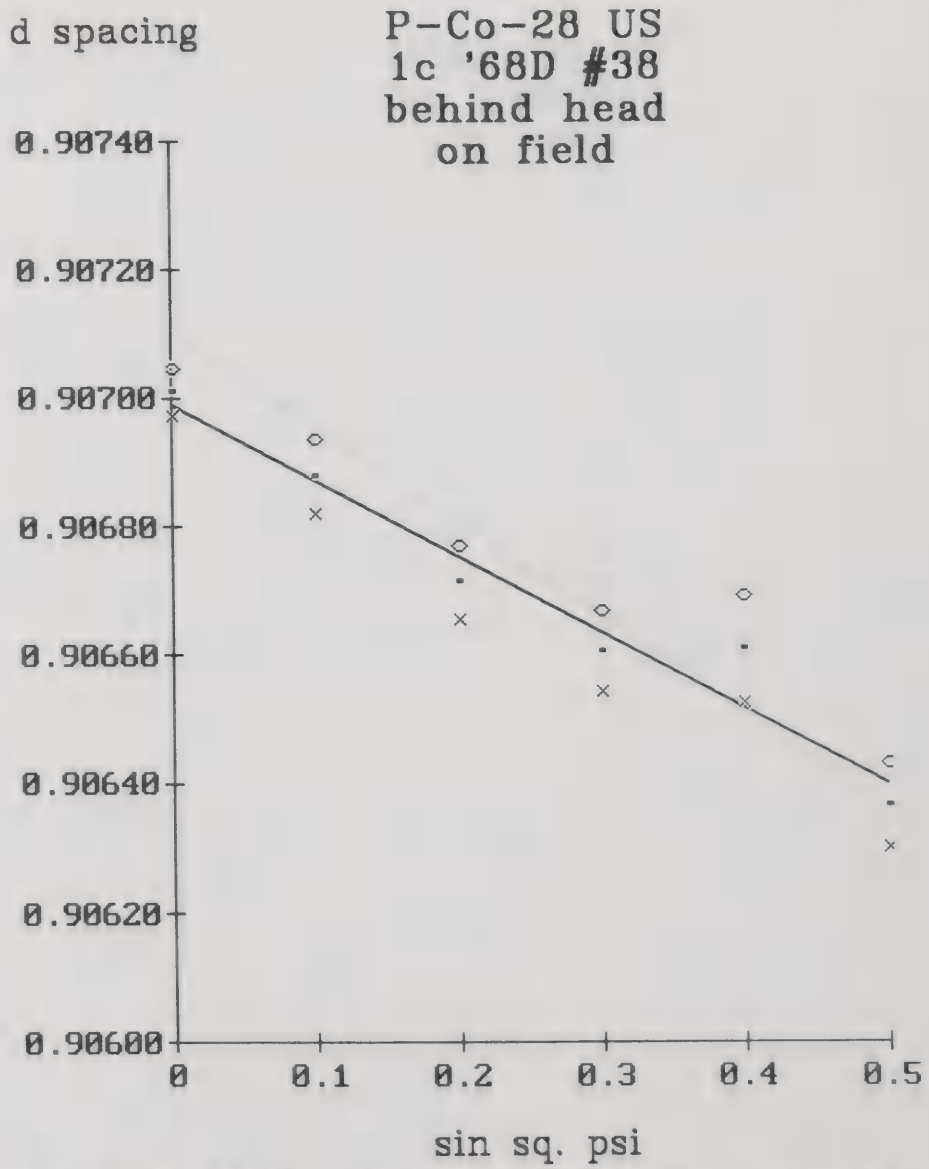

Figure 71. A plot of the d spacing versus $\sin^2$ psi, using cobalt radiation, taken on the 1968 D mint issue U.S. one cent piece (#38) located on ton the field behind the portrait on the coin.
(#P-Co-28).

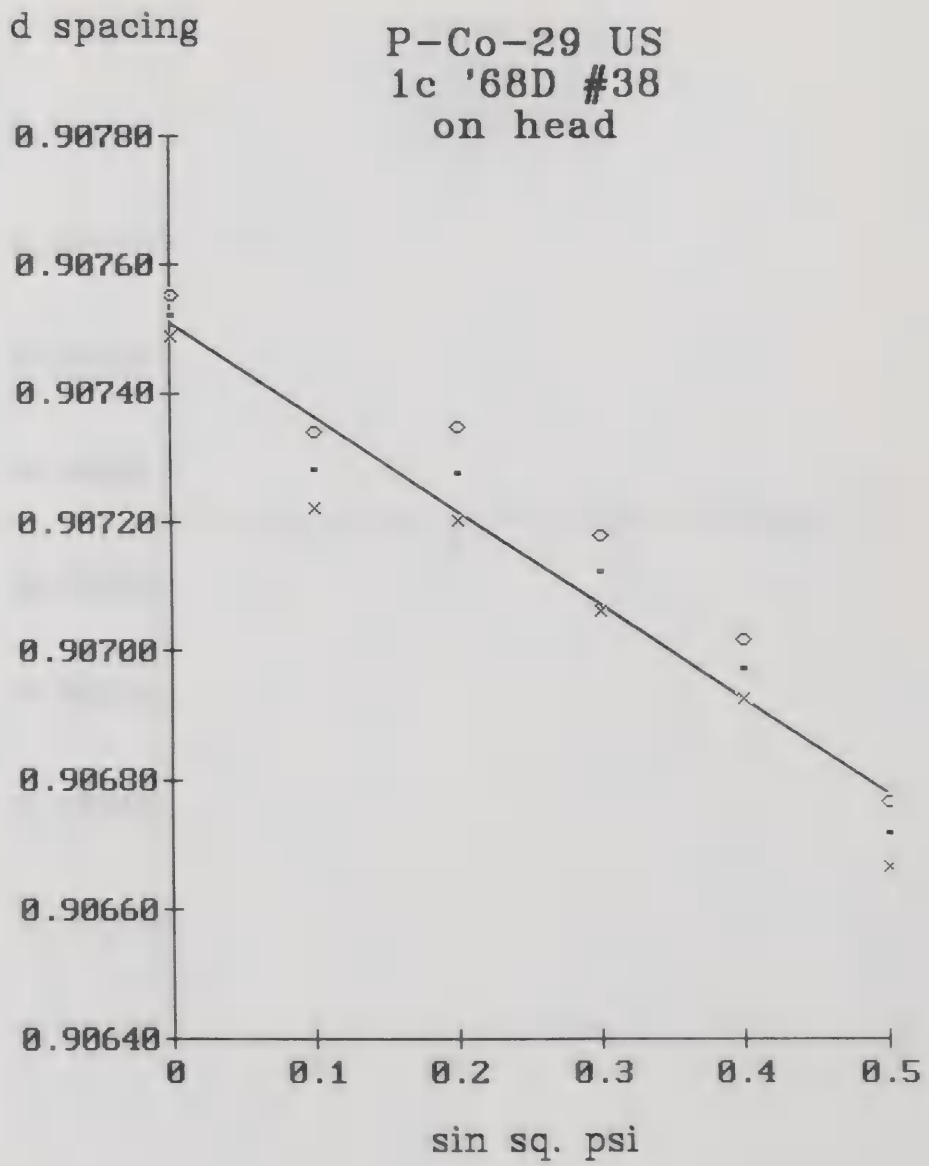

Figure 72. A plot of the d spacing versus $\sin^2$ psi, using cobalt radiation, taken on the 1968 D mint issue U.S. one cent piece (#38) located on the head of the portrait on the coin.
(#P-Co-29).

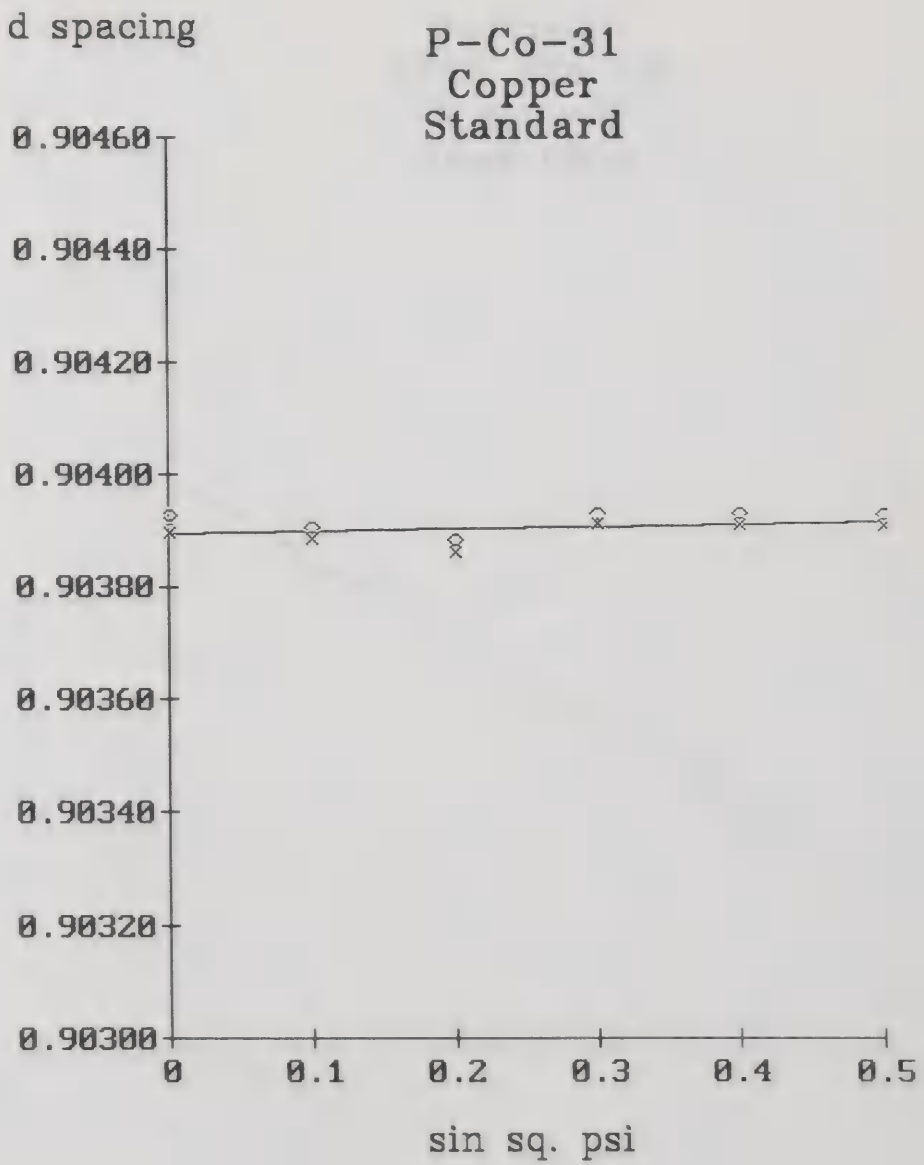

Figure 73. A plot of the d spacing versus $\sin^2$ psi, using cobalt radiation, taken on a stress free powdered copper standard.
(#P-Co-31).

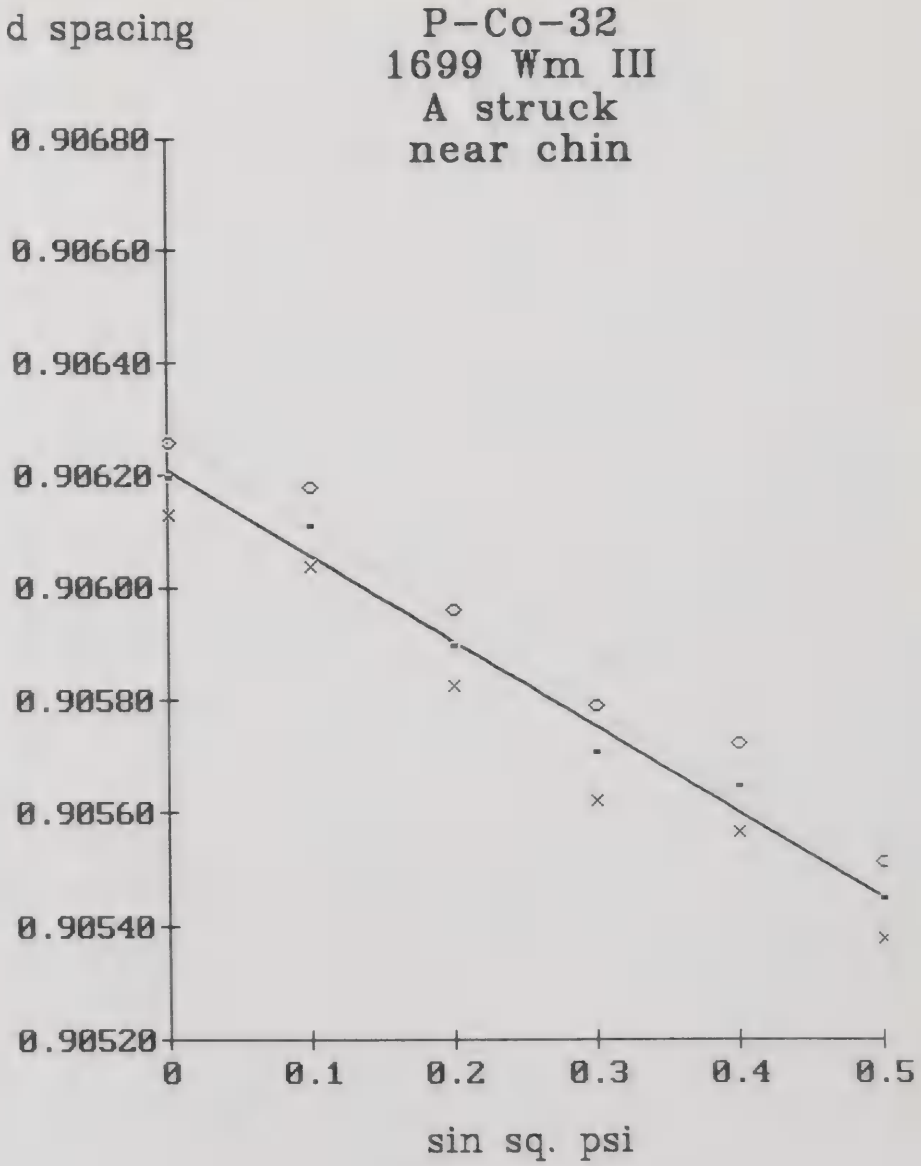

Figure 74. A plot of the d spacing versus $\sin^2$ psi, using cobalt radiation, taken on the 1699 (A) struck William III halfpenny, located near the chin. (#P-Co-32).

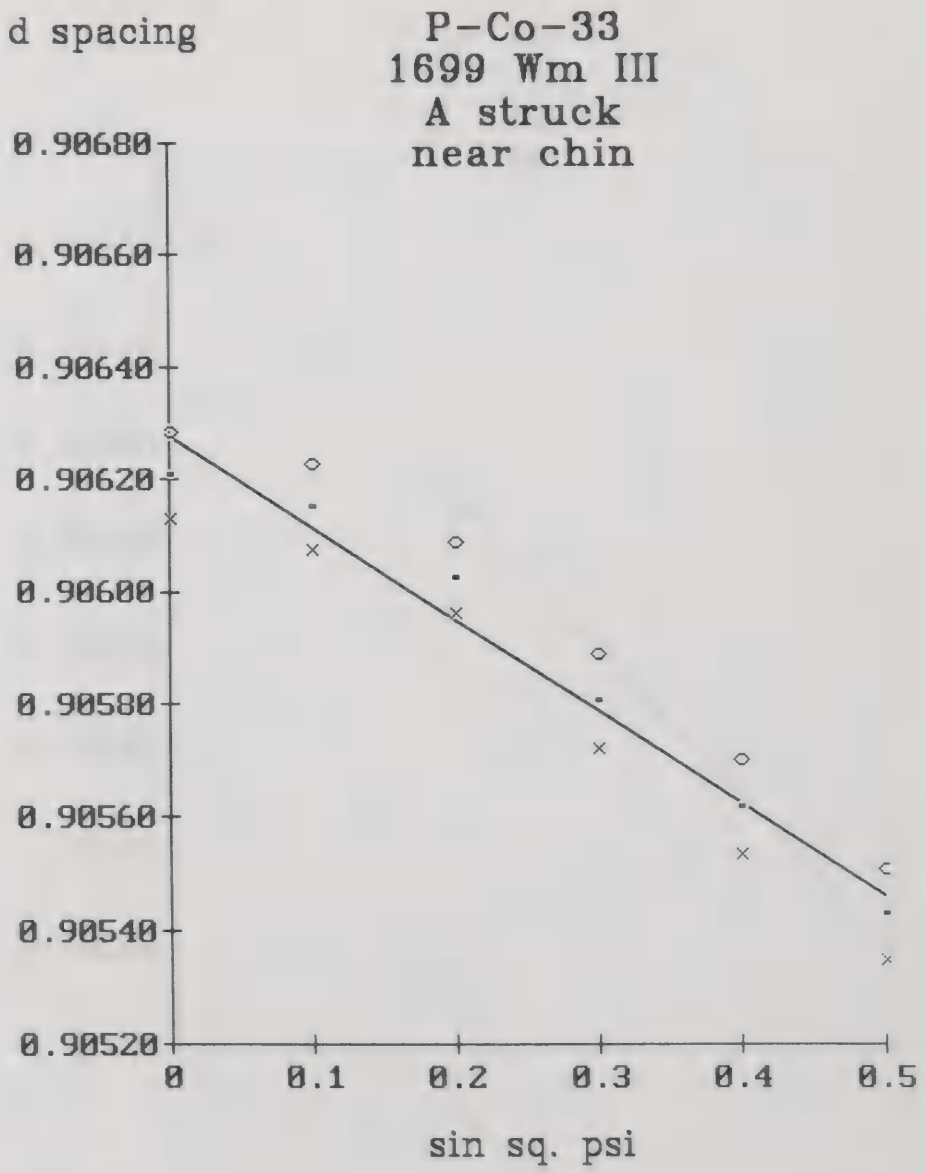

Figure 75 A plot of the d spacing versus $\sin^2$ psi, using cobalt radiation, taken on the 1699 (A) struck William III halfpenny, located near the chin. (#P-Co-33).

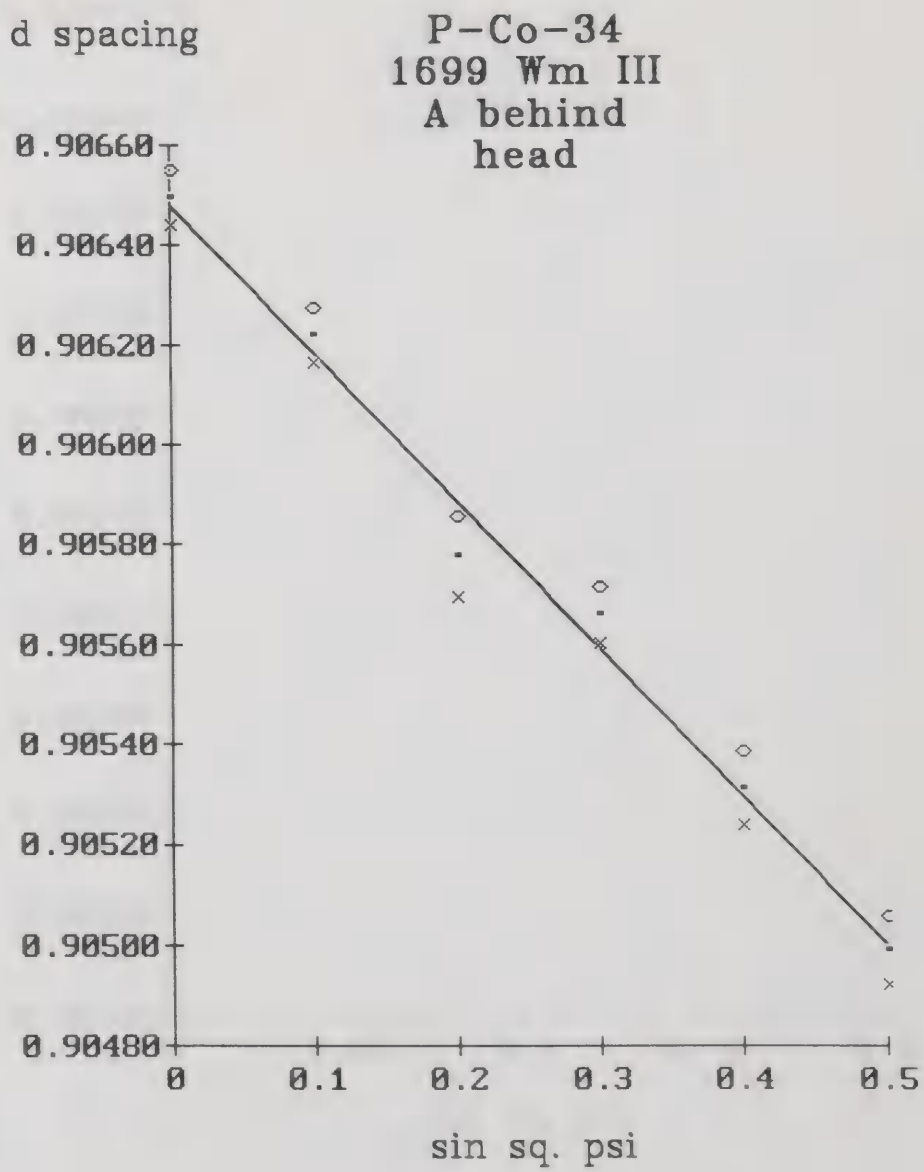

Figure 76. A plot of the d spacing versus $\sin^2$ psi, using cobalt radiation, taken on the 1699 (A) struck William III halfpenny, located behind the head of the portrait. (#P-Co-34).

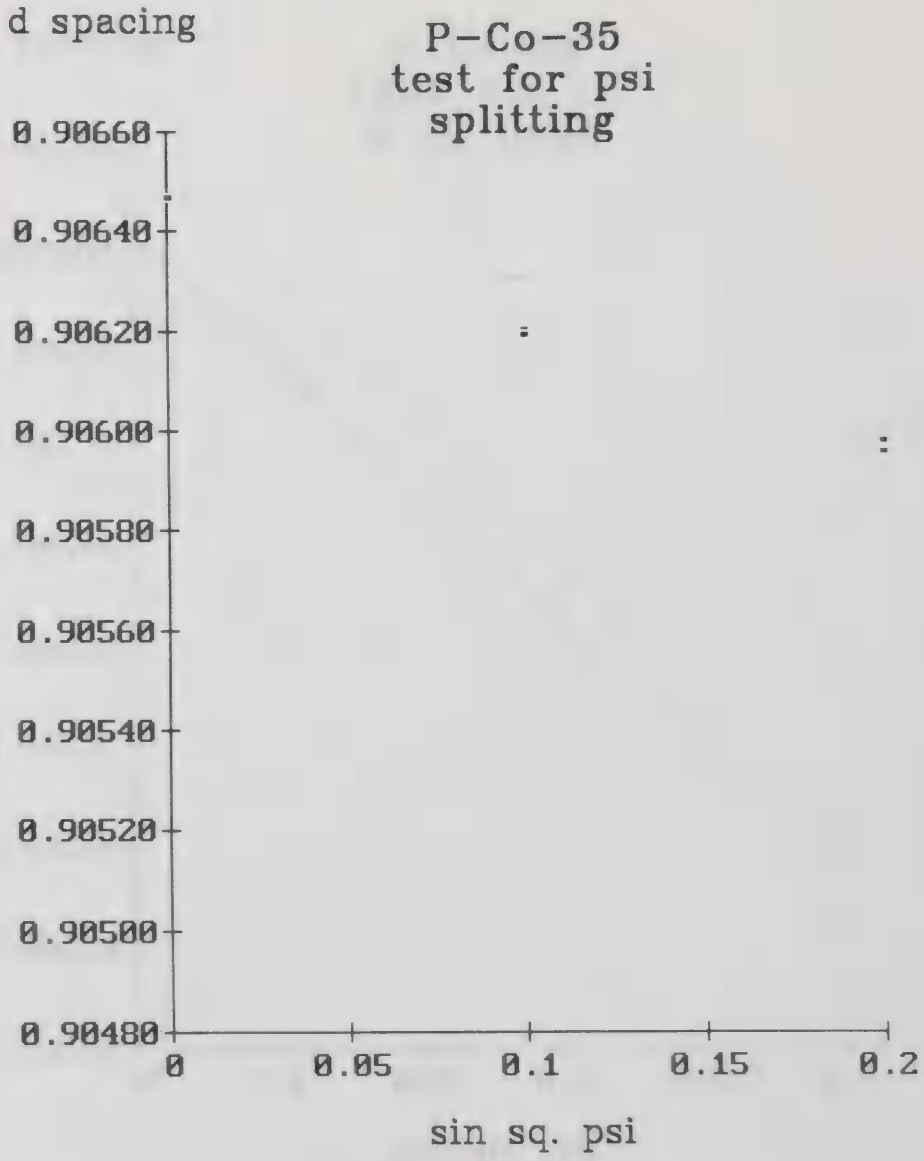

Figure 77. A plot of the d spacing versus the $\sin^2$ psi, using cobalt radiation, taken on the 1699 (A) struck William III halfpenny, located behind the head of the portrait, to determine the presence of psi splitting.
(#P-Co-35).

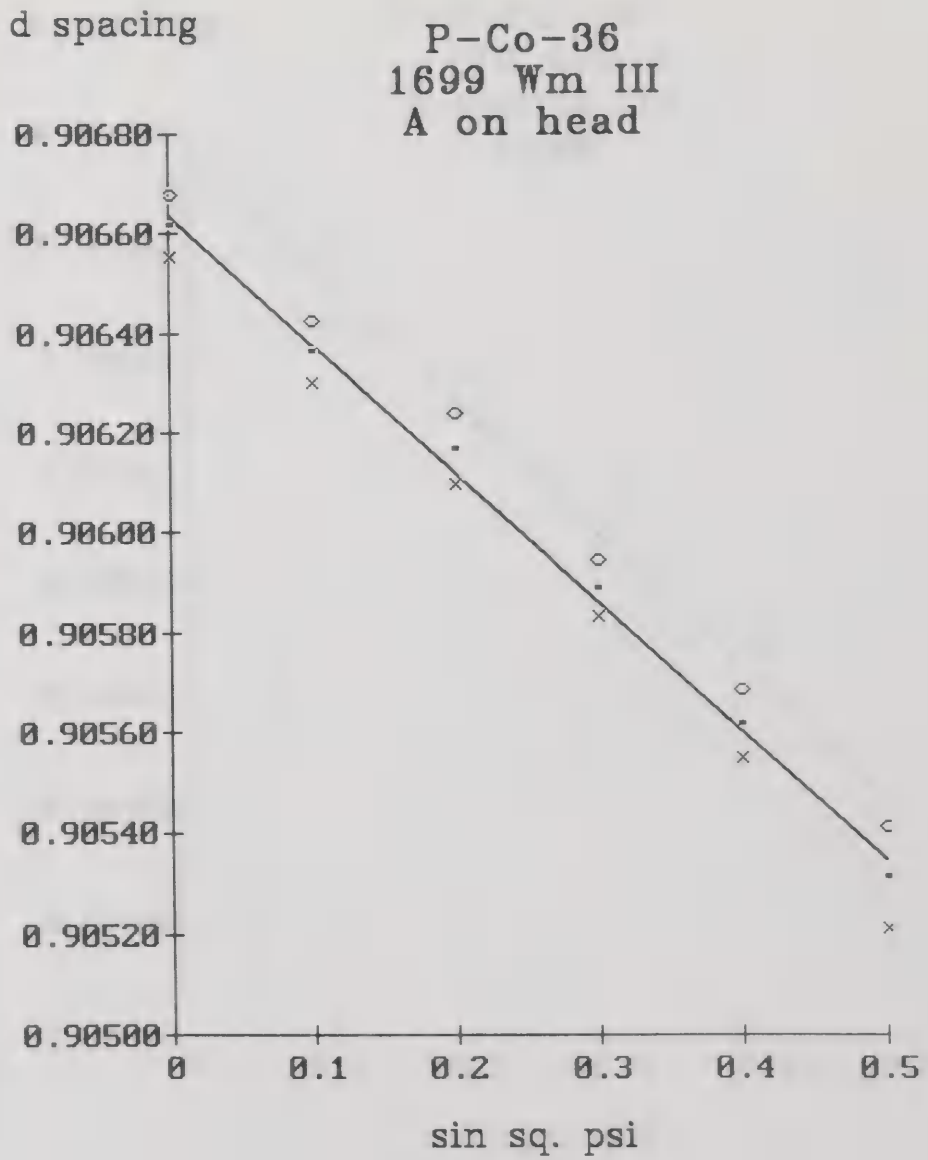

Figure 78. A plot of the d spacing versus $\sin^2$ psi, using cobalt radiation, taken on the 1699 (A) struck William III halfpenny, located on the head of the portrait. (#P-Co-36).

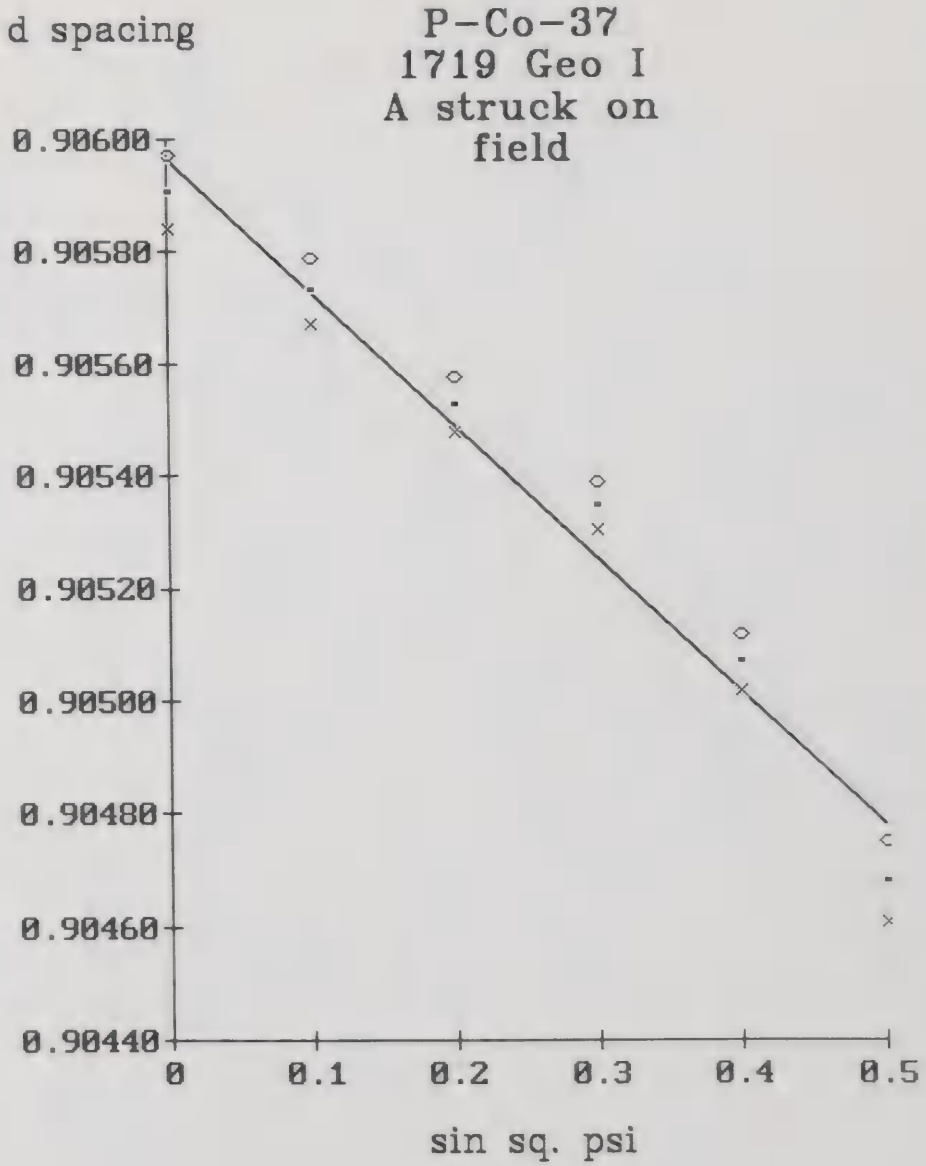

Figure 79. A plot of the d spacing versus $\sin^2$ psi, using cobalt radiation, taken on the 1719 (A) struck George I halfpenny, located on the field of the coin (#P-Co-37).

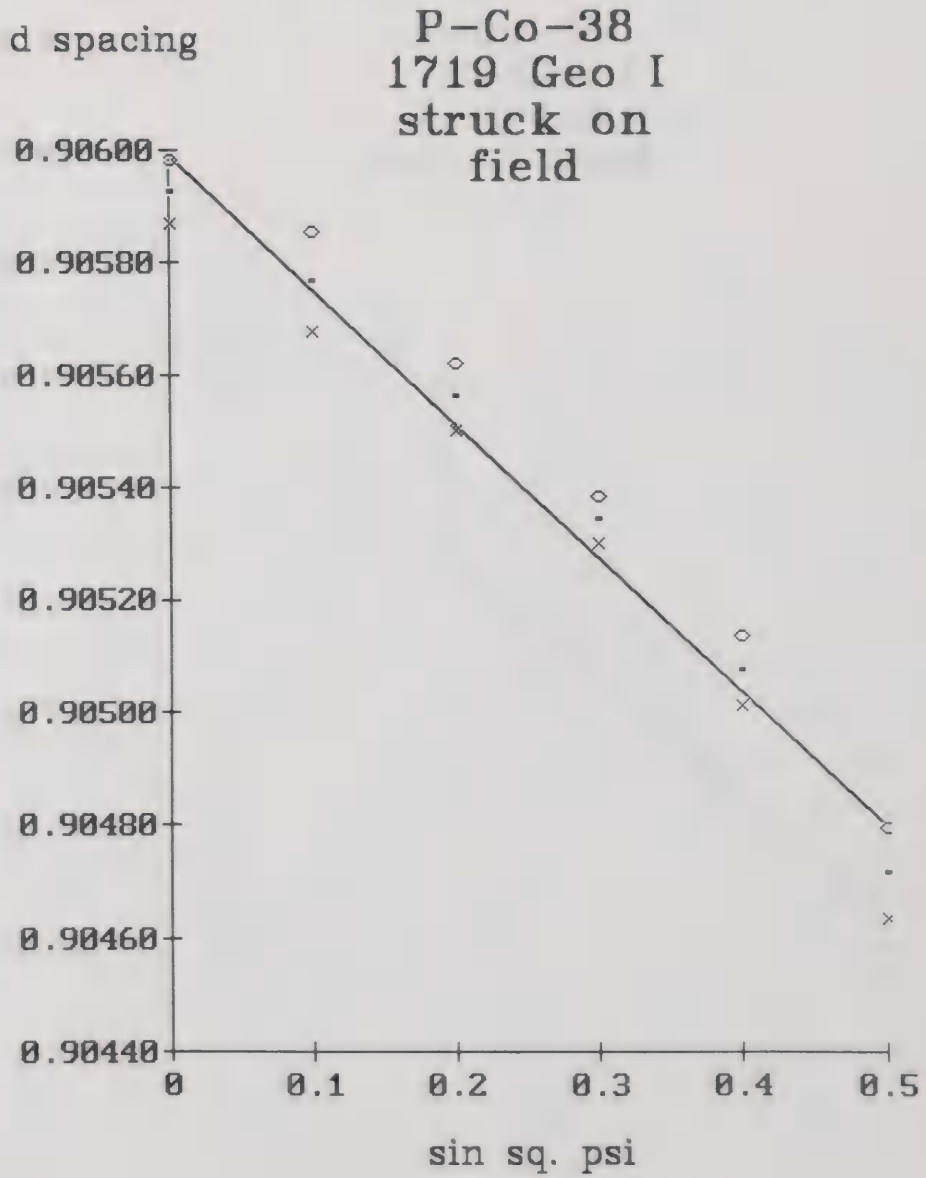

Figure 80 A plot of the d spacing versus $\sin^2$ psi, using cobalt radiation, taken on the 1719 (A) struck George I halfpenny, located on the field of the coin (#P-Co-38).

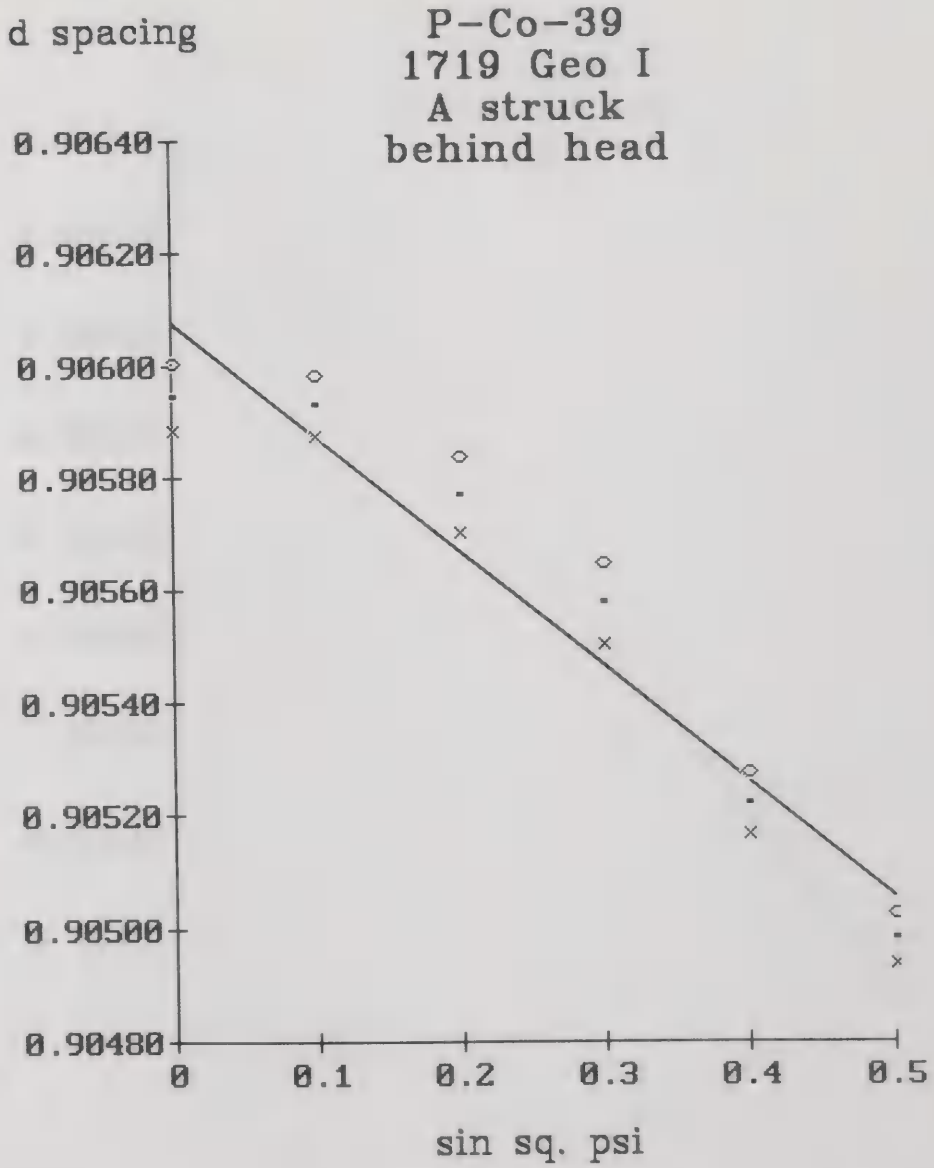

Figure 81. A plot of the d spacing versus $\sin^2$ psi, using cobalt radiation, taken on the 1719 (A) struck George I halfpenny, located behind the head of the portrait (#P-Co-39).

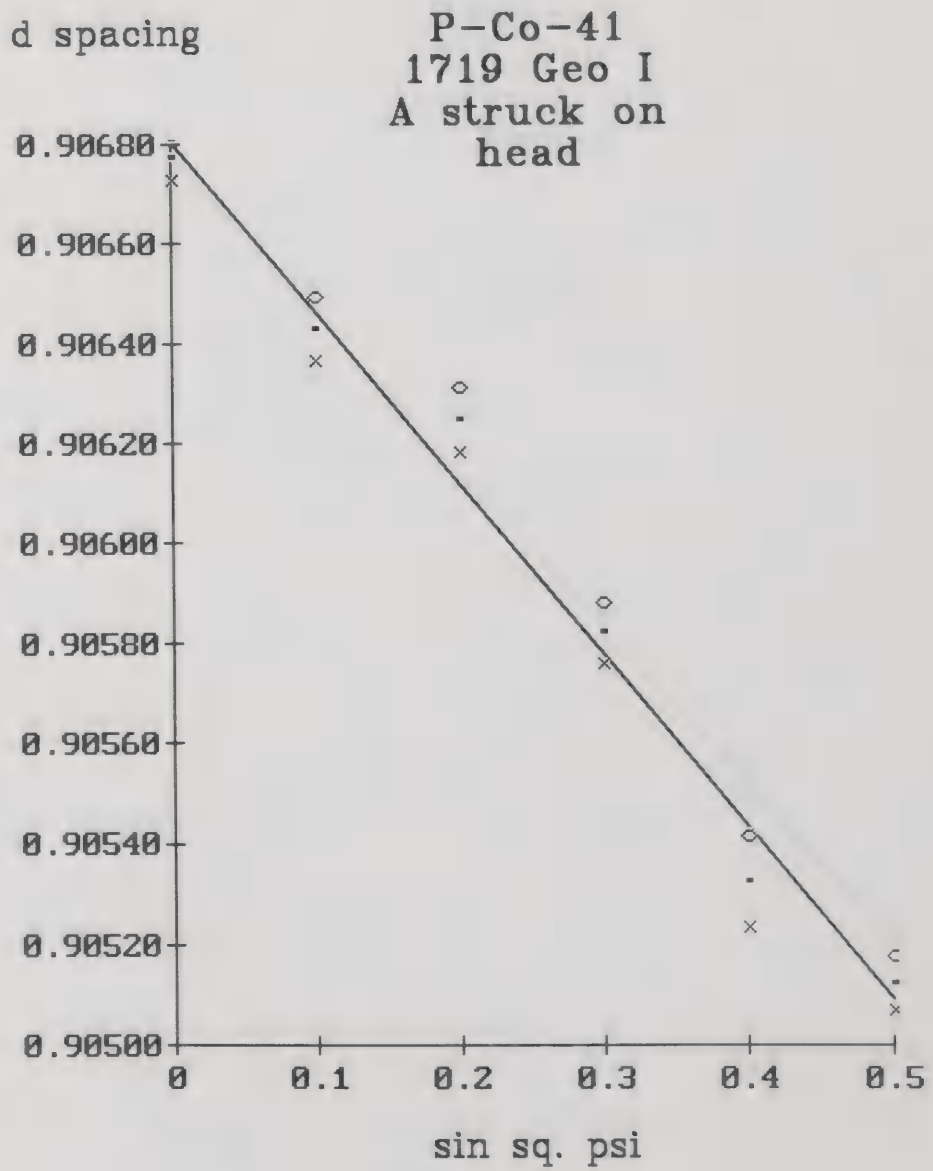

Figure 82. A plot of the d spacing versus $\sin^2$ psi, using cobalt radiation, taken on the 1719 (A) struck George I halfpenny, located on the head of the portrait (#P-Co-40).

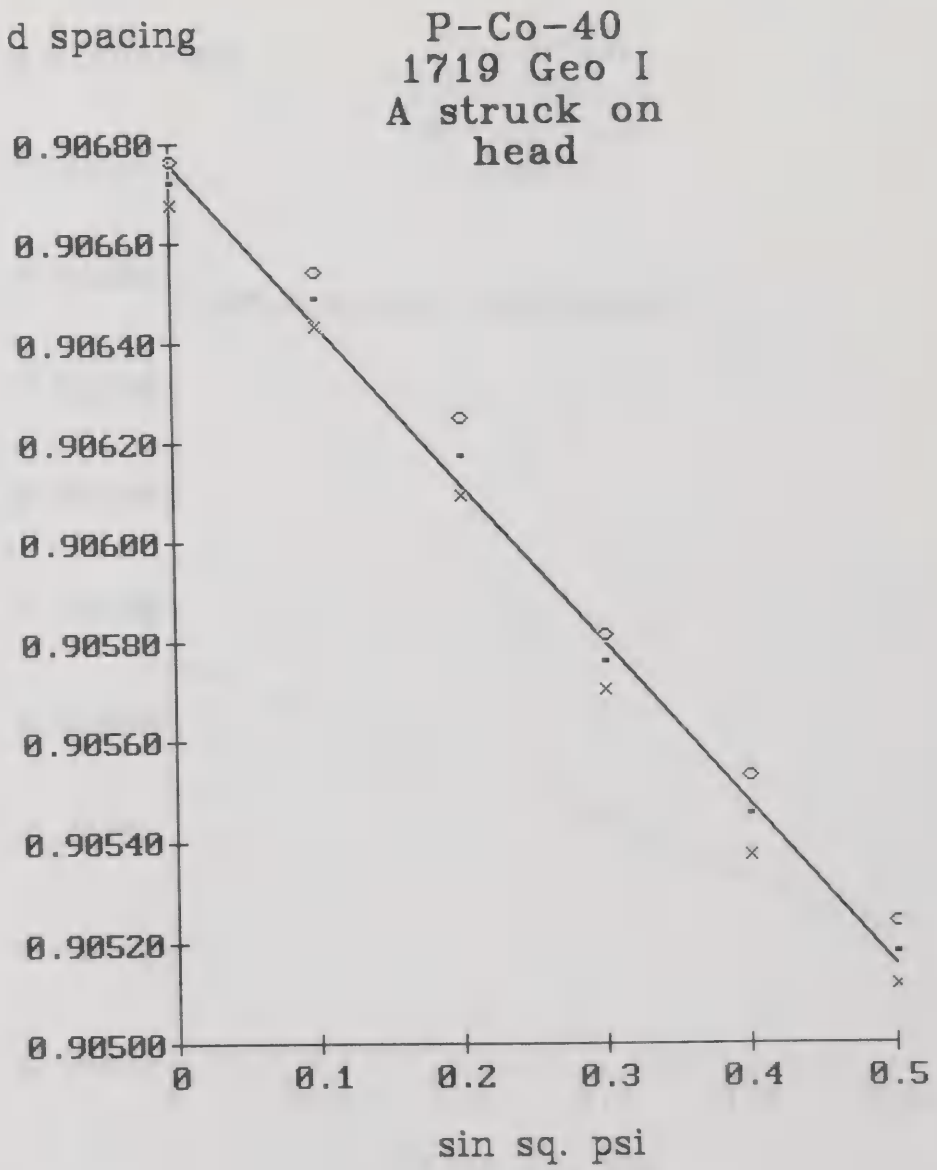

Figure 83. A plot of the d spacing versus $\sin^2$ psi, using cobalt radiation, taken on the 1719 (A) struck George I halfpenny, located on the head of the portrait (#P-Co-40).

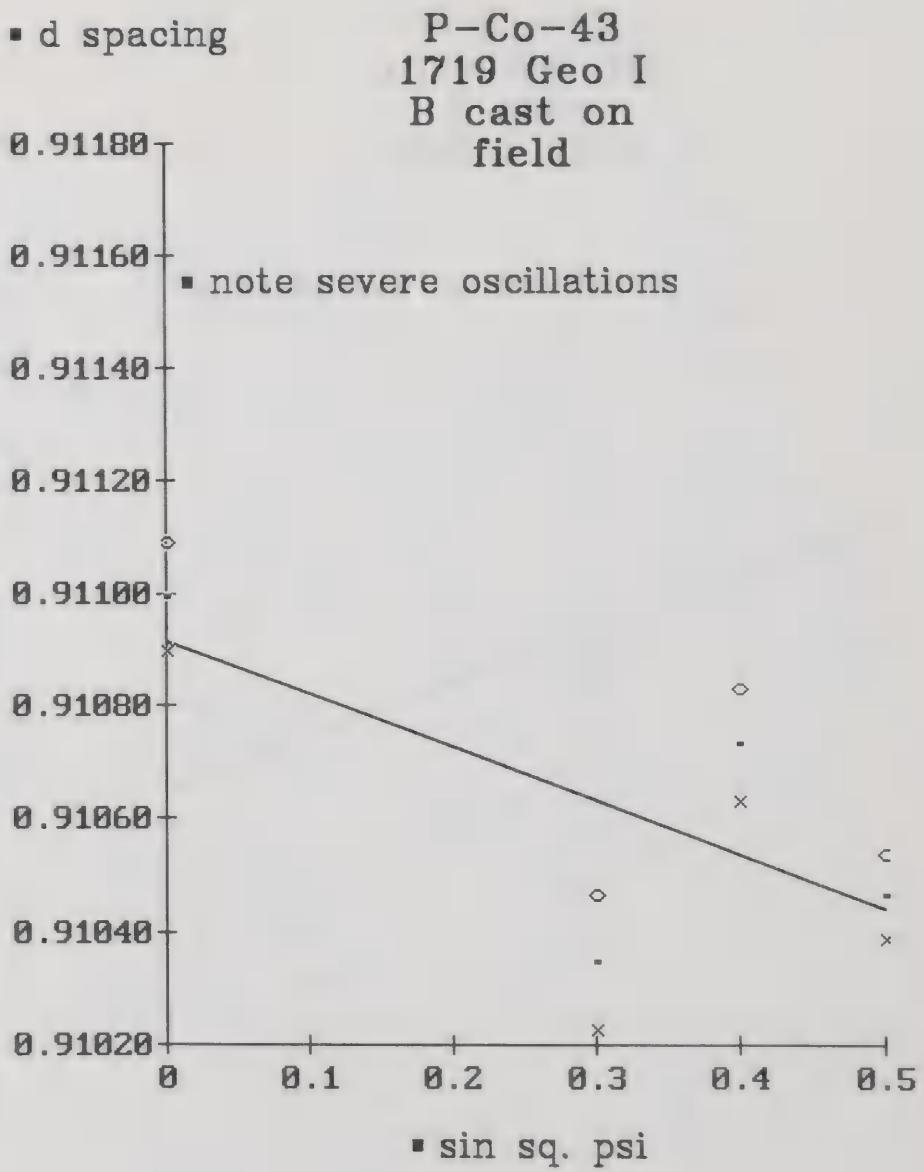

Figure 84. A plot of the d spacing versus $\sin^2$ psi, using cobalt radiation, taken on the 1719 (B) cast George I halfpenny, located on the field of the coin. (#P-Co-43).

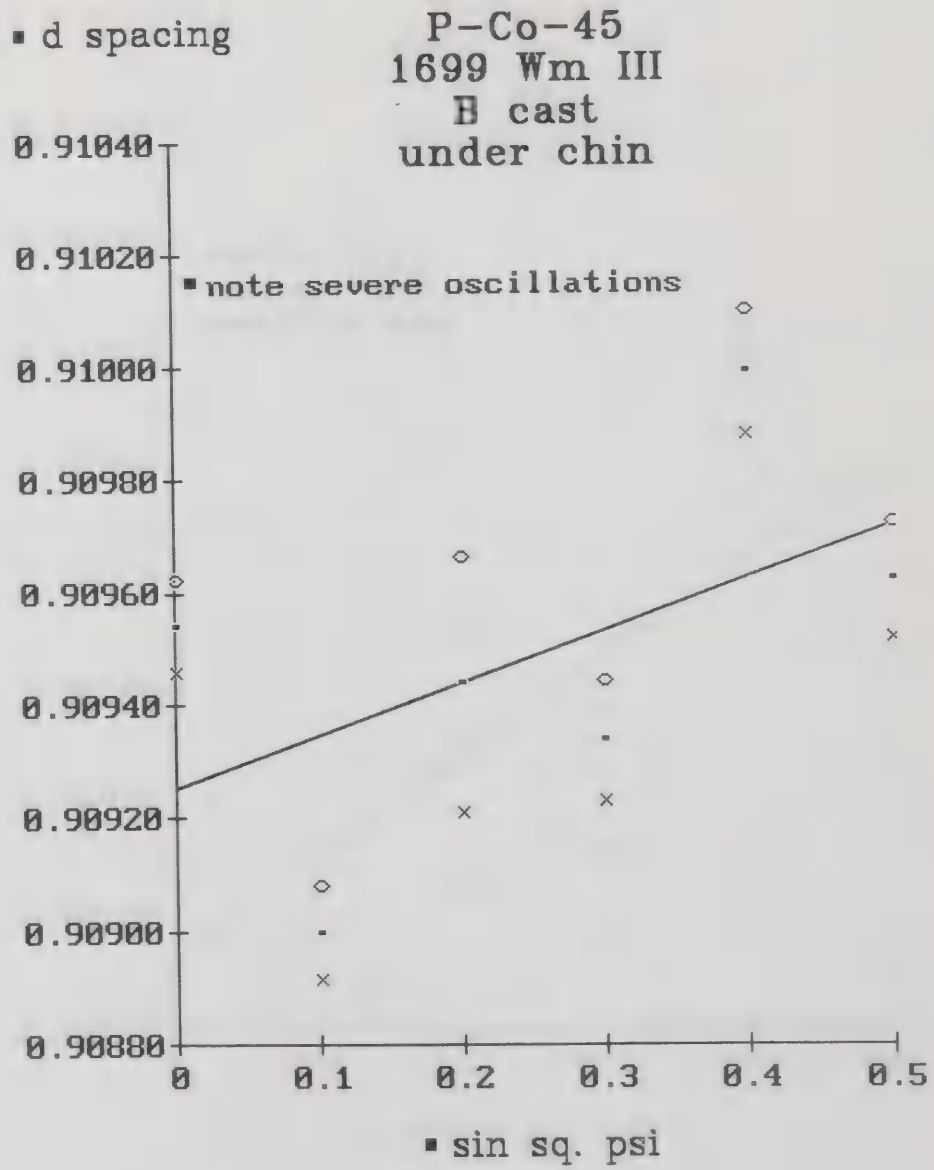

Figure 85. A plot of the d spacing versus $\sin^2$ psi, using cobalt radiation, taken on the 1699 (B) cast William III halfpenny, located under the chin of the portrait. (#P-Co-45).

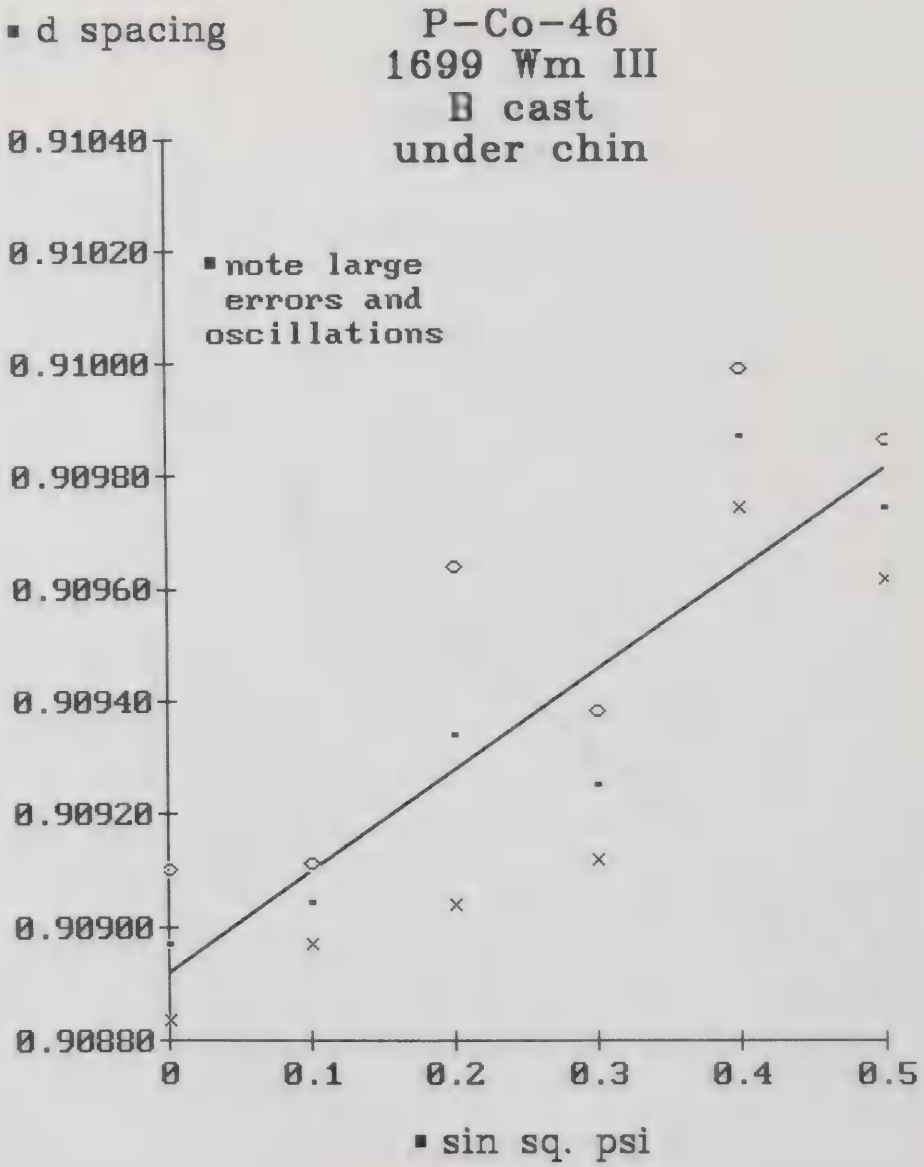

Figure 86 A plot of the d spacing versus $\sin^2$ psi, using cobalt radiation, taken on the 1699 (B) cast William III halfpenny, located under the chin of the portrait. (#P-Co-46).

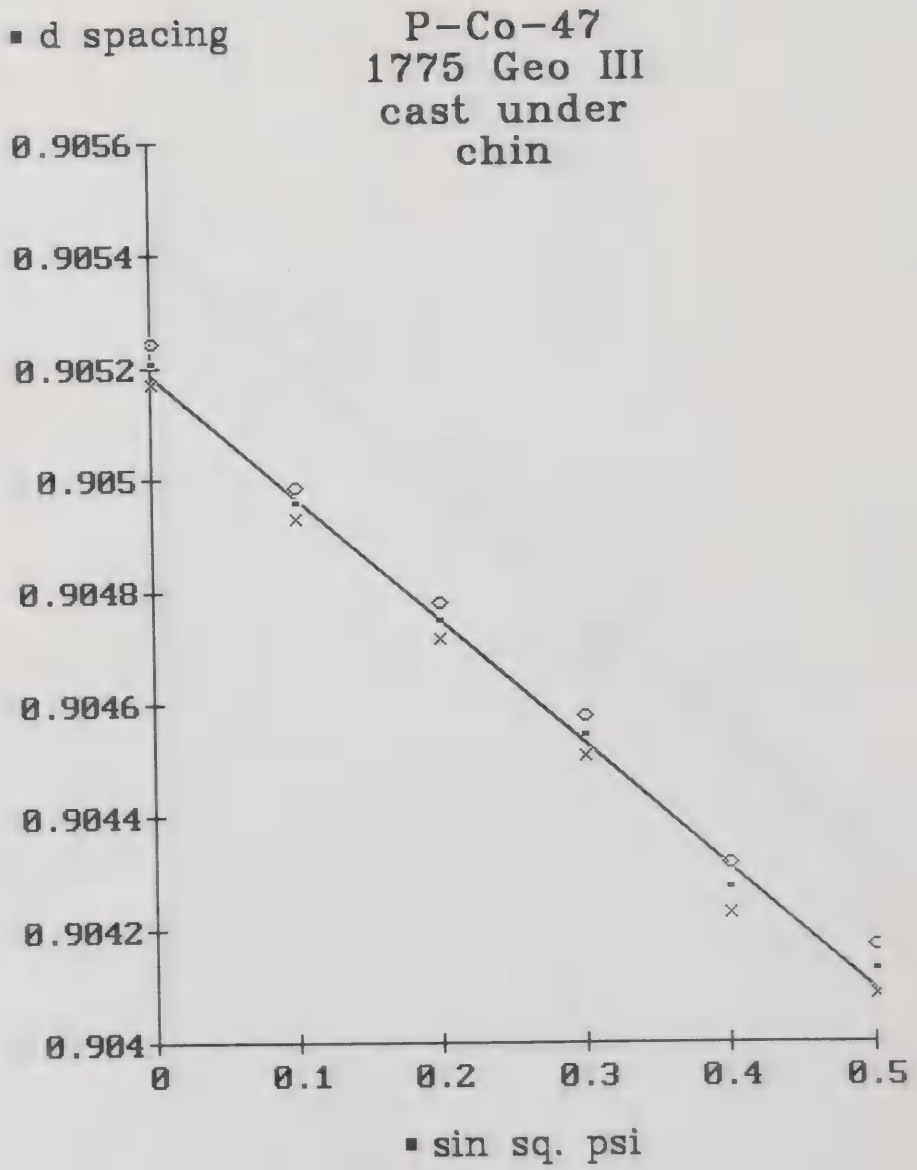

Figure 87. A plot of the d spacing versus $\sin^2$ psi, using cobalt radiation, taken on the 1775 cast George III halfpenny, located under the chin of the portrait. (#P-Co-47).

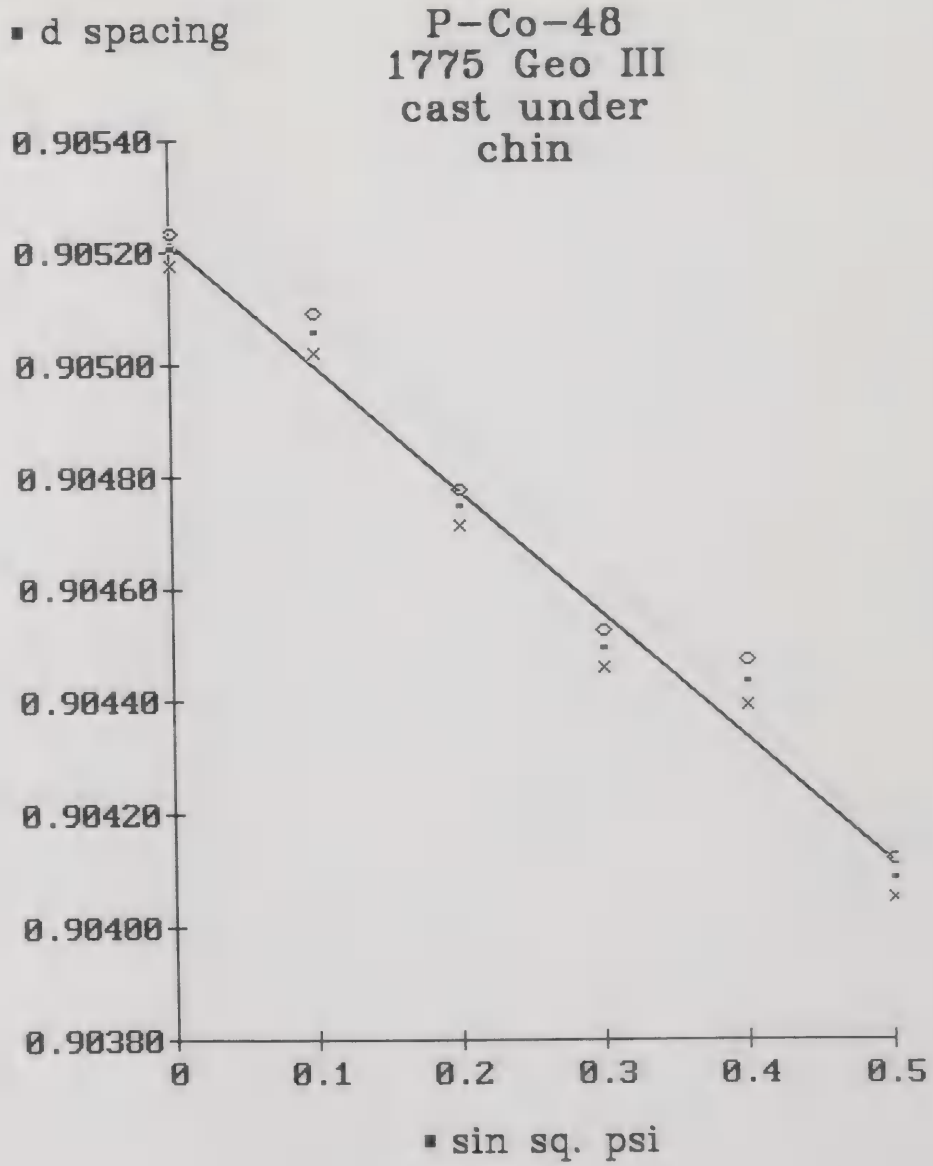

Figure 88. A plot of the d spacing versus $\sin^2$ psi, using cobalt radiation, taken on the 1775 cast George III halfpenny, located under the chin of the portrait. (#P-Co-48).

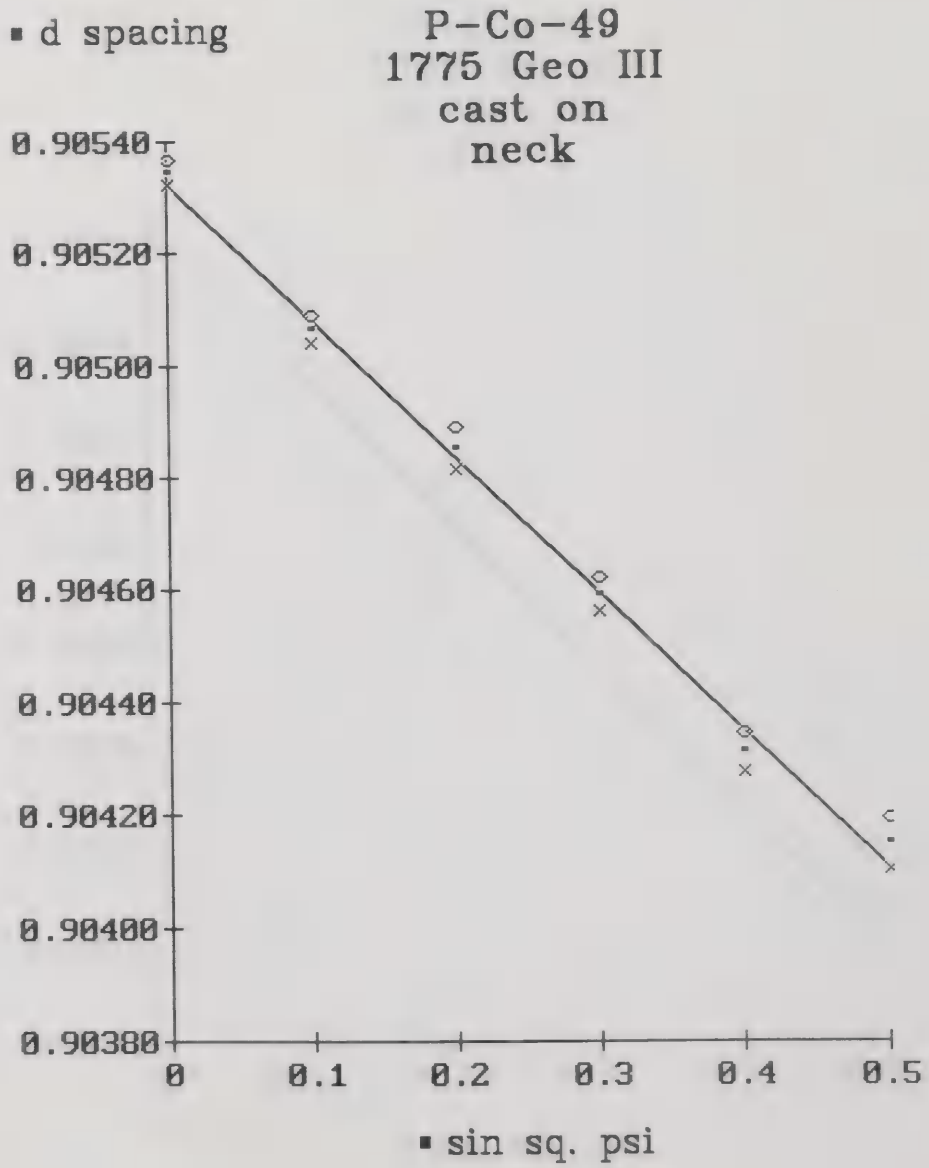

Figure 89. A plot of the d spacing versus $\sin^2$ psi, using cobalt radiation, taken on the 1775 cast George III halfpenny, located on the neck of the portrait. (#P-Co-49).

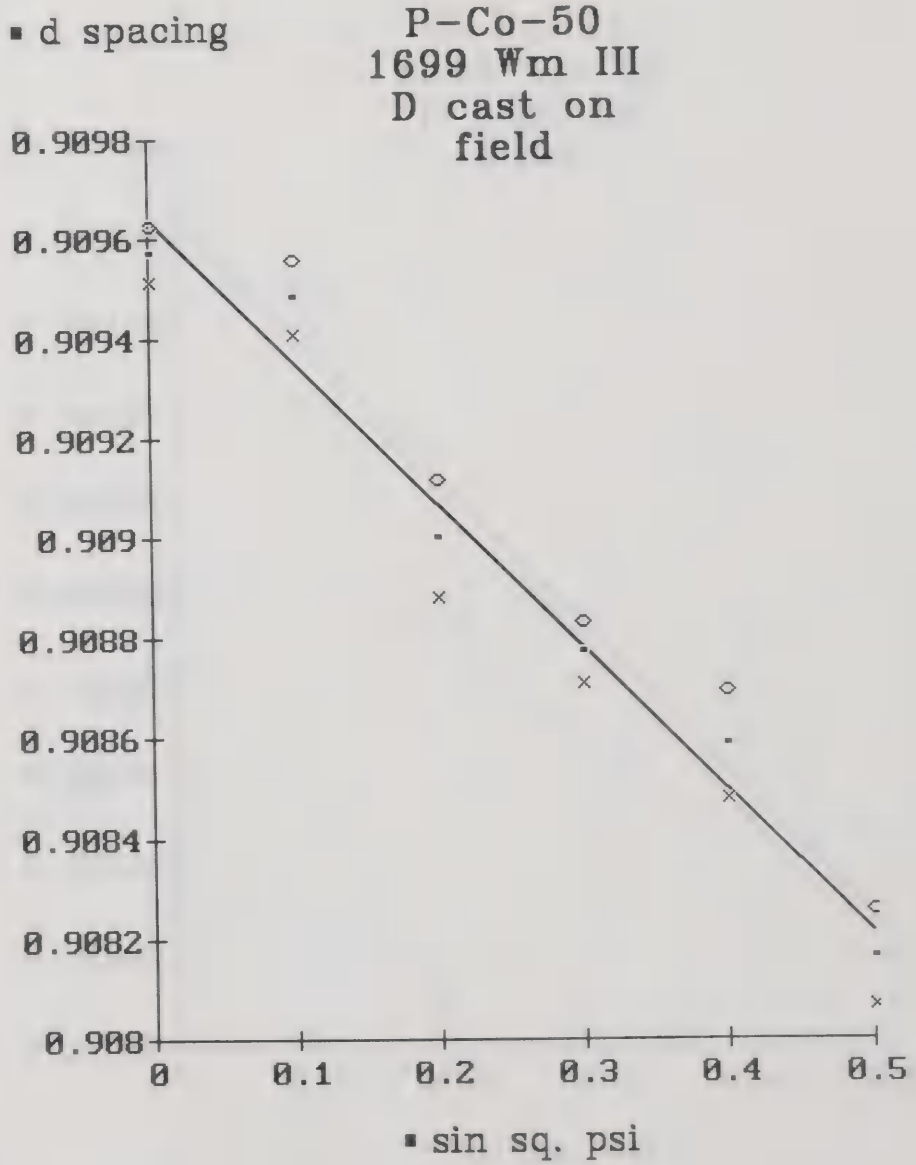

Figure 90. A plot of the d spacing versus $\sin^2$ psi, using cobalt radiation, taken on the 1699 (D) cast William III halfpenny, located on the field of the coin (#P-Co-50).

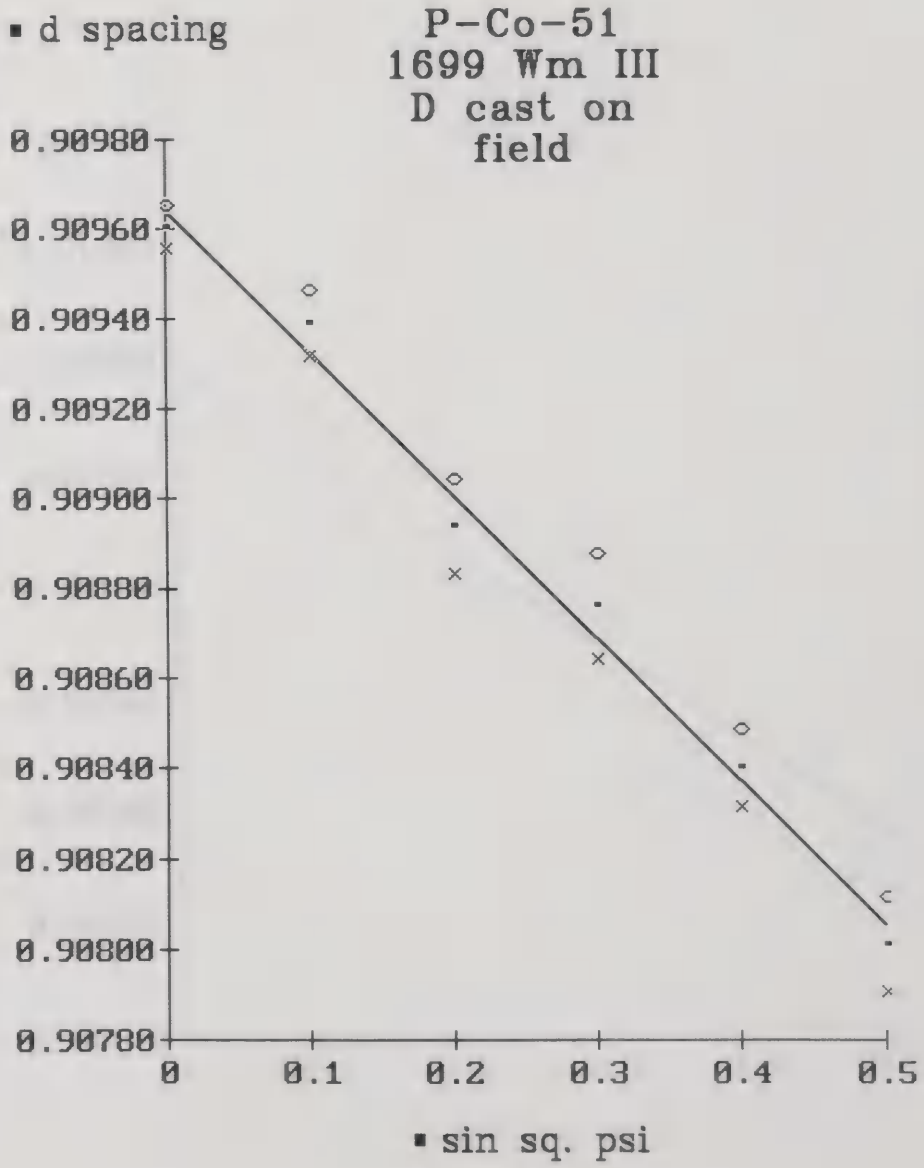

Figure 91. A plot of the d spacing versus $\sin^2$ psi, using cobalt radiation, taken on the 1699 (D) cast William III halfpenny, located on the field of the coin (#P-Co-51).

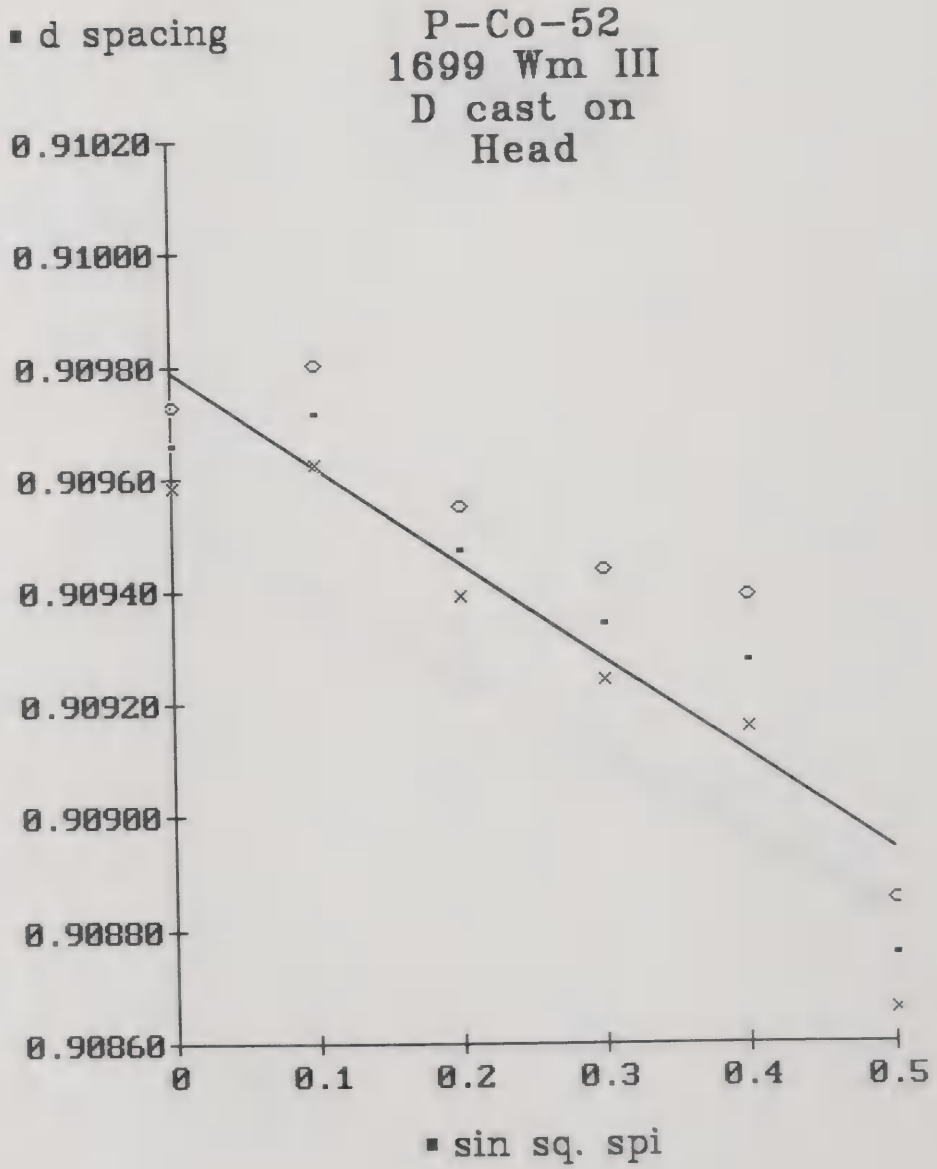

Figure 92. A plot of the d spacing versus $\sin^2$ psi, using cobalt radiation, taken on the 1699 (D) cast William III halfpenny, located on the head of the portrait. (#P-Co-52).

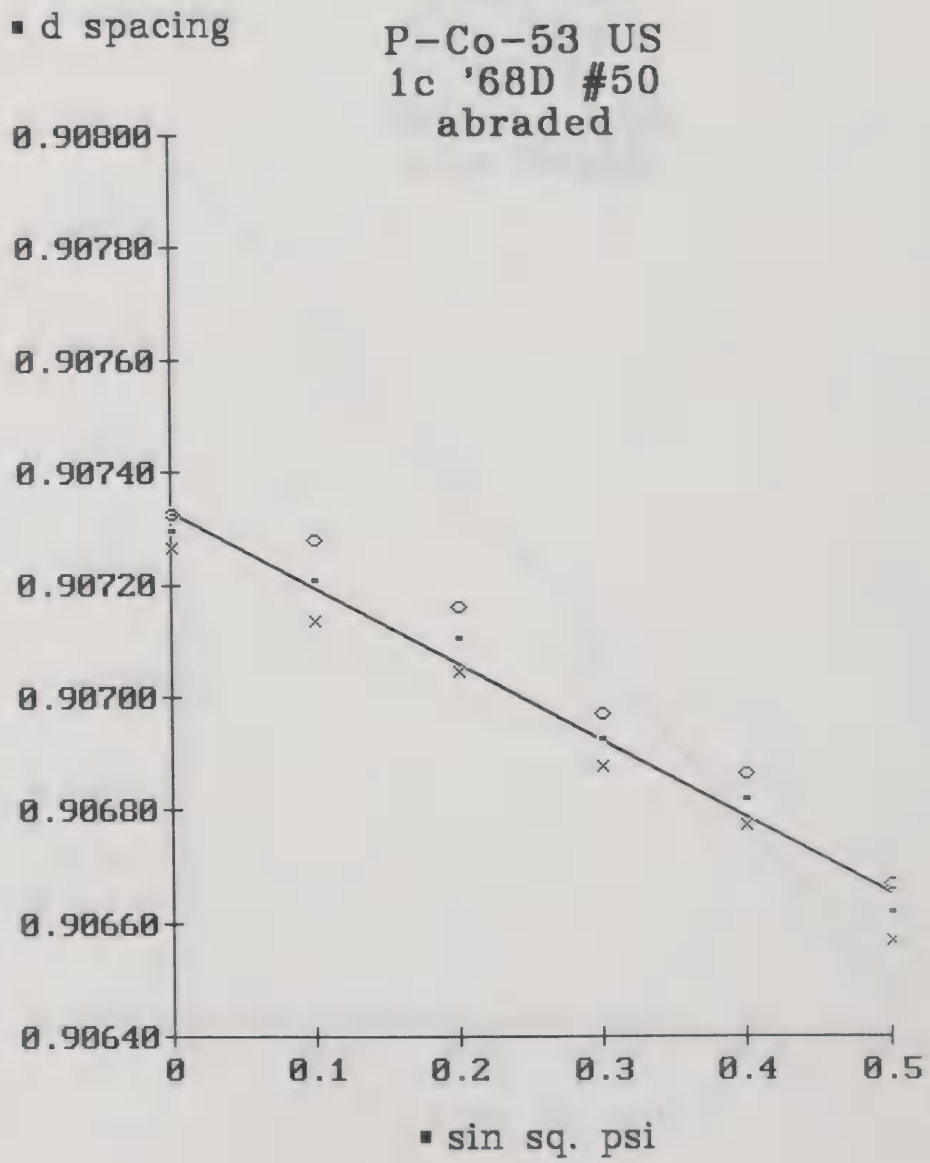

Figure 93. A plot of the d spacing versus $\sin^2$ psi, using cobalt radiation, taken on the 1968 D mint issue U.S. one cent piece (#50), abraded mechanically using a wire brush attached to a flexible shaft drill.
(#P-Co-53).

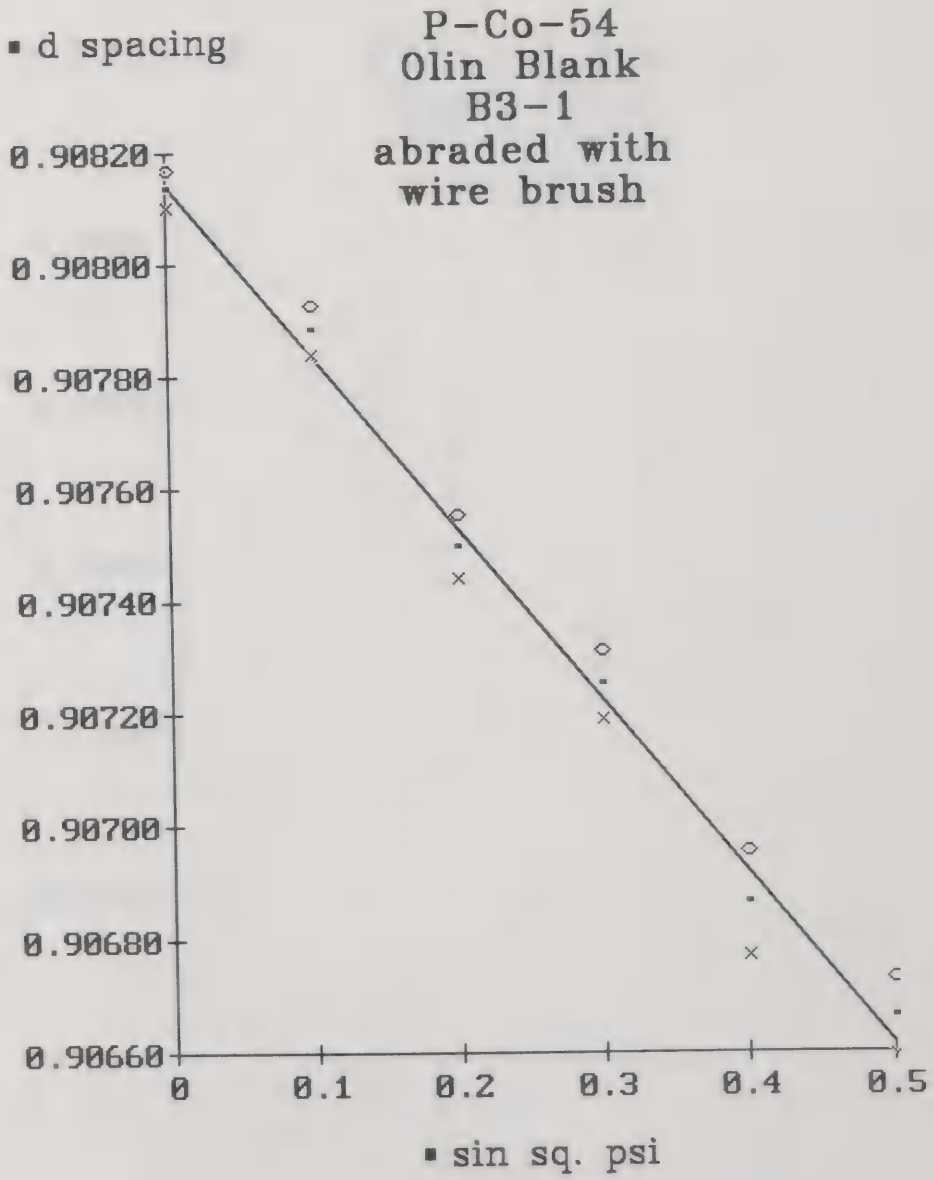

Figure 94. A plot of the d spacing versus $\sin^2$ psi, using cobalt radiation, taken on the U.S. "Type I" one cent blank (#B3-1), abraded by hand using a wire brush. (#P-Co-54).

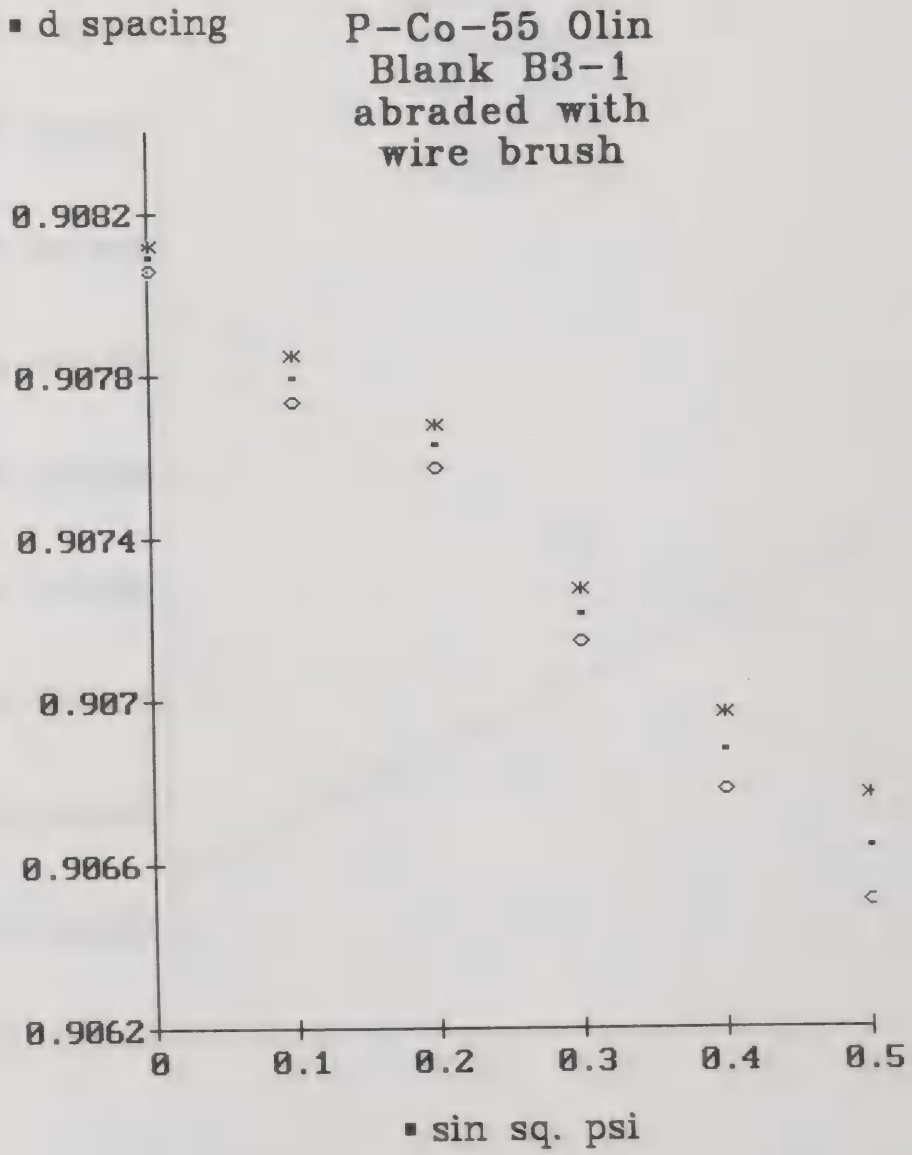

Figure 95. A plot of the d spacing versus $\sin^2$ psi, using cobalt radiation, taken on the U.S. "Type I" one cent blank (#B3-1), abraded by hand using a wire brush. (#P-Co-55).

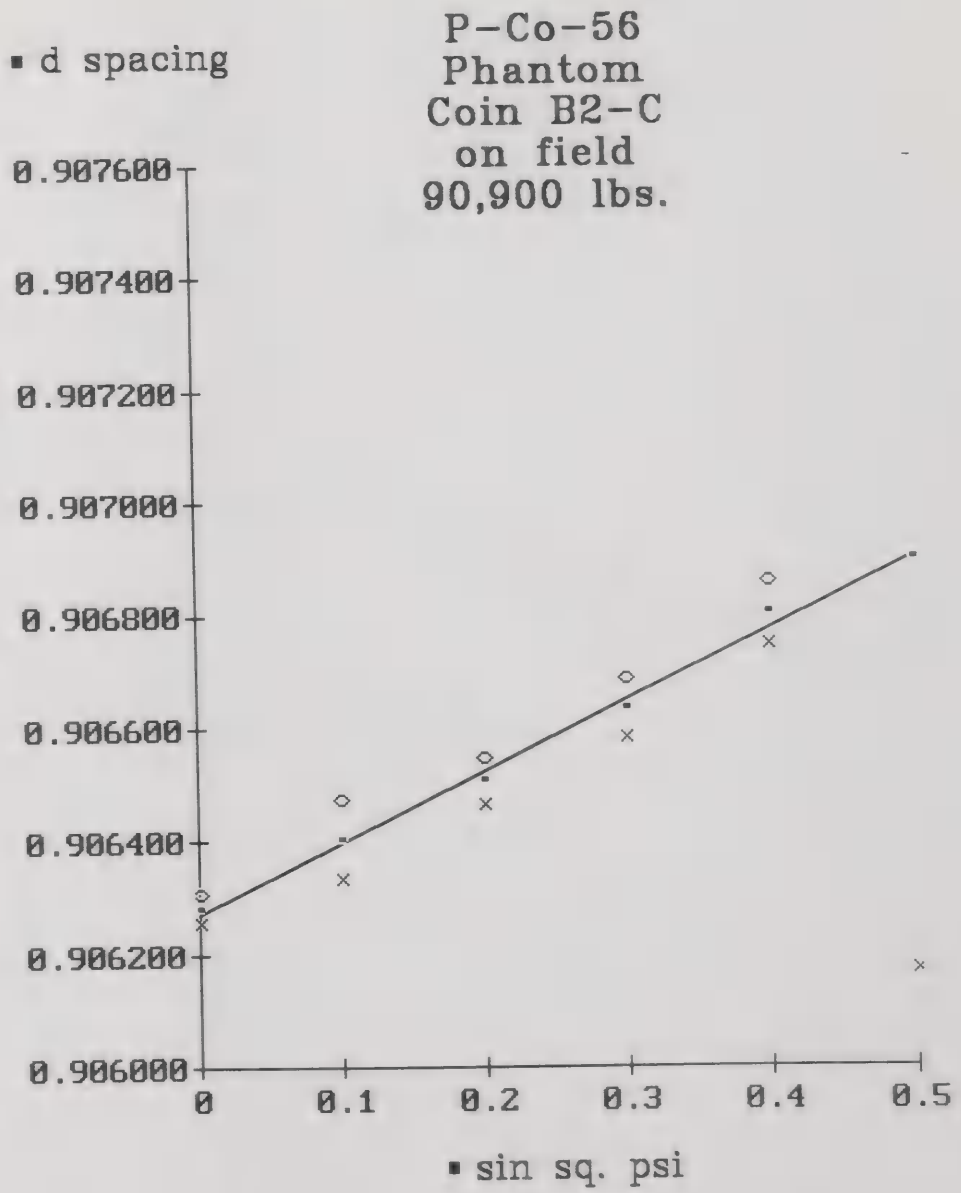

Figure 96 A plot of the d spacing versus $\sin^2$ psi, using cobalt radiation, taken on the "Phantom" Coin (#B2-C), struck at 90,900 lb. coining pressure, located on the field of the coin..
(#P-Co-56).

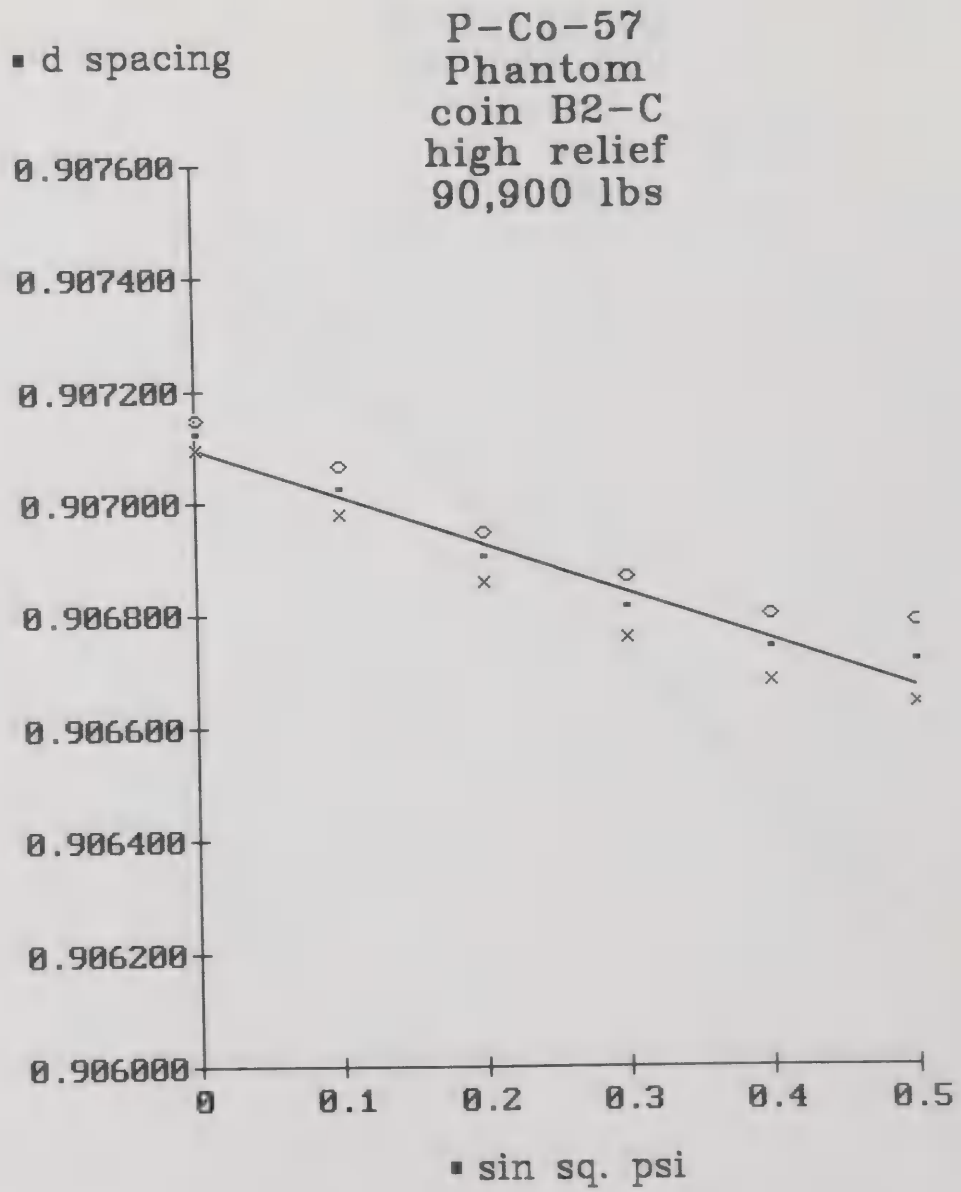

Figure 97. A plot of the d spacing versus $\sin^2$ psi, using cobalt radiation, taken on the "Phantom" Coin (#B2-C), struck at 90,900 lb. coining pressure, located on the high relief of the coin..
(#P-Co-57).

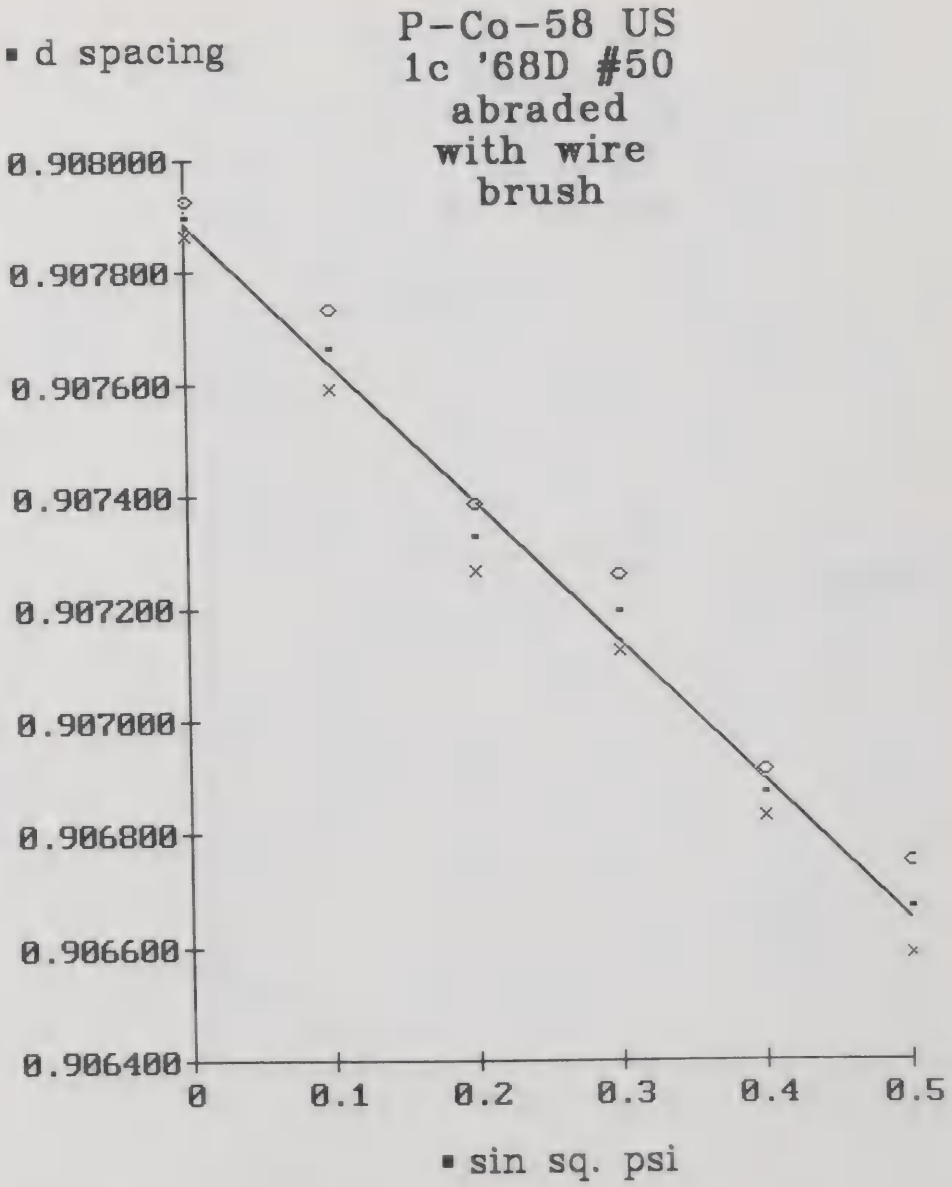

Figure 98. A plot of the d spacing versus $\sin^2$ psi, using cobalt radiation, taken on the 1968 D mint issue U.S. one cent piece (#50), abraded by hand using a wire brush. (#P-Co-58).

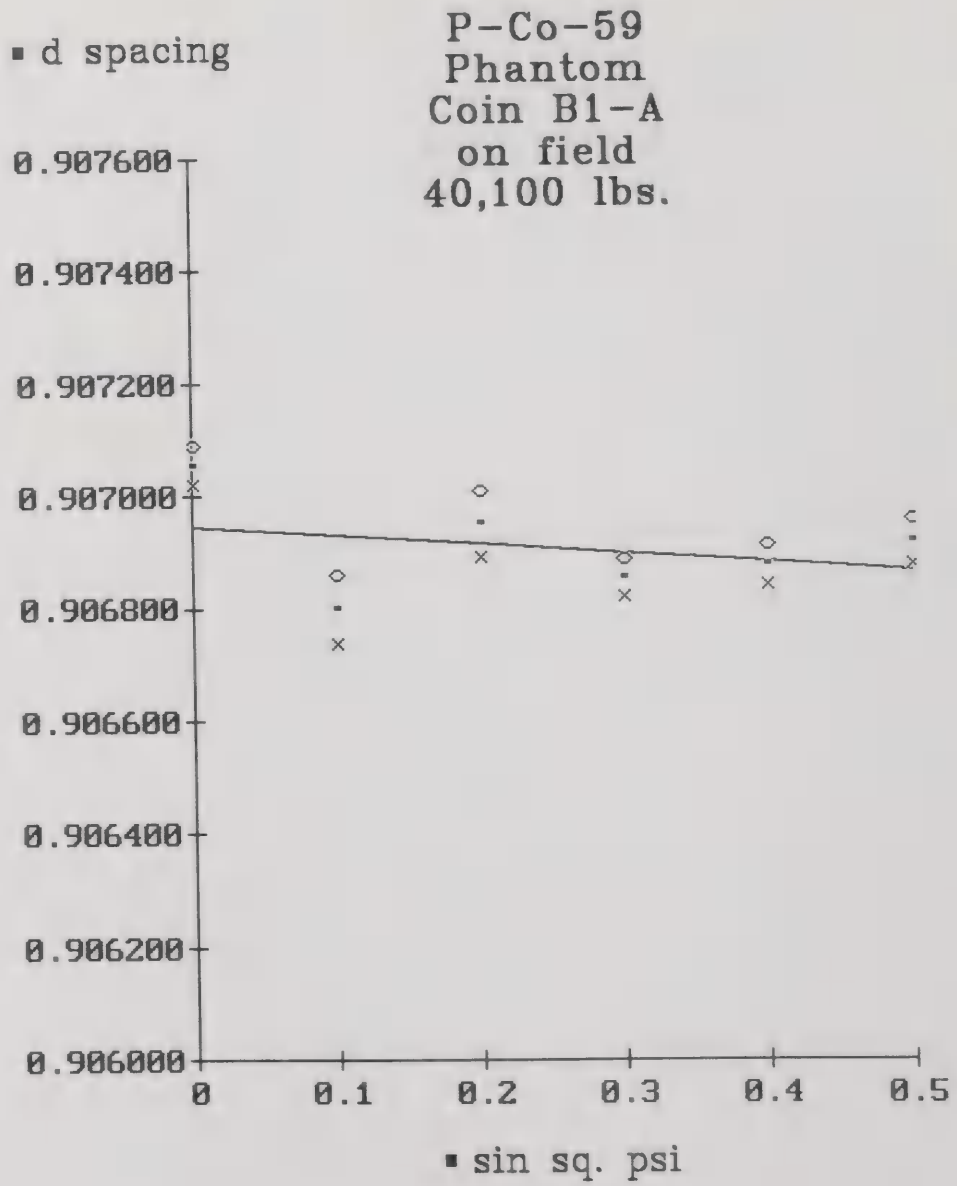

Figure 99. A plot of the d spacing versus $\sin^2$ psi, using cobalt radiation, taken on the "Phantom" Coin (#B1-A), struck at 40,100 lb. coining pressure, located on the field of the coin.
(#P-Co-59)

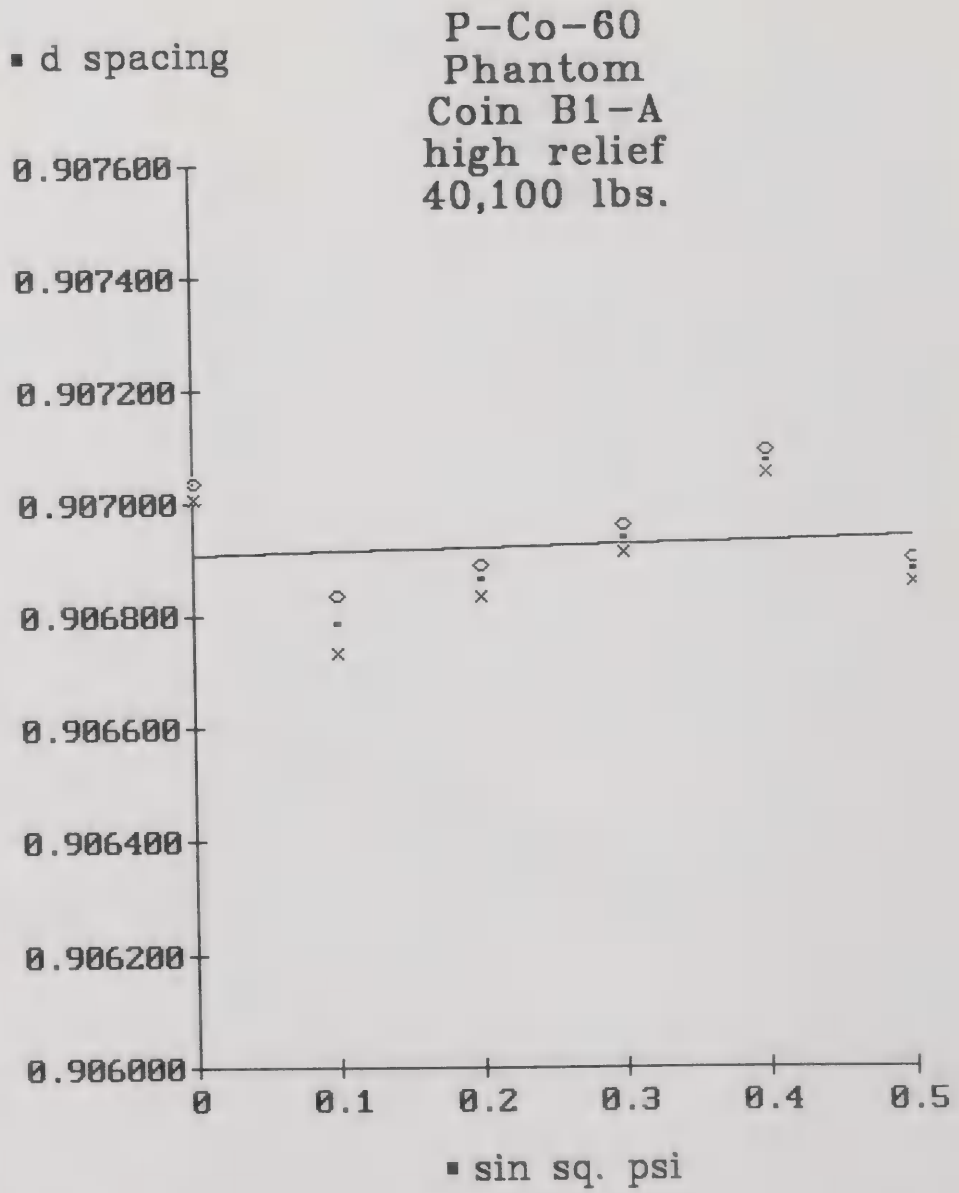

Figure 100. A plot of the d spacing versus $\sin^2$ psi, using cobalt radiation, taken on the "Phantom" Coin (#B1-A), struck at 40,100 lb. coining pressure, located on the high relief of the coin..
(#P-Co-60).

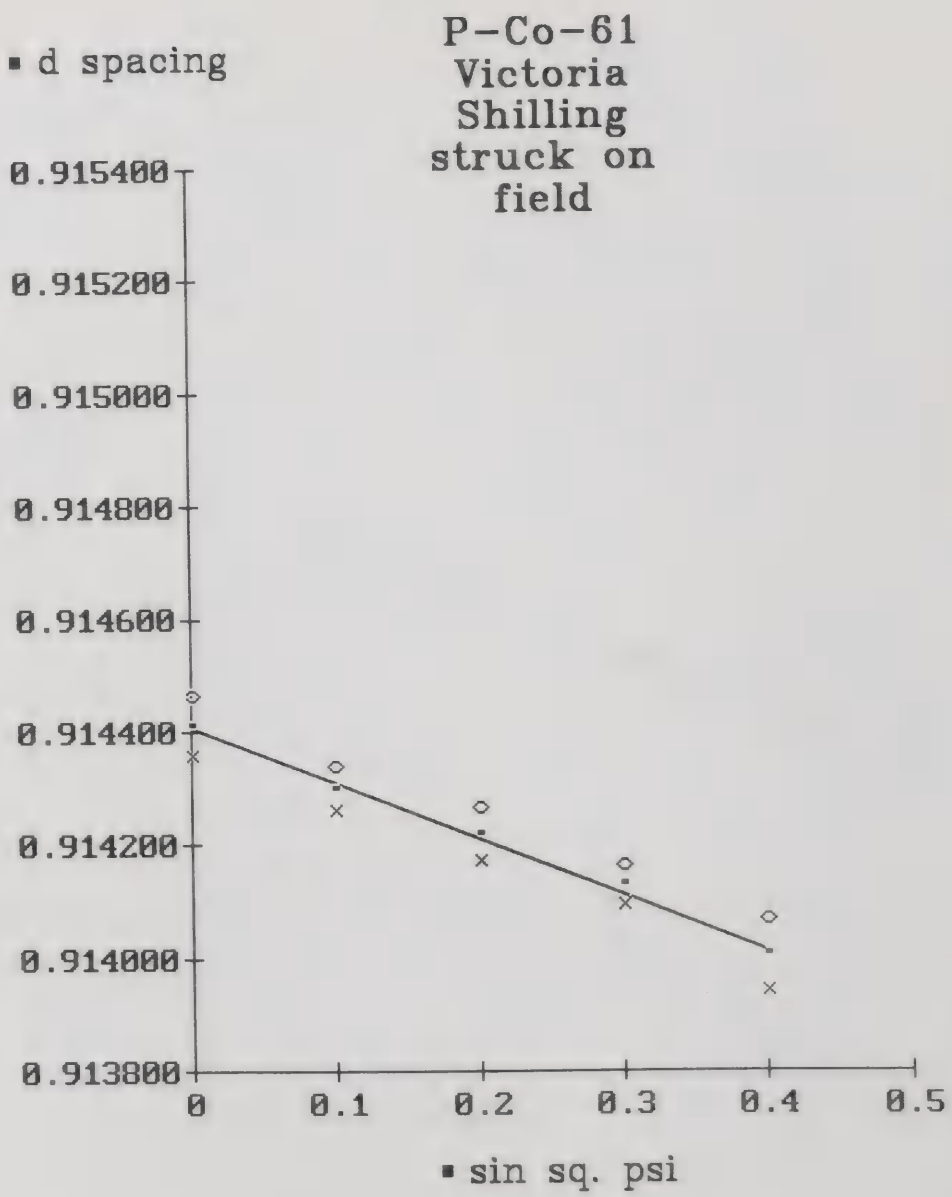

Figure 101. A plot of the d spacing versus $\sin^2$ psi, using cobalt radiation, taken on the struck Victoria shilling, located on the field of the coin (#P-Co-61).

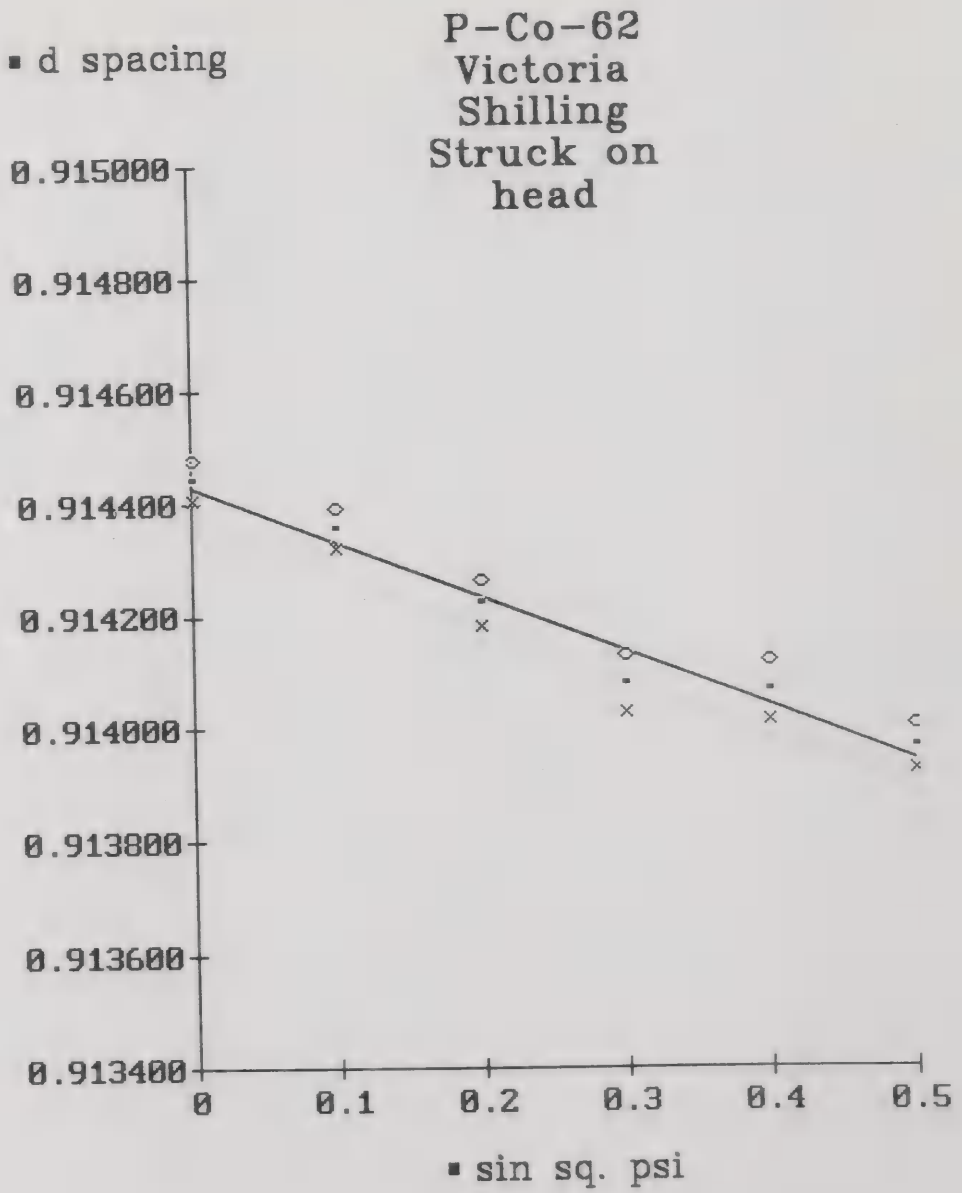

Figure 102. A plot of the d spacing versus $\sin^2$ psi, using cobalt radiation, taken on the struck Victoria shilling, located on the head of the portrait . (#P-Co-62).

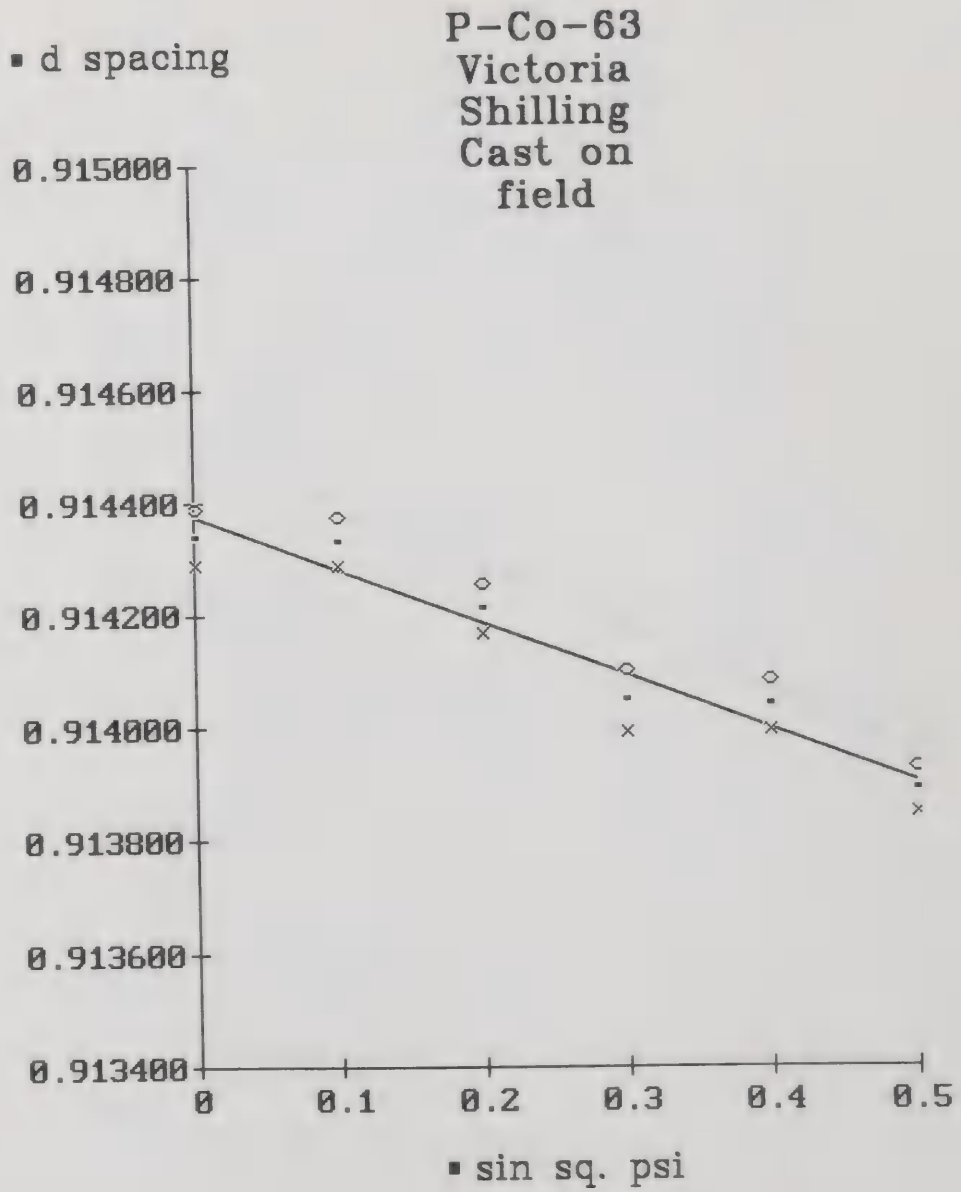

Figure 103. A plot of the d spacing versus $\sin^2$ psi, using cobalt radiation, taken on the cast Victoria shilling, located on the field of the coin .
(#P-Co-63).

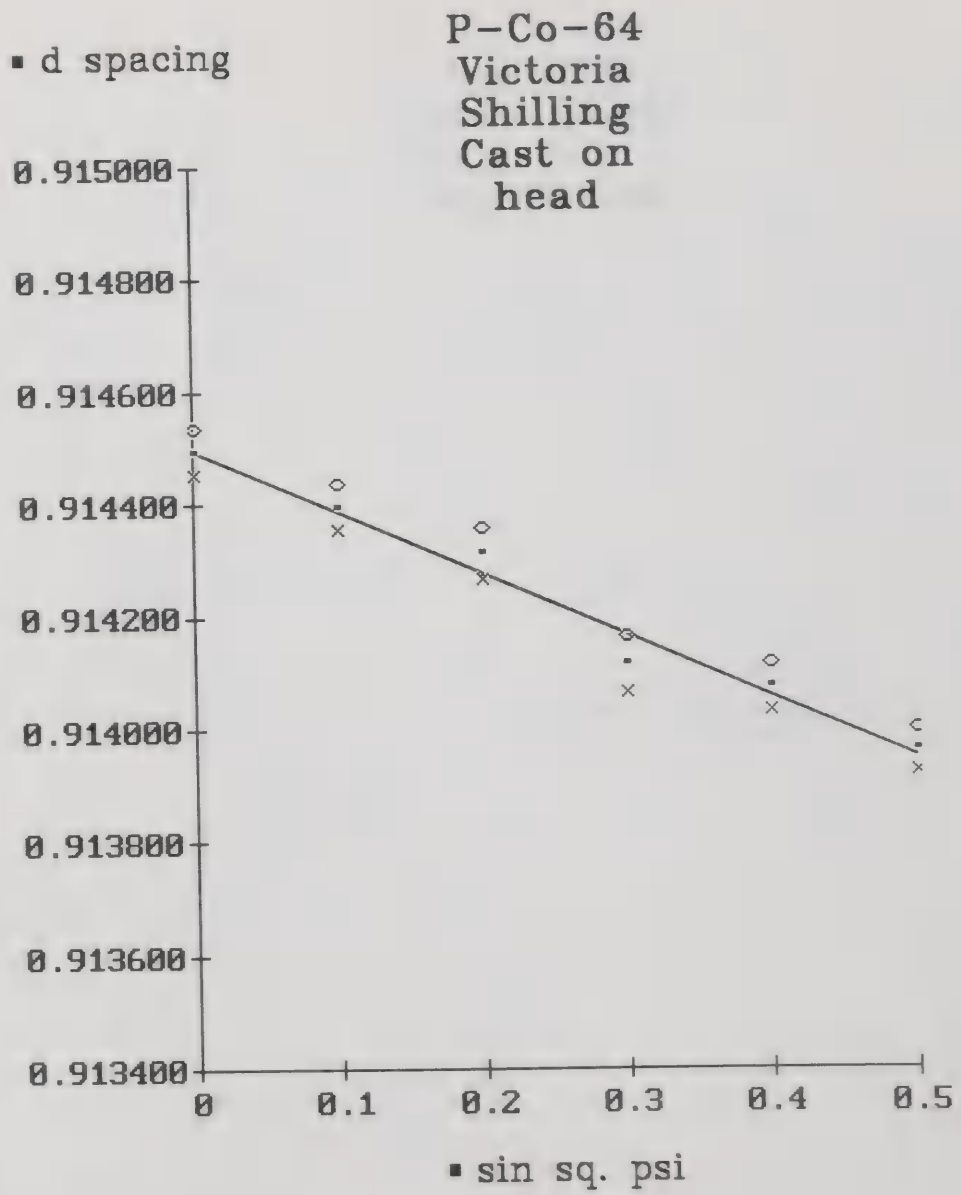

Figure 104. A plot of the d spacing versus $\sin^2$ psi, using cobalt radiation, taken on the cast Victoria shilling, located on the head of the portrait .
(#P-Co-64).

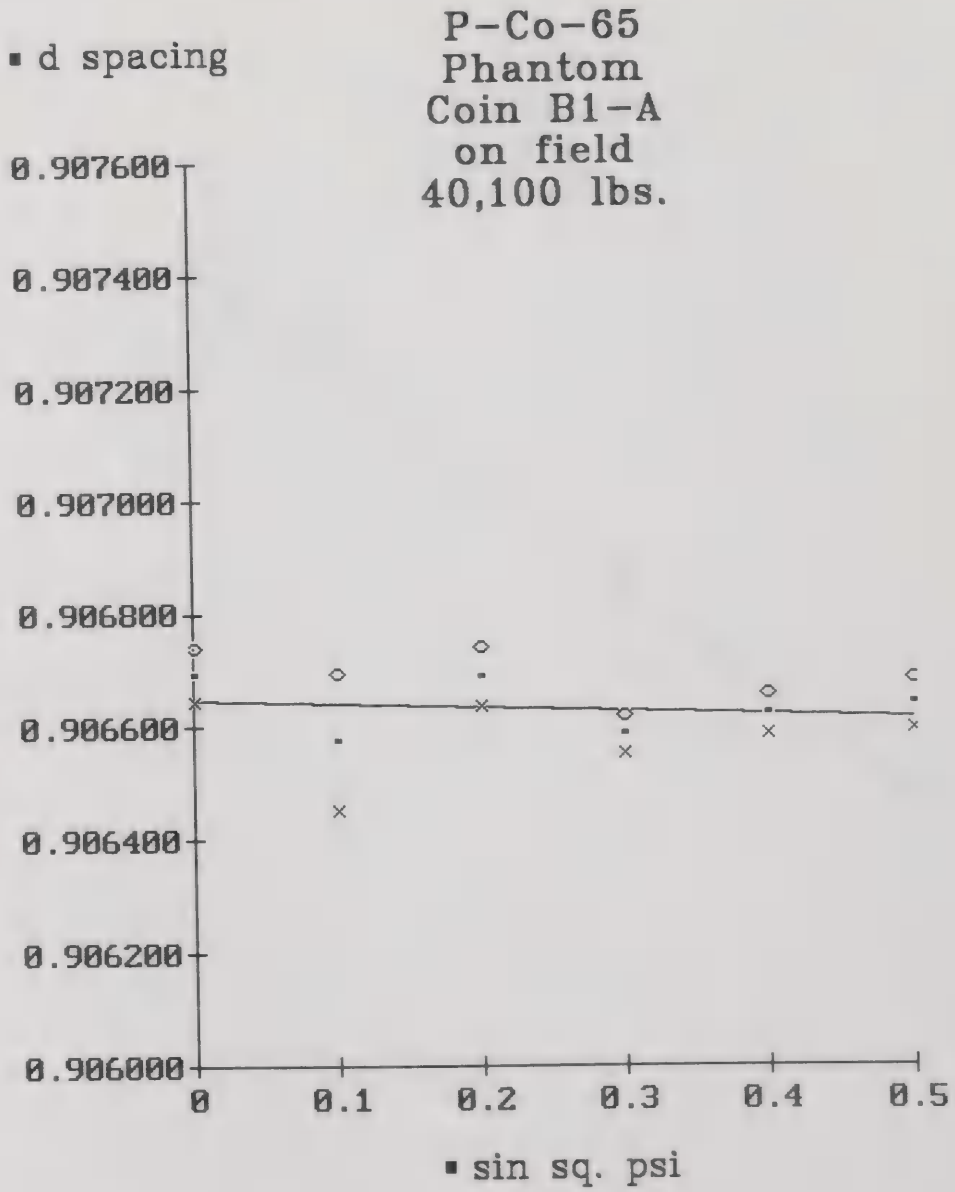

Figure 105. A plot of the d spacing versus $\sin^2$ psi, using cobalt radiation, taken on the "Phantom" Coin (#B1-A), struck at 40,100 lb. coining pressure, located on the field of the coin.
(#P-Co-65).

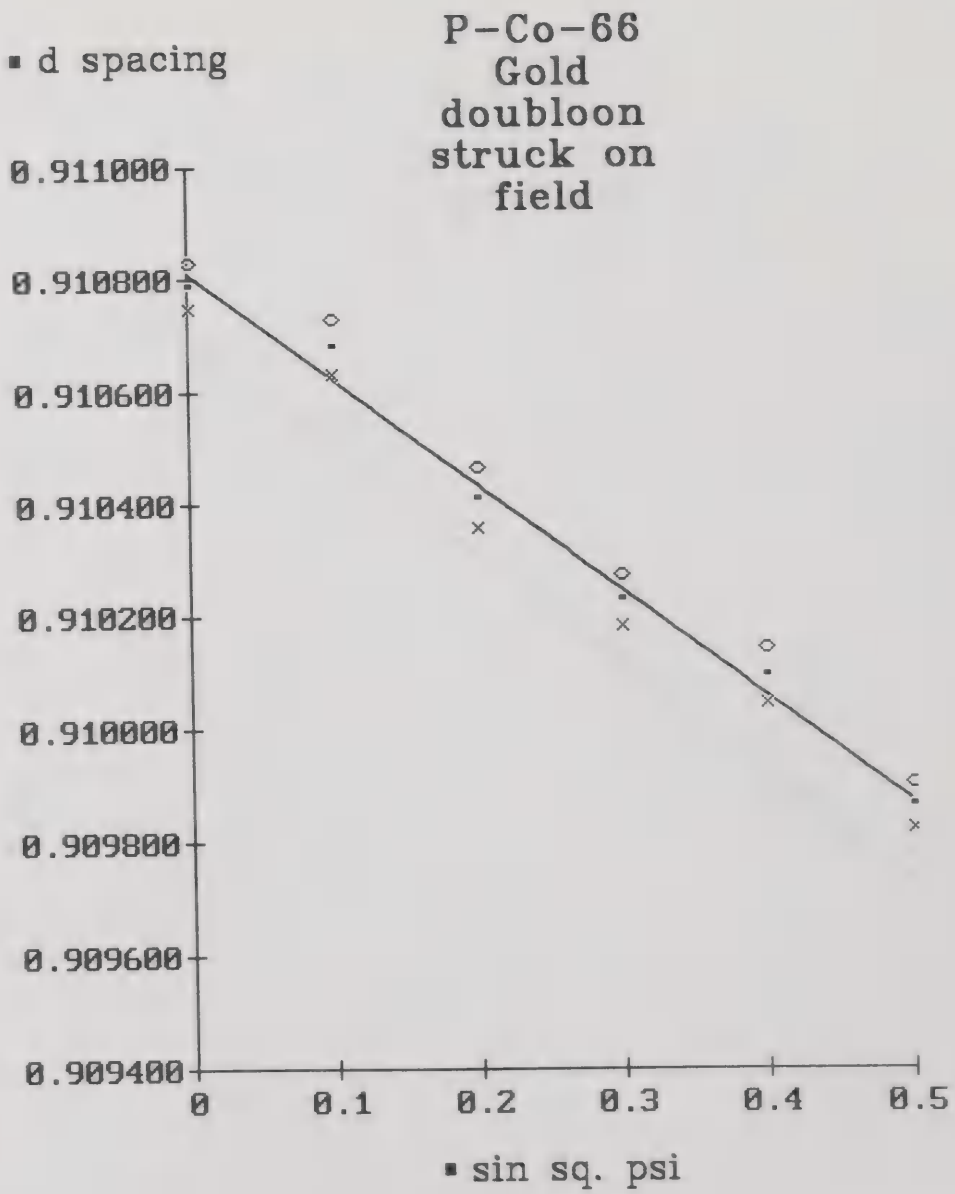

Figure 106. A plot of the d spacing versus $\sin^2$ psi, using cobalt radiation, taken on the struck gold Doubloon, located on the field of the coin.
(#P-Co-66).

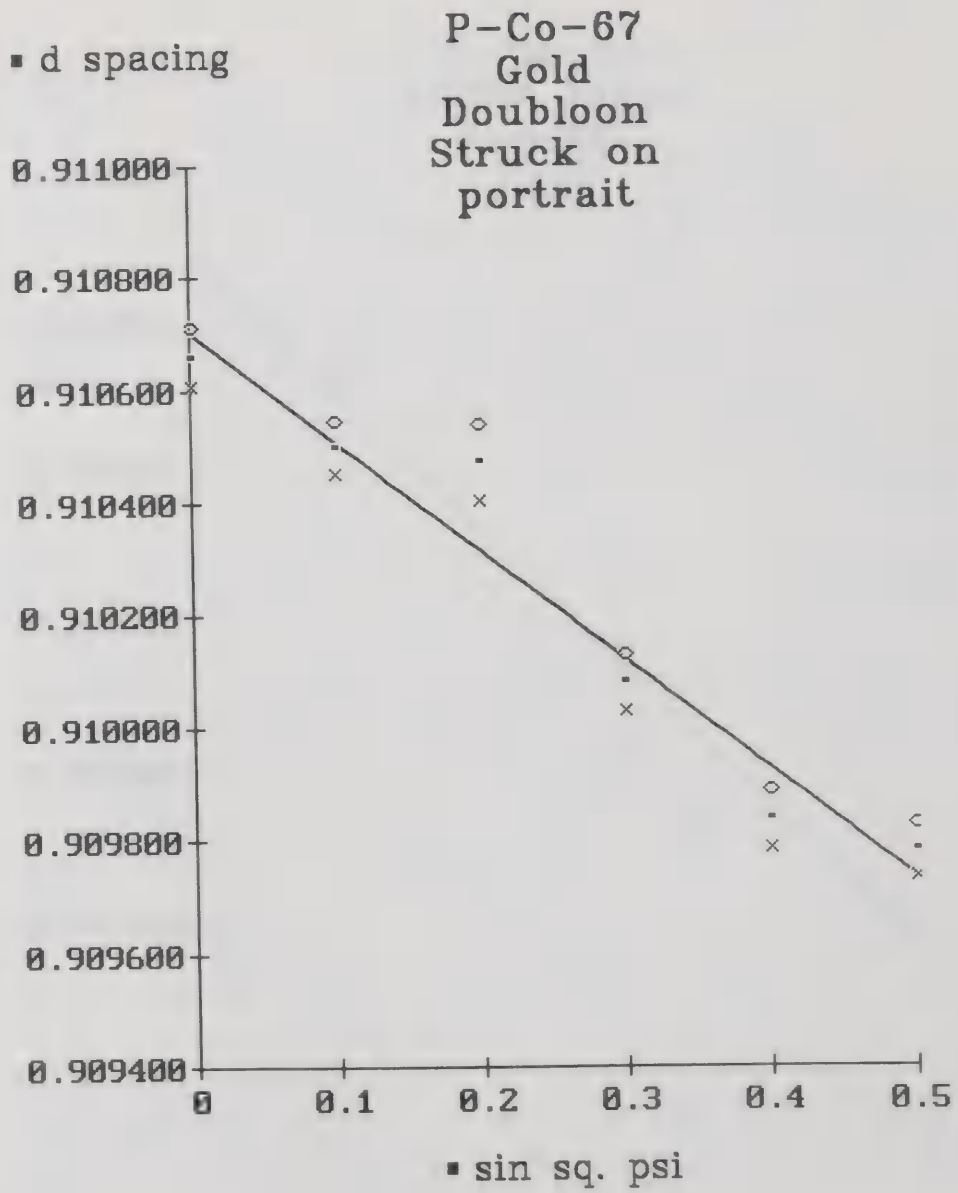

Figure 107. A plot of the d spacing versus $\sin^2$ psi, using cobalt radiation, taken on the struck gold Doubloon, located on the portrait of the coin. (#P-Co-67).

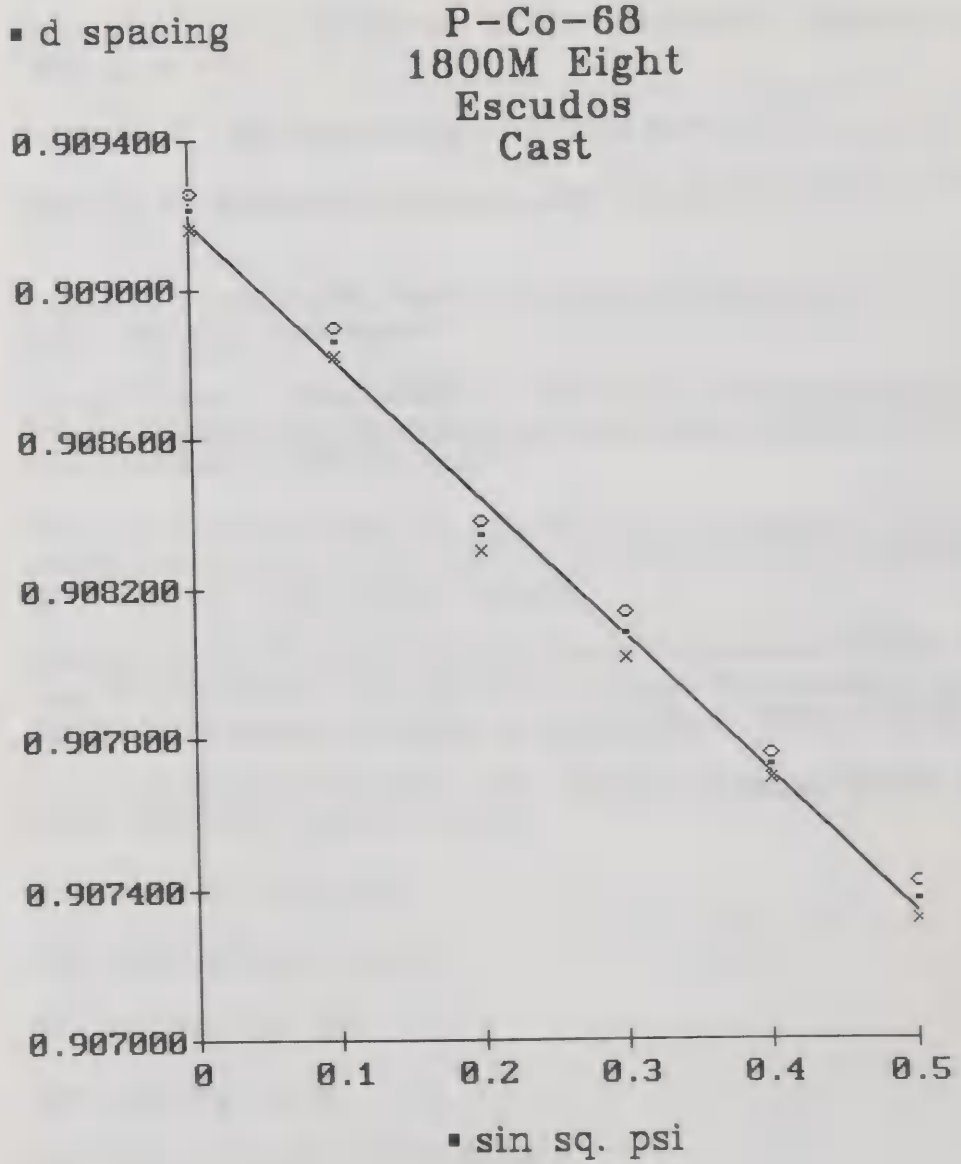

Figure 108. A plot of the d spacing versus $\sin^2$ psi, using cobalt radiation, taken on the cast 1800 Spanish Gold doubloon, located on the field of the coin. (#P-Co-68).

LIST OF REFERENCES

1. Hurter, Sylvia, "Two Dangerous, Sicilian Counterfeits,"' Bulletin on Counterfeits, **1980**, 5, pp 6-8.

2. Schlösser, E., Die Münztechnik; Hahn'sche Buchhandling: Hannover, 1884.

3. Dieter, G. E., Mechanical Metallurgy, 2nd. ed.; McGraw-Hill: New York, 1976; chapter 2.

4. Krausz, A. S.; and Eyring, Henry, Deformation Kinetics; John Wiley and Sons: New York, 1975, see chapter 1.

5. Young, William J., "Examination of Works of Art Embracing Various Fields of Science"; Application of Science in the Examination of Works of Art; Museum of Fine Arts: Boston, 1959; pp 26,30.

6. Terry, K.W.; and De Laeter, J.R., "X-ray Diffraction Analysis of Reproductions among Seventeenth-century Spanish Silver Reales", The Numismatic Chronicle, **1974**, Seventh series, XIV, pp 198-202.

7. Wharton, Glenn, "Technical Examination of Renaissance Medals, The Use of Laue Back Reflection X-ray Diffraction to Identify Electroformed Reproductions"; Journal of the American Institute for Conservation, **1984**, 23, pp 88-100.

8. Barrett, Charles; and Massalski, T.B., Structure of Metals; 3rd rev. ed.; Pergamon Press: New York, 1980; pp 156-157.

9. See reference 8, pp.90-99.

10, See reference 8, pp.156-157.

11. See reference 6, p 198.

12. See reference 7, p 88.

13. See reference 3, pp 430-432, 580-581.

14. See reference 3, pp 5-8,19-20.

15. See reference 3, p 7.

16. See reference 8, pp.471-472.

17. Noyan, I.C.; and Cohen, J.B., Residual Stress, Measurement by Diffraction and Interpretation; Springer-Verlag: New York, 1987, p 15.

18. See reference 3, pp 64-66, 91-101.

19. See reference 4, chapter 1.

20. See reference 3, p 430.

21. Cullity, B. D., Elements of X-Ray Diffraction, 2nd. ed.; Addison-Wesley: Reading, Mass., 1978, p 286.

22. See reference 17, pp 1-3.

23. See reference 8, chapter 17, pp 466-485.

24. Ruud, Clayton O., "A Review of Nondestructive Methods for Residual Stress Measurement"; Journal of Metals, 1981, July, 35-40.

25. Barrett, Charles; and Massalski, T.B., Structure of Metals; 3rd rev. ed.; Pergamon Press: New York, 1980; pp 156-157.

26. Klug, H.P. and Alexander, L.E., X-ray Diffraction Procedures, John Wiley and Sons: New York,1974,755-790.

27. Residual Stress Measurement by X-ray Diffraction- SAE J 784a, 2nd Edition, Society of Automotive Engineers,1971.

28. See reference 3, pp 23-37; see reference 8, p 472.

29. See reference 8, p 469.

30. See reference 8, p 472.

31. a) Krausz, A. S.; Eyring, Henry, Deformation Kinetics; John Wiley and Sons: New York, 1975, p 257. b) Krausz, A. S., The University of Ottawa at Ottawa, Ontario, Canada, personal communication, 1986.

32. a) Cagle,Jr. F. Wm.; Eyring, Henry, Journal of Applied Physics, **1951**, 22, p 771. b) Fredrickson, Jay W.; Eyring, Henry, In Metals Technology Technical Publication No. 2423 Vol. 15, 1948; The American Institute of Mining, Metallurgical and Petrolium Engineers (AIME); pp 11-33.

33. See reference 4, chapters 3.3-3.4.

34. See reference 32.

35. Wilson, J.F. and Garofalo, F., Materials Research Standards, ASTM, **1986**, 6, p 85;

36. Authentic Struck William III Halfpenny, BMC 675.

37. James, Michael Royston, An Examination of Experimental Techniques in X-ray Residual Stress Analysis, Ph.D. Dissertation, Northwestern University, January, 1977.

38. See reference 37, pp 65-69.

39. See reference 17, pp 196-203.

40. James, M.R.; and Cohen, J.B., Advances in X-ray Analysis, **1977**, 20, 291

41. See reference 37, pp 119-122.

42. Cohen, J.B., "Report on Tungsten Lattice Parameter Round Robin," X-ray Subcommittee of SAE Iron and Steel Technical Committee, Division 4, 1964.

43. See reference 37, pp 132-135.

44. See reference 37, p 110.

45. See reference 17, pp 203-205.

46. International Tables for Crystallography, Vol IV, J.A. Ibers and W.C. Hamilton, eds., Kynoch Press: Birmingham, Eng, 1974, pp 47-66.

47. Hauk, V.; and Krug, W.K., "Determination of Residual Stress Distribution in the Surface Region by X-rays"; In Residual Stress in Science and Technology; Macherauch, E. and Hauk, V. Eds.; Deutsche Gesellschaft für Metallkunde: Oberursel, Germany, 1987; pp303-310.

48. See reference 17, pp 133-136.

49. See reference 17, pp 118-119.

50. See reference 47.

51. See reference 47.

52. See reference 17, pp 203-205.

53. See reference 17, pp 196-198.

54. Smith, William F., Structure and Properties of Engineering Alloys: McGraw-Hill: New York, 1981; pp 54-57.

55. Pettiford, P. H., Notes on the Coining Processes for Royal Mint Apprentices; internal document, The Royal Mint; 1952, pp 47-49.

56. Delamare, F.; and Montmitonnet, P., "A Mechanical Analysis of Coin Striking: Application to the Study of Byzantine Gold Solidi Minted in Constantinople and Carthage", Journal of Mechanical Working Technology, **1984**, 10, pp 253-271.

57. Baque, P.; Felder, E.; Hyafil, J.; and D'Eascatha,Y., Mise en forme des metaux, calculs par la plasticite; Dunod: Paris, 1973.

58. Ruud, Clayton O., " X-ray diffaction- Nondestructive Method for Residual Stress Measurement"; In International Advances in nondestructive Testing, 1981,8, 295-315.

59. Dolle, H., "The Influence of multiaxial Stress States, Stress Gradients and Elastic Anisotrophy on the Evaluation of (Residual) Stresses by X-rays", Journal of Applied Crystallography, 1979, 12,489-501.

60. Marion, R.H. and Cohen, J.B., "Anomalies in Measurement of Residual Stress by X-Ray Diffraction", Advances in X-ray Analysis, **1977**, 18, 466-501.

61 See reference 7, p 99.

62. Moore, M.A.; and Douthwaite , R.M., "Plastic Deformation Below Worn Surfaces", Metallurgical Transactions A, **1976**, 7A, pp 1833-1839.

63 See reference 62, p 1833.

64. Noyan, I.C. and Cohen, J.B., An X-ray Diffraction Study of Two Phase Brass; Technical Report #16, contract # N00 014-80-C8116, January 1978, Office of Naval Research.

65. Metals Handbook; Ninth ed.; Volume 2, "Properties and Selection: Nonferrous Alloys and Pure Metals"; American Society for Metals: Metals Park, Ohio; pp679-680.

66. Report on Visit to U.S.A. and Canadian Mints in April 1949; Internal report, The Royal Mint; 1949.

67. Hunter, George, Assistant Director of Technology, The U.S. Mint, personal communication, 1987.

68. See reference 3, pp 553-555.

69. Thompson, F.C., "The Use of the Microscope in Numismatic Studies". In The Numismatic Chronicle, Sixth Series, Vol. XVI, 1956, pp 329-338.

70. a) Krawitz, A.D.; Brune, J.E.; and Schumank, M.J., "Measurements of Stress in the Interior of Solids with Neutrons". In Residual Stress and Stress Relaxation; Eric Kula Ed.; Plenum Press:New York, 1982; pp 139-155. b) Pintschovius, L.; Jung, V.; Macherauch, E.; Schäfer, R.; and Vöhriner, O., "Determination of Residual Stress Distributions in the Interior of Technical Parts by Means of Neutron Diffraction". In Residual Stress and Stress Relaxation; Eric Kula Ed.: Plenum Press: New York, 1982; pp 467-482. c) Noyan, I. C. and Cohen, J.B. Residual Stress Measurement by Diffraction and Interpretation: Springer-Verlag: New York, 1987, pp 111-116.

71. See reference 17, p 115.

72. Krawitz, A.D.; Brune, J.E.; and Schumank, M.J., "Measurements of Stress in the Interior of Solids with Neutrons". In Residual Stress and Stress Relaxation; Eric Kula Ed.; Plenum Press:New York, 1982; pp 139-155.

73. See reference 17, p 115.

74. See reference 72, p 154.

75. Friedhander, G.; Kennedy, J.W.; Macias, E.S.; and Miller, J.M., Nuclear and Radiochemistry, third ed., Wiley and Sons: New York, 1981, pp 22, 614, 622-623.

76. Halliday, David; and Resnick, Robert., Fundamentals of Physics, revised ed, John Wiley and Sons: New York; 1974, p 323.

77. Lemons, Ross A. and Quate, Calvin F., "Acoustic Microscopy", In Physical Acoustics, W.P. Mason Ed., Academic Press: New York; 1979, Vol XIV, pp 1-92, see p 1.

78. Nikoonahad, Mehrdad, "Recent Advances in High Resolution Acoustic Microscopy", Contemporary Physics, **1984**, 25, pp 129-158.

79. See reference 79, p 323.

80. "Acoustics," Van Nostrand's Scientific Enclycopedia, 1989, 1, pp 20-26.

81. Halliday, David; and Resnick, Robert, Fundamentals of Physics, revised ed, John Wiley and Sons: New York; 1974, p 306.

82. Pollard, H.F., Sound Waves in Solids, Pion: London; 1977, p 23.

83. See reference 82, p 69.

84. See reference 82, p 69-73.

85. Briggs, Andrew, An Introduction to Scanning Acoustic Microscopy, Microscopy Handbooks,12 ,Royal Microscopy Society: Oxford, 1985, p 21-24.

86. Szilard, John, "Ultrasonics," Encyclopedia of Physical Science and Technology, Academic Press: Orlando, Florida, 1987, 14, pp 191-209.

87. See reference 80, p21.

88. Krautkraemer, Josef, Ultrasonic Testing of Materials, 2nd ed., translation of the 3rd rev. german ed., Springer Verlag: Berlin, 1977, pp 119-120.

89. See reference 88, p 126.

90. Sittig, Erhard K., "Acoustic Wave Devices," Encyclopedia of Physical Science and Technology, Academic Press: Orlando, Florida, 1987, 1, pp 83 - 109.

91. See reference 85, p 4.

92. Cheeke, J.D.N., "Cryogenic Acoustic Microscopy." In Ultrasonic Methods of Evaluation of Inhomogeneous Materials; NATO Advanced Study Institute series E, Applied Sciences, No. 126: Erice, Italy, 1985, pp .

93. See reference 77, pp 3-20.

94. Kessler, Lawrence W.; and Yuhas, Donald E., "Acoustic Microscopy - 1989," Proceedings of the IEEE, **1979**, 67, pp 526-536.

95, a) Lemons, Ross A. and Quate, Calvin F., "Acoustic Microscope-- Scanning Version," Applied Physics Letters, **1974**, 24, pp163-165.
b) Nikoonahad, Mehrdad, "Recent Advances in High Resolution Acoustic Microscopy", Contemporary Physics, **1984**, 25, p 1.

96 Gilmore, R., "Acoustic Microscopy"; In the Encyclopedia of Materials Science and Engineering, Pergamon Press: Oxford, **1986**, 1, pp 38-43.

97 Gilmore, R.S.; Tam, K.C.; and Howard, D.R., Acoustic Microscopy from 10 to 100 MHz for Industrial Applications; Technical Report No. 86CRD015; General Electric Technical Information Series; General Electric Company: Schenectady, New York, 1986, p3.

98. Somekl, M.G., "Consequences of Resonant Surface-Wave Excitation on contrast in reflection Scanning Acoustic Microscope", IEE Proceedings, **1987**, 134, pp 290-300.

99. See reference 98, p 290.

100. Jipson, V. and Quate, C.F., "Acoustic Microscopy at Optical Wavelengths," Applied Physics Letters, **1978**, 32, pp789-791.

101. Burton, Nigel, "NDT Applications of Scanning Acoustic Microscopy," IEE Proceedings, **1987**, 134, pp283-289.

102. See reference 101, p284.

103. Korpel, A.; Kessler, L.W.; and Palmero, P.R., "Acoustic Microscope Operating at 100 MHz," Nature, **1971**, 232, pp 110-111.

104. Kessler, L.W., "Imaging with Dynamic-Ripple Diffraction", In Acoustic Imaging, G. Wade, Ed. Plenum: New York, 1976, pp 229-239.

105. See reference 96, p 45.

106. See reference 96, p 39.

107. See reference 88, p 115.

108. Preston,Jr., K., "Advances in Acoustic Holography", Angewandte Chemie International Edition, **1972**, 11, pp 279-287, see p 280.

109. Holt, A.E.; and Brophy, J.W., "Acoustic Holography." In the Encyclopedia of Materials Science and Engineering, Pergamon Press: Oxford, **1986**, 1, pp 35-38.

110. Kock, Winston E., "Sound Visualization and holography," The Physics Teacher, **1975**, 13, pp 14-22, see p 18.

111. See reference 79, p 708.

112. See reference 82, p 309-310.

113. See reference 108, p 281.

114. Aldridge, Edward E., Acoustical Holography, Merrow: Watford, England; 1971, p 7.

115. See reference 88, p 187.

116. See reference 88, p 188.

117. See reference 88, p 190.

118. See reference 109, p35.

119. Brenden, Byron B., "Acoustical Holography", Optical Engineering, **1975**, 14, pp 495 -497.

120. See reference 114, p 20-25.

121 See reference 114, p 22.

122. Lin,Z.; Lee, H.: Wade, G.; Oravecz, M.G.; and Kessler, L.W., "Holographic Image Reconstruction in Scanning Laser Acoustic Microscopy," IEEE Transactions on Ultrasonic, Ferroelectrics and Frequency Control, **1987**, UFFC-34, pp 293-299.

123. Yu, B.Y.; Oravecz, M.G.; and Kessler, L.W., "Multimedia Holographic Image Reconstruction in a Scanning Laser Acoustic Microscope," In Acoustic Imaging, Lawrence W. Kessler, Ed., New York: Plenum, 1988, 16, pp 535-542.

124. Wey, A.C.: Kessler, L.W., "3-D Localization of Flaws in Structural Ceramics by Use of Scanning Laser Acoustic Microscopy." Presented at the 13th Annual Conference on Composites and Advanced Ceramics, Cocoa Beach, Fla, 1/15 - 1/18/89.

125. Hurley, Dan, Sonoscan, Corp., Chicago,Il, personal communication, April 20, 1989.

126. See reference 122, p 299.

127. Charles, J.A. and Leake, J.A., "Problems in the Fluorescence Analysis of Cu/Ag Byzantine Trachea and Metallurgical Information from Sections," In Methods of Chemical and Metallurgical Investigation of Ancient Coinage, E.T. Hall and D.M. Metcalf ED., Royal Numismatic Society Special Publication Number 8: London, 1972, pp 211 - 218.

128 Condamin, J. and Picon, M., "Changes suffered by Coins in the course of time and the Influence of these on the Results of Different Methods of Analysis, " In Methods of Chemical and Metallurgical Investigation of Ancient Coinage, E.T. Hall and D.M. Metcalf ED., Royal Numismatic Society Special Publication Number 8: London, 1972, pp 49 - 66.

129. Saryan, L.A., "Better Numismatics through Chemistry", World Coin News,**1987**,14(11), 8-16.

130. Brooks, C.J; Bentteley, I.G.; and Loxston, Mathematics and Statistics for Chemists John Wiley and Sons: New York,1966, p 352.

131. See reference 37, p 99.

132. See reference 17, p 186.

133. Bevington, Philip R., Data Reduction and Analysis for the Physical Sciences, McGraw-Hill: New York,1969, p 88.

134. See Reference 130, p 294.

135. See reference 66.

136. See reference 55.

Mary Frances Striegel

VITA

Date of Birth:	February 7, 1958
Place of Birth:	Louisville, Kentucky
Undergraduate Study:	University of Louisville, Louisville Kentucky B.A. Fine Arts, B.A. Chemistry, 1980
Graduate Study:	Indiana University Purdue University at Indianapolis, Indianapolis, Indiana M.S. Analytical Chemistry, 1983 Washington University, St. Louis, Missouri Ph.D. expected May, 1989
Professional Societies:	American Chemical Society
Honors/Awards:	National Scholastic Art Scholarship, University of Louisville, 1976-1977 Dissertation Fellowship, Washington University 1987-1988
Scholastic and Professional Experience:	Consultant, Washington University Technical Associates, 1987 Teaching Assistant, Washington University, 1983-1987 Teaching Assistant, Indiana University Purdue University at Indianapolis, 1981-1983 Teaching Assistant, Lab Technician University of Louisville, 1979-1981

Publications:

Stodulski,L; Bass, P.; & Striegel, M.F., "Analyses of Bronzes", Technical Appendix, Oriental Art, Indianapolis Museum of Art, 1983.
Stahl, Alan M., Gaspar, Peter P., and Striegel, Mary F., "The Analysis of a Hoard of Venetian Torneselli", Metallurgy in Numismatics, in press.